A GPS modeling study of earthquakes and deformation in northern Central America and along the Middle America trench: 1999 to 2017

by

Andria P. Ellis

A dissertation submitted in partial fulfillment of

the requirements for the degree of

Doctor of Philosophy

(Geophysics)

at the

UNIVERSITY OF WISCONSIN-MADISON

2017

Date of final oral examination: 12/04/2017

The dissertation is approved by the following members of the Final Oral Committee:

Dr. Charles DeMets, Albert and Alice Weeks Professor, Geoscience
Dr. Harold J. Tobin, Professor, Geoscience
Dr. Basil Tikoff, Professor, Geoscience
Dr. Clifford H. Thurber, Professor, Geoscience
Dr. Michael Plesha, Professor, Engineering Physics

In loving memory of

Uncle Jerry

ACKNOWLEDGEMENTS

Prior to beginning my graduate career, I had many teachers and professors who nurtured me as a young student, engineer, and scientist. I would be remiss if I did not mention Dr. Kurtis Burmeister (Professor of Geoscience) and Dr. Camilla Saviz (Professor of Civil Engineering) at the University of the Pacific for initially seeing my academic potential and for encouraging me to continue my studies. Both of your support and friendship over the last 10+ years has helped me in many, tangible and intangible ways. Thank you for being outstanding undergraduate professors and being completely dedicated to my success and growth. I appreciate our continued relationship, both academic and personal. You are my dearest role models and sources of inspiration.

I would like to sincerely thank Dr. Chuck DeMets for being an amazing PhD advisor and for making my graduate school experience positive and enjoyable. Your continued instruction, support, and availability helped me grow intellectually and made my PhD endeavor possible. I deeply appreciate your patience and the time you dedicated to perfecting our science and developing me into a better scientist and writer. I also want to thank you and Lynn for your unwavering support throughout the last 6.5 years with all the ups and downs of my young adult life. I am very lucky to have you as my PhD advisor.

Many thanks to the other members of my PhD defense committee: Basil Tikoff, Cliff Thurber, Harold Tobin, and Mike Plesha. I appreciate the time that you all gave to guide me through my PhD candidacy and to review my final dissertation materials. Basil, thank you for bringing me in as a graduate student to Weeks Hall and introducing me to Geoscience and the neotectonics of Central America. Cliff, your classes in Seismology and Inverse Theory challenged me to become a better mathematician, programmer, and modeler. I continue to use

the knowledge that I gained from your classes as the platform for my research. Harold, thank you for celebrating with me when good luck was on my side and for showing empathy and understanding through difficult times. I appreciate your easygoing nature and ability to put perspective on seemingly overwhelming situations. Finally, Dr. Plesha, I thoroughly enjoyed your Finite Elements class and am grateful for the time you have dedicated over the years to attend my Preliminary Examination and my review my PhD Thesis. Congratulations on your recent retirement!

I feel very lucky to be a member of the Weeks Hall Geoscience community, which was a great source of friendship and feedback over the last 6.5 years. I am forever grateful to Hélène LeMével for always being confident in my academic ability even when I doubted myself. I will always treasure the countless cups of tea, conversations, and adventures we shared. Thank you for being a self-assured, unwavering friend. Double thanks for traveling from D.C. to attend my PhD defense! I feel honored to have your support and to have you as a friend. Nathan Andersen, thanks for being my first friend in Weeks Hall and for supporting me to the very bitter end. I am grateful for your availability to listen to my struggles and the easy confidence you have in my intellectual and personal capacity. I look forward to seeing your research and family grow over the next several years. And Tyler Blum, our incredible rock climbing outings to Devils Lake, rounds of Pandemic (board game), near death experience(s), trips to Culver's, and painful puns are beyond words. Thank you for your great company, easy going nature, and willingness to be a rock-solid friend when I needed you.

I was fortunate to have great discussions and friendships with several other Weeks Hall folks that have passed through over the years including: Brooke Norsted, Ninfa Bennington, Shannon Graham, Jake (Codye) Cammack, Daniel Alvarado, Susanna Webb, Tamara Jeppson,

Chloe Bonamici, Bin Guo, Sarah Lemon, Bryn Benford, JoAnn Gage, Nick Levitt, and Jessica Feenstra. Thank you all for sharing your time here with me.

I am also in debt to my non-academic friends for making Madison my new home. My Thursday-night ceramics group (Todd Hafele, Bernice Armold, John Cejka, Tiffanie Petkus, Gail Hutchinson, and Kate Marker) were a tremendous source of creativity, encouragement, light-hearted laughs, deep discussions, and unbiased advice over the last several years. I also express my appreciation to Dan Sutton for teaching me how to sail Badger Sloops and Scows and for sharing the wonders of wind and water with me. Catalina Munteanu and Simon Goldberg, thank you for being my closest friends in the Tenney Park neighborhood. The meals, cups of tea, tunes, celebrations, and companionship we shared will always be precious to me. I appreciate your warm hearts and generous spirits. I miss you two dearly, and Madison will never be complete without you.

Finally I would like to thank my mom, dad, twin brother, and grandma in California for their love and support through my academic journey. Twenty-one semesters of college may seem a little insane, but thank you for being confident in my ability to succeed. I also appreciate you traveling to Wisconsin during the middle of winter to celebrate my graduation with me.

ABSTRACT

Northern Central America is a tectonically complicated region prone to hazardous earthquakes due to the confluence of the Motagua-Polochic fault zone with the Middle America trench and strike-slip faults in the Central America volcanic arc. These three major fault zones converge at the western end of the Caribbean plate where the Cocos plate subducts under the North America and Caribbean plates. Literature from the 1970s and 1980s focused on whether a discrete North America-Caribbean-Cocos plate triple junction existed, and how the relative motions of the upper North America and Caribbean plates were accommodated. The discovery of a fourth major crustal block, the Central America forearc sliver, from seismic and geodetic observations made a three-plate triple junction geometrically impossible and introduced a new set of questions related to how deformation of the upper plate accommodates relative movements between the Caribbean plate, North America plate, and Central America forearc sliver where they intersect in the upper plate. My dissertation uses GPS and numerical modeling to measure and quantify earthquake transients and crustal deformation related to fault interactions in northern Central America and consists of three related chapters.

The first chapter of my dissertation is a geodetic study of a M_w = 7.4 subduction zone earthquake that occurred in 2012 offshore from our Guatemala GPS (Global Positioning System) network. For this study, I inverted coseismic site offsets and postseismic amplitudes to determine best-fitting coseismic and afterslip rupture distributions on the Middle America trench. I also determined the maximum likely viscoelastic deformation for the earthquake to test whether the transient postseismic deformation was dominated by fault afterslip or viscoelastic flow. This work was published in *Geophysical Journal International* in January 2015.

The second chapter of my dissertation derives a new 200+ site GPS velocity field for

northern Central America. Doing so was complicated by the occurrence of four M>7 earthquakes since 2009, which perturbed the velocities of many of the GPS sites. To extract the interseismic velocity field from position time-series, we use TDEFNODE software to simultaneously model source parameters for coseismic rupture and transient afterslip from the 2012 El Salvador (M_w=7.3), 2012 Guatemala (M_w=7.4), and 2009 Swan Islands (M_w=7.3) earthquakes. The resulting, corrected best-fitting GPS site velocities are used in my third and final chapter.

Finally, I address a variety of questions regarding several major faults that are the root of natural hazard studies in northern Central America. The 200+ site GPS velocity field derived in Chapter 2 far exceeds any previous velocity field for this region and represents a new standard for studying the tectonics of northern Central America. An inversion of the new velocity field using an eight-block elastic model gives the following unique or improved results with respect to previous work: 1) First evidence for a nearly rigid Chortis block south of the Motagua fault; 2) Evidence for southward transfer of slip from the western Motagua fault into the Guatemala City graben and other nearby normal faults; 3) A well-bounded estimate on partitioning of plate boundary slip on the Motagua and Polochic faults; 4) A first plate tectonic estimate of Cocos plate subduction below the Central America forearc sliver; 5) The first geodetic estimate of slip rate variations along the Central America volcanic arc, including the first slip rate estimate for the poorly-understood Jalpatagua fault in southern Guatemala; 6) The first geodetic estimate of distributed deformation in the Chiapas Tectonic Province; 7) Evidence for stronger locking offshore southern Mexico and even weaker shallow locking offshore Guatemala and El Salvador than previously estimated; 8) A refined estimate of how extension is distributed across the grabens of western Honduras and southern Guatemala; 9) Strain-rate tensors consistent with no significant deformation of the elongate Central America forearc sliver, but extension within the

Gulf of Fonseca step-over in the Central America volcanic arc; 10) Evidence for slower slip along the Motagua fault than any previous estimate and a well-determined geodetic estimate for the long-term slip rate of the Polochic fault.

TABLE OF CONTENTS

CHAPTER 1

Geodetic slip solutions for the M_w=7.4 Champerico (Guatemala) earthquake of 2012 November 7 and its postseismic deformation

Published in Geophysical Journal International, January 2015, v. 201 (2), p. 856-868.

SUMMARY

As the first large subduction thrust earthquake off the coast of western Guatemala in the past several decades, the 2012 November 7 M_w = 7.4 earthquake offers the first opportunity to study coseismic and postseismic behavior along a segment of the Middle America trench where frictional locking makes a transition from weak locking off the coast of El Salvador to strong locking in southern Mexico. We use measurements at 19 continuous GPS sites in Guatemala, El Salvador, and Mexico to estimate the coseismic slip and postseismic deformation of the November 2012 Champerico (Guatemala) earthquake. An inversion of the coseismic offsets, which range up to ~47 mm at the surface near the epicenter, indicates that up to ~2 m of coseismic slip occurred on a ~30 x 30 km rupture area between ~10 and 30 km depth, which is near the global CMT centroid. The geodetic moment of 13 x 10^{19} N·m and corresponding magnitude of 7.4 both agree well with independent seismological estimates. Transient postseismic deformation that was recorded at 11 GPS sites is attributable to a combination of fault afterslip and viscoelastic flow in the lower crust and/or mantle. Modeling of the viscoelastic deformation suggests that it constituted no more than ~30 per cent of the short-term postseismic deformation. GPS observations that extend six months after the earthquake are well fit by a model in which most afterslip occurred at the same depth or directly downdip from the rupture zone and released energy equivalent to no more than ~20 per cent of the coseismic moment. An independent seismological slip solution that features more highly concentrated coseismic slip than our own fits the GPS offsets well if its slip centroid is translated ~50 km to the west to a position close to our slip centroid. The geodetic and seismologic

slip solutions thus suggest bounds of 2–7 m for the peak slip along a region of the interface no larger than 30 x 30 km.

1.1 INTRODUCTION

During the past century, approximately ten M>7 earthquakes have ruptured the Cocos plate subduction interface below western Guatemala and adjacent areas of the Mexican state of Chiapas (Fig. 1.1; White *et al.* 2004; Franco *et al.* 2005), resulting in numerous fatalities and extensive property damage. The focus of this study is the M_w=7.4 2012 November 7 earthquake off the western coast of Guatemala (Fig. 1.1), which caused ~50 deaths and extensive damage to houses and buildings in the coastal city of Champerico and the inland cities of San Marcos and Quetzaltenango. As the most recent large earthquake to rupture the Guatemala trench segment and the first since regional GPS measurements began in the late 1990s (Lyon-Caen *et al.* 2006), the 2012 Champerico earthquake offers an excellent opportunity to study a poorly understood segment of the Middle America trench, where frictional locking makes a transition from weak locking offshore from El Salvador (Lyon-Caen *et al.* 2006; Correa-Mora *et al.* 2009; LaFemina *et al.* 2009; Franco *et al.* 2012) to strong locking (Correa-Mora *et al.* 2008; Franco *et al.* 2012) offshore from the Chiapas trench segment of southern Mexico. Here, we use observations from 19 GPS sites in northern Central America to determine best-fitting solutions for coseismic and postseismic slip associated with the 2012 Champerico earthquake, including first estimates of the magnitude and depth range of fault afterslip triggered by a subduction thrust earthquake along the Guatemala trench segment. Our analysis complements the seismological study of Ye *et al.* (2013), who inverted regional seismic and teleseismic P waves from the earthquake to determine a coseismic slip solution. Their results suggest that coseismic slip of up to 6.6 m at depths of 20–25 km

released most of the seismic energy within a relatively compact area, with the remaining geodetic moment released by lesser slip (0.7 m) along a broader region updip from the region of high slip. As part of our analysis, we examine whether the location and distribution of the seismologically derived slip are consistent with our geodetic measurements of the coseismic elastic deformation at locations immediately onshore from the earthquake.

1.2 PLATE TECTONIC SETTING

At the location of the 2012 Champerico earthquake, the Cocos Plate subducts beneath the North America and Caribbean plates at respective velocities of 77 ± 3 mm yr^{-1} towards N32°E ± 1° and 71 ± 3 mm yr^{-1} towards N21°E ± 1° (Fig. 1.1; DeMets *et al.* 2010), roughly orthogonal to the trench (DeMets 2001). The subduction interface must thus accommodate ~78 m of thrust motion per century through some combination of thrust earthquakes and possibly creep. Since 1900, nearly all of the Middle America subduction interface along the coast of El Salvador, Guatemala, and southern Mexico has ruptured in earthquakes with magnitudes between 7 and 8 (Fig. 1.1). Seismic observations of nearly all these earthquakes are non-existent or of poor quality (White *et al.* 2004). Little therefore is known about the seismogenic behavior of the interface, including the typical depth and magnitude of thrust earthquakes, the extent of their rupture zones, their recurrence intervals, and whether earthquakes are accompanied by significant afterslip.

Seismological and geodetic studies have defined several first-order characteristics of the subduction interface in this area. One important characteristic is progressive steepening of the dip of the subducting Cocos Plate to the southeast (Fig. 1.2b; Burbach *et al.* 1984), corresponding to the transition from Cocos-North America plate subduction in the northwest to Cocos Caribbean plate subduction in the southeast (Fig. 1.2a). Although the effects of the transition on thrust

earthquake frequency, depths, and magnitudes are poorly understood, GPS observations indicate that the transition coincides with strong locking below southern Mexico, where the slab dip is shallower and North America is the upper plate (Correa-Mora *et al.* 2008; Franco *et al.* 2012) to weak locking below El Salvador and Guatemala, where the slab dip is much steeper than below southern Mexico and the upper plate is the Central American forearc sliver (Lyon Caen *et al.* 2006; Correa-Mora *et al.* 2009; LaFemina *et al.* 2009; Franco *et al.* 2012). The 2012 Champerico earthquake occurred near the transition between the strongly and weakly locking interfaces (Fig. 1.2a).

1.3 DATA

1.3.1 GPS network and observations

The data used for our modeling are from 23 continuous GPS stations in Guatemala, El Salvador and southern Mexico, 19 of which were operating during the 2012 Champerico earthquake and four of which were installed to monitor postseismic deformation (sites CHPO, MAZ0, QUE1 and SMHO; Fig. 1.3). The majority (12) of the stations are operated by Guatemala's Instituto Geográfico Nacional. The others are operated by a variety of national agencies and geophysical investigators. All 23 sites consist of modern dual-frequency P-code GPS receivers and antennas.

GPS data from these stations were processed with Release 6.1 of the GIPSY software suite from the Jet Propulsion Laboratory (JPL). No-fiducial daily GPS station coordinates were estimated using a precise point-positioning strategy (Zumberge *et al.* 1997), including constraints on *a priori* tropospheric hydrostatic and wet delays from Vienna Mapping Function (VMF1) parameters (http://ggosatm.hg.tuwien.ac.at), elevation dependent and azimuthally dependent GPS and satellite antenna phase centre corrections from IGS08 ANTEX files (available via ftp from

sideshow.jpl.nasa.gov), and corrections for ocean tidal loading (http://froste.oso.chalmers.se). Wide- and narrow-lane-phase ambiguities were resolved for all the data using GIPSY's single-station ambiguity resolution feature (Bertiger *et al.* 2010).

All daily no-fiducial station location estimates were transformed to ITRF2008 (Altamimi *et al.* 2011) using daily seven-parameter Helmert transformations from JPL. Spatially correlated noise between stations is estimated from the coordinate time-series of well-behaved continuous stations from within and outside the study area and is removed from the time-series of all sites (Márquez-Azúa & DeMets 2003). Noise in the daily 3-D site locations averages 1.5 mm in the northing and easting components and 3–4 mm in the vertical component.

Fig. 1.3 shows the estimated coseismic offsets. At sites COAT, COTZ, HUEH, and MTP1, where rapid postseismic deformation was measured, we estimated the post-earthquake site locations from only 24 hr of data after the earthquake. At stations more distant from the earthquake, where no significant postseismic deformation was detected, we estimated the post-earthquake site locations from 5 to 14 d of observations after the earthquake. The largest measured offsets were at COAT (47±3 mm), MTP1 (37±1 mm) and HUEH (15±3 mm). The pattern of coseismic offsets is consistent with that expected for a shallow-thrust earthquake, with the site offsets pointing towards the offshore rupture zone and decreasing in magnitude with distance from the rupture zone. No clear pattern of vertical offsets was observed, indicating that vertical deformation from the earthquake was below the vertical resolution of the GPS data.

Overall, 11 continuous GPS sites recorded significant postseismic deformation (Fig. 1.4). Seven sites were operating during the earthquake and four were added within two weeks of the earthquake (locations indicated by blue symbols in Fig. 1.3). Results from modeling the postseismic deformation recorded at these 11 sites are described in Section 1.5.

1.4 COSEISMIC SLIP SOLUTION

1.4.1 Inverse method and assumptions

We estimate the distribution of slip during the Champerico earthquake from a standard inversion of the 3-D coseismic offsets and their uncertainties assuming that the deformation occurs on a fault embedded in a homogeneous, elastic half-space (Okada 1985). We discretized the subduction interface near the Champerico earthquake into 42, ~30 x 30 km rectangular subfaults (Fig. 1.5a). We adopt subduction contours from Hayes *et al.* (2012) to approximate the along-strike and downdip geometry of the subducting plate. In Section 1.4.2, we describe results that suggest our geodetic slip solution is robust with respect to plausible variations of the subduction interface geometry.

We estimate the slip magnitude for each of *m* fault patches by solving a version of the linear system **d=Gm**, as follows:

$$\begin{bmatrix} \mathbf{WG} \\ \alpha\mathbf{F} \end{bmatrix} \mathbf{m} = \begin{bmatrix} \mathbf{Wd} \\ 0 \end{bmatrix}, \quad (1)$$

where **G** is a 3*n* x *m* Greens function that specifies the surface deformation in response to assumed unit slip across each patch on the fault, **d** is a 3*n*-element vector that contains the north, east and vertical offsets at *n* GPS sites, **m** contains the best estimate of the slip magnitude at each fault patch on the subduction interface, **W** is a 3*n* x 3*n* diagonal weighting matrix composed of the reciprocal of the offset uncertainties, α is the smoothing coefficient, and **F** is a smoothing matrix with first-order Tikhonov regularization (Aster *et al.* 2013). Forward modeling of the surface deformation to generate the **G** matrix was done with DISL, a code for elastic half-space dislocation modeling (Larsen 1992).

The inversion procedure enforces smoothing and sense-of-slip (non-negativity) constraints using a bounded-variables least-squares algorithm (Stark & Parker 1995) to avoid physically implausible solutions. The algorithm minimizes $||\mathbf{Gm}-\mathbf{d}||^2$ for all elements of m greater than zero.

During different parts of the analysis, we also use the model resolution ($\mathbf{R}_m=\mathbf{G}^{\sharp}\mathbf{G}$) and data resolution ($\mathbf{R}_d=\mathbf{GG}$) matrices, where $\mathbf{G}^{\sharp}=(\mathbf{G}^T\mathbf{G}+\alpha^2\mathbf{F}^T\mathbf{F})^{-1}\mathbf{G}^T$. The former matrix specifies the resolution of the slip solution as a function of location on the fault plane, whereas the diagonal elements of $\mathbf{R}_d$, which are known as the data importance, specify the relative amount of information that individual data contribute to the solution.

Best-fitting slip solutions were optimized by uniformly varying the slip rake between 68◦ and 100° for all 42 fault patches for a range of possible smoothing coefficients (α) that minimize reduced chi-square (χ^2_v), where χ^2_v is χ^2/dof and the degrees of freedom (dof) are defined by Hansen (1992) as:

$$\text{dof} = trace[\mathbf{I} - \mathbf{G}(\mathbf{G}^{\mathrm{T}}\mathbf{G} + \alpha^2\mathbf{F}^{\mathrm{T}}\mathbf{F})^{-1}\mathbf{G}^{\mathrm{T}}] \qquad (2)$$

The reduced chi-square criteria is a robust means for finding the optimal trade-off between the data least-squares fit and the complexity of the best-slip distribution.

1.4.2 Coseismic slip solution: preferred and alternative estimates

Fig. 1.5a shows the best-fitting coseismic fault-slip solution for an optimized rake of 82°, where 90° constitutes pure dip-parallel thrusting. The most slip (~220 cm) occurred on a fault patch between 10 and 20 km depth and close to the earthquake centroid (red star in Fig. 1.5a). Lesser slip (90 and 30 cm) extended downdip to 30 km depth northeast of the main slip area (Fig. 1.5a). The geodetic moment estimated from the best-fitting slip solution, 12.7 x 10^{19} N·m (M_w= 7.36) for a shear modulus of 40 GPa, agrees well with the seismological moments of 14.5 x 10^{19} N·m

(M_w=7.41) from the Global CMT catalogue (Dziewonski *et al.* 1981; Ekström *et al.* 2012), 13.3 x 10^{19} (M_w=7.34) from the U.S.G.S. and 15 x 10^{19} N·m from Ye *et al.* (2013). The three highest-slip patches, all between depths of 10 and 20 km, account for most (~85 per cent) of the estimated moment. We interpret lesser slip along several deeper, isolated fault patches as artifacts of the inversion that modestly improve the fits at nearby high importance sites, with no physical significance and no impact on our solution.

The north, east, and vertical offsets at the 19 GPS sites are well fit by the best-fitting slip solution (Fig. 1.5b and Table 1.1), with a weighted RMS (WRMS) misfit of 1.0 mm and reduced chi-square of 2.57. The offsets at the four sites nearest the rupture zone (MTP1, COAT, COTZ, and HUEH), where small variations in the location or magnitude of the modeled slip cause large changes in the predicted site offsets and hence model fit, have a summed data importance of 85.4 per cent (Table 1.1). By implication, the best-fitting slip solution is determined principally from those four offsets. That the best-fitting slip solution fits the other 15 site offsets so well (Fig. 1.5b) indicates that the data and solution are highly consistent.

As a blind test of the slip solution described above, a subset of the coauthors estimated an alternative slip solution in parallel with the analysis described above. The alternative slip solution imposes a simpler form on the coseismic slip, consisting of a single fault patch with uniform coseismic slip (Fig. S1.2b). The strike (293°), dip (29°) and rake (78°) of the fault patch were fixed to seismologically derived estimates from Ye *et al*. (2013). The dimensions and location of the slip patch were varied to optimize the fit. The best-fitting solution consists of ~2.8 m of slip along a rectangular fault area that is 42 km along-strike, 20 km downdip, and has its upper edge at a depth of 20 km (location indicated by the black rectangle in Fig. S1.2b). The location, dimensions and slip amount are similar to those for our preferred solution. The geodetic moment of this solution, 8

x 10^{19} N·m, is roughly 60 per cent smaller than for our preferred solution and is smaller than any of the seismologic estimates. The WRMS misfit is ~1.5 mm, roughly 50 per cent larger than for the preferred solution. Given the simplicity of this solution, we are encouraged by its good agreement with both the data and our preferred solution and conclude that to first-order, our estimate of the coseismic slip is robust (Table S1.1).

1.4.3 GPS network resolution and robustness of the slip solution

Given the one-sided distribution of the GPS sites with respect to the offshore rupture, we used a variation of the checkerboard test to evaluate how accurately the GPS offsets resolve the location and magnitude of offshore slip. The slip solutions described above and the seismologic slip solution of Ye *et al.* (2013) indicate that most slip during the Champerico earthquake was concentrated in a compact rupture zone. We thus elected to test how well the slip magnitude and location can be recovered for a hypothetical thrust earthquake in which 1m of downdip slip occurred along two adjacent slip patches (Figs S1.3–S1.5). For a series of hypothetical earthquakes that are located progressively farther down the subduction interface (locations shown in panels A1–G1 of Figs S1.3–S1.5), we used DISL to predict synthetic displacements at each GPS benchmark and perturbed the synthetic offsets with random Gaussian noise assuming GPS uncertainties of ±1 mm for the north and east offset components and ±2.5 mm for the vertical offset components. Inversions of the noisy synthetic data for each model correctly recovered the slip-patch locations for depths between 10 and 60 km, independent of the assumed rupture depth, and slip magnitudes (panels B3-F3 of Figs S1.3-S1.5). Slip at the depths recovered from our observed coseismic offsets is thus well resolved by the GPS network. Hypothetical slip at depths

shallower than 10 km or below 60 km could not however be recovered (panels A3 and G3 of Figs S1.3 and S1.5). Our ability to resolve slip at these depths is thus limited.

1.5 POSTSEIMSIC DEFORMATION: NOVEMBER 2012 TO MAY 2013

Deformation after a large subduction earthquake represents a superposition of a site's long-term interseismic motion and transient deformation from an unknown combination of fault afterslip and viscoelastic flow in the lower crust and upper mantle. We first evaluate whether viscoelastic flow triggered by the earthquake could be responsible for most or all of the postseismic deformation. We then invert the postseismic GPS time-series in a two-stage process to constrain the location and magnitude of fault afterslip.

1.5.1 Viscoelastic deformation

We first test the hypothesis that all or most of the postseismic deformation (e.g. Fig. 1.4) occurred in response to viscoelastic flow that may have been triggered by the Champerico earthquake. To approximate the viscoelastic deformation, we applied Visco-1-D software (version 3) of Pollitz (1997) to our preferred coseismic slip solution (Fig. 1.5a) assuming a spherical, layered earth model that approximates the properties of continental crust. We approximated the properties of continental crust with a modified version of crustal model M1 of Hearn *et al.* (2013), which consists of an elastic layer from the surface to a depth of 25 km, a Maxwell viscoelastic layer from 25 to 30 km, a stronger layer from 30 to 50 km, and Maxwell viscoelastic material everywhere below 50 km. Unlike Hearn *et al.*, who assumed respective viscosities of 3×10^{19} and 3×10^{18} Pa·s for the lower crust and mantle, we assign a viscosity of 5×10^{17} Pa·s to these two layers in order to approximate a maximum likely viscoelastic response during the months after the earthquake. We

adopt this viscosity from Hu & Wang (2012), who conclude from their analysis of short-term postseismic deformation from the 2004 Sumatra earthquake that the mantle below the upper plate behaves as a biviscous Burgers body with a transient short-term viscosity of 5 x 10^{17} Pa·s and a long-term, steady state viscosity of 10^{19} Pa·s.

Fig. 1.6 shows the predicted viscoelastic deformation onshore from the Guatemala earthquake for the above rheological model and our preferred coseismic slip solution. During the first eight months after the earthquake (the period spanned by our postseismic analysis), the predicted site motions are to the south and west (Figs 1.6a and b), in accord with the directions recorded by continuous GPS sites in the region. The predicted displacements are however too small. For example, at site COAT near the rupture zone, the viscoelastic model predicts motion that is no more than ~30 per cent of that observed after correcting COAT's observed motion for its long-term interseismic movement. The viscoelastic model also incorrectly predicts slow, postseismic subsidence at COAT (Fig. 1.6c), whereas no significant vertical motion was recorded.

We conclude that viscoelastic deformation triggered by the earthquake was at most a minor component of the postseismic deformation and focus hereafter on the more likely explanation, that fault afterslip caused most of the postseismic deformation during the period examined here.

1.5.2 Inversion for best-fitting postseismic surface deformation

Following an earthquake at time t_{eq}, the 3-D displacement $u_i(t)$ at the ith GPS site due to postseismic afterslip and long-term secular motion of the station v_i is given by

$$u_i(t)^{n,e,v} = u_{0i}^{n,e,v} + v_i^{n,e,v} \times (t - t_{eq}) + A_i^{n,e,v} \times \ln\left(1 + \frac{t - t_{\text{eq}}}{\beta}\right) \quad (3)$$

where β is the temporal decay constant for the afterslip and is assumed to be the same at all sites, A_i are the 3-D amplitudes of postseismic deformation at each GPS site, and u_{0i} are the 3-D site

positions immediately after the earthquake (Marone *et al.* 1991). The deformation amplitudes, which are dictated by the elastic response of the crust to afterslip on the subduction interface, vary with location and are used below to model the fault afterslip.

Using eq. (3), we inverted the daily 3-D site positions at all 11 GPS sites where postseismic deformation was detected to estimate the temporal decay constant β, the amplitudes A_i, the intercepts u_{0i} and if necessary, secular velocity components v_i at each site for the north, east and vertical components. We limited the time spanned by the observations to the first six months after the earthquake to increase the likelihood that the deformation samples fault afterslip rather than viscoelastic deformation. At seven sites, we estimated the interseismic velocity components from a year or more of measurements before the earthquake and fixed their velocity terms during the inversion. At the four stations that were installed after the earthquake, we estimated the interseismic velocities v_i along with the amplitudes A_i and initial positions u_{0i}.

Fig. 1.4 shows the fits of the resulting optimized model to selected GPS position time-series. Reduced chi-square is 1.0 for the best-fitting model, indicating that the GPS time-series are fit within their estimated uncertainties for deformation that obeys eq. (3). The normalized misfit is minimized for a decay constant of 10 days (Fig. 1.7a).

1.5.3 Inversion results for postseismic fault afterslip

The spatial pattern of postseismic deformation amplitudes estimated from our inversion of the postseismic station time-series (Fig. 1.7b and Table 1.1) shares many characteristics with the pattern of coseismic offsets (compare Figs 1.5b and d). In both cases, sites move to the SSW towards the rupture zone, with amplitudes/offsets that diminish with distance from the rupture area. The site directions after the earthquake (Fig. 1.5d) however point more uniformly to the SSW

than during the earthquake (Fig. 1.5b), particularly for sites near the coast. Specifically, the direction of postseismic motion at site MTP1 is rotated ~15° clockwise from the coseismic direction at that site (Figs 1.5b and d), possibly indicating that some afterslip occurred directly offshore from MTP1, where no coseismic slip occurred.

Using methods described in Section 1.4.1, we inverted the 33 north, east and vertical site amplitudes and their uncertainties (Table 1.1) to estimate the pattern of afterslip on the subduction interface and optimal direction for the slip. Fig. 1.5c shows the best-fitting afterslip solution for a rake of 82°, for which the fit is optimized. More than 70 per cent of the postseismic slip occurred at depths of 20–30 km or immediately downdip (Fig. 1.5c). In contrast, ~90 per cent of the coseismic slip was concentrated at the same depth or updip from the epicenter (Fig. 1.5a). Our best-fitting afterslip solution includes some afterslip at depths of 30–60 km at most locations that are directly offshore from the GPS sites (Figs 1.5c and d). The earthquake thus may have triggered afterslip along a broader area of the subduction interface than ruptured during the earthquake.

The WRMS misfit of the best-fitting afterslip solution is 0.6 mm with reduced chi-square of 11.8. The amplitudes for sites CHPO, COAT, MAZ0, and MTP1 contribute ~80 per cent of the data importance and thus dominate the slip solution, a fact attributable to their proximity to the zone of afterslip.

Six months after the earthquake, the cumulative energy released by the afterslip was 2.4 x 10^{19} N·m, ~20 per cent of the main shock and equivalent to a M_w=6.9 earthquake. Afterslip was largely concentrated at the same depth or downdip from the earthquake (Fig. 1.5c). In contrast, the earthquake aftershocks were concentrated mostly updip from the hypocentre (Fig. 1.5e). Afterslip and aftershocks therefore appear to have affected different areas of the subduction interface.

1.5.4 Resolution of and constraints on the afterslip location

The number and distribution of GPS stations that recorded postseismic deformation is significantly smaller and more compact than for the earthquake, thereby implying lower resolution of the source of postseismic afterslip. We therefore repeated the resolution tests described in Section 1.4.3 using the 11 GPS stations that recorded postseismic deformation. Tests of a variety of assumed slip locations and imposed slip magnitudes suggest that hypothetical afterslip greater than 50 cm is well resolved at most depths below 10 km. In contrast, slip at the shallowest level in our mesh (0-10 km), where many aftershocks occurred (Fig. 1.5), cannot be resolved if its magnitude is under 50 cm.

We evaluated how well the GPS data constrain the depth of afterslip by comparing the fits of three alternative models for afterslip, one of which restricts all afterslip to depths shallower than 30 km (Fig. 1.8c), a second of which restricts afterslip to depths from 10 to 40 km (Fig. 1.8d), and the third of which restricts afterslip to depths below 40 km (Fig.1. 8e). The first and last of these fit the data poorly, with respective values for reduced chi-square that are ~65 per cent greater and an order-of-magnitude greater (Fig. 1.8a) than for the best-fitting afterslip solution. The deep subfault model is rejected at much greater than the 99 per cent confidence level based on an F-ratio comparison of their fits to that of the preferred solution. The model that forces afterslip to occur between depths of 10 and 40 km increases the misfit by ~20 per cent relative to the preferred solution (Figs 1.8a and d), constituting a marginally significant increase in misfit (97.7 per cent confidence level).

The above results thus exclude models in which most or all of the afterslip was located updip from the earthquake, where numerous aftershocks were recorded (Fig. 1.5e), or in which

afterslip occurred exclusively on deeper areas of the subduction interface. Our results instead require that afterslip occurred at the same depth or deeper than the main shock.

1.6 DISCUSSION

1.6.1 Comparison to a seismological slip solution

Ye *et al.* (2013), who estimate the distribution of slip during the Champerico earthquake from regional seismic and teleseismic P waves, find that coseismic slip of up to 6.6 m occurred (Fig. 1.9a), with most of the seismic energy concentrated in a compact area at depths of 20–25 km and lesser slip (0.7 m) along a broader region updip from the region of high slip. Their slip solution is more concentrated, farther updip, has higher peak slip and is located ~50 km ESE from both our preferred solution and the CMT centroid (compare Figs 1.5a and 1.9a). Below, we examine the significance and cause of these discrepancies.

Fig. 1.9a compares the coseismic offsets that are predicted by the Ye *et al*. (2013) seismic slip solution to the offsets we measured at each of the 19 GPS sites. Nearly all of the predicted offsets are larger than the observed offsets and are rotated systematically anti-clockwise at the sites near the rupture (Fig. 1.9a), where the predicted deformation directions are sensitive to any mislocation of the modeled slip on the subduction interface. The WRMS misfit, 6.4 mm, is a factor of six larger than for our preferred solution (WRMS=1.0 mm). The seismological slip solution at the location used by Ye *et al.* (2013) is strongly rejected by the GPS data (Fig. 1.9a).

As a test, we systematically translated the Ye *et al.* slip solution towards the earthquake epicenter while reevaluating its misfits to the GPS data. Translating the seismic slip solution 51 km westward to the location shown in Fig. 1.9b greatly improves the fit (Fig. 1.9b). The slip centroid for the translated solution (Fig. S1.2c) coincides with the centroid of our preferred solution (Fig.

S1.2a) and the WRMS misfit for the translated solution is 1.8 mm, much closer to that for our preferred solution. Most of the misfit thus comes from a suboptimal location of the original seismologic slip solution rather than a mischaracterization of how the slip was distributed.

The relatively good fit of the translated seismologic slip solution to the GPS offsets is instructive. That a solution with more concentrated slip and 2–3x higher peak slip amplitude fits the data nearly as well as our preferred solution suggests that the geodetic and translated seismologic solutions constitute possible end-members for the Champerico earthquake slip distribution. Both indicate that coseismic rupture extended no deeper than 30 km, with most energy release occurring at depths of 15–30 km. The seismologic slip solution suggests that lesser slip may have extended up to the trench (Fig. 1.9a), in agreement with the distribution of locally recorded earthquake aftershocks (Fig. 1.5e).

1.6.2 Middle America trench: implications for the Guatemala segment

Our analysis and that of Ye *et al.* (2013) clearly indicate that the 2012 Champerico earthquake was a subduction thrust earthquake that is typical of other strongly locked segments of the Middle America trench/Mexico subduction zone. Unlike the exceptionally shallow 1992 Nicaragua slow earthquake (Satake 1994) and 2012 El Salvador thrust earthquake (Ye *et al.* 2013; Geirsson *et al*., 2015), the Champerico earthquake ruptured the subduction interface at depths of 15–35 km, typical of numerous other thrust earthquakes along strongly locked segments of the Mexico subduction zone. Contrary to the 2012 El Salvador earthquake, whose seismic wave spectra and long-lasting rupture duration resemble those of the 1992 slow Nicaragua earthquake (Ye *et al.* 2013), the Champerico earthquake seismic-source spectra were normal for a subduction earthquake (Ye *et al.* 2013). By inference, strong locking appears to extend along the Guatemala segment at least as far

southeast as the Guatemala/Chiapas border, in accord with GPS results reported by Franco *et al*. (2012). Whether the subduction interface remains strongly locked even farther to the southeast offshore from Guatemala is unknown. The GPS stations that were used by Franco *et al.* (2012) to constrain the location of the offshore transition from strong to weak locking were spaced too far apart to define whether the along strike transition occurs gradually or suddenly. Either seems possible given that factor-of-two variations in locking over distances of several tens-of-km are well documented along the Mexico subduction zone (Correa-Mora *et al.* 2008) and under the Nicoya Peninsula in Costa Rica (Feng *et al*. 2012). GPS measurements at more closely spaced stations along Guatemala's Pacific coast will resolve this in the next few years.

1.7 CONCLUSIONS

Inversions of GPS-recorded coseismic offsets caused by the M_w=7.4 2012 Champerico subduction-thrust earthquake indicate that coseismic fault-slip was concentrated at depths of 10–30 km and extended along strike by ~50 km, in good accord with the locations and distribution of aftershocks associated with the earthquake. Peak slip of ~2 m occurred near 14.0°N, 92.5°W, close to the centroid estimated by the Global CMT project. The geodetic moment of 12.7 x 10^{19} Nm (M_w=7.4) also agrees well with most seismologic estimates. SSW station movement towards the trench dominated transient postseismic deformation recorded by 11 GPS sites near the rupture zone. Forward modeling of the expected viscoelastic deformation based on our best-fitting geodetic solution suggests that it constitutes no more than ~30 per cent of the total postseismic deformation. Further modeling indicates that fault afterslip caused most of the transient deformation, occurred mostly downdip from the main shock, and released energy equal to ~20 per cent of the 2012 rupture (M_w=6.9) within 6 months of the earthquake. The seismological derived

slip solution of Ye *et al.* (2013), which has more concentrated slip and higher peak slip values, fits our coseismic GPS offsets well if the slip solution is translated to the approximate location of our geodetic slip solution.

ACKNOWLEDGEMENTS

This work was funded by NSF grant EAR-1144418 (DeMets) and is based upon work supported by the National Science Foundation under grant EAR-1042906 to UNAVCO. We thank Universidad Mariano Galvez and Universidad San Carlos for logistical support. Data critical for this work were procured from El Instituto Geográfico Nacional (IGN). Postseismic measurements at sites MAZ0, SMH0, QUE1, and CHP0 were possible thanks to funding from INSU-CNRS in France and the help of the French Embassy in Guatemala City. Figures were produced using Generic Mapping Tools software (Wessel & Smith 1991).

REFERENCES

Altamimi, Z., Collilieux, X. & Metivier, L., 2011. ITRF2008: an improved solution of the international terrestrial reference frame, *J. Geod*., **85**, 457– 473.

Aster, R.C., Borchers, B. & Thurber, C.H., 2013. Parameter Estimation and Inverse Problems, *Academic Press*.

Bertiger, W., Desai, S.D., Haines, B., Harvey, N., Moore, A.W., Owen, S. &Weiss, J.P., 2010. Single receiver phase ambiguity resolution with GPS data, *J. Geod*., **84.5**, 327–337.

Burbach, G.V., Frohlich, C., Pennington, W.D. & Matumoto, T., 1984. Seismicity and tectonics of the subducted Cocos Plate, *J. geophys. Res*., **89**, 7719–7735.

Correa-Mora, F. et al., 2009. GPS-derived coupling estimates for the Central America subduction zone and volcanic arc faults: El Salvador, Honduras and Nicaragua, *Geophys. J. Int*., **179**, 1279 1291.

Correa-Mora, F., DeMets, C., Cabral-Cano, E., Marquez-Azua, B. & Diaz-Molina, O., 2008. Interplate coupling and transient slip along the subduction interface beneath Oaxaca, Mexico, *Geophys. J. Int*., **175**, 269–290.

DeMets, C., 2001. A new estimate for present-day Cocos-Caribbean plate motion: implications for slip along the Central American volcanic arc, *Geophys. Res. Lett.*, **28**, 4043–4046.

DeMets, C., Gordon, R.G. & Argus, D.F., 2010. Geologically current plate motions, *Geophys. J. Int*., **181**, doi:10.1111/j.1365-246X.2009.04491.

Dziewonski, A.M., Chou, T.A. & Woodhouse, J.H., 1981. Determination of earthquake source parameters from waveform data for studies of global and regional seismicity, *J. geophys. Res.*, **86**, 2825–2852.

Ekstrom, G., Nettles, M. & Dziewonski, A.M., 2012. The global CMT project 2004–2010: centroid-moment tensors for 13,017 earthquakes, *Phys. Earth planet. Inter*., **200–201**, 1–9.

Engdahl, E.R., van der Hilst, R. & Buland, R., 1998. Global teleseismic earthquake relocation with improved travel times and procedures for depth determination, *Bull. seism. Soc. Am*., **88**, 722–743.

Feng, L., Newman, A.V., Protti, N.M., Gonzales, V., Jiang, Y. & Dixon, T.H., 2012. Active deformation near the Nicoya Peninsula, northwestern Costa Rica, between 1996 and 2010: interseismic megathrust coupling, *J. geophys. Res*., **117**, B06407, doi:10.1029/2012JB009230.

Franco, A., Lasserre, C., Lyon-Caen, H., Kostoglodov, V., Molina, E., Guzmán-Speziale, M., Monterosso, D., Robles, V., Figueroa, C., & Amaya, W., 2012. Fault kinematics in northern Central America and coupling along the subduction interface of the Cocos plate, from GPS data in Chiapas (Mexico), Guatemala and El Salvador, *Geophysical Journal International,* **189**(3): 1223-1236.

Franco, S.I., Kostoglodov, V., Larson, K.M., Manea, V.C., Manea, M. & Santiago, J.A., 2005. Propagation of the 2001–2002 silent earthquake and interplate coupling in the Oaxaca subduction zone, Mexico, *Earth, Planets Space*, **57**, 973–985.

Geirsson, H., LaFemina, P. C., DeMets, C., Hernandez, D. A., Mattioli, G. S., Rogers, R., Rodriguez, M., Marroquin, G., & Tenorio, V., 2015. The 2012 August 27 M_w 7.3 El Salvador earthquake: expression of weak coupling on the Middle America subduction zone, *Geophys. J. Int.,* **202***,* 1677-1689.

Hansen, P.C., 1992. Analysis of discrete ill-posed problems by means of the l-curve, *SIAM Rev*., **34**, 561–580.

Hayes, G.P.,Wald, D.J. & Johnson, R.L., 2012. Slab1.0: a three-dimensional model of global subduction zone geometries, *J. geophys. Res*., **117**, B01302, doi:10.1029/2011JB008524.

Hearn, E.H., Onishi, C.T., Pollitz, F.F. & Thatcher, W.R., 2013. How do "ghost transients" from past earthquakes affect GPS slip rate estimates on southern California faults?, *Geochem. Geophys. Geosys*., **14**, doi:10.1002/ggge.20080.

Hu, Y. & Wang, K., 2012. Spherical-Earth fintie element model of short-term postseismic deformation following the 2004 Sumatra earthquake, *J. geophys. Res*., **117**, doi:10.1029/2012JB009153.

LaFemina, P., Dixon, T. H., Govers, R., Norabuena, E., Turner, H., Saballos, A., Mattioli, G., & Strauch, W., 2009. Fore-arc motion and Cocos Ridge collision in Central America, *Geochem. Geophys. Geosyst*., **10**(5), Q05S14, doi:10.1029/2008GC002181.

Larsen, S.C., 1992. Displacement modeling of dislocations, PhD thesis, California Institute of Technology, Pasadena, CA.

Lyon-Caen, H., Barrier, E., Lasserre, C., Franco, A., Arzu, I., Chiquin, L., Chiquin, M., Duquesnoy, T., Flores, O., & Galicia, O., 2006. Kinematics of the North American-Caribbean-Cocos plates in Central America from new GPS measurements across the Polochic-Motagua fault system, *Geophysical Research Letters,* **33** (19).

Marone, C.J., Scholtz, C.H. & Bilham, R., 1991. On the mechanics of earthquake afterslip, *J. geophys. Res.: Solid Earth (1978–2012)*, **96**, 8441– 8452.

Márquez-Azúa, B. & DeMets, C., 2003. Crustal velocity field of Mexico from continuous GPS measurements, 1993 to June 2001: implications for the Neotectonics of Mexico, *J. geophys. Res.: Solid Earth (1978–2012)*, **108**, doi:10.1029/2002JB002241.

Okada, Y., 1985. Surface deformation due to shear and tensile faults in a half-space, *Bull. seism. Soc. Am*., **75**, 1135–1154.

Pollitz, F.F., 1997. Gravitational viscoelastic postseismic relaxation on a layered spherical Earth, *J. geophys. Res*., **102**, 17 921–17 941.

Satake, K., 1994. Mechanism of the 1992 Nicaragua tsunami earthquake, *Geophys. Res. Lett*., **21**, 2519–2522.

Stark, P.B. & Parker, R.L., 1995. Bounded-variable least-squares: an algorithm and applications, *Comp. Stat.*, **10**, 129–129.

Wessel, P. & Smith,W.H.F., 1991. Free software helps map and display data, *EOS, Trans. Am. geophys. Un*., **72**, 441–446.

White, R.A., Ligorr<<aa, J.P. & Cifuentes, I.L., 2004. Seismic history of the Middle America subduction zone along El Salvador, Guatemala, and Chiapas, Mexico: 1526–2000, *Geol. Soc. Am. Spec. Paper*, **375**, 379– 396.

Ye, L., Lay, T. & Kanamori, H., 2013. Large earthquake rupture process variations on the Middle America megathrust, *Earth planet. Sci. Lett.*, **381**, 147–155.

Zumberge, J.F., Heflin, M.B., Jefferson, D.C.,Watkins, M.M. &Webb, F.H., 1997. Precise point positioning for the efficient and robust analysis of GPS data from large networks, *J. geophys. Res.: Solid Earth (1978–2012)*, **102**, 5005–5017.

Table 1. GPS station information, earthquake offsets, and postseismic amplitudes.

	Site			Coseisimic offsets										Postseismic amplitudes		
				East (mm)			North (mm)			Vertical (mm)			Imp.	East (mm)	North (mm)	Vertical (mm)
	Lat.^{o}N	Lon.^{o}E	Height (m)	$Obs_e \pm 1\sigma$	$Model_e$	$Misfit_e$	$Obs_n \pm 1\sigma$	$Model_n$	$Misfit_n$	$Obs_v \pm 1\sigma$	$Model_v$	$Misfiti_v$	per cent	$Obs_e \pm 1\sigma$	$Obs_n \pm 1\sigma$	$Obs_v \pm 1\sigma$
MTP1	14.791	−92.368	52.70	−5.7±1.3	−5.5	−0.2	−36.7±1.3	−36.8	0.1	4.3±7.0	−1.0	5.3	35.2	−2.7±0.1	−5.6±0.1	−0.7±0.5
COAT	14.702	−91.885	425.96	−21.7±1.8	−20.1	−1.6	−41.3±2.0	−40.9	−0.4	1.8±2.0	−3.5	5.3	24.5	−4.7±0.1	−6.4±0.1	−0.3±0.5
COTZ	14.335	−91.058	302.24	−9.9±1.3	−9.4	−0.5	−5.5±2.0	−6.7	1.2	1.5±7.6	−0.5	2.0	15.0	−0.9±0.1	−1.2±0.1	−1.1±0.5
HUEH	15.328	−91.503	1874.88	−7.2±1.5	−7.4	0.2	−13.5±2.1	−14.7	1.2	−1.9±5.9	−0.7	−1.2	10.7	−2.2±0.2	−3.4±0.2	0.5±0.6
BARI	15.802	−91.315	1459.13	−3.8±0.5	−4.1	0.3	−9.0±0.5	−8.6	−0.4	−1.9±2.0	0.1	−2.0	3.4	−1.0±0.1	−1.4±0.1	0.5±0.5
TAXI	14.035	−90.465	45.02	−2.8±0.5	−2.2	−0.6	−1.6±0.5	−1.8	0.2	0.5±2.0	−0.9	1.4	3.3	−0.1±0.2	−0.3±0.2	−0.9±0.5
CHQG	15.350	−90.752	1278.40	−5.0±0.5	−5.8	0.8	−8.5±0.5	−7.0	−1.5	−5.1±1.1	−0.2	−4.9	2.9	−0.1±0.2	−1.6±0.2	1.0±0.6
GUAT	14.590	−90.520	1519.87	−5.7±0.5	−5.7	0.0	−4.3±0.5	−4.1	−0.2	0.8±2.0	−0.8	1.6	2.2	–	–	–
TINT	15.318	−89.875	114.61	−2.1±0.5	−3.1	1.0	−1.8±0.5	−2.7	0.9	−3.1±2.0	0.0	−3.1	0.5	–	–	–
SAYA	16.520	−90.192	141.85	−1.5±0.5	−2.0	0.5	−3.4±0.5	−3.0	−0.4	−0.3±2.0	0.3	−0.5	0.4	–	–	–
NARA	17.228	−90.810	71.31	−0.7±0.5	−1.3	0.6	−3.3±0.5	−2.8	−0.5	3.3±2.0	0.3	3.0	0.4	–	–	–
SNJE	13.868	−89.601	1656.96	−1.8±0.5	−0.9	−0.9	−4.3±0.5	−0.7	−3.7	6.2±2.0	−0.6	6.8	0.3	–	–	–
ELEN	16.916	−89.868	116.02	−0.8±0.5	−1.5	0.7	−2.3±0.5	−2.2	−0.1	−4.4±2.0	0.2	−4.6	0.3	–	–	–
ZACA	15.113	−89.356	130.31	−1.2±0.5	−2.0	0.8	−1.2±0.5	−1.6	0.4	−1.5±2.0	−0.1	−1.4	0.2	–	–	–
CNR1	13.670	−89.289	924.44	−1.7±0.5	−0.5	−1.2	−0.9±0.5	−0.4	−0.5	−2.0±2.0	−0.6	−1.4	0.2	–	–	–
MRLS	15.462	−88.850	44.15	−0.7±0.5	−1.5	0.8	−1.3±0.5	−1.2	−0.1	−4.2±2.0	0.0	−4.2	0.1	–	–	–
SSIA	13.697	−89.117	624.39	0.6±0.5	−0.5	1.1	−1.0±0.5	−0.4	−0.6	−5.7±2.0	−0.5	−5.2	0.1	–	–	–
AIES	13.447	−89.050	35.82	−2.1±0.5	−0.3	−1.8	−7.3±0.5	−0.3	−6.9	2.0±2.0	−0.5	2.5	0.1	–	–	–
VMIG	13.396	−88.305	374.85	−1.8±0.5	−0.2	−1.6	−6.3±0.5	−0.2	−6.1	2.2±2.0	−0.3	2.5	0.0	–	–	–
CHPO	14.294	−91.915	9.86	–	–	—	–	–	–	–	–	–	–	−4.2±1.3	−4.8±1.3	12.5±4.2
MAZ0	14.537	−91.550	342.00	–	–	–	–	–	–	–	–	–	–	−2.2±0.2	−3.4±0.2	0.5±0.6
QUE1	14.871	−91.515	2386.53	–	–	–	–	–	–	–	–	–	–	−3.7±1.3	−3.1±1.3	12.5±4.4
SMHO	14.953	−91.808	2412.13	–	–	–	–	–	–	–	–	–	–	−3.2±1.3	−4.2±1.3	15.0±4.4

Notes: Coseismic offsets are estimated using methods described in text. Postseismic amplitudes are calculated from eq. (3). Modelled offsets are for the preferred slip distribution shown in Fig. 5(a). 'Imp.' gives the summed importance for the north, east, and vertical coseismic offsets per site and represents the relative contribution of the site offset to the best slip solution (see text).

FIGURES

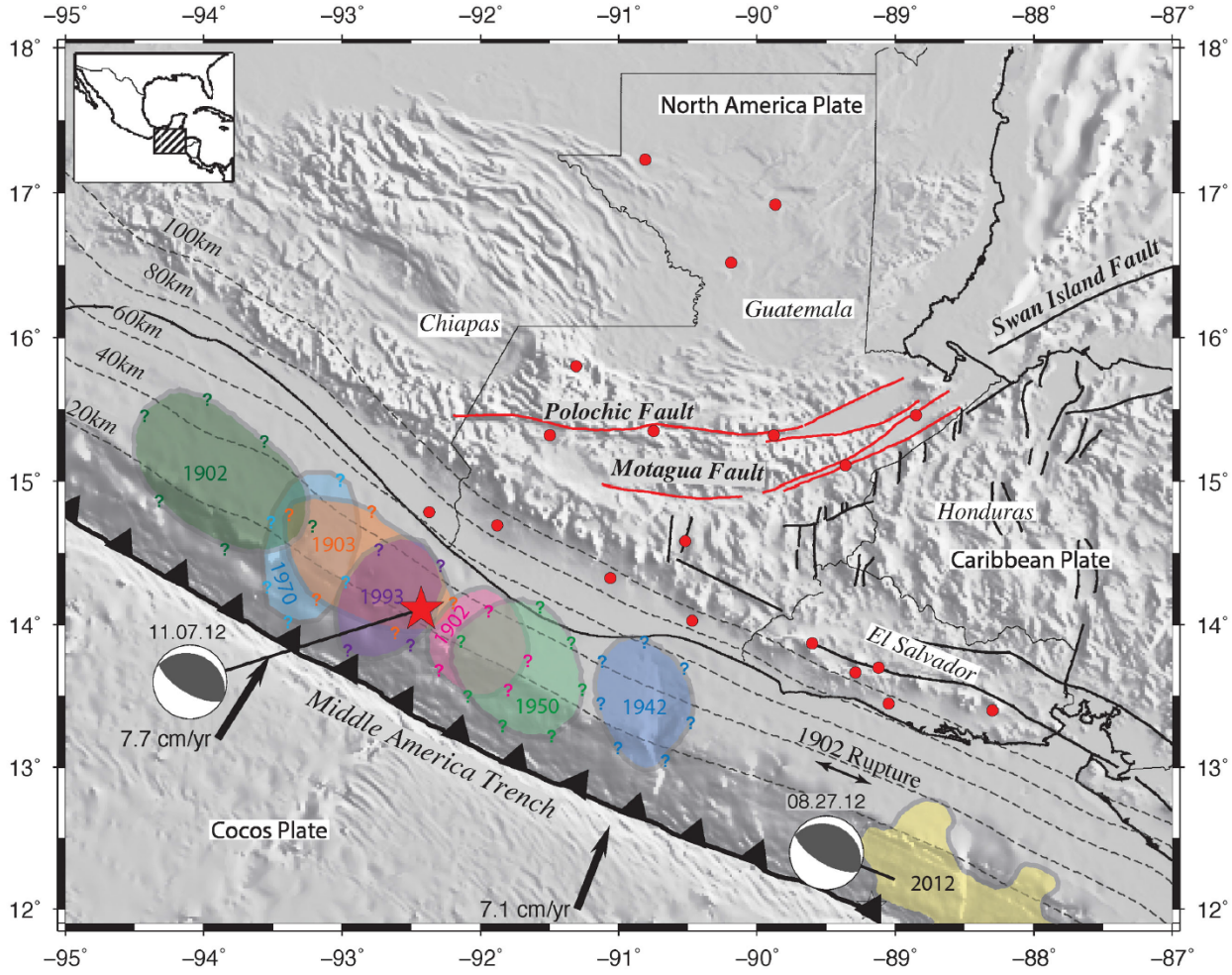

Figure 1.1. Seismotectonic setting of the study area with subducting slab contours (Hayes *et al.* 2012). Colored regions show the approximate rupture zones of M > 7 shallow thrust subduction earthquakes since 1900 digitized from White *et al*. (2004) and Franco *et al.* (2005). The Mw = 7.3 2012 El Salvador slip area is from Geirsson *et al*. (2015). Focal mechanisms (but not rupture zones) of the M = 7.4 2012 August 27 earthquake off the coast of El Salvador and the M = 7.4 2012 November 7 Champerico earthquake studied herein are also shown. Red circles show the locations of all 19 continuous GPS stations used in this study.

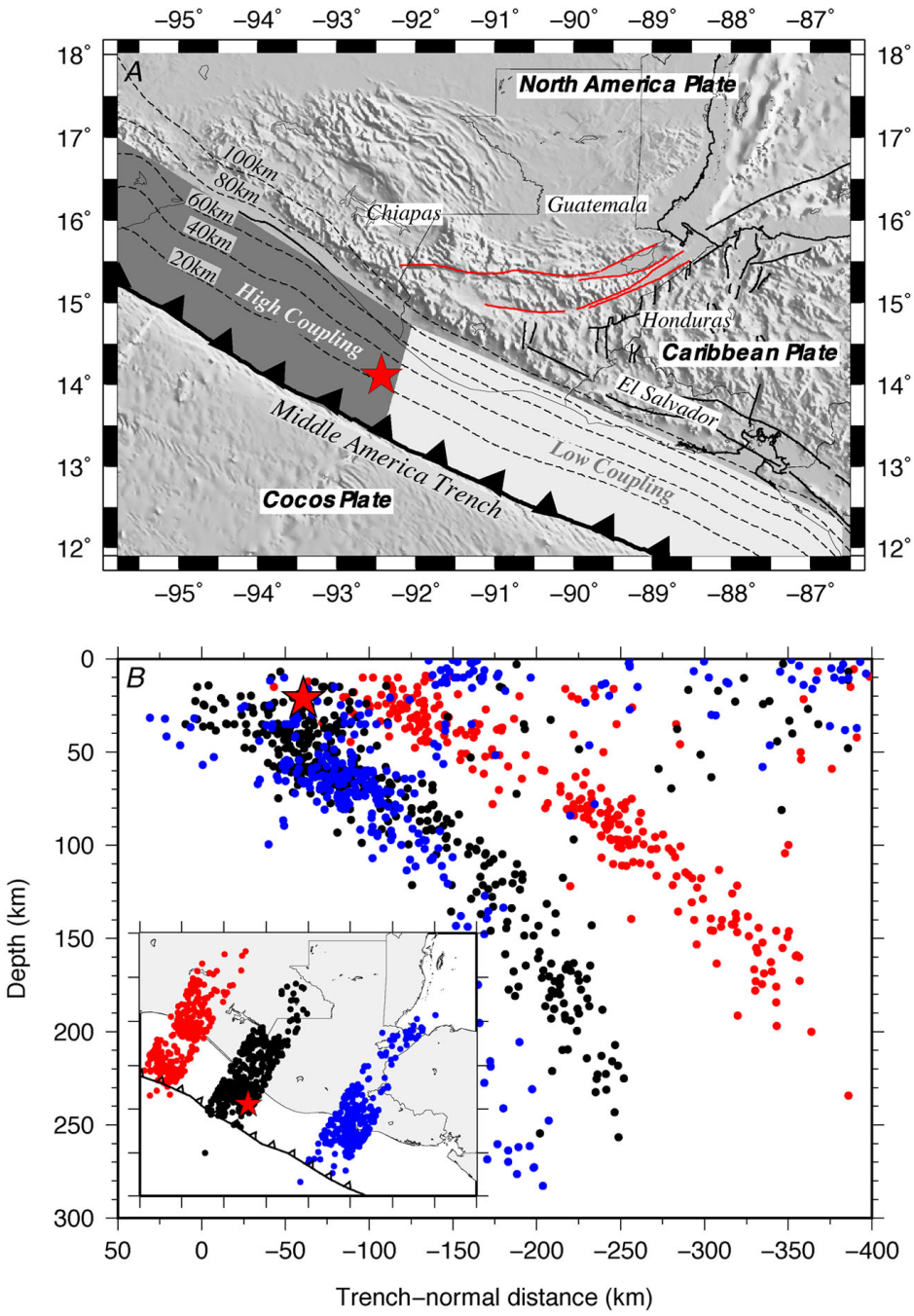

Figure 1.2. (a) Fault locking along the Middle America trench from Franco *et al.* (2012). (b) Vertical earthquake cross-section for three 50-km-wide transects of the Coco Plate subduction interface. One transect spans the North America Plate boundary (red), a second spans the Caribbean forearc sliver (blue), and a third is in the transitional region (black). Earthquake hypocentres are teleseismic relocations of earthquakes in the period from 1960 to 2008 (Engdahl *et al.* 1998). The 2012 Champerico earthquake centroid (red star) in both panels is from the Global CMT catalogue (Dziewonski *et al.* 1981; Ekström *et al*. 2012).

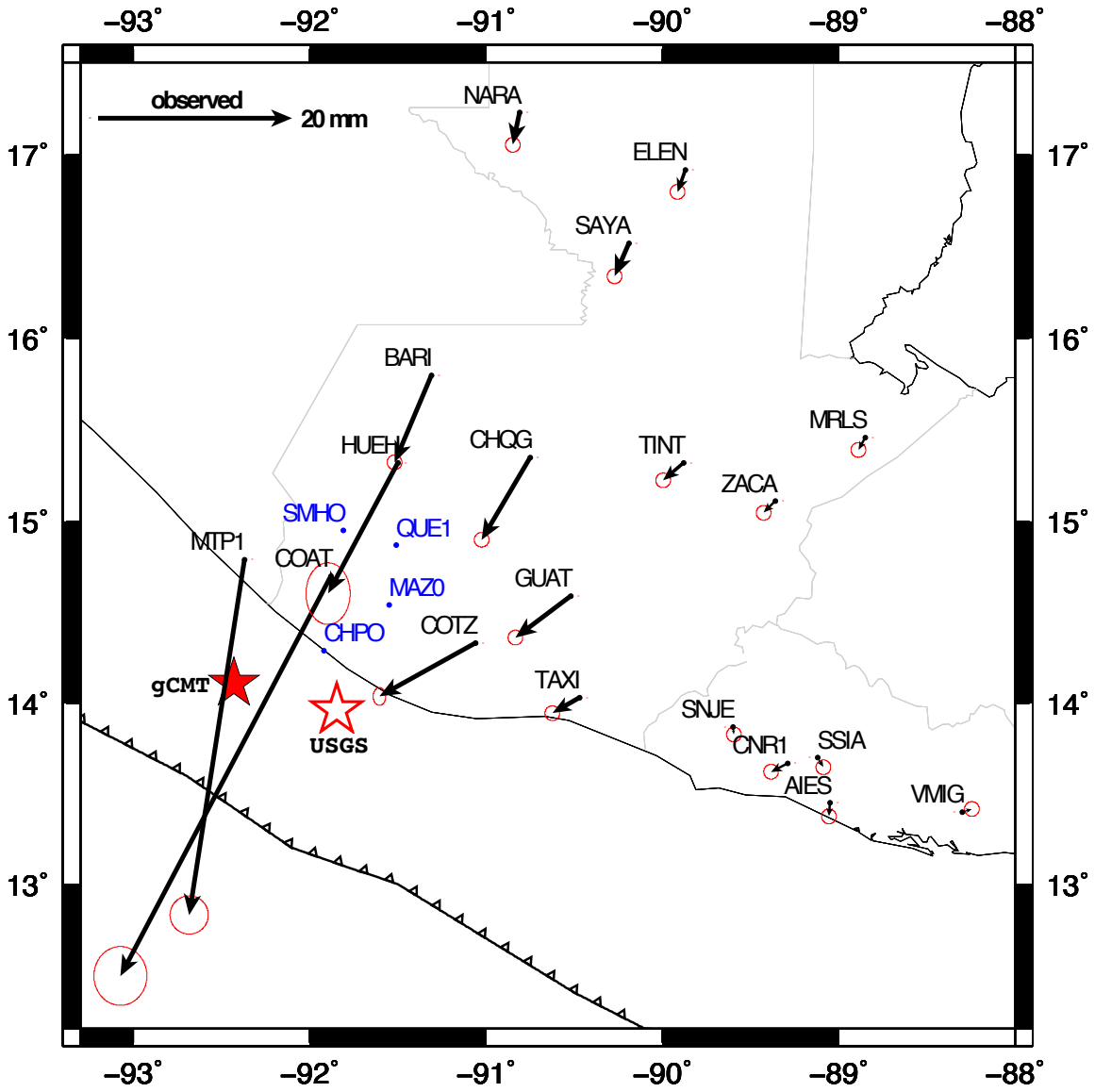

Figure 1.3. Observed horizontal GPS site offsets and 1-D, 1-σ uncertainties for the 2012 Champerico earthquake. Sites with blue labels but no offsets were installed after the earthquake for monitoring postseismic deformation.

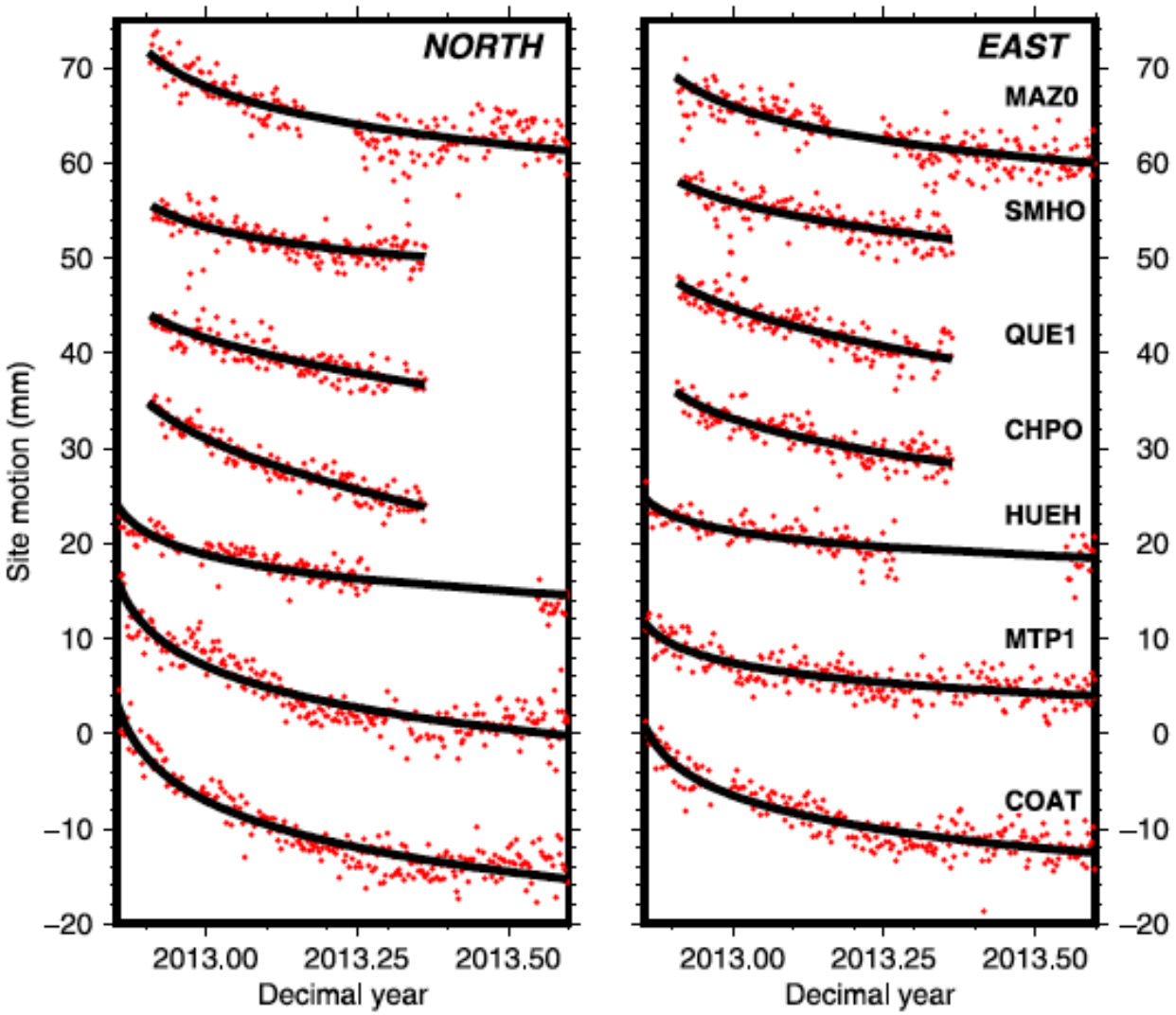

Figure 1.4. Postseismic position time-series for selected GPS stations, northing and easting components, and best-fitting logarithmic decay models (black lines) from the time-series inversions described in the text. Circles show daily GPS position estimates. Stations are labeled in Fig. 1.3. Linear trends corresponding to the secular station movements in ITRF08 have been removed at each site.

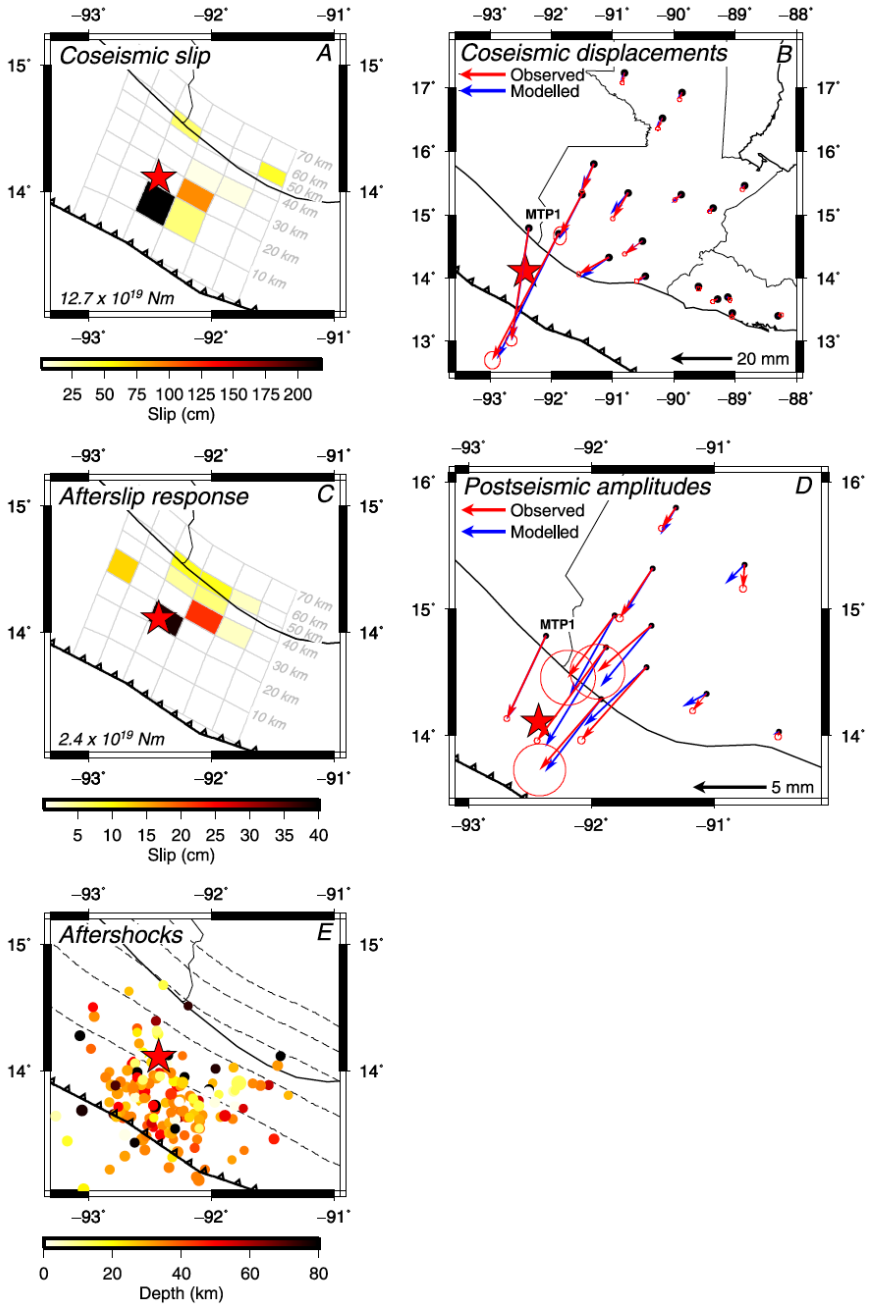

Figure 1.5. (a) Best-fitting coseismic slip solution of the 2012 Champerico earthquake. (b) Modeled and observed horizontal coseismic GPS site displacements and associated 2-D, 1-σ offset uncertainties for the 2012 earthquake. (c) Best-fitting postseismic afterslip solution for six months after the Champerico earthquake. (d) Modeled and observed horizontal postseismic time-series amplitudes and associated 2-D, 1-σ offset uncertainties. (e) Two-week aftershocks with depths for the Champerico earthquake from the seismic database of the Instituto Nacional de Sismología, Vulcanología, Meteorología e Hidrología in Guatemala. The red star indicates the Champerico earthquake location from the Global CMT catalogue (Dziewonski *et al*. 1981; Ekstrom *et al*. 2012).

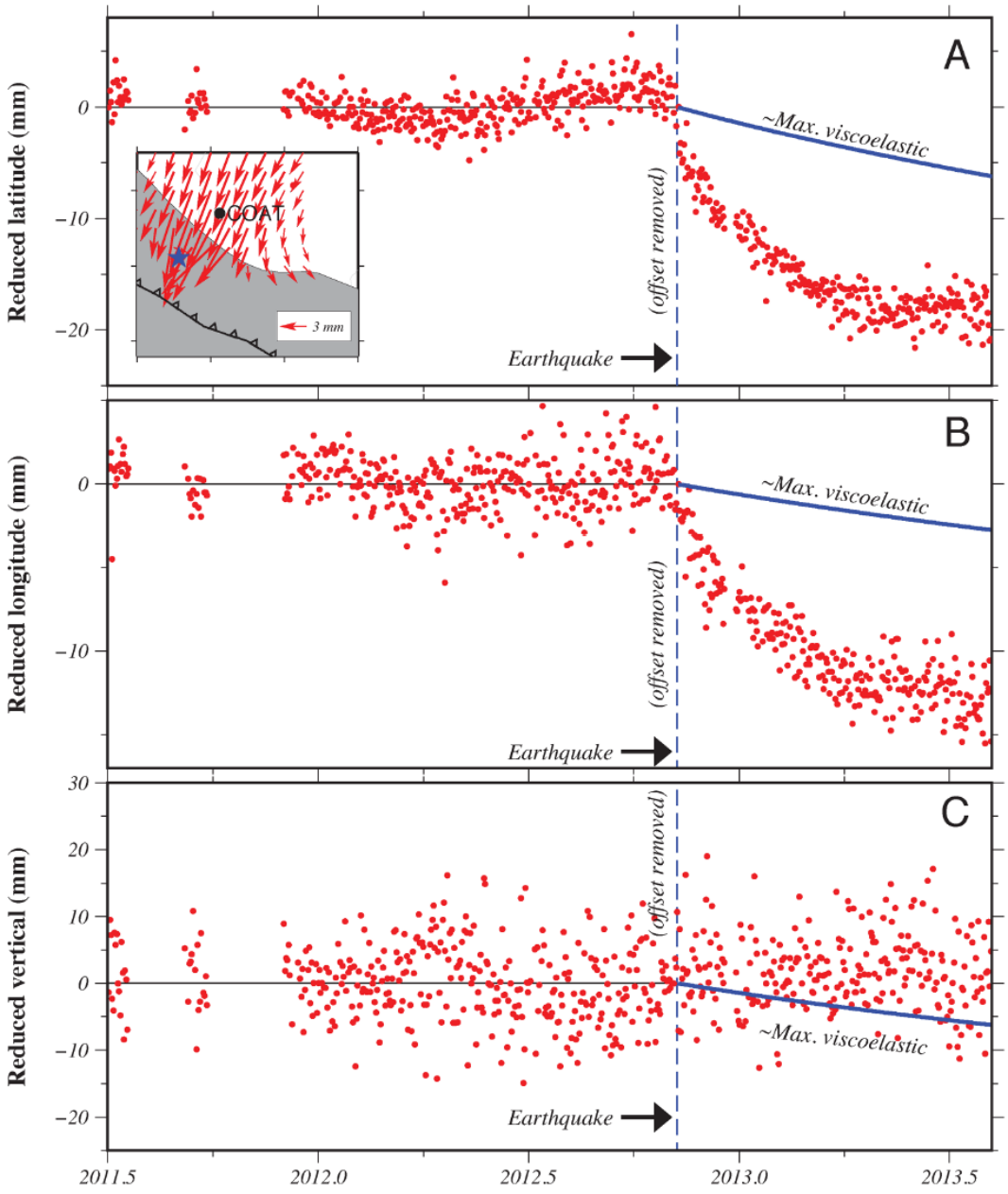

Figure 1.6. Reduced position time-series for GPS site COAT and viscoelastic deformation (blue lines) predicted for an Earth structure that maximizes the viscoelastic response to the Champerico earthquake (see text). Panels (a), (b), and (c), respectively show the north, east and vertical daily site positions (red symbols) reduced by the slope that best fits the observations from the years before the earthquake. Systematic departures of the postseismic daily positions from the interseismic site motion (black line) measure the postseismic deformation. The coseismic offset has been removed for clarity. The maximum predicted viscoelastic deformation (blue line) is much less than the observed deformation; fault afterslip is thus responsible for most of the deformation. Red arrows in the inset map show the cumulative predicted viscoelastic movement during the first eight months after the earthquake.

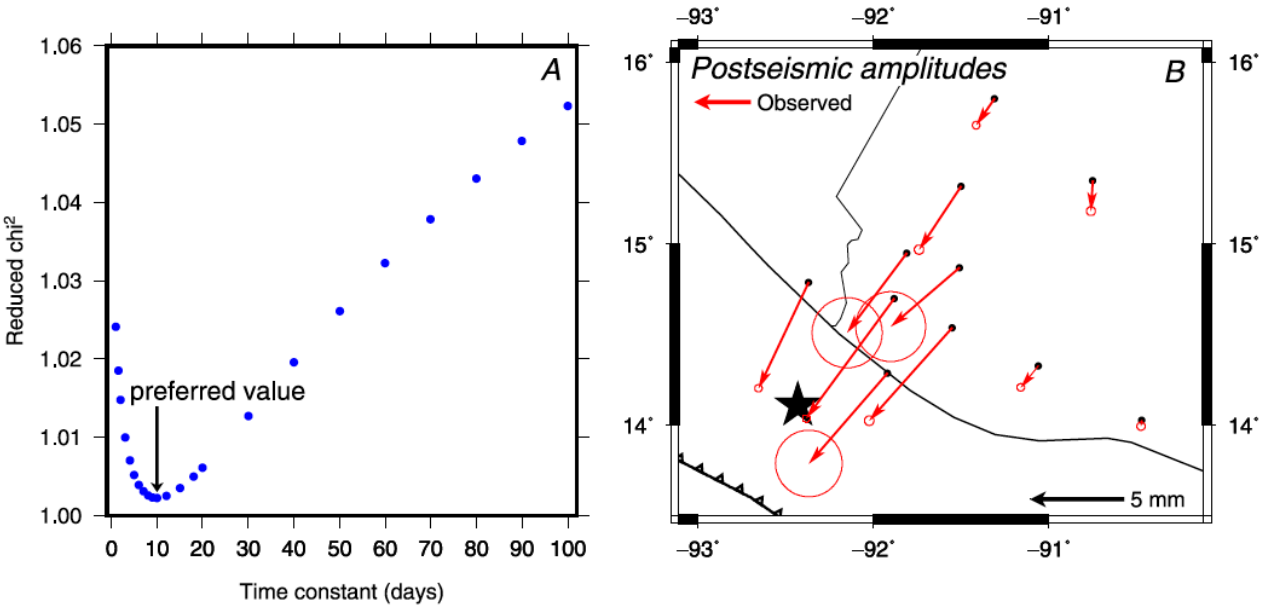

Figure 1.7. (a) Variations in the normalized misfit to postseismic GPS position time-series as a function of different assumed time constants for logarithmically decaying deformation (see text). Fits to the time-series for the 11 stations that recorded postseismic deformation are optimized for a time constant of 10 d. (b) Amplitudes of postseismic deformation from a joint inversion of all 11 station time-series for a decay constant of 10 d. Uncertainties are 1-σ and are propagated from the observations.

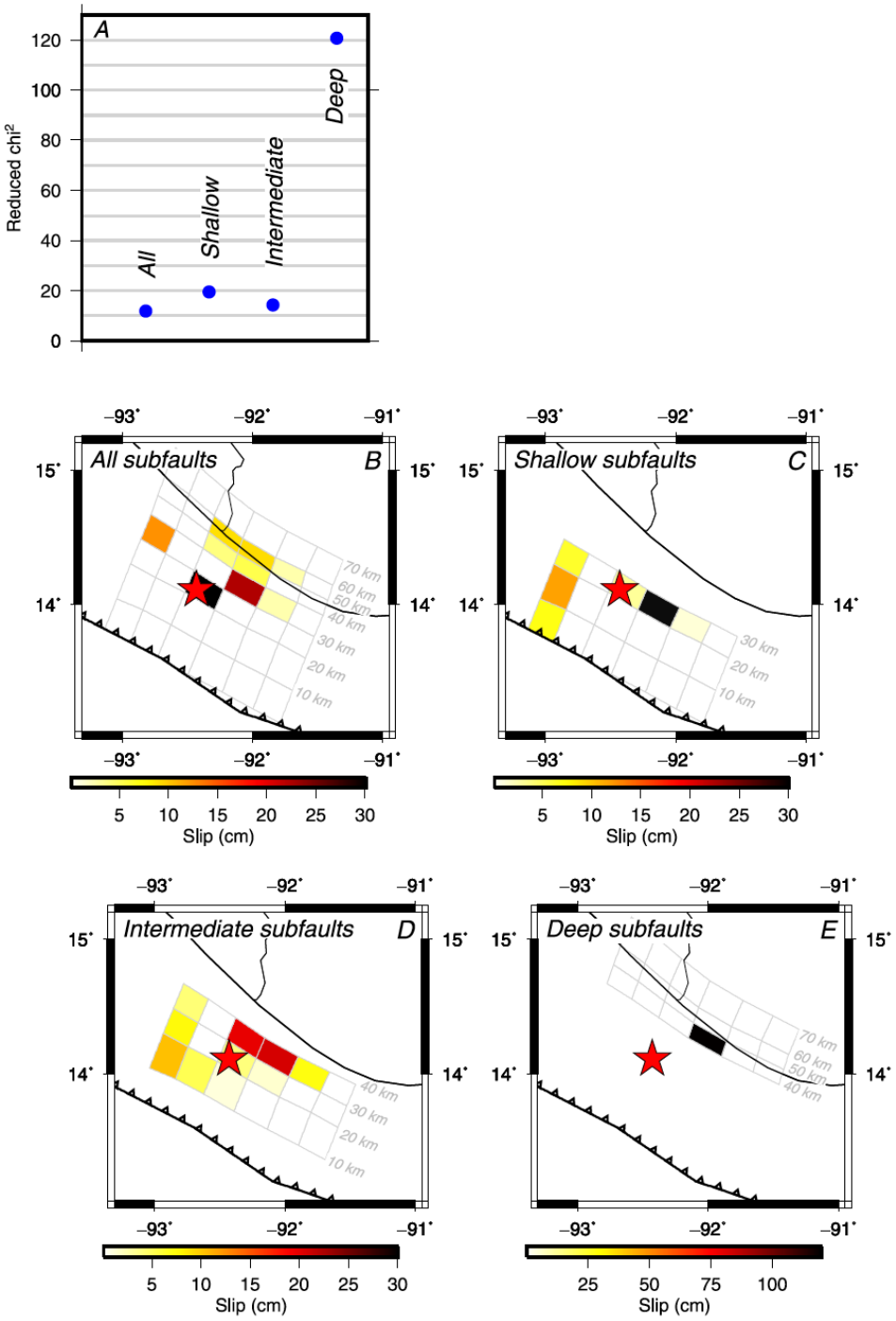

Figure 1.8. (a) Variations in fits to postseismic deformation amplitudes as a function of four different configurations of subfaults shown in (b)–(e). Configuration in (b) repeats the least-constrained configuration, corresponding to Fig. 1.5(c). The configuration in (c), which forces all slip onto subfaults above depths of 30 km, increases the misfit by a factor of six (see a). Configurations that permit slip at intermediate depths (d) and below depths of 40 km (e) also increase the misfit. Configuration (e), which greatly increases the misfit, is excluded at high significance levels.

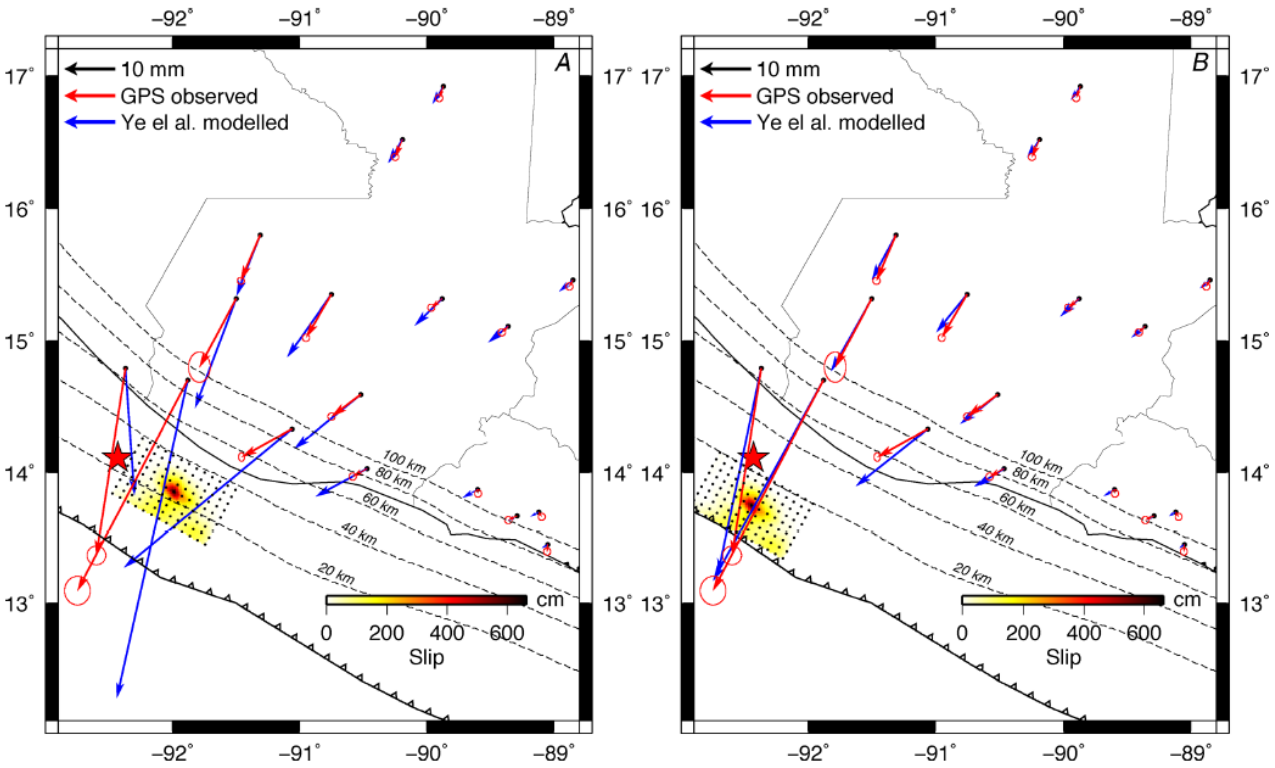

Figure 1.9. Comparison of our measured GPS offsets (red arrows) and those predicted by Ye *et al.'s* (2013) coseismic slip solution (blue arrows). (a) Subfaults and slip solution from Ye *et al.* (2013) in their original location. (b) Fit of seismic slip solution when centroid is translated 51 km west of its initial position in (a).

S1.8 Supplementary information

S1.1 Summary

This supplementary document contains text, figures, and one table that augment the main document, including tests of synthetic data sets to determine how well the Guatemala GPS network can resolve slip along the subduction interface and descriptions of blind tests of the coseismic GPS offsets and coseismic slip solution presented in the main document.

S1.2 Repeatability of coseismic offsets estimated at the GPS sites

As part of our analysis, a subset of the authors, hereafter referred to as Team 2, independently processed the raw GPS observations used for this analysis and estimated coseismic offsets to evaluate the reproducibility of the offsets (Table 1.1) that were used for the main analysis. Team 2 processed the raw observations with GIPSY software and standard point-positioning procedures and estimated coseismic offsets at each site by fitting each station position time series with an equation that incorporated an instantaneous offset the day of the earthquake, linear motion before the earthquake, exponentially-decaying postseismic deformation, and a sinusoidal term to remove seasonal variations. Encouragingly, a comparison of the coseismic offsets from the primary analysis (Table 1.1 of the main document) to the alternative estimates (Fig. 1.1 and Table S1.1) yields similar offsets at most of the sites.

Team 2 also estimated offsets at seven campaign sites that were not included in the primary analysis (Supplemental Table S1.1). The offsets at the campaign sites were estimated by extrapolating site positions determined from campaign measurements that were variously made in 1999, 2003, and/or 2006 forward to the time of the 2012 earthquake and determining the offset between that extrapolated location and the location measured after the earthquake. Measurements

at these seven sites after the earthquake did not occur until two weeks to six months after the earthquake. The coseismic offsets for the seven campaign sites thus include some postseismic deformation. Offsets at the seven campaign sites are shown in Fig. S1.1 below.

S1.3 Robustness of the coseismic slip solution

As described in Section 1.4.2 of the main document, we also did a blind comparison of coseismic slip solutions determined from the preferred and alternative coseismic offsets. Fig. 1.2 compares the solutions determined from the two sets of coseismic offsets. As is described in Section 1.4.2 of the main document, the major features of the two solutions agree well despite the independent approaches that were used both determine their underlying coseismic GPS offsets and estimate the two solutions. We conclude that the geodetic solutions are robust. Readers are referred to Section 1.4.2 of the main chapter for further information.

S1.4 Resolution of coseismic slip from synthetic slip solutions

Section 1.4.3 of the main document describes a series of tests that we used to determine how well the location and magnitude of coseismic slip can be resolved on the Middle America subduction interface from synthetic offsets at the locations of the 19 GPS sites that recorded coseismic slip for the 2012 Champerico earthquake. Figs. 1.3-5 show seven hypothetical distributions of coseismic slip that we imposed on an elastic half space to determine 3-D elastic displacements at each of the 19 GPS sites that recorded coseismic slip for the 2012 Champerico earthquake. The slip imposed along each fault patch consists of one meter of downdip motion uniformly distributed along the fault. The displacements predicted at the 19 GPS sites were inverted using the method described in the text to find a best-fitting slip solution for each of the seven starting models. In the absence of

any noise in the synthetic displacements, the starting slip solutions were recovered perfectly (Figs. S1.3, panels B2 to F2). We simulated more realistic data by adding Gaussian noise to the synthetic displacements (Section 1.4.3). Inversions of the noisy synthetic displacements also correctly recovered the locations of the fault patches and slip magnitudes for depths between 10-60 km (Figs. S1.3, panels B3 to F3) to within 15 per cent of their starting values. Concentrated slip imposed above 10 km was instead recovered as diffuse amplitude slip between 0-20 km (Fig S1.3, panel A3). Our ability to resolve shallow slip is thus limited.

The outcome of the synthetic tests indicates that the onshore GPS network has sufficient geometric strength with respect to a range of plausible offshore rupture locations to reliably recover the location and magnitude of the slip.

Site Information				Preferred Solution										Alternative Solution			
				East (mm)			North (mm)			Vertical (mm)			East (mm)		North (mm)	
Site	*Lat °N*	*Lon °E*	*Height (m)*	Obs_e	$Model_e$	$\pm 1\sigma$	Obs_n	$Model_n$	$\pm 1\sigma$	Obs_v	$Model_v$	$\pm 1\sigma$	Obs_e	$Model_e$	Obs_n	$Model_n$
AIES	13.447	-89.050	35.82	-2.1	-0.3	0.5	-7.3	-0.3	0.5	2.0	-0.5	2.0	----	----	----	----
BARI	15.802	-91.315	1459.13	-3.8	-4.1	0.5	-9.0	-8.6	0.5	-1.9	0.1	2.0	-2.0	-3.1	-6.0	-7.1
CATR	14.463	-89.743	686.07	----	----	----	----	----	----	----	----	----	1.0	-1.0	0.0	-1.0
CHL0*	14.075	-90.382	228.76	----	----	----	----	----	----	----	----	----	-2.0	-0.9	-2.0	-1.1
CHQG	15.350	-90.752	1278.40	-5.0	-5.8	0.5	-8.5	-7.0	0.5	-5.1	-0.2	1.1	-1.0	-3.7	-6.0	-5.0
CNR1	13.670	-89.289	924.44	-1.7	-0.5	0.5	-0.9	-0.4	0.5	-2.0	-0.6	2.0	----	----	----	----
COAT	14.702	-91.885	425.96	-21.7	-20.1	1.8	-41.3	-40.9	2.0	1.8	-3.5	2.0	-20.0	-17.3	-39.0	-37.4
COTZ	14.335	-91.058	302.24	-9.9	-9.4	1.3	-5.5	-6.7	2.0	1.5	-0.5	7.6	-8.0	-5.7	-2.0	-4.9
ELEN	16.916	-89.868	116.02	-0.8	-1.5	0.5	-2.3	-2.2	0.5	-4.4	0.2	2.0	-1.0	-1.0	-2.0	-1.8
GUAT	14.590	-90.520	1519.87	-5.7	-5.7	0.5	-4.3	-4.1	0.5	0.8	-0.8	2.0	-6.0	-2.9	-5.0	-2.7
HUEH	15.328	-91.503	1874.88	-7.2	-7.4	1.5	-13.5	-14.7	2.1	-1.9	-0.7	5.9	-6.0	-5.7	-13.0	-12.0
MAZ0*	14.537	-91.550	342.00	----	----	----	----	----	----	----	----	----	-16.0	-16.8	-20.0	-20.2
MRLS	15.462	-88.850	44.15	-0.7	-1.5	0.5	-1.3	-1.2	0.5	-4.2	0.0	2.0	-1.0	-0.8	-1.0	-0.8
MTP1	14.791	-92.368	52.70	-5.7	-5.5	1.3	-36.7	-36.8	1.3	4.3	-1.0	7.0	-2.0	-1.6	-41.0	-42.2
NARA	17.228	-90.810	71.31	-0.7	-1.3	0.5	-3.3	-2.8	0.5	3.3	0.3	2.0	0.0	-0.9	-4.0	-2.5
POPT	16.325	-89.411	519.52	----	----	----	----	----	----	----	----	----	0.0	-1.1	-4.0	-1.5
QUE1*	14.871	-91.515	2386.53	----	----	----	----	----	----	----	----	----	-9.0	-10.8	-15.0	-17.0
SAN0*	14.816	-90.249	994.43	----	----	----	----	----	----	----	----	----	-1.0	-2.3	-2.0	-2.3
SAYA	16.520	-90.192	141.85	-1.5	-2.0	0.5	-3.4	-3.0	0.5	-0.3	0.3	2.0	0.0	-1.4	-4.0	-2.4
SNJE	13.868	-89.601	1656.96	-1.8	-0.9	0.5	-4.3	-0.7	0.5	6.2	-0.6	2.0	----	----	----	----
SOL0*	15.571	-91.494	3356.79	----	----	----	----	----	----	----	----	----	-3.0	-4.0	-9.0	-9.6
SSIA	13.697	-89.117	624.39	0.6	-0.5	0.5	-1.0	-0.4	0.5	-5.7	-0.5	2.0	----	----	----	----
TAXI	14.035	-90.465	45.02	-2.8	-2.2	0.5	-1.6	-1.8	0.5	0.5	-0.9	2.0	-2.0	-0.8	-1.0	-1.1
TIKA	17.225	-89.612	237.84	----	----	----	----	----	----	----	----	----	1.0	-0.9	-3.0	-1.5
TINT	15.318	-89.875	114.61	-2.1	-3.1	0.5	-1.8	-2.7	0.5	-3.1	0.0	2.0	-2.0	-1.8	-2.0	-1.9
VMIG	13.396	-88.305	374.85	-1.8	-0.2	0.5	-6.3	-0.2	0.5	2.2	-0.3	2.0	----	----	----	----
ZAC0*	14.981	-89.501	303.94	----	----	----	----	----	----	----	----	----	-1.0	-1.2	-3.0	-1.2
ZACA	15.113	-89.356	130.31	-1.2	-2.0	0.5	-1.2	-1.6	0.5	-1.5	-0.1	2.0	-1.0	-1.1	-2.0	-1.1

*Denotes campaign station

Table S1.1. Coseismic observed offsets and estimated offsets from preferred and alternative solutions described in main document.

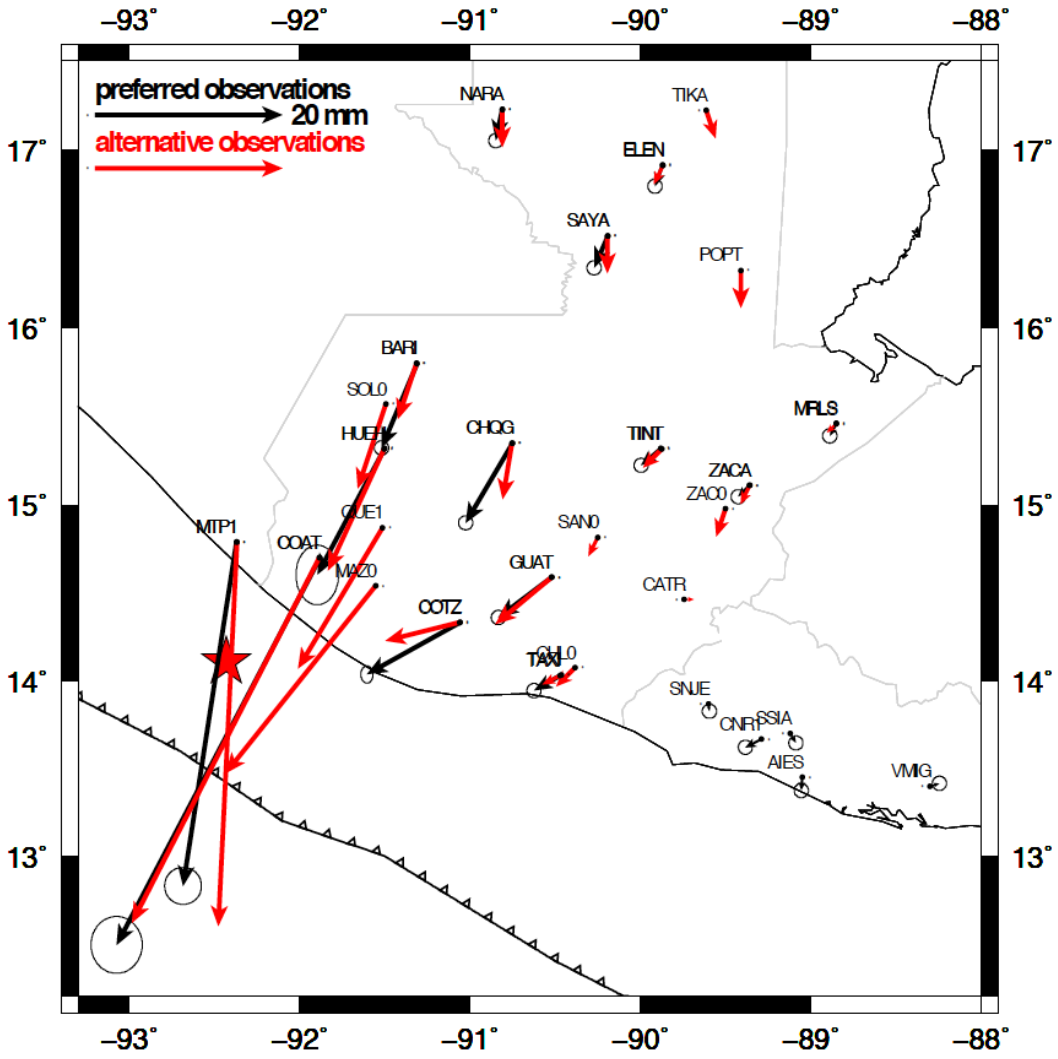

Figure S1.1. Comparison of coseismic offsets for the Champerico earthquake from the primary analysis (black arrows and Table 1.1) and the alternative analysis (red arrows and Table S1.1).

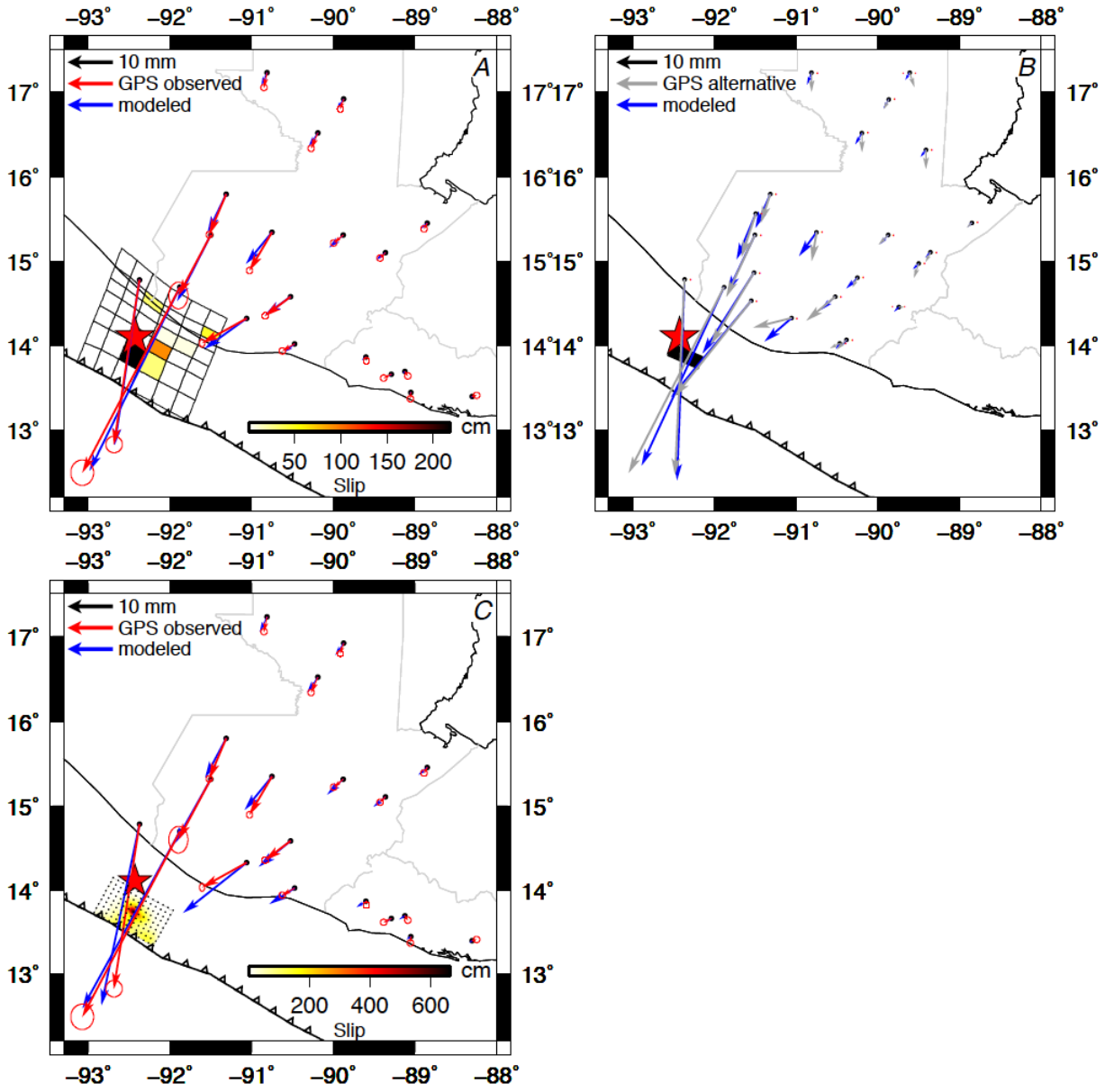

Figure S1.2. Measured horizontal coseismic offsets and predictions of three solutions for the coseismic slip. (a) The preferred geodetic solution (Fig. 1.5a and Table 1.1 from the main document). (b) Alternative geodetic solution with ~2.8 m of slip on a single fault. (c) Seismologically-derived slip solution of Ye *et al.* (2013) after translating the solution 51 km to the west from the solution location indicated by Ye *et al.* (2013).

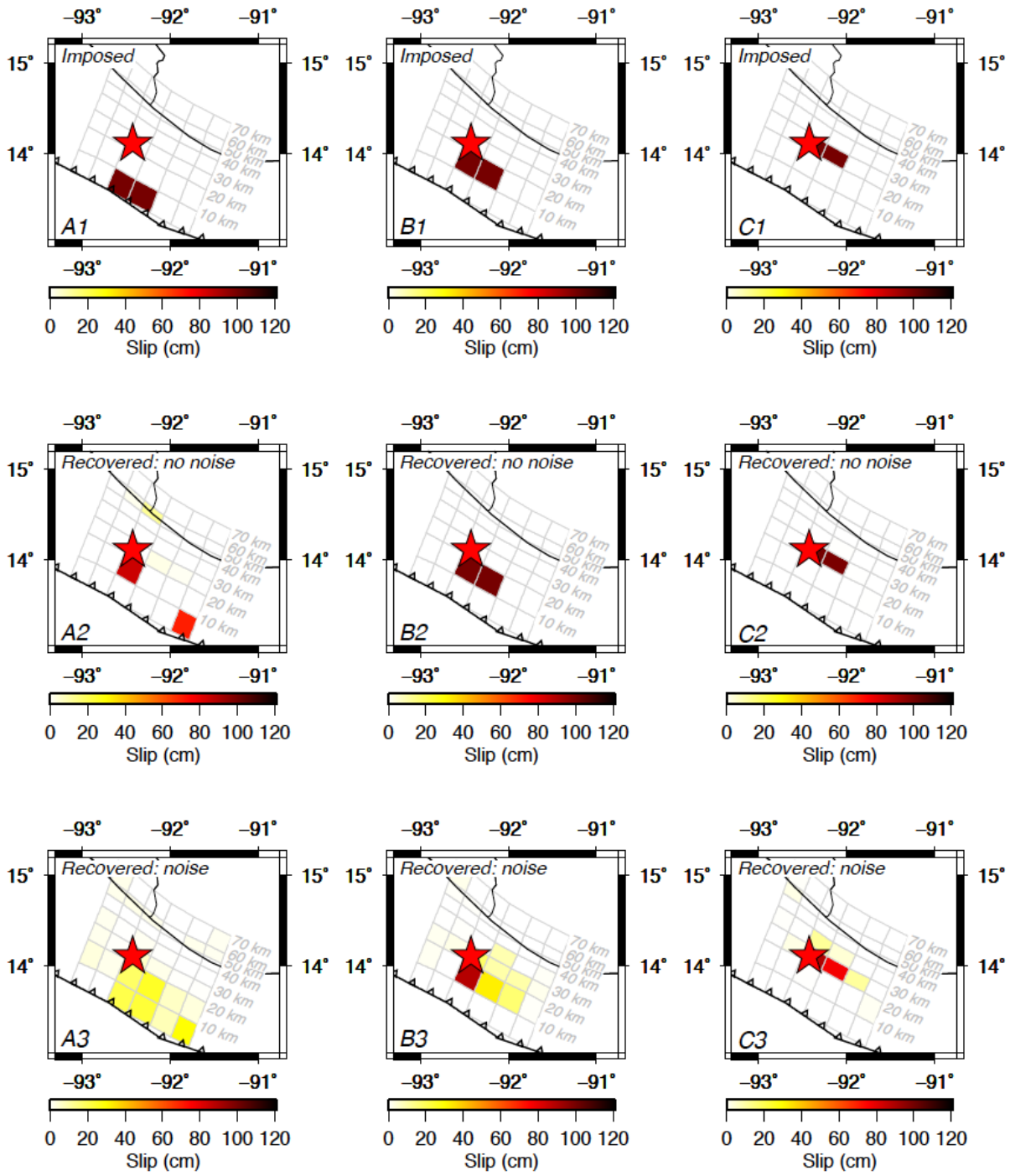

Figure S1.3. Results from slip-patch resolution test. Colored squares show fault patches where 1m of slip is either imposed (panels A1– G1) or slip is estimated via inversions of synthetic coseismic offsets created with the imposed solutions (panels A2–G2 and A3–G3). Red star indicates the epicenter of the 2012 Champerico earthquake.

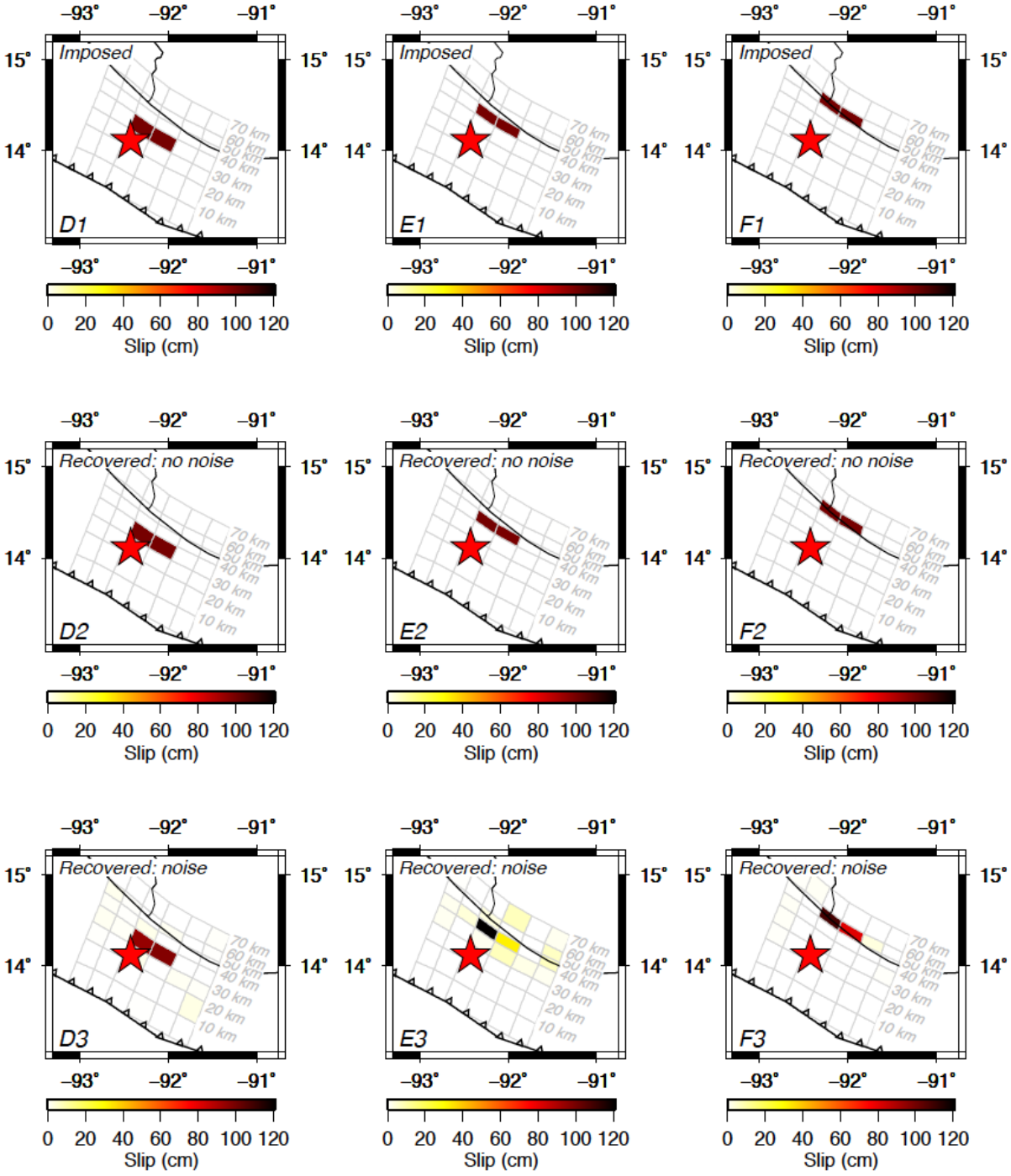

Figure S1.4: See caption to Fig. S1.3.

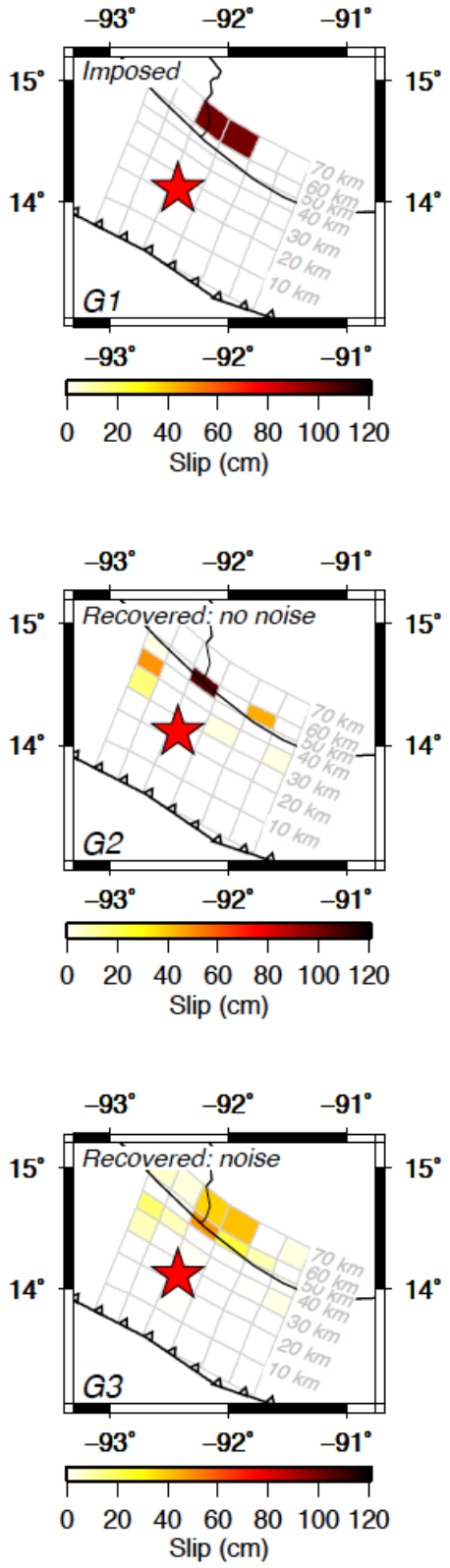

Figure S1.5: See caption to Fig. S1.3.

CHAPTER 2

Deformation in northern Central America from 1999 to 2017 using GPS observations, Part 1: Time-dependent modeling of large regional earthquakes and their postseismic effects

SUMMARY

We use continuous and campaign measurements from 215 GPS sites in northern Central America, including parts of southern Mexico, to estimate coseismic and afterslip solutions for the 2009 Swan Islands fault (M_w=7.3) strike-slip earthquake and the 2012 M_w=7.3 El Salvador and M_w=7.4 Guatemala thrust-faulting earthquakes on the Middle America trench. Our simultaneous inversion of all the GPS data gives the first estimates of the coseismic slips for all three earthquakes, their combined time-dependent effects, and regional GPS site velocities corrected for the coseismic and postseismic deformation. Our coseismic slip solutions for all three earthquakes agree with previous estimates based on static modeling of their coseismic offsets. We find however that afterslip triggered by the 2012 El Salvador earthquake was more localized than previously determined static modeling. Our new time-dependent model, which assumes that earthquake afterslip remains at the same location on the fault and decays logarithmically, fits nearly all of the continuous GPS site time-series in the region within their several-millimeter position noise. The GPS data are thus consistent with afterslip as an important mode of postseismic deformation. Forward modeling of the viscous flow triggered by all three earthquakes for a range of assumed mantle and lower crustal viscosities suggests that viscoelastic deformation accounts for less than 20 per cent of the postseismic deformation and possibly less than 10 per cent. Forward modeling of afterslip and viscoelastic deformation triggered by the larger M_w=7.6 September 2012 Costa Rica thrust earthquake suggests that one or both caused a small, but significant change in the observed long-term motion of GPS site SAN0, which is located more than 500 km from all four earthquakes. This

observation underlines the importance of time-dependent modeling as a prelude to studies of long-term plate rotations. In Part 2 (Chapter 3) of our analysis, we use the interseismic GPS site velocities produced by our time-dependent inversion to estimate plate/block rotations, fault locking, and long-term slip rates in northern Central America

2.1 INTRODUCTION

GPS measurements in northern Central America and southern Mexico, including Guatemala, Honduras, El Salvador, and the Mexican state of Chiapas (Fig. 2.1), began between 1999 and 2003 with the goal of characterizing and understanding the regional block and plate motions and seismic hazards. In broad terms, deformation in this region is driven by a combination of 20 mm yr^{-1} of left-lateral strike-slip movement between the Caribbean and North America plates across the Motagua-Polochic fault zone and Swan Islands fault (Fig. 2.1), 70-80 mm yr^{-1} of northeast-directed subduction of the Cocos plate below the western limits of the Caribbean and North America plates (DeMets *et al.* 2010), and 10-15 mm yr^{-1} of northwestward translation of the Central America forearc toward a poorly understood continental triple junction in southern Guatemala (e.g. DeMets 2001; Authemayou *et al.* 2011). The devastating M_w=7.5 1976 Motagua Fault earthquake (Plafker 1976) and numerous destructive 20th-century volcanic arc earthquakes (White & Harlow 1993) strongly motivate efforts to better understand the region's major faults, including the plate and block motions that drive slip along those faults, their degree of interseismic lock`ing, and the depths at which interseismic locking and afterslip occur. Important related topics include efforts to estimate strain-rate tensors that quantify distributed deformation on the region's numerous minor faults (*e.g.* Cáceres *et al.* 2005) and to use Coulomb stress changes as a basis for improved seismic hazard estimates in the region (Martínez-Díaz *et al.* 2004; Graham *et al.* 2012).

In this first part of our two-part analysis, we undertake time-dependent modeling of the GPS-recorded coseismic and postseismic movements associated with the 28 May 2009 M_w=7.3 Swan Islands fault earthquake, the 27 August 2012 M_w=7.3 El Salvador earthquake, and the 07 November 2012 M_w=7.4 Champerico (Guatemala) earthquake, constituting all three M>7 earthquakes that occurred in our study area between 1999 and 2017. In Part 2 of our analysis, we invert 209 regional GPS velocities that are corrected for the effects of all three earthquakes to estimate the regional plate and block angular velocities, interseismic fault locking, and strain-rate tensors, constituting the steady-state component of the regional deformation. Although other authors have estimated geodetic coseismic slip solutions for these three earthquakes (Graham *et al.* 2012; Ellis *et al.* 2015; Geirsson *et al*. 2015) and have approximated afterslip solutions for two of the earthquakes from static modeling of their postseismic deformation (Ellis *et al.* 2015; Geirsson *et al*. 2015), we revisit these earthquakes for two reasons. First, we fit the transient postseismic deformation using a time-dependent model, rather than the static approximation used in previous studies. Second, we use data from more GPS sites and a longer time period than in previous studies. Via forward modeling, we also systematically evaluate whether transient deformation that was recorded at GPS sites hundreds of kilometers from these earthquakes might be a viscous response to one or more of the three earthquakes or to the M_w=7.6 05 September 2012 Costa Rica earthquake, which was the largest of the three subduction thrust earthquakes to rupture the Middle America trench in 2012. A key by-product of our modeling method is a set of GPS site velocities that are corrected in a consistent, rigorous manner for the effects of these three earthquakes and are thus suited for studies of long-term deformation in the region.

2.2 GPS DATA

2.2.1 GPS data and processing methods

We compiled and processed daily GPS measurements from 74 continuous and 141 campaign GPS sites, including all sites in Belize, El Salvador, Guatemala, Honduras, the Mexican state of Chiapas, the western portion of the Caribbean Sea, and some stations in Nicaragua (Fig. 2.2; Table 2.1). The GPS data span the period 1999 to 2017. As shown in Fig. 2.2, 70 per cent of the GPS sites became operational before 2009, when the first of the three earthquakes modeled herein occurred.

We processed all of the GPS code-phase data with release 6.3 of the GIPSY software suite from the Jet Propulsion Laboratory. No-fiducial daily GPS station coordinates were estimated using the precise point-positioning strategy described by Zumberge *et al.* (1997). Our processing methodology includes constraints on *a priori* tropospheric hydrostatic and wet delays from Vienna Mapping Function parameters (http:ggosatm.hg.tuwien.ac.at), elevation-dependent and azimuthally dependent GPS and satellite antenna phase center corrections from IGS08 ANTEX files (available via ftp from sideshow.jpl.nasa.gov), and FES2004 corrections for ocean tidal loading (http://holt.oso.chalmers.se). Phase ambiguities were resolved using GIPSY's single-station ambiguity resolution feature (Bertiger *et al.* 2010). Daily no-fiducial station location estimates were transformed to IGS08, which conforms to ITRF2008 (Altamimi *et al.* 2011), using daily seven-parameter Helmert transformations from the Jet Propulsion Lab. We estimated daily correlated noise between stations from the coordinate time-series of linearly moving continuous stations outside the study area (Marquez-Azua & DeMets 2003). Corrections of the raw daily GPS site positions for this common-mode noise reduced the daily scatter and amplitude of the longer-period noise in the GPS time-series by 20-50 per cent. All GPS coordinate time-series were also

corrected for equipment-related offsets and other discontinuities not related to earthquakes. Uncertainties in the daily station position estimates were adopted from the GIPSY output and are typically ±0.6 mm in longitude, ±0.5 mm in latitude, and ±2.5 mm in elevation (1-σ).

One of our continuous GPS sites, VMIG in El Salvador, is impacted by multipath noise due to a partially blocked antenna (Fig. S2.1). To mitigate this noise, we subdivided the non-linear time-series into five approximately linear segments and applied a filter based on a linear Theil Sen regression (Sen 1968; Blewitt *et al.* 2009) to identify and remove daily position values for each segment that lie outside ±5 mm in the east and north and ±10 mm in the vertical.

2.2.2 Example GPS position time-series

The position time-series for site SNJE in El Salvador (Fig. 2.3) illustrates the challenge in extracting information about earthquakes, their postseismic deformations, and secular deformation from GPS data in our study area. Offsets and transient deformation associated with at least two earthquakes were clearly recorded at this site. The 2009 Swan Islands earthquake moved site SNJE 3.3±1 mm northward toward the Swan Island fault rupture ~400 km north of the site. The northward component of motion accelerated immediately after the earthquake (Fig. 2.3), likely due to afterslip on the rupture zone. The accelerated northward motion continued until the 27 August 2012 El Salvador thrust earthquake, which triggered rapid southward transient motion of SNJE toward the offshore rupture zone ~200 km southeast of the GPS site. Separating the transient effects of the two earthquakes from their coseismic effects and the steady-state secular station motion requires time-dependent modeling, which we describe next.

2.3 METHODS: TIME-DEPENDENT MODELING

Fault afterslip and viscoelastic relaxation are the primary causes of transient postseismic deformation following large earthquakes, although their relative contributions are hard to determine given limited information about crust and mantle rheologies and the location, magnitude, and temporal characteristics of afterslip (Hu *et al.* 2004; Suito & Freymuller 2009; Hu & Wang *et al.* 2012; Wang *et al.* 2012; Kogan *et al.* 2013; Sun & Wang 2015). In our analysis, we model the two processes separately to estimate a maximum bound for afterslip and to find approximate upper and lower bounds for viscoelastic deformation. None of the observed GPS time-series are corrected for the modeled viscoelastic deformation prior to our TDEFNODE inversion. All transient postseismic deformation is thus attributable to fault afterslip estimated in our model inversions.

2.3.1 Time-dependent elastic deformation: Inverse modeling with TDEFNODE

TDEFNODE, which calculates time-dependent or static deformation with Okada's (1985) elastic half-space dislocation algorithm, can concurrently estimate coseismic slip solutions, afterslip solutions, afterslip decay rates, interseismic fault locking, linear station velocities, plate/block angular velocities, and strain-rate tensors from campaign and continuous GPS position time-series and a variety of other seismologic or plate kinematic data (McCaffrey 2009). In this analysis (Part 1; Chapter 2), we estimate coseismic and afterslip solutions, afterslip decay rates, linear station velocities, and annual seasonal periodic signals. Interseismic fault locking, plate/block angular velocities, and strain-rate tensors are estimated in Part 2 (Chapter 3).

Faults in the TDEFNODE elastic half-space are defined by an irregular grid of nodes that approximate a fault's location and 3-D orientation. Green's functions that quantify the 3-D elastic

response at surface locations to unit slip at each node are calculated and gathered to form the basis for the time-dependent inversion. A simultaneous time-dependent inversion of all the data confers the advantage that all of the secular site velocities are corrected consistently for the elastic effects of the coseismic slip and afterslip for all three earthquakes. Simulated annealing and grid search iterations are employed to minimize the reduced chi-square statistic.

For the Swan Islands fault, we use the fault geometry of Graham *et al.* (2012), who adopted the fault trace defined by a Sea Marc II seafloor survey (Rosencratz & Mann 1991; Rogers & Mann 2007) and assumed a vertical fault to a depth of 15 km. Our approximation of the Middle America subduction interface uses the slab geometry of Hayes *et al.* (2012), with node spacings of ~20 km along-strike and 10-km down-dip.

Checkerboard tests of the resolvability of slip for all three earthquakes modeled herein were previously done by Graham *et al.* (2012), Ellis *et al.* (2015), and Geirsson *et al.* (2015). For the 2009 Swan Islands earthquake, starting slip values for Graham *et al.*'s six-patch fault geometry, which we adopted in this study, are recovered to within 10 per cent for the central four fault patches. Slip is most poorly resolved on the eastern, offshore end of the fault. The Geirsson *et al.* (2015) checkerboard test for the 2012 El Salvador earthquake suggests that the locations of shallow and intermediate-depth slip patches are moderately well resolved, but the slip amplitudes are poorly recovered. Finally, Ellis *et al.* (2015) find that synthetic slip patches off the coast of Guatemala near the Champerico earthquake are well resolved between depths of 10 km to 60 km.

Given the limited ability of the land-based GPS stations to resolve offshore slip during all three earthquakes modeled herein, we applied smoothing when estimating their coseismic and afterslip solutions. To remain consistent with the Graham *et al.* (2012) Swan Islands earthquake modeling, we subdivided the offshore fault into six ~50-km-long rectangular patches and estimated

slip for each patch. For the El Salvador and Champerico earthquakes, we employed a spread penalty smoothing parameter to penalize large slip values at distances progressively farther from the slip centroid (McCaffrey 2009). We explored whether simpler 2-D Gaussian slip sources, whereby afterslip tapers outward from a central region of an elliptical slip source following a Gaussian distribution, fit the data better, but found that these significantly degraded the fits to the GPS time-series relative to our preferred solutions.

2.3.2 Viscoelastic deformation: Forward modeling with VISCO-1D

We use VISCO-1D software (version 3) of Pollitz (1997) to forward model viscoelastic deformation caused by earthquakes. VISCO-1D solves for viscoelastic deformation of a spherically layered Earth given a user-defined viscosity structure and linear Maxwell or bi-viscous rheologies for each layer. Following previous authors, we estimated the range of possible short-term and long-term viscoelastic responses using several viscosity structures appropriate for continental crust (Fig. 2.4). These include the Hearn *et al.* (2013) M1 Earth structure (left panel in Fig. 2.4), which was designed to estimate an upper bound on long-term viscoelastic deformation triggered by historic earthquakes in California. To estimate an upper bound for short-term viscoelastic deformation (*i.e.* deformation within the first 1-2 years after an earthquake), we changed the 3×10^{18} Pa·s mantle viscosity assumed for the M1 Earth model to 5×10^{17} Pa·s, as estimated by Hu & Wang (2012) from their analysis of short-term postseismic deformation for the 2004 Sumatra earthquake. We refer to this Earth structure as our maximum-response model (right panel in Fig. 2.4). We approximated a lower limit for viscoelastic deformation by increasing the 3×10^{18} Pa·s M1 mantle viscosity to 1×10^{19} Pa·s. We refer to this Earth structure as our minimum-response model (center panel in Fig. 2.4).

2.4 RESULTS: COSEISMIC AND POSTSEISMIC DEFORMATION

We inverted simultaneously all 357,627 north, east, and vertical daily positions at the 215 GPS sites in our study area to estimate the following: (1) the locations and magnitudes of coseismic slip for all three earthquakes; (2) afterslip decay constants and afterslip amplitudes per earthquake; and (3) linear velocities at each GPS site. At the 74 continuous GPS stations, the weighted root-mean-square (WRMS) misfits of our best-fitting model are ~2 mm for the north and east position components and 7 mm in the vertical. At the 141 campaign GPS sites, the WRMS misfits are ~3 mm for the two horizontal components and 8 mm in the vertical. For comparison, well-behaved, linearly-moving GPS position time-series estimated by ourselves and many other authors exhibit daily scatter of 1-3 mm, comparable to our WRMS misfits. We conclude that our parameterizations of the fault geometries and of the earthquake and afterslip sources are consistent with the GPS observations. We next describe results for each of the three earthquakes that we modeled, including their predicted viscoelastic deformation.

2.4.1 2009 Swan Islands earthquake

2.4.1.1 Background

The 28 May 2009 M_w=7.3 earthquake on the Swan Islands fault was the largest earthquake on the North America-Caribbean plate boundary since the 1976 M_w=7.5 Motagua fault earthquake in Guatemala (Plafker 1976; Fig. 2.1). Inversions by Graham *et al.* (2012) of GPS station offsets and seismic waveforms for this earthquake give geodetic (Fig. 2.5b) and seismic slip solutions that are consistent with as much as 1 meter of slip along the western ~250 km of the Swan Islands fault. Afterslip associated with this earthquake has not been estimated previously.

2.4.1.2 Coseismic slip solution

Figure 2.5 compares our new coseismic slip solution (Fig. 2.5a) to the Graham *et al.* (2012) geodetic slip solution (Fig. 2.5b). Our new estimate uses the same planar fault geometry and is constrained to have slip amplitudes within 30 per cent of the Graham *et al*. (2012) solution. One of the five continuous GPS sites that were operating during the earthquake, site ROA0 on Roatan Island, was adjacent to the ruptured segment of the fault (Fig. 2.5d). Its position time-series is fit well by our time-dependent model (Fig. 2.6). The position time-series for four continuous GPS sites in El Salvador ~400 km south of the rupture are also well fit with residual positions of only a few millimeters relative to the daily positions estimated by our best-fitting TDEFNODE model (Fig. 2.7).

We estimate a geodetic moment of 1.2 x 10^{20} N·m (M_w=7.35) for the Swan Islands earthquake, close to the 1.3 x 10^{20} N·m Global centroid-moment-tensor (gCMT) catalogue estimate (Dziewonski *et al.* 1981; Ekström *et al.* 2012; Table 2.2). Maximum slip on the fault was ~900 mm, close to the ~1000 mm maximum estimated by Graham *et al.* (2012).

2.4.1.3 Afterslip solution

Most of the information about afterslip triggered by the Swan Islands earthquake comes from the continuous observations at GPS site ROA0 (Fig. 2.6) due to its proximity to the earthquake (Fig. 2.5d). The ROA0 time-series shows clear evidence for transient, decaying motion, particularly in the east position component, which records motion nearly parallel to the N70°E-striking fault. The logarithmically decaying afterslip estimated with our time-dependent TDEFNODE inversion fits the curvature of the east component of motion within the ±2 mm daily noise (Figs. 2.6, 2.7, and

2.8). A simple log-decay afterslip model is thus sufficient to describe the postseismic deformation, although some of the deformation may also record a viscoelastic response to the earthquake (Section 2.4.1.4).

In the extreme case, if all the postseismic deformation is attributable to fault afterslip, our afterslip solution (Fig. 2.5c) implies there was as much as 480 mm of cumulative afterslip by 2017.0. The best-fitting log-decay time constant is 30 days and the moment released by afterslip, 3.55 x 10^{19} N·m, was ~35 per cent of the geodetic moment for the earthquake. We find no evidence for significant afterslip at the western end of the Swan Islands fault where it transitions onshore to the seismically hazardous Motagua fault. The postseismic deformation attributable to fault afterslip diminishes rapidly with distance from the earthquake rupture zone (Fig. 2.5d). For example, by 2017.0, 7.6 years after the earthquake, the postseismic motion predicted on the north coast of Honduras was only 20 mm (Fig. 2.5d). Even smaller postseismic deformation is predicted at locations farther south in Central America.

2.4.1.4 Viscoelastic estimate

Figure 2.8 shows viscoelastic deformation through early 2017 at site ROA0 for our Swan Islands earthquake slip solution for all three Earth models described in Section 2.3.2 and shown in Fig. 2.4. The maximum-response model predicts 3-4 times more postseismic deformation than was measured at site SNJE ~400 km from the earthquake (Fig. 2.9), arguing against the usefulness of this model for predicting deformation within ~1 year of the earthquake or at longer time periods. In contrast, the M1 model correctly predicts the postseismic deformation measured at SNJE (Fig. 2.9) but predicts less than 30 per cent of the deformation observed at site ROA0 near the earthquake (Fig. 2.8). If the M1 model better approximates the rheological structure of northern Central

America, then by inference, most (~70 per cent) of the of the postseismic deformation measured at ROA0 is attributable to fault afterslip.

2.4.2 2012 El Salvador earthquake

2.4.2.1 Background

Slip solutions for the 27 August 2012 El Salvador thrust earthquake have been estimated from seismic waveforms (Ye *et al.* 2013) and geodetic data (Geirsson *et al.* 2015). The Ye *et al* inversion of 83 broadband P waves indicates that coseismic slip was concentrated above depths of 30 km and had peak amplitude of 1.2 m. The Geirsson *et al.* inversions of 22 GPS site offsets also suggest that slip was shallow (above 20 km depth) and generally averaged ~1 m (Fig. 2.10b).

2.4.2.2 Coseismic slip solution

Coseismic slip for the 2012 El Salvador earthquake was estimated in our TDEFNODE inversion via smoothing of the slip values at independent nodes that represent the Middle America subduction interface. Our new coseismic slip solution (Fig. 2.10a) agrees well in location and amplitude with previous estimates (Ye *et al.* 2013; Geirsson *et al.* 2015) and has a geodetic moment of 1.3 x 10^{20} N·m (M_w=7.3), the same as the gCMT moment (Dziewonski *et al.* 1981; Ekström *et al.* 2012; Table 2.2). The coseismic offsets, which point nearly due south (blue arrows in Fig. 2.10d), are well fit by the model (Fig. 2.11). Our new solution confirms that the earthquake was an unusually shallow, low-slip event, as concluded by Ye *et al.* (2013) and Geirsson *et al.* (2015).

2.4.2.3 Afterslip solution

We estimated logarithmically-decaying afterslip for the 2012 El Salvador earthquake via smoothing of slip values at independent nodes, the same as for the coseismic slip solution. Our inversion indicates that most afterslip was concentrated west-northwest of and 10-km downdip from the coseismic slip (compare Figs. 2.10a and 2.10c). The migration of afterslip to a location WNW of the coseismic slip is consistent with a ~10° clockwise rotation of the postseismic GPS station directions (red arrows in Fig. 2.10d) relative to the more southward-pointing coseismic directions (blue arrows in Fig. 2.10d). By 2017.0, 4.5 years after the earthquake, the cumulative afterslip moment was 1.8 x 10^{20} N·m, 1.4 times larger than the geodetic earthquake moment, and the GPS displacements attributable solely to afterslip were 2-10 times larger than the coseismic offsets (red versus blue arrows in Fig. 2.10d).

Our new afterslip solution fits most of the GPS station position time-series within their 1-2 mm daily noise (Figs. 2.3, 2.9, 2.12-14). The largest misfit occurs at site AIES in central El Salvador, where the north component of the transient motion is systematically misfit by ~5 mm for one year after the earthquake (Figs. 2.11 and 2.12). We explored numerous alternative combinations of the estimated parameters including the log-decay time constant, slip rake, and different degrees of smoothing to reduce this misfit, but were unsuccessful. We suspect that the misfit is partly or fully attributable to our approximations that afterslip remained at the same location on the fault and that viscoelastic deformation did not contribute to the postseismic deformation. Any migration of slow afterslip along the weakly locked subduction interface would alter the expected spatial-temporal pattern of postseismic deformation recorded by GPS sites on land relative to the simpler pattern created by stationary afterslip.

Finally, the logarithmic decay-constant estimated from our time-dependent inversion is 500 days, much longer than our 30-day estimates for the Swan Islands earthquake (Section 2.4.1.3) and Champerico earthquake (Section 2.4.3.3). Enforcing much shorter decay-constants (*i.e.* 3-100 days) significantly degrades the fits at other continuous sites. Enforcing a 300-day time-constant leads to similar fits and does not significantly alter any of the results shown in Fig. 2.10. The 2012 El Salvador thrust earthquake thus triggered more protracted afterslip and larger amplitude afterslip than the other two earthquakes we studied.

2.4.2.4 Viscoelastic deformation

Figures 2.13 and 2.14 show the viscoelastic deformation at sites SSIA and SNJE calculated with VISCO-1D for our new coseismic slip solution. None of the three rheological models we considered (Fig. 2.4), including the maximum-response model, match the postseismic deformation measured at the two sites (Fig. 2.13 and 2.14). The maximum-response model predicts motion of only ~10 per cent of that observed. We concur with Geirsson *et al.* (2015) that relatively little postseismic deformation was caused by viscous relaxation and afterslip dominated the deformation.

2.4.3 2012 Champerico earthquake

2.4.3.1 Background

The 2012 Champerico earthquake ruptured the Middle America trench offshore from southern Guatemala, where locking transitions from strong near Chiapas to weak offshore El Salvador (Lyon-Caen *et al.* 2006; Correa-Mora *et al.* 2009; LaFemina *et al.* 2009; Franco *et al.* 2012). Inversions by Ellis *et al.* (2015; see Chapter 1) of coseismic offsets and afterslip amplitudes at 19

continuous GPS sites in Guatemala, El Salvador, and southern Mexico indicate that coseismic slip of up to 2 m was concentrated in a relatively compact region above 30 km depth, immediately updip from the afterslip. Their coseismic slip estimate agrees well with an independent solution from an inversion of regional and teleseismic P waves (Ye *et al.* 2013).

2.4.3.2 Coseismic slip solution

Fig. 2.15 shows our new 2012 Champerico earthquake slip solution, which was derived via smoothing of the slip values estimated at nodes that approximate the Middle America subduction interface. Slip of 0.5-1.2 m was concentrated at depths of 10-30 km, close to the Global CMT earthquake centroid (white star in Fig. 2.15a) and in good agreement with the Ellis *et al.* (2015) slip solution shown in Fig. 2.15b. The estimated geodetic moment, 1.45 x 10^{20} N·m is close to the 1.3 x 10^{20} N·m moment estimated by Ellis *et al.* (2015) and 1.33-1.5 x 10^{20} N·m seismological estimates (Ekström *et al.* 2012; Ye *et al.* 2013). The coseismic offsets recorded in the position time-series of nearby continuous GPS stations are well fit by the new TDEFNODE model (Fig. 2.16) and agree well with the static offsets estimated and inverted by Ellis *et al.* (2015).

2.4.3.3 Afterslip solution

Our new afterslip solution, which we derived by smoothing slip values at the fault nodes, suggests that most afterslip occurred at depths of 40- 60 km (Fig. 2.15b), ~20 km downdip from the region of coseismic slip. A ~30° clockwise rotation of the postseismic station directions compared to the coseismic offset directions (compare red to blue arrows in Fig. 2.15d) supports the downdip migration of the afterslip relative to the coseismic slip. By 2017.0, 4.2 years after the earthquake,

the cumulative moment for the afterslip was 1 x 10^{20} N·m (Table 2.2), ~70 per cent of the geodetic earthquake moment. The best-fitting log-decay constant is 30 days.

The TDEFNODE model fits the position time-series for nearby continuous GPS sites within their several mm daily noise (Fig. 2.12, 2.16, 2.17). The largest misfit occurs at site COAT directly inland from the earthquake, where measurements within six months of the earthquake are systematically misfit in the east component by 2-5 mm (Figs. 2.12b and 2.17b). We experimented with different degrees of smoothing and different log-decay constraints to reduce this misfit but were unable to improve the fit without concurrently degrading the fit at other continuous sites.

2.4.3.4 Viscoelastic estimate

Figure 2.17 shows the cumulative predicted viscoelastic response at site COAT for the 2012 Champerico earthquake (2012.8511 to 2017.0), as determined with VISCO-1D and our new coseismic slip solution. The maximum-response model predicts only ~50 per cent of the observed postseismic deformation by ~3 years after the earthquake. The M1 and minimum-response estimates, which may approximate the viscoelastic deformation more accurately than the maximum-response model (Section 2.4.1.4), are less than 10 per cent of the observed postseismic deformation. Afterslip thus appears to have been the primary cause of postseismic deformation, as was also the case for the 2009 Swan Islands earthquake.

2.4.4 2012 Nicoya Peninsula earthquake

On 09 September 2012, nine days after the El Salvador earthquake, a M_w=7.6 megathrust earthquake ruptured the Middle America trench at the Nicoya Peninsula in Costa Rica (Protti *et al.* 2013). Although we excluded this earthquake and the relevant GPS data from our TDEFNODE

inversion because it falls outside our study area, we evaluated its far-field effects, which may impact some stations used in our analysis. Supplemental Fig. S2.2 shows coseismic and afterslip solutions determined by Protti *et al.* (2013) and Malservisi *et al.* (2015) from inversions of the coseismic offsets and postseismic deformation that were recorded by the dense Nicoya Peninsula GPS network and nearby sites. The maximum fault slip during the earthquake was more than 4 m and afterslip was as high as 300-500 mm on significant portions of the subduction interface by 70 days after the earthquake (Supplementary Fig. S2.2b). The cumulative afterslip moment 70 days after the earthquake was ~2 per cent of the geodetic earthquake moment (Table 2.2).

We calculate the viscoelastic response for the 2012 Nicoya earthquake using VISCO-1D, the Protti *et al*. (2013) coseismic slip solution shown in Supplemental Fig. S2.2a, and all three rheological models in Fig. 2.4. For locations on the Nicoya Peninsula, near the rupture zone, the viscoelastic deformation predicted by our minimum- and maximum-response models ranges from ~10 mm to 50-200 mm by 2017.0. The magnitude of the viscoelastic deformation is larger than for the other three earthquakes in this study (Fig. 2.18), as expected given that the geodetic moment for the Nicoya earthquake was a factor of two or more larger than for the other three earthquakes that are evaluated herein.

Relevant to our study, we examined the observed and predicted postseismic deformation at the high-importance continuous GPS station SAN0, 530 km northeast of the Nicoya earthquake rupture zone (Figs. 2.18 and 2.19). Continuous measurements at SAN0 after the Nicoya earthquake reveal ~4 mm of southward transient motion between 2012.8 and 2015 (Fig. 2.19a), but only 0-1 mm of transient deformation in the east component during the same period (Fig. 2.19b). The SAN0 station time-series also clearly shows that the station moved more rapidly southward after the Nicoya Peninsula earthquake than during the preceding 4.5 years (Fig. 2.19a).

The viscoelastic deformation predicted at SAN0 by 2017.0 ranges from 2 mm for the minimum-response model to 15-20 mm for the maximum-response model (Figs. 2.18 and 2.19). Given that the maximum predicted deformation exceeds the observed deformation by a factor of 4 or more, the observations favor the M1 or minimum-response viscoelastic models. This was also true for the Swan Islands earthquake (Section 2.4.1.4).

We also forward calculated the elastic response at SAN0 to the 70-day afterslip solution of Malservisi *et al.* (2015) for comparison to the observed transient deformation (Supplemental Fig. S2.2). At 70 days after the earthquake, SAN0 is predicted to have moved ~1 mm in both horizontal components to the southwest, toward the rupture zone. During the same period, the observed movements in the north and east components are ~1 mm and 0-1 mm, respectively (Fig. 2.19). The observations are consistent with all the deformation being caused by afterslip during the first 70 days.

2.5 RESULTS: INTERSEISMIC VELOCITY FIELD AND ROBUSTNESS

A major outcome of our time-dependent TDEFNODE model is a series of daily positions for 219 GPS sites that are systematically corrected for the coseismic and afterslip effects of the 2009 Swan Islands and 2012 El Salvador and Champerico earthquakes. Fig. 2.20 shows the velocities determined from linear regressions of the corrected daily station positions, representing the first regional velocity field in our study area that has been corrected for the effects of these earthquakes. In Chapter 3, static elastic modeling of these velocities is used to estimate the angular velocities for the plates and blocks in the region, the locking coefficients for the region's major faults, and strain rate tensors for some areas. Here we evaluate the robustness of these velocities and effectiveness

of our time-dependent modeling via a comparison of the root-mean-square (RMS) misfits to a sample of the GPS station time-series before and after our time-dependent modeling.

A key test of the effectiveness of our time-dependent modeling is the improvement in fit that it achieves for a given GPS station time-series. For example, a simple linear regression of the original, uncorrected position time-series for site COAT in Guatemala (Fig. 2.16) gives RMS misfits of 8.1 and 13.5 mm in the east and north components, respectively. In contrast, a linear regression of the COAT time-series corrected for the coseismic and postseismic effects of all 3 earthquakes gives RMS values of 1.9 mm in both components (Fig. 2.12), respectively 77 per cent and 85 percent lower than the original RMS misfits. For comparison, the RMS misfits for 910 linearly-moving continuous stations in the North America plate interior average 1.6 mm in the north and east components. The 1.9 mm RMS values for site COAT are thus close to those of GPS sites in a stable plate interior. TDEFNODE RMS misfits at 9 other continuous GPS sites in our study area, all with large transient deformations in at least one component of station motion range from 1.2-3.1 mm (Fig. 2.12), 50 to 92 per cent less than their original, uncorrected values. Given the similarity of the RMS misfits from our analysis to those for the 910 well-behaved North America plate stations, we conclude that transient effects that were present in our original station position time-series are minimized effectively through our time-dependent modeling.

2.6 DISCUSSION AND CONCLUSIONS

2.6.1 Earthquake comparisons

Of the three earthquakes we modeled with TDEFNODE, the 2009 Swan Islands and 2012 Champerico earthquakes occurred at normal seismogenic depths and had afterslip-to-earthquake moment ratios (35 per cent and 70 per cent) typical of other large strike-slip (Freed 2006) and

subduction-thrust earthquakes (Lin *et al.* 2013). Postseismic observations for both earthquakes are consistent with our assumptions of logarithmically decaying, stationary afterslip. Our modeling suggests that most afterslip for the 2009 Swan Islands earthquake occurred on the eastern end of the rupture zone rather than its western end (Fig. 2.5c), where large afterslip could have altered the stresses acting on the seismically hazardous Motagua fault.

Slip during the 2012 El Salvador earthquake averaged ~1 m and was shallower than 20 km (Fig. 2.10a), consistent with previous results (Ye *et al.* 2013, Geirsson *et al.* 2015). The earthquake triggered an additional ~1 m of nearby afterslip (Fig. 2.10c) with a moment equivalent to 1.4 times the geodetic earthquake moment. Lin *et al.* (2013) report that afterslip following most subduction thrust earthquakes has an equivalent moment release less than 50 per cent of the coseismic moment. The 2012 El Salvador earthquake thus triggered an usually large amount of afterslip. Given geodetic evidence for weak or zero locking at normal seismogenic depths along the El Salvador trench segment (Correa-Mora *et al.* 2009), coseismic slip at seismogenic depths appears to accommodate little or none of the plate convergence. Afterslip may instead play an important role in accommodating convergence at normal seismogenic depths.

Finally, the evidence described above that afterslip dominated the postseismic deformation for the 2009 Swan Islands and 2012 El Salvador and Champerico earthquakes is consistent with modeling evidence that postseismic deformation associated with earthquakes with M_w<7.5 can be well approximated solely via an elastic afterslip model (Sun & Wang 2015).

2.6.2 Implications of far-field postseismic deformation for western Caribbean tectonic studies

Numerous previous studies show that processes such as postglacial rebound, earthquake afterslip, and viscoelastic flow trigger deformation that extends far into nominally rigid plate interiors (e.g. Sella *et al.* 2007; Argus *et al.* 2010; DeMets *et al.* 2016). Our observations and modeling indicate

transient postseismic effects associated with four M>7 earthquakes in Central America are resolvable at distances of 500 km or more from their rupture zones, including most of Central America. Our results imply that corrections to GPS position time-series for the transient effects of earthquakes are essential for efforts to quantify plate/block rotations and interseismic fault locking in Central America. Such corrections are challenging for several reasons. First, the viscoelastic effects of historic earthquakes such as the 1976 M_w=7.5 Motagua fault (Guatemala) strike-slip earthquake (Fig. 2.1) can be difficult to estimate because their coseismic slip solutions are uncertain or unknown. Second, uncertainties about the appropriate rheological models for the lower crust and upper mantle, including whether one or both layers have linear Maxwell, bi-viscous Burgers, or power-law rheologies, make it difficult to predict viscoelastic responses with any confidence. Finally, the close resemblance of afterslip and viscoelastic deformation in the horizontal components of the GPS observations make it difficult to separate the two effects. Despite their challenges, we show that GPS time-series that are corrected in a consistent manner for earthquake cycle effects are well approximated by simple linearly moving sites as gauged by a comparison of their RMS misfits to those for GPS sites in plate interiors.

ACKNOWLEDGEMENTS

The first author was supported by a UNAVCO Graduate COCONet Fellowship. This work was funded by NSF grant EAR-1144418 (DeMets) and also benefited from National Science Foundation support for UNAVCO under grant EAR-1042906. We thank Central American institutions that provided technical, data, and logistical support, including Universidad Nacional Autonoma de Honduras, Universidad Nacional Autonoma de Mexico, Universidad Mariano Galvez (Guatemala City), Universidad San Carlos (Guatemala City), Ministerios de Medio

Ambiente y Recursos Naturales El Salvador, Instituto Geografico Nacional of El Salvador and Guatemala, INSIVUMEH of Guatemala, and CONRED of Guatemala. Figures were prepared using Generic Mapping Tools software (Wessel & Smith 1991).

REFERENCES

Altamimi, Z., Collilieux, X., & Metivier, L., 2011. ITRF2008: an improved solution of the international terrestrial reference frame, *J. Geodyn*., **85**, 457-473.

Alvarado, D., DeMets, C., Tikoff, B., Hernández, D., Wawrzyniec, T.F., Pullinger, C., Mattioli, G., Turner, H.L., Rodriguez, M. and Correa-Mora, F., 2011. Forearc motion and deformation between El Salvador and Nicaragua: GPS, seismic, structural, and paleomagnetic observations, *Lithosphere*, *3*(1), pp.3-21.

Argus, D.F. and Peltier, W.R., 2010. Constraining models of postglacial rebound using space geodesy: a detailed assessment of model ICE-5G (VM2) and its relatives, *Geophysical Journal International*, *181*(2), pp.697-723.

Authemayou, C., Brocard, G., Teyssier, C., Simon‐Labric, T., Guttiérrez, A., Chiquín, E.N. and Morán, S., 2011. The Caribbean–North America–Cocos Triple Junction and the dynamics of the Polochic–Motagua fault systems: Pull‐up and zipper models, *Tectonics*, *30*(3).

Bertiger, W., S. Desai, B. Haines, N. Harvey, A. Moore, S. Owen, & J. Weiss, 2010. Single receiver phase ambiguity resolution with GPS data, *J. Geodesy*, **84**, 327-337.

Blewitt, G., Kreemer, C., & Hammond, W. C., 2009. Geodetic observation of contemporary deformation in the northern Walker Lane: 1. Semipermanent GPS strategy, *Geol. Soc. Am.*, **447**, 1–15, doi:10.1130/2009.2447(01).

Cáceres, D., Monterroso, D. & Tavakoli, B., 2005. Crustal deformation in northern Central America, *Tectonophysics*, *404*(1), pp.119-131.

Correa-Mora, F., DeMets, C., Alvarado, D., Turner, H. L., Mattioli, G., Hernandez, D., & Tenorio, C., 2009. GPS-derived coupling estimates for the Central America subduction zone and volcanic arc faults: El Salvador, Honduras and Nicaragua, *Geophysical Journal International*, **179**(3), 1279-1291.

DeMets, Charles, 2000. Honduras 2000, UNAVCO, GPS Data Set, doi:10.7283/T55D8PZC.

DeMets, C., 2001. A new estimate for present-day Cocos-Caribbean plate motion: Implications for slip along the Central American volcanic arc, *Geophysical Research Letters,* **28**(21), 4043-4046.

DeMets, C., 2004. Central America 2003/2004, UNAVCO, GPS Data Set, doi:10.7283/T5MG7MKZ.

DeMets, C., 2007. Central America 2006: El Salvador, UNAVCO, GPS Data Set, doi:10.7283/T5T151RS.

DeMets, C., 2007. Central America 2006: Honduras, UNAVCO, GPS Data Set, doi:10.7283/T5P8491G.

DeMets, C., 2008. Central America 2007: El Salvador, UNAVCO, GPS Data Set, doi:10.7283/T5NC5Z91.

DeMets, C., 2008. Central America 2007: Honduras, UNAVCO, GPS Data Set, doi:10.7283/T5HM56KP.

DeMets, C., 2009. Central America 2008: El Salvador, UNAVCO, GPS Data Set, doi:10.7283/T5CV4FVZ.

DeMets, C., 2011. Honduras 2008, UNAVCO, GPS Data Set, doi:10.7283/T5GM85F9.

DeMets, C., 2011. Honduras 2009, UNAVCO, GPS Data Set, doi:10.7283/T5BV7DQK.

DeMets, C., 2011. Honduras 2010, UNAVCO, GPS Data Set, doi:10.7283/T5736P0K.

DeMets, C. & Tikoff, B., 2015. Central America 2009: El Salvador, UNAVCO, GPS Data Set, doi:10.7283/T58P5XT1.

DeMets, C. & Tikoff, B., 2015. Central America 2010: El Salvador, UNAVCO, GPS Data Set, doi:10.7283/T54X5633.

DeMets, C. & Tikoff, B., 2015. Central America 2012: El Salvador, UNAVCO, GPS Data Set, doi:10.7283/T56Q1VHC.

DeMets, C. & Tikoff, B., 2015. Central America 2012: Guatemala, UNAVCO, GPS Data Set, doi:10.7283/T52Z13TG.

DeMets, C. & Tikoff, B., 2015. Central America 2013: El Salvador, UNAVCO, GPS Data Set, doi:10.7283/T5Z60MCZ.

DeMets, C. & Tikoff, B., 2015. Central America 2013: Guatemala, UNAVCO, GPS Data Set, doi:10.7283/T5TH8K0H.

DeMets, C. & Tikoff, B., 2015. Central America 2013: Honduras, UNAVCO, GPS Data Set, doi:10.7283/T5PR7T97.

DeMets, C. & Tikoff, B., 2015. Central America 2014: El Salvador, UNAVCO, GPS Data Set, doi:10.7283/T5K072K6.

DeMets, C. & Merkouriev, S., 2016. High-resolution reconstructions of Pacific–North America plate motion: 20 Ma to present, *Geophysical Supplements to the Monthly Notices of the Royal Astronomical Society*, *207*(2), pp.741-773.

DeMets, C., Gordon, R. G., & Argus, D. F., 2010. Geologically current plate motions. *Geophysical Journal International*, **181**(1), 1-80.

Dixon, T. H., 2001. Nicaragua 2001, UNAVCO, GPS Data Set, doi:10.7283/T5JQ0Z5V.

Dixon, T. H., 2003. Costa Rica 2003, UNAVCO, GPS Data Set, doi:10.7283/T5PN93R3.

Dixon, T. H., 2004. Nicaragua 2003, UNAVCO, GPS Data Set, doi:10.7283/T5DZ06FH.

Dixon, T. H., 2010. Costa Rica GPS Network: CABA-Caballito P.S., UNAVCO, GPS Data Set, doi:10.7283/T5GX48QQ.

Dziewonski, A. M., Chou, T. A., & Woodhouse, J. H., 1981. Determination of earthquake source parameters from waveform data for studies of global and regional seismicity, *J. Geophys. Res.*, **86**, 2825-2852.

Ellis, A. P., DeMets, C., Briole, P., Molina, E., Flores, O., Rivera, J., Lasserre, C., Lyon-Caen, H., & Lord, N., 2015. Geodetic slip solutions for the M_w = 7.4 Champerico (Guatemala) earthquake of 2012 November 7 and its postseismic deformation, *Geophys. J. Int.*, **201**(2), 856-868.

Ekström, G., Nettles, M., & Dziewonski, A. M., 2012. The global CMT project 2004-2010: centroid-moment tensors for 13,017 earthquakes, *Phys. Earth planet. Inter.*, **200–201**, 1-9.

Franco, A., Lasserre, C., Lyon-Caen, H., Kostoglodov, V., Molina, E., Guzmán-Speziale, M., Monterosso, D., Robles, V., Figueroa, C., & Amaya, W., 2012. Fault kinematics in northern Central America and coupling along the subduction interface of the Cocos plate, from GPS data in Chiapas (Mexico), Guatemala and El Salvador, *Geophysical Journal International,* **189**(3): 1223-1236.

Freed, A.M., Bürgmann, R., Calais, E. & Freymueller, J., 2006. Stress-dependent power-law flow in the upper mantle following the 2002 Denali, Alaska, earthquake, *Earth and Planetary Science Letters*, *252*(3), pp.481-489.

Geirsson, H., LaFemina, P. C., DeMets, C., Hernandez, D. A., Mattioli, G. S., Rogers, R., Rodriguez, M., Marroquin, G., & Tenorio, V., 2015. The 2012 August 27 M_w 7.3 El Salvador

earthquake: expression of weak coupling on the Middle America subduction zone, *Geophys. J. Int.,* **202***,* 1677-1689.

Graham, S. E., DeMets, C., DeShon, H. R., Rogers, R., Maradiaga, M. R., Strauch, W., & Wiese, K., 2012. GPS and seismic constraints on the M=7.3 2009 Swan Islands earthquake: implications for stress changes along the Motagua fault and other nearby faults, *Geophys. J. Int.*, **190,** 1625-1639.

Hayes, G. P., Wald, D. J., & Johnson, R. L., 2012. Slab1.0: a three-dimensional model of global subduction zone geometries, *J. geophys. Res*., **117**, B01302, doi:10.1029/2011JB008524.

Hearn, E. H., Onishi, C. T., Pollitz, F. F., & Thatcher, W. R., 2013. How do "ghost transients" from past earthquakes affect GPS slip rate estimates on southern California faults?, *Geochem. Geophys. Geosys*., **14**, doi:10.1002/ggge.20080.

Hu, Y. & Wang, K., 2012. Spherical-Earth finie element model of short-term postseismic deformation following the 2004 Sumatra earthquake, *J. geophys. Res*., 117, doi:10.1029/2012JB009153.

Hu, Y., Wang, K., He, J., Klotz, J., & Khazaradze, G., 2004.Three-dimensional viscoelastic finite element model for post-seismic deformation of the great 1960 Chile earthquake, *J. Geophys. Res.* **109**, B12403.

Kobayashi, D., LaFemina, P., Geirsson, H., Chichaco, E., Abrego, A. A., Mora, H., & Camacho, E., 2014. Kinematics of the western Caribbean: collision of the Cocos Ridge and upper plate deformation, *Geochem. Geophys. Geosyst*., **15**, 1671-1683.

Kogan, M. G., Vasilenko, N. F., Frolov, D. I., Freymueller, J. T., Steblov, G. M., Prytkov, A. S., & Ekström, G., 2013. Rapid postseismic relaxation after the great 2006–2007 Kuril earthquakes from GPS observations in 2007–2011, *Journal of Geophysical Research: Solid Earth*, **118**(7), 3691-3706.

LaFemina, P., 2013. Nicaragua 2010: October 2010, UNAVCO, GPS Data Set, doi:10.7283/T54J0C4X.

LaFemina, P., 2013. Nicaragua 2011: May 2011, UNAVCO, GPS Data Set, doi:10.7283/T5NK3C25.

LaFemina, P., 2013. Nicaragua 2011: November 2011, UNAVCO, GPS Data Set, doi:10.7283/T50R9MDN.

LaFemina, P., 2013. Nicaragua 2012, UNAVCO, GPS Data Set, doi:10.7283/T5KD1W9D.

LaFemina, P., 2013. Nicaragua 2013: January 2013, UNAVCO, GPS Data Set, doi:10.7283/T5Q52N14.

LaFemina, P., Dixon, T. H., Govers, R., Norabuena, E., Turner, H., Saballos, A., Mattioli, G., & Strauch, W., 2009. Fore-arc motion and Cocos Ridge collision in Central America, *Geochem. Geophys. Geosyst*., **10**(5), Q05S14, doi:10.1029/2008GC002181.

Lin, Y. N. N., Sladen, A., Ortega-Culaciati, F., Simons, M., Avouac, J. P., Fielding, E. J., & Vigny, C., 2013. Coseismic and postseismic slip associated with the 2010 Maule Earthquake, Chile: Characterizing the Arauco Peninsula barrier effect, *Journal of Geophysical Research: Solid Earth*, **118**(6), 3142-3159.

Lyon-Caen, H., Barrier, E., Lasserre, C., Franco, A., Arzu, I., Chiquin, L., Chiquin, M., Duquesnoy, T., Flores, O., & Galicia, O., 2006. Kinematics of the North American-Caribbean-Cocos plates in Central America from new GPS measurements across the Polochic-Motagua fault system, *Geophysical Research Letters,* **33** (19).

Malservisi, R., Schwartz, S. Y., Voss, N., Protti, M., Gonzalez, V., Dixon, T. H., & Voyenko, D., 2015. Multiscale postseismic behavior on a megathrust: The 2012 Nicoya earthquake, Costa Rica, *Geochemistry, Geophysics, Geosystems*, **16**(6), 1848-1864.

Márquez-Azúa, B. & DeMets, C., 2003. Crustal velocity field of Mexico from continuous GPS measurements, 1993 to June 2001: implications for the neotectonics of Mexico, *J. geophys. Res*., **108**, 2450, doi:10.1029/2002JB002241.

Martínez-Díaz, J.J., Alvarez-Gómez, J.A., Benito, B. & Hernández, D., 2004. Triggering of destructive earthquakes in El Salvador, *Geology*, *32*(1), pp.65-68.

McCaffrey, R., 2009. Time-dependent inversion of three-component continuous GPS for steady and transient sources in northern Cascadia, *Geophys. Res. Lett*., **36**, L07304, doi:10.1029/2008GL036784.

Newman, Andrew, 2010, Nicoya 2010, UNAVCO, GPS Data Set, doi:10.7283/T59G5JX2.

Okada, Y., 1985. Surface deformation due to shear and tensile faults in a half-space, *Bulletin of the Seismological Society of America*, **75**, 1135-1154.

Plafker, G., 1976. Tectonic Aspects of the Guatemala Earthquake of 4 February 1976, *Science*, **103,** 4259.

Pollitz, F.F., 1997. Gravitational viscoelastic postseismic relaxation on a layered spherical Earth, *J. geophys. Res*., **102**, 17 921-17 941.

Protti, M., González, V., Newman, A. V., Dixon, T. H., Schwartz, S. Y., Marshall, J. S., Feng, L., Walter, J. I., Malservisi, R., & Owen, S. E., 2013. Nicoya earthquake rupture anticipated by geodetic measurement of the locked plate interface, *Nat. Geosci.*, **7**(2), 117-121.

Rogers, R. D. & Mann, P., 2007. Transtensional deformation of the western Caribbean-North America plate boundary zone, *Geol. Soc. Am. Spec. Pap.*, **428**, 37-64.

Rosencrantz, E. & Mann, P., 1991. SeaMARC II mapping of transform faults in the Cayman Trough, Caribbean Sea, *Geology*, **19**, 690-693.

Schwartz, S., Dixon, T. H., 2000. Costa Rica 2000, UNAVCO, GPS Data Set, doi:10.7283/T5FN149G.

Sella, G.F., Stein, S., Dixon, T.H., Craymer, M., James, T.S., Mazzotti, S. and Dokka, R.K., 2007. Observation of glacial isostatic adjustment in "stable" North America with GPS, *Geophysical Research Letters*, *34*(2).

Sen, P. K., 1968. Estimates of the regression coefficient based on Kendall's tau, *Journal of the American Statistical Association*, ***63***(324), 1379-1389.

Staller, A., Martínez-Díaz, J.J., Benito, B., Alonso-Henar, J., Hernández, D., Hernandez-Rey, R. & Diaz, M., 2016. Present-day crustal deformation along the El Salvador Fault Zone from ZFESNet GPS network, *Tectonophysics*, *670*, pp.66-81.

Suito, H. & Freymueller, J. T., 2009. A viscoelastic and afterslip postseismic deformation model for the 1964 Alaska earthquake, *J. Geophys. Res.,* **114**, B11404.

Sun, T. & Wang, K., 2015. Viscoelastic relaxation following subduction earthquakes and its effects on afterslip determination, *Journal of Geophysical Research: Solid Earth*, **120**(2), 1329-1344.

Wang, K., Hu, Y., & He, J., 2012. Deformation cycles of subduction earthquakes in a viscoelastic Earth, *Nature*, **484**(7394), 327.
Wessel, P. & Smith, W.H., 1991. Free software helps map and display data, *Eos, Transactions American Geophysical Union*, *72*(41), pp.441-446.

White, R. A. & Harlow, D. H., 1993. Destructive upper-crustal earthquakes of Central America since 1900, *Bulletin of the Seismological Society of America*, **83**(4), 1115-1142.

White, R. A., Ligorría, J. P., & Cifuentes, I. L., 2004. Seismic history of the Middle America subduction zone along El Salvador, Guatemala, and Chiapas, Mexico: 1526-2000, *Special Papers-Geological Society of America,* 379-396.

Ye, L., Lay, T., & Kanamori, H., 2013. Large earthquake rupture process variations on the Middle America megathrust, *Earth planet. Sci. Lett*., **381**, 147-155.

Zumberge, J. F., Heflin, M. B., Jefferson, D. C., Watkins, M. M., & Webb, F. H., 1997. Precise point positioning for the efficient and robust analysis of GPS data from large networks, *J. geophys. Res*., **102**, 5005-5017.

TABLES

Table 2.1: GPS site information showing station locations and data timespans

Site ID	Longitude (°E)	Latitude (°N)	Start date (decimal year)	End date (decimal year)	Number of observations (days)
ACAJ	270.17	13.58	2004.23	2017.21	59
AGLA	270.32	13.84	2008.73	2013.19	6
AHUA	270.19	13.91	2004.25	2009.19	48
AIES	270.95	13.45	2007.35	2016.63	2567
ALAR	270.22	14.00	2014.56	2016.66	346
AMAT	272.00	13.41	2007.88	2012.39	4
AVES	296.38	15.67	1994.37	1998.25	28
AZTE	266.06	16.22	2002.05	2005.14	13
BARI	268.69	15.80	2010.62	2015.78	1188
BEND	269.40	14.18	2013.16	2015.07	8
BLUX	276.23	11.99	2002.54	2012.75	9
BT10	271.49	13.53	2006.34	2012.36	60
CABA	271.32	13.73	2007.84	2012.36	7
CAH0	270.18	15.61	1999.07	2015.06	11
CAM0	270.94	15.39	2003.10	2015.06	9
CAMP	269.46	19.84	1995.67	2008.95	2683
CARI	272.31	13.83	2004.54	2013.45	20
CATR	270.26	14.46	2011.88	2015.99	754
CAYS	280.15	15.80	2010.69	2014.10	686
CBSB	280.17	19.71	2005.88	2014.25	2405
CEGD	271.10	13.94	2004.33	2012.35	52
CGUI	272.44	12.98	2012.71	2016.25	928
CH15	271.44	13.62	2004.07	2014.88	75
CHA0	270.48	14.83	2003.10	2015.10	6
CHET	271.70	18.50	1993.28	2016.81	5415
CHI0	270.35	14.78	1999.07	2012.91	15
CHIQ	272.49	14.28	2003.95	2013.46	27
CHIS	269.71	15.81	2011.65	2015.92	1146
CHL0	269.62	14.08	1999.06	2015.07	17
CHNN	272.86	12.64	2001.05	2012.72	33
CHPO	268.09	14.29	2012.90	2016.13	1146
CHQG	269.25	15.35	2010.59	2013.44	863
CLV2	273.15	12.57	2010.20	2014.52	1530
CML0	269.20	14.64	1999.07	2015.08	19
CMP1	274.29	14.51	2000.19	2005.41	6
CN18	276.06	17.41	2014.74	2016.85	605
CN21	272.57	13.40	2014.33	2016.85	825
CN22	272.96	12.38	2012.11	2014.00	652
CN23	271.22	17.26	2012.56	2016.85	1508
CN24	271.95	19.58	2013.83	2016.85	1094
CN25	267.86	16.23	2014.12	2016.81	970
CN30	276.23	11.99	2012.12	2012.67	205
CNCC	267.31	16.12	2002.12	2015.13	17
CNCH	271.66	14.03	2004.52	2013.54	17
CNG2	273.30	12.50	2011.39	2016.85	655
CNR1	270.71	13.67	2012.25	2016.66	1299
COA0	269.60	15.47	2003.09	2006.08	2
COAT	268.12	14.70	2010.52	2015.43	1251
COB0	269.61	15.46	1999.06	2015.06	27

COMI	267.86	16.28	2002.07	2016.81	1639
CON0	270.55	14.52	1999.07	2015.10	17
CORI	272.80	12.52	2003.16	2012.72	22
CORN	276.94	12.18	2001.03	2003.15	10
COTZ	268.94	14.33	2011.82	2015.99	940
CPJ0	270.76	14.85	2003.10	2006.08	5
CRM1	271.10	13.73	2007.88	2012.35	4
CRO1	295.42	17.76	1998.23	2010.86	2383
CRR1	271.27	13.67	2007.84	2012.35	8
CSJO	271.61	13.49	2007.86	2012.37	5
CUCU	271.14	14.58	2008.07	2013.56	9
DERA	271.18	13.67	2004.17	2007.84	31
DOL2	269.43	14.35	2012.93	2015.04	7
DOLO	269.42	14.35	2012.93	2015.04	7
ECOP	271.68	15.33	2004.41	2006.47	10
ELCO	272.60	12.81	2001.05	2012.70	21
ELEN	270.13	16.92	2001.93	2015.92	3499
ERAN	271.54	14.23	2004.52	2013.55	17
ERAZ	272.89	14.60	2004.64	2010.48	21
ESPI	267.93	15.70	2002.10	2015.13	13
ESPO	266.40	15.94	2002.05	2005.14	13
ESTC	266.52	17.46	2004.10	2015.13	14
FMIN	270.33	15.08	1999.08	2015.09	18
FRT1	271.96	15.78	2004.58	2013.15	24
FSD0	298.85	14.73	1994.39	1999.87	15
GCGT	278.62	19.29	2005.44	2011.90	2093
GLCO	273.93	15.03	2000.18	2010.47	11
GOME	268.92	14.03	2013.16	2015.27	8
GRAC	271.42	14.59	2004.50	2013.55	17
GRUT	267.14	16.42	2003.11	2015.13	14
GUAJ	270.53	14.23	2004.28	2009.33	45
GUAT	269.48	14.59	2000.57	2013.49	4375
GUAY	270.84	13.84	2008.88	2012.34	6
HERH	273.17	12.61	2010.19	2015.29	1762
HON0	270.39	15.03	1999.08	2006.10	8
HON1	270.38	15.03	2012.92	2015.09	8
HOYN	273.17	12.60	2010.19	2015.60	1771
HUE0	268.53	15.28	1999.06	2006.08	9
HUEH	268.50	15.32	2002.43	2015.67	1143
ICAM	269.47	19.85	2010.03	2016.81	2389
ICHA	271.28	13.56	2007.85	2012.35	4
IPA0	270.37	14.62	2006.09	2015.10	10
ISCO	272.94	5.54	2011.38	2016.71	1527
ITUX	266.88	16.75	2013.50	2015.88	836
IXTA	269.73	14.18	2012.95	2015.06	8
JAGU	271.29	15.10	2004.43	2013.57	20
JALA	269.99	14.62	2013.01	2015.05	7
JCFI	273.17	12.68	2010.76	2016.59	816
JOY0	269.17	15.01	2003.10	2006.09	4
JUCU	271.75	13.25	2004.87	2012.72	48
LAGO	272.00	14.94	2008.08	2010.44	7
LCAN	271.56	14.73	2004.50	2013.55	14
LCEB	273.16	15.75	2004.02	2013.59	24

LEME	273.09	12.43	2009.90	2016.84	1594
LEON	273.09	12.43	2001.05	2003.15	7
LESP	271.84	14.31	2004.10	2010.42	24
LJAS	272.25	13.60	2004.54	2013.45	28
LNUB	270.22	13.90	2014.56	2016.66	535
LOLO	271.63	13.56	2007.86	2012.37	8
LPIN	272.08	13.68	2007.88	2012.39	5
LPZW	272.31	14.31	2003.95	2013.53	30
LSSJ	271.80	13.38	2007.87	2017.10	7
MALP	273.32	12.55	2003.14	2012.69	8
MANA	273.75	12.15	2000.39	2012.68	2495
MAYA	270.87	14.84	2004.50	2013.58	19
MAZ0	268.45	14.54	1999.06	2012.95	8
MAZ2	268.45	14.54	2012.90	2016.13	1105
MEZA	272.07	15.45	2003.81	2013.59	38
MGL1	271.85	13.53	2007.87	2012.39	13
MNGO	270.80	13.97	2004.31	2017.09	57
MNTO	273.62	14.92	2000.16	2010.47	13
MOD0	270.77	15.93	2003.10	2015.06	9
MON0	270.14	14.50	2006.10	2015.05	9
MORO	273.08	13.60	2006.29	2013.45	15
MOYU	269.92	14.03	2013.01	2015.06	8
MPSC	267.11	15.46	2002.05	2015.13	19
MRLS	271.15	15.46	2011.88	2016.00	1112
MTP1	267.63	14.79	2008.31	2016.85	2598
NAJO	272.38	15.56	2004.60	2005.75	11
NARA	269.19	17.23	2010.37	2016.12	1505
NDAM	272.64	13.68	2004.74	2013.44	20
NOCO	270.80	14.44	2004.45	2013.57	34
NONU	271.05	13.57	2007.83	2012.34	6
OCOM	272.05	14.70	2004.51	2013.58	21
OPAC	271.63	13.72	2007.85	2012.37	5
OSIC	271.85	13.81	2004.11	2012.39	49
PAM0	269.37	15.46	2003.09	2006.09	5
PASA	272.17	13.59	2007.88	2012.39	4
PAZC	273.41	12.29	2001.05	2012.69	11
PCYA	269.36	14.41	2009.05	2012.03	84
PIN0	269.62	14.55	1999.06	2006.10	25
PIN2	269.61	14.55	2012.95	2015.04	10
PLAY	270.65	13.79	2008.88	2017.09	4
POCH	273.49	11.77	2000.44	2012.72	15
POLS	273.19	12.65	2010.18	2016.85	1227
PONE	272.98	12.38	2001.06	2012.69	18
POPT	270.59	16.33	2010.36	2014.81	1027
PRT1	274.63	12.57	2000.61	2012.73	23
PRUS	271.39	13.35	2007.85	2012.36	7
PUEC	276.62	14.04	2001.04	2006.16	13
QICH	268.85	15.03	2013.02	2015.12	7
QUE0	268.49	14.87	1999.06	2006.08	9
QUE1	268.49	14.87	1999.06	2016.13	1005
QUEN	273.15	12.59	2010.20	2014.10	1394
RECA	272.85	13.33	2004.54	2013.44	29
RIOB	274.78	12.92	2000.60	2003.15	12

ROA0	273.47	16.32	2007.35	2016.81	3047
ROG1	271.42	13.82	2007.84	2012.35	5
ROSA	271.22	14.77	2004.51	2013.56	16
ROTB	273.26	12.52	2010.78	2014.41	95
RUB0	269.55	15.99	1999.07	2015.12	13
SABY	268.81	18.97	2004.50	2016.81	2226
SAIN	272.18	13.32	2004.38	2014.88	88
SAL0	269.72	15.08	1999.06	2015.13	12
SALN	273.14	12.62	2010.19	2014.35	1099
SAN0	278.28	12.58	2007.93	2016.85	2963
SAN2	269.75	14.82	1999.07	2015.13	14
SANA	278.27	12.52	1994.10	2003.27	25
SAYA	269.81	16.52	2010.59	2014.85	683
SBAR	271.65	13.63	2007.85	2012.37	5
SCAR	271.92	13.64	2007.87	2012.39	6
SCW2	272.98	12.70	2013.02	2016.25	1138
SFDP	273.76	14.97	2000.17	2004.54	6
SGTO	272.94	13.10	2004.55	2013.44	20
SIGN	270.68	13.49	2003.09	2006.19	6
SJAN	271.79	14.82	2004.51	2013.58	19
SJUL	273.41	14.14	2008.08	2010.46	7
SLOR	272.56	13.42	2000.72	2010.46	603
SMCO	271.05	14.40	2008.06	2013.57	11
SMHO	268.19	14.95	2012.91	2014.80	646
SNJE	270.40	13.87	2007.22	2016.61	3349
SNTA	272.05	14.07	2004.52	2013.54	19
SOL0	268.51	15.57	1999.06	2015.07	14
SOLE	267.48	16.68	2002.12	2015.12	17
SSAS	270.95	13.45	2004.35	2009.08	49
SSIA	270.88	13.70	2004.79	2016.96	3264
SUNZ	270.61	13.50	2004.21	2009.10	44
SVCI	271.21	13.64	2014.55	2016.66	518
SVIC	271.21	13.63	2007.88	2012.35	9
TACA	270.65	13.97	2008.88	2017.09	6
TAXI	269.53	14.03	2011.04	2015.39	1253
TECF	273.16	12.60	2010.76	2015.41	1543
TECP	269.01	14.76	2013.16	2016.14	973
TEG2	272.79	14.09	2011.32	2016.85	1512
TEGU	272.79	14.09	2000.37	2014.02	4009
TEJU	270.90	14.18	2003.09	2006.19	6
TELN	273.17	12.61	2009.98	2016.05	1953
TEUS	274.19	12.41	2000.59	2006.13	21
TGIG	266.88	16.78	2015.50	2016.81	284
THIG	267.70	14.88	2015.50	2016.81	281
TIKA	270.39	17.22	2011.03	2013.08	362
TINT	270.12	15.32	2010.60	2014.16	979
TNPJ	266.78	15.70	2014.88	2016.06	429
TONU	273.16	13.93	2004.69	2013.46	21
TOTO	268.67	15.02	2013.03	2015.12	7
TPCH	267.70	14.88	2003.49	2006.50	570
TRAN	273.31	12.03	2001.07	2012.73	12
USP0	269.13	15.35	2003.09	2006.09	5
USUL	271.52	13.38	2007.87	2012.38	9

UVGS	268.82	14.79	2013.16	2015.08	10
VIEJ	271.01	13.51	2007.83	2010.30	4
VIKH	295.20	17.72	2006.64	2016.77	3182
VILL	267.09	18.00	1993.14	2016.81	5337
VMIG	271.70	13.40	2007.49	2016.02	2301
ZAC0	270.50	14.98	2003.10	2015.09	19
ZACA	270.64	15.11	2010.57	2013.75	1026
ZAPO	270.17	14.14	2013.01	2015.06	8

Table 2.2: Characteristics of M>7 earthquakes in northern Central America from 2009-2017

Earthquake	Transient Type	Timing *(decimal year)*	Location Down-dip (km)	Moment Magnitude (M_w)	Estimated Scalar[1] Moment (N•m)	gCMT Scalar Moment (N•m)	Previous studies
Swan Islands *(Honduras)*	coseismic	2009.39	0-15	7.3	1.2E+20	1.3E+20	Graham *et al.* 2012
Swan Islands *(Honduras)*	postseismic *(afterslip)*	2009.39-2017.0	0-15	7.0	3.6E+19	n/a	n/a
Gulf of Fonseca *(El Salvador)*	coseismic	2012.6544	0-20	7.3	1.3E+20	1.3E+20	Ye *et al.* 2014; Geirsson *et al.* 2012
Gulf of Fonseca *(El Salvador)*	postseismic *(afterslip)*	2012.6544-2017.0	10-30	7.4	1.8E+20	n/a	Geirsson *et al.* 2012
Champerico *(Guatemala)*	coseismic	2012.8511	10-30	7.4	1.5E+20	1.5E+20	Ellis *et al.* 2015; Ye *et al.* 2013
Champerico *(Guatemala)*	postseismic *(afterslip)*	2012.8511-2017.0	30-50	7.3	9.6E+19	n/a	Ellis *et al.* 2015
Nicoya[2] *(Costa Rica)*	coseismic	2012.6790	10-40	7.6	n/a	3.4E+21	Protti *et al.* 2013
Nicoya[2] *(Costa Rica)*	postseismic *(afterslip)*	2012.6790-2012.8706	10-40	7.2	6.9E+19	n/a	Malservisi *et al.* 2015

[1] Table values are from our preferred model results unless otherwise noted

[2] Table values are from previous studies (listed) and not a product of our modelling

FIGURES

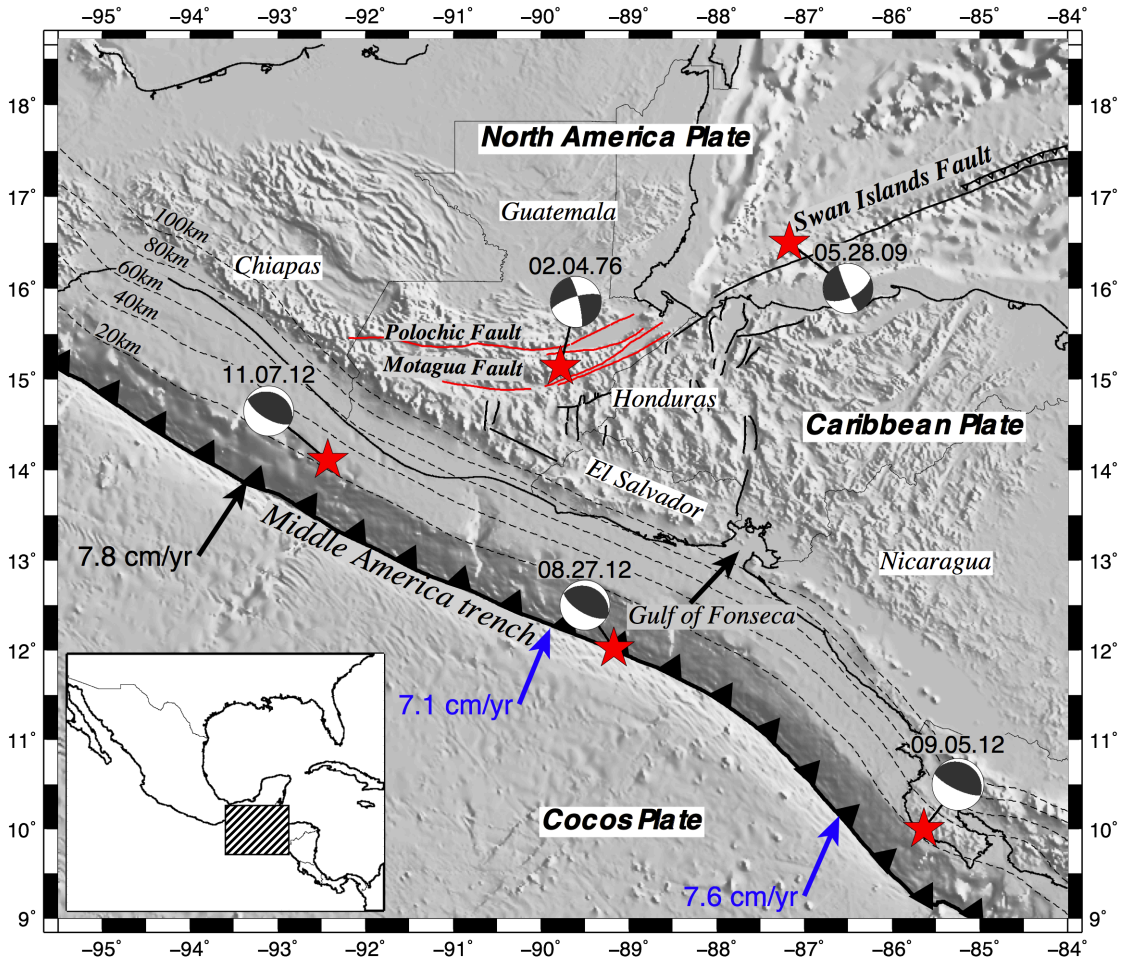

Figure 2.1. Seismotectonics and geography of the study area. Dashed lines denote subducting slab contours. Red stars show epicenters for the major earthquakes in Central America since 2009 along with the 1976 Guatemala earthquake. Associated earthquake focal mechanisms are the global centroid−moment−tensors (Ekström *et al.* 2012) and are offset from epicenter locations. Black and blue vectors show Cocos Plate velocities relative to the North America and Caribbean plates, respectively (DeMets *et al.* 2010).

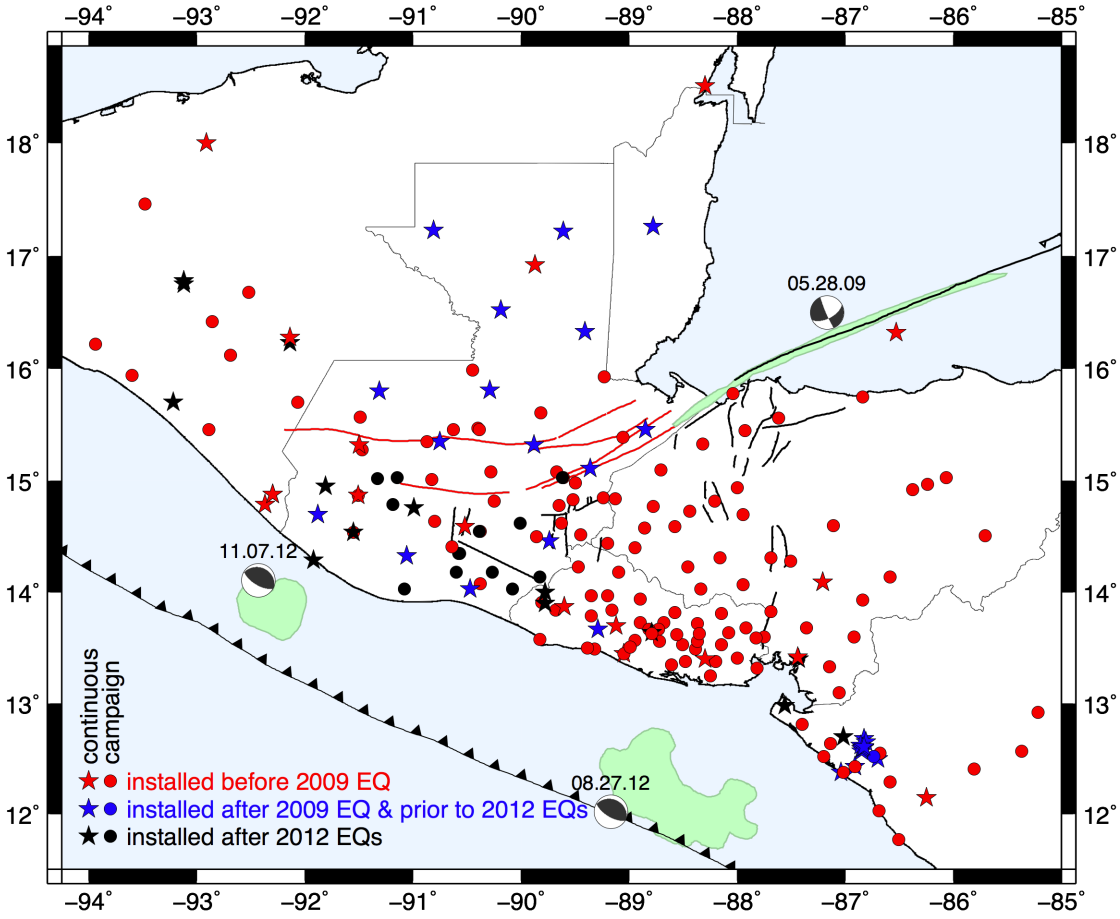

Figure 2.2. Locations of GPS stations used in this study. Light green patches show the rupture areas of three major earthquakes since 2009 (see text). Focal mechanisms are from Fig. 2.1. and coincide with the earthquake epicenters. Abbreviation: EQ; earthquake.

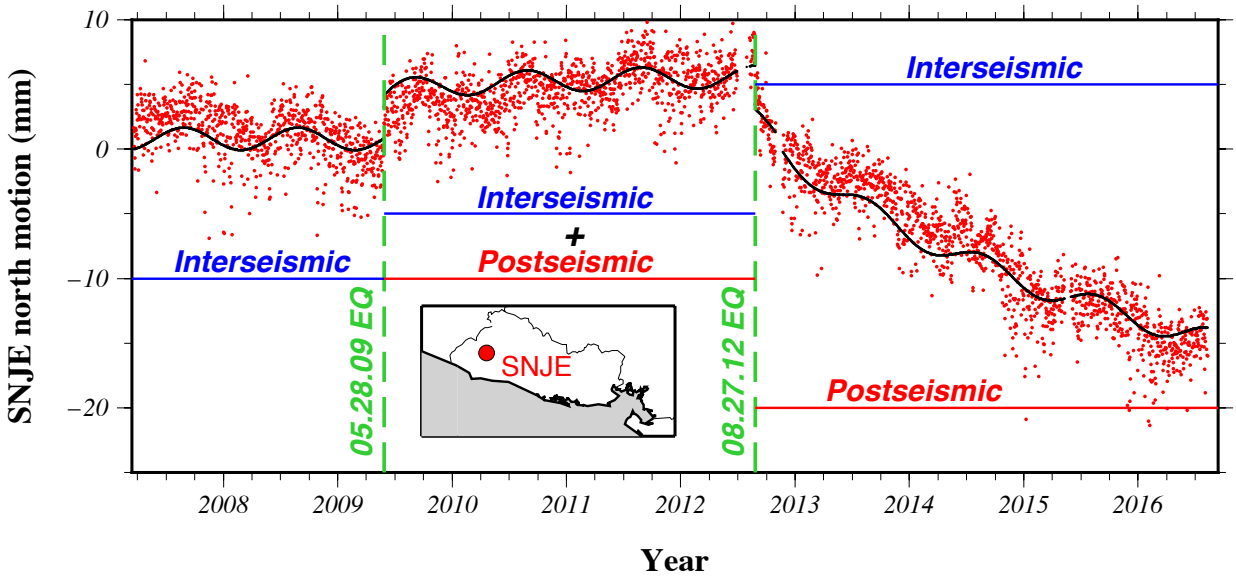

Figure 2.3. GPS daily position time-series for the north component of site SNJE in El Salvador. Site positions (red circles) are reduced by SNJE's long-term slope to enhance signals associated with earthquakes in 2009 and 2012. The daily site positions are offset by the 28 May 2009 Swan Islands and 27 August 2012 El Salvador earthquakes (green vertical dashed lines) and are further influenced by the transient postseismic effects of both events. Black lines show the fit estimated with our TDEFNODE inversion (see text). Abbreviation: EQ; earthquake.

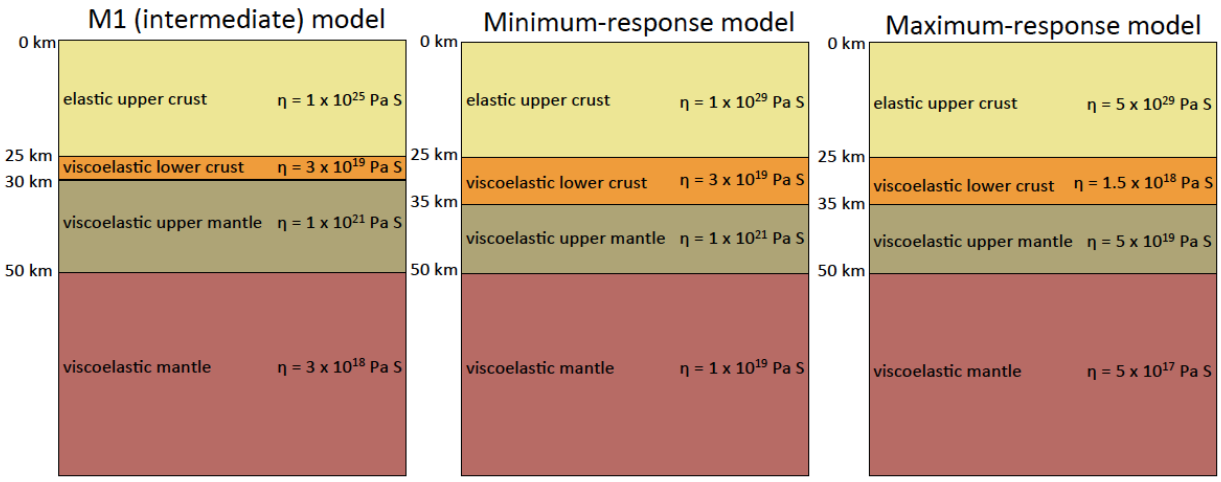

Figure 2.4. Diagrams of layer viscosities and depths for the three Earth structure models used for our viscoelastic modeling.

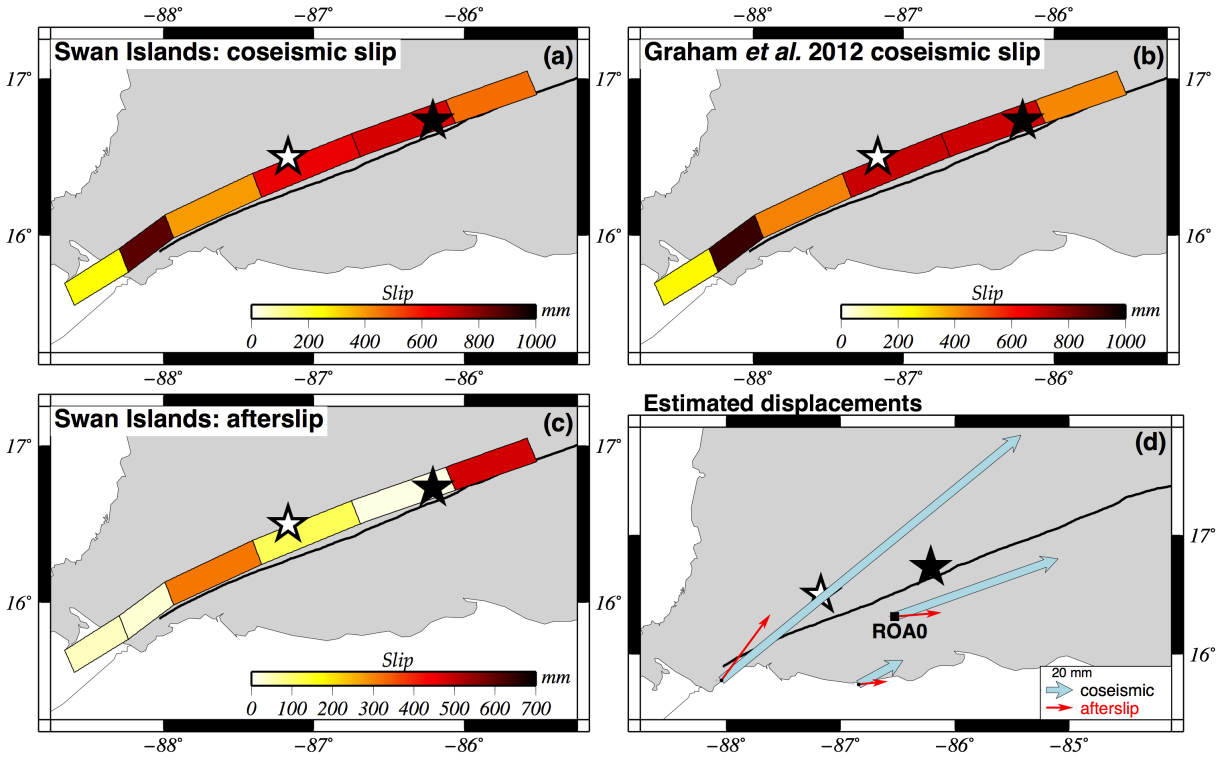

Figure 2.5. (a) TDEFNODE coseismic slip estimate for the 2009 Swan Islands earthquake. (b) Graham *et al.* (2012) coseismic slip solution. (c) TDEFNODE postseismic afterslip estimate for years 2009.4 to 2017.0. (d) Site motions predicted by the coseismic and afterslip solutions are shown in panels (a) and (c). The white and black stars are earthquake centroids from the Global CMT catalogue (Dziewonski *et al.* 1981; Ekström *et al.* 2012) and United States Geological Survey, respectively.

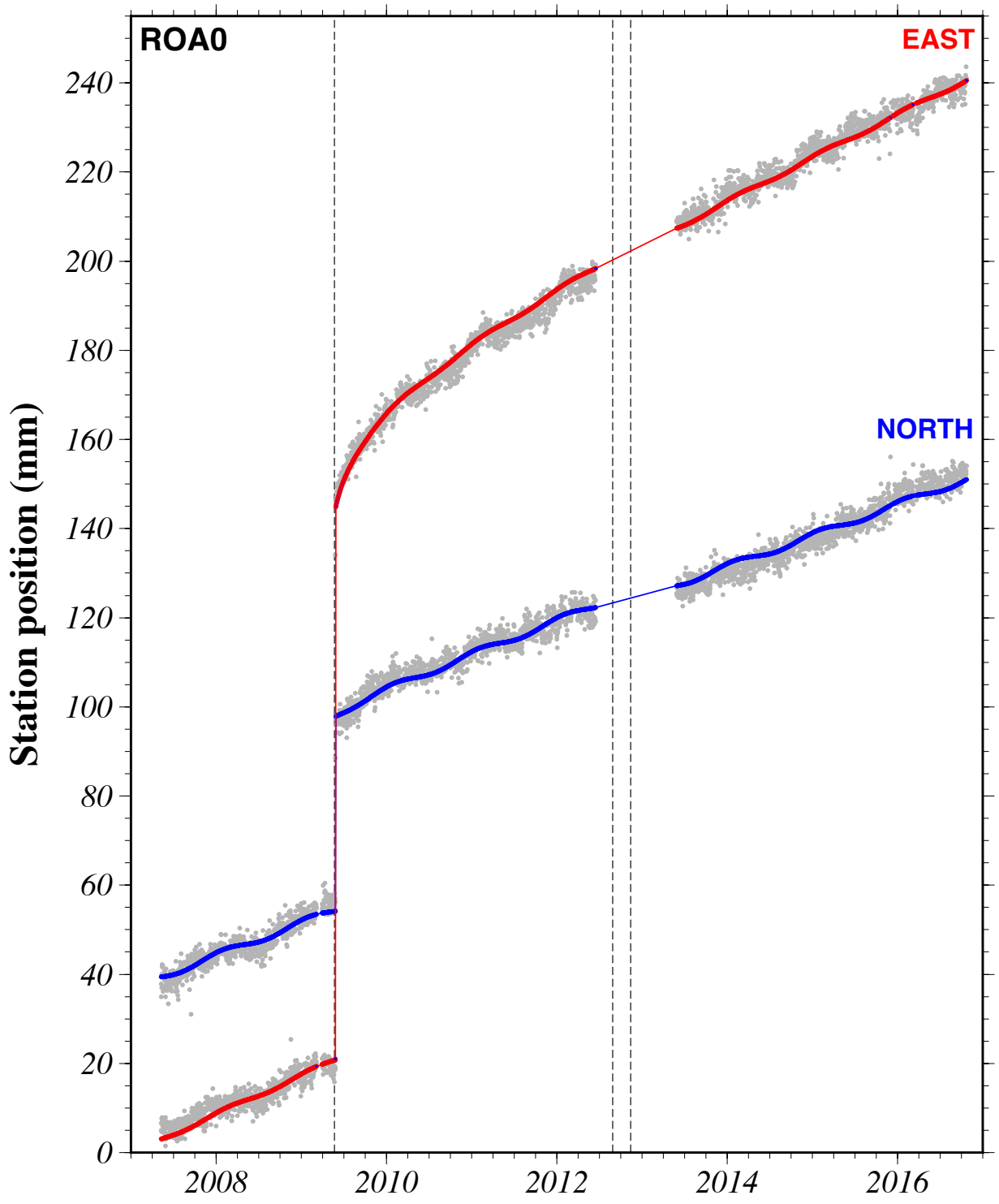

Figure 2.6. Horizontal fits of TDEFNODE time-dependent model at site ROA0. Gray circles show changes in the east and north components of the daily station positions with respect to ITRF08. Red (east) and blue (north) lines show the TDEFNODE model estimates. Dashed lines denote times of the 2009 Swan Islands and 2012 El Salvador and Champerico earthquakes.

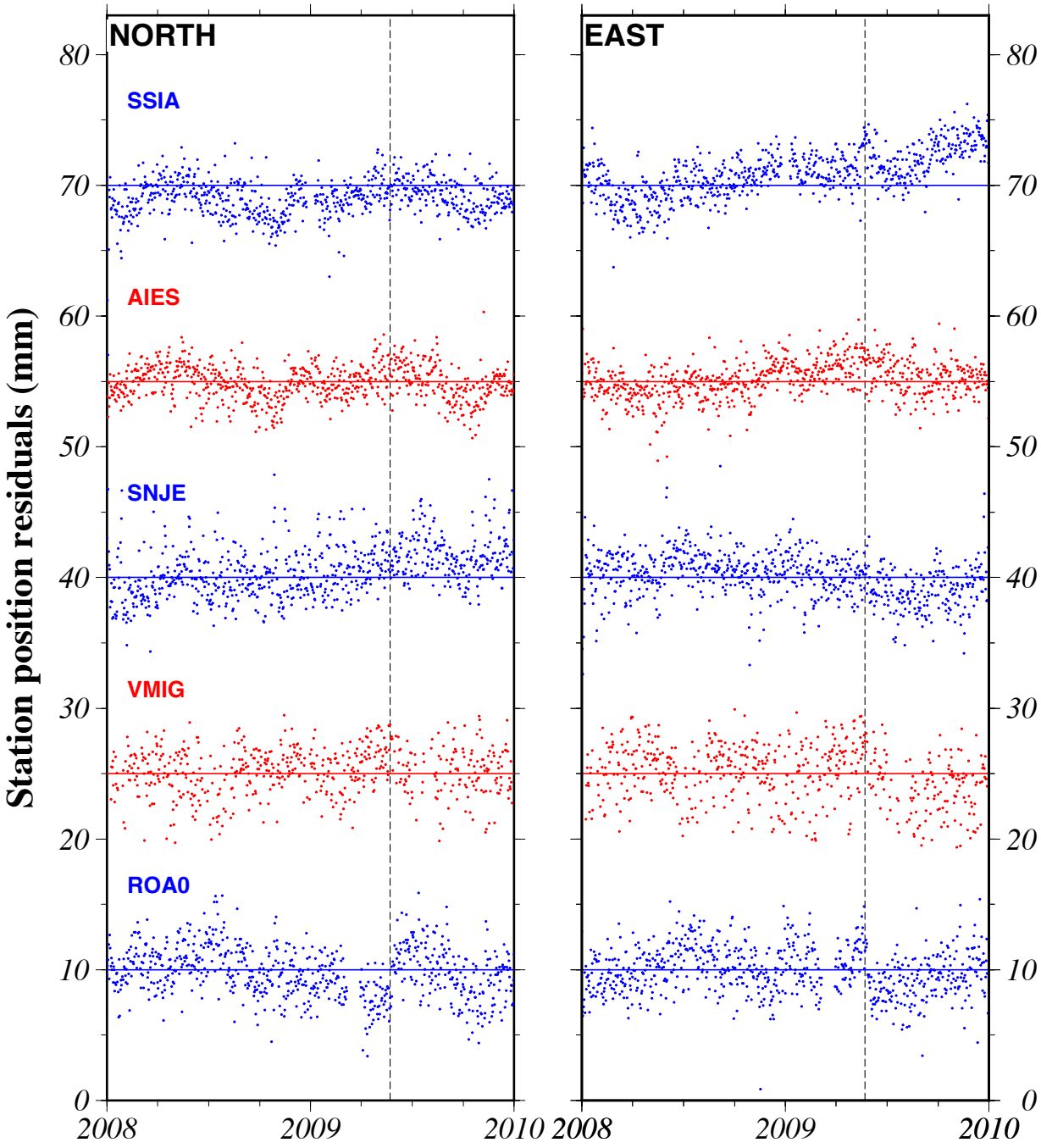

Figure 2.7. Residual daily GPS site positions (red and blue circles) for all five continuous GPS position time-series that were measurably offset by the 2009 Swan Islands earthquake. Daily site positions are shown relative to positions estimated by the TDEFNODE model. Dashed line denotes time of the 2009 Swan Islands earthquake. Locations for sites AIES, SNJE, SSIA, and VMIG are shown in Fig. 2.10d.

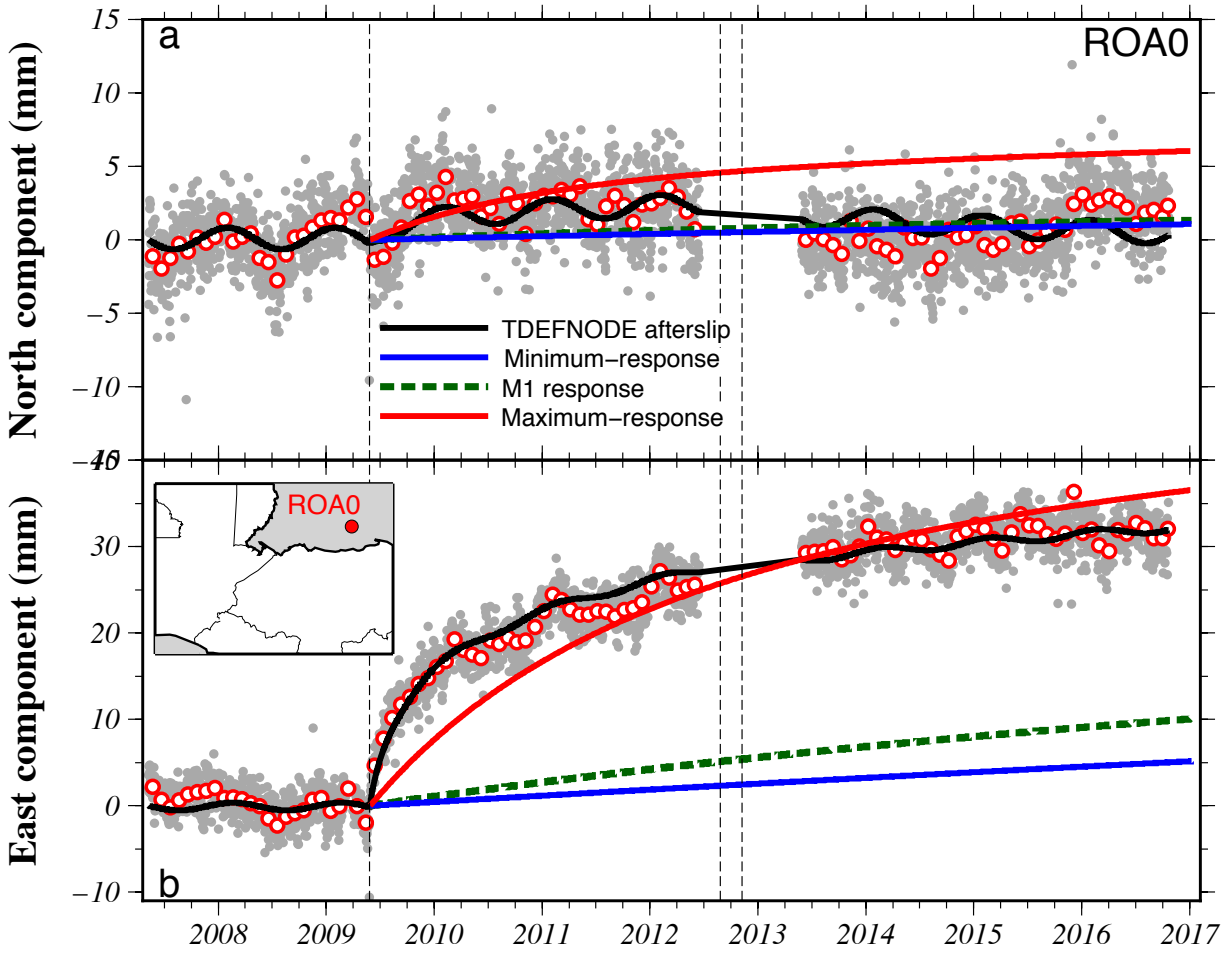

Figure 2.8. North (a) and east (b) daily positions (gray circles) for GPS site ROA0 reduced by the site's long-term velocity and corrected for coseismic offsets (see text) to emphasize the transient site motion due to earthquake afterslip and viscoelastic rebound. White circles with red outlines are 30-day averages of observed daily positions. Black curve shows TDEFNODE afterslip model. Colored curves show viscoelastic deformation solely attributable to the 2009 Swan Islands earthquake for all three rheological models described in Section 2.3.2 and shown in Fig. 2.4. Dashed lines denote earthquake times.

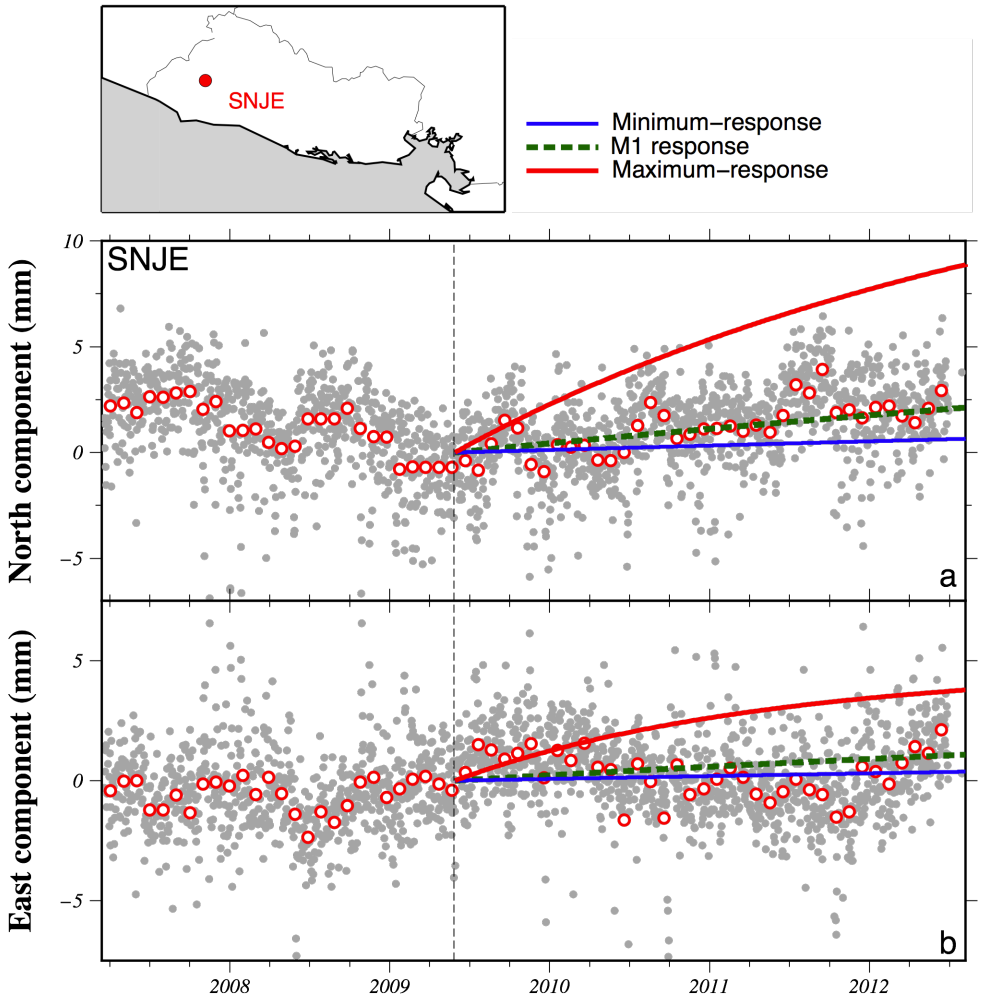

Figure 2.9. North (a) and east (b) daily positions (gray circles) for GPS site SNJE reduced by the site's long-term velocity and corrected for coseismic offsets (see text) to emphasize the transient site motion due to earthquake afterslip and viscoelastic rebound. White circles with red outlines are 30-day averages of observed daily positions. Colored curves show viscoelastic deformation solely attributable to the 2009 Swan Islands earthquake for all three rheological models described in Section 2.3.2 and shown in Fig. 2.4. Dashed lines denote earthquake times.

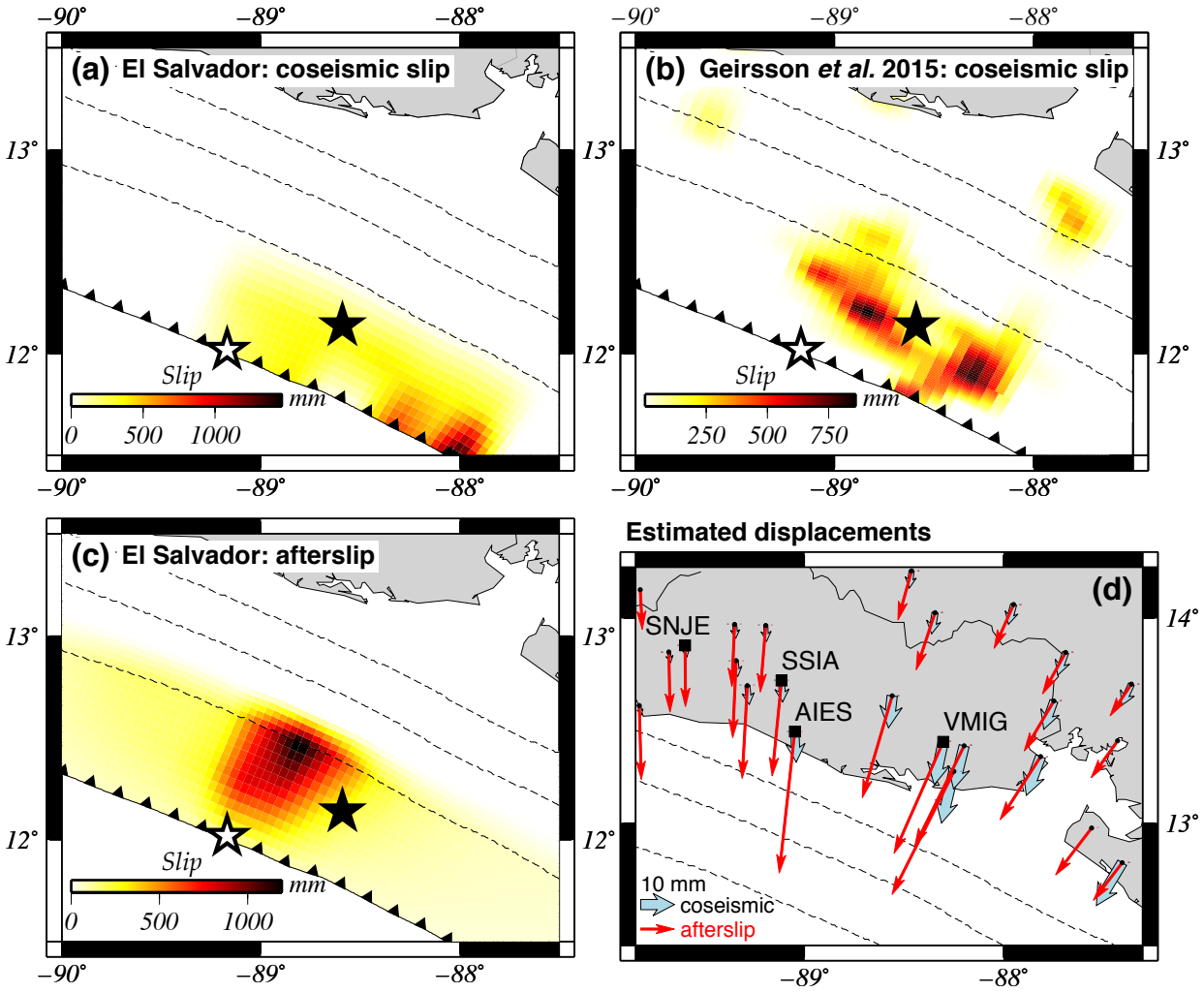

Figure 2.10. (a) New TDEFNODE coseismic slip solution for the 2012 El Salvador earthquake. (b) Coseismic slip estimate from Figure 6a of Geirsson *et al.* (2015). (c) TDEFNODE postseismic afterslip estimate for 2012.656 to 2017.0. (d) Site motions predicted by the coseismic and afterslip solutions shown in (a) and (c). White and black stars show the earthquake centroids from the Global CMT catalogue (Dziewonski *et al.* 1981; Ekström *et al.* 2012) and the United States Geological Survey, respectively. Named GPS sites are continuous stations. Dashed lines denote subduction slab contours spaced every 20-km in depth.

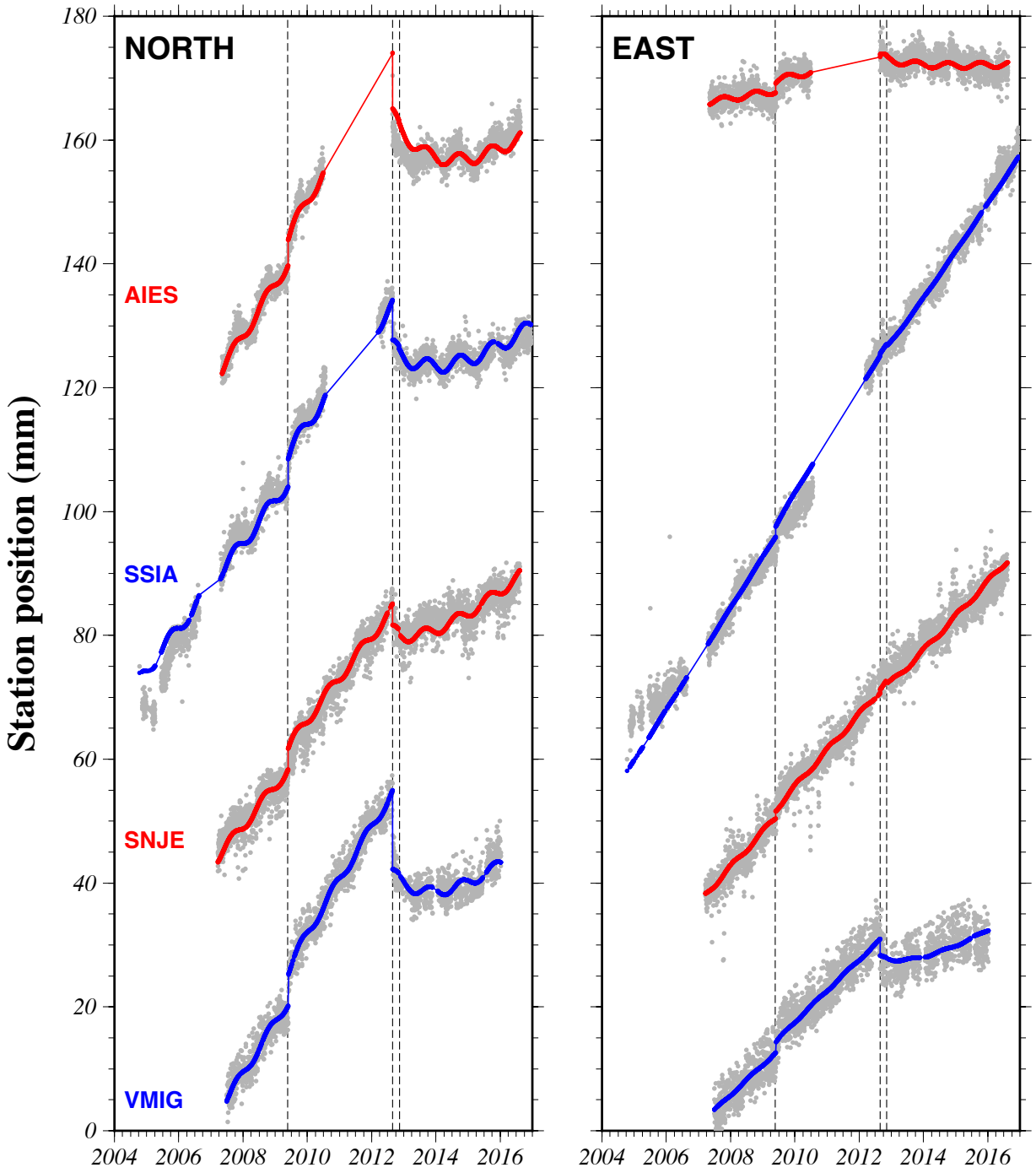

Figure 2.11. TDEFNODE fits (red and blue lines) to north and east station positions for continuous sites in El Salvador near the 2012 El Salvador earthquake. Gray circles show daily station positions with respect to ITRF08. Dashed lines denote times of the 2009 Swan Islands and 2012 El Salvador and Champerico earthquakes. Locations for sites AIES, SNJE, SSIA, and VMIG are shown in Fig. 2.10d.

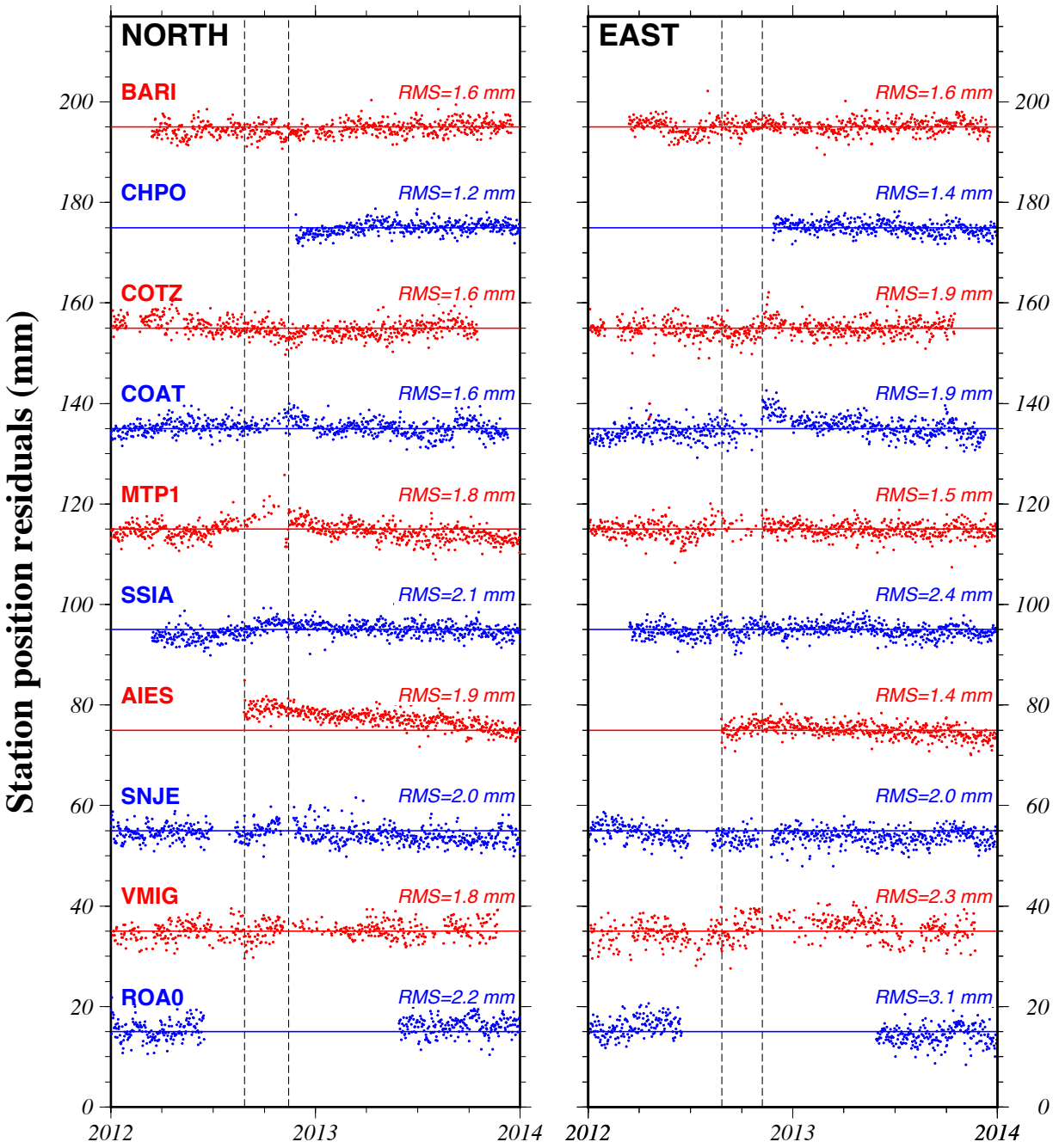

Figure 2.12. Residual daily positions (red and blue circles) relative to positions estimated by the TDEFNODE model. Dashed lines denote time of the 2012 El Salvador and Champerico earthquakes. Locations for sites BARI, CHPO, COTZ, COAT, and MTP1 are variously shown in Fig. 2.15a and 2.15d. RMS values for the TDEFNODE misfits include station positions for all time spanned by the data for each station, as specified in Table 2.1.

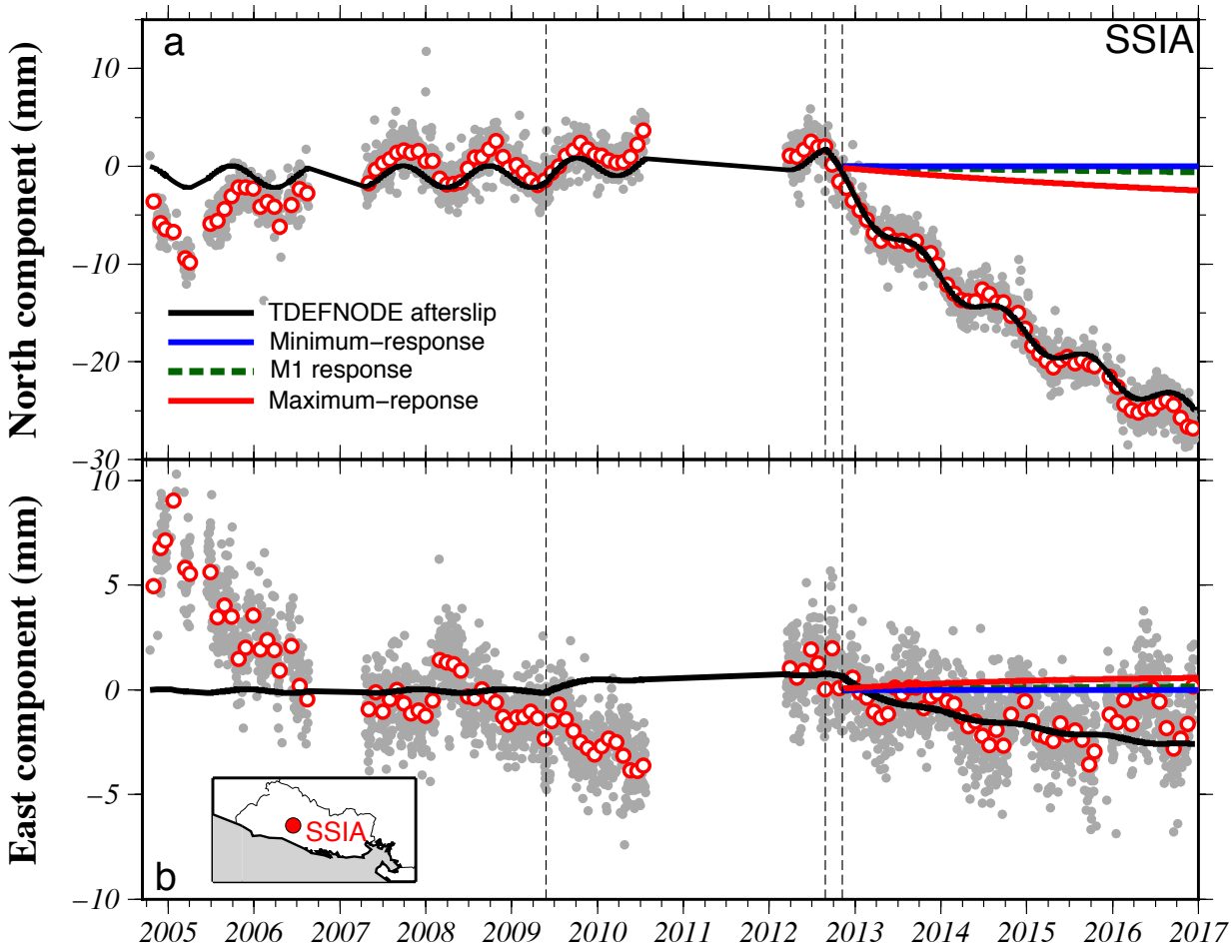

Figure 2.13. North (a) and east (b) daily positions (gray circles) for GPS site SSIA reduced by the site's long-term velocity and corrected for any coseismic. White circles with red outlines are 30-day averages of observed daily positions. Black curve shows TDEFNODE model estimate; colored curves show viscoelastic deformation solely attributable to the 2012 El Salvador earthquake for all three rheological models shown in Fig. 2.4. Dashed lines denote earthquake times.

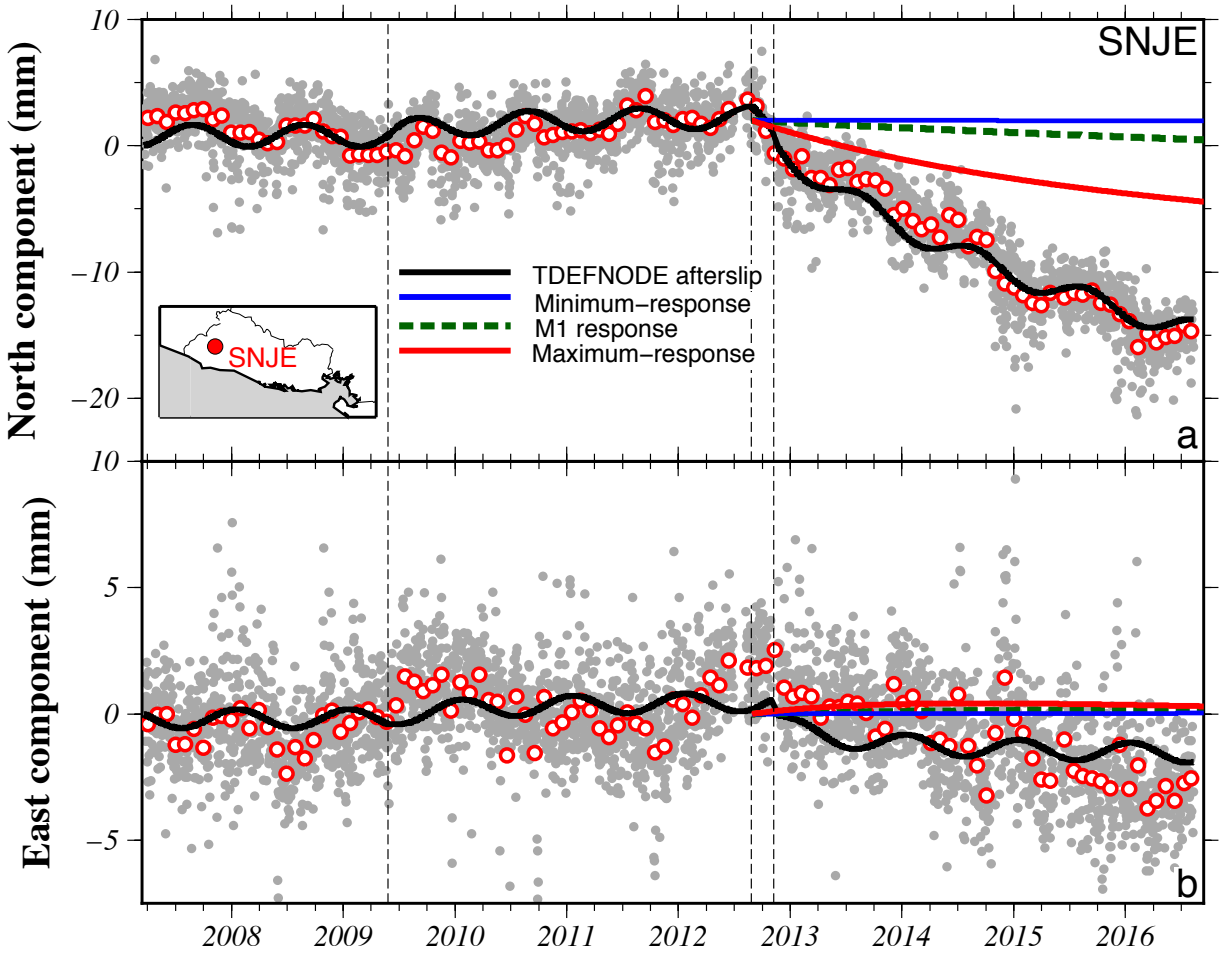

Figure 2.14. North (a) and east (b) daily positions (gray circles) for GPS site SNJE reduced by the site's long-term velocity and corrected for any coseismic offsets. See previous figure caption for further information.

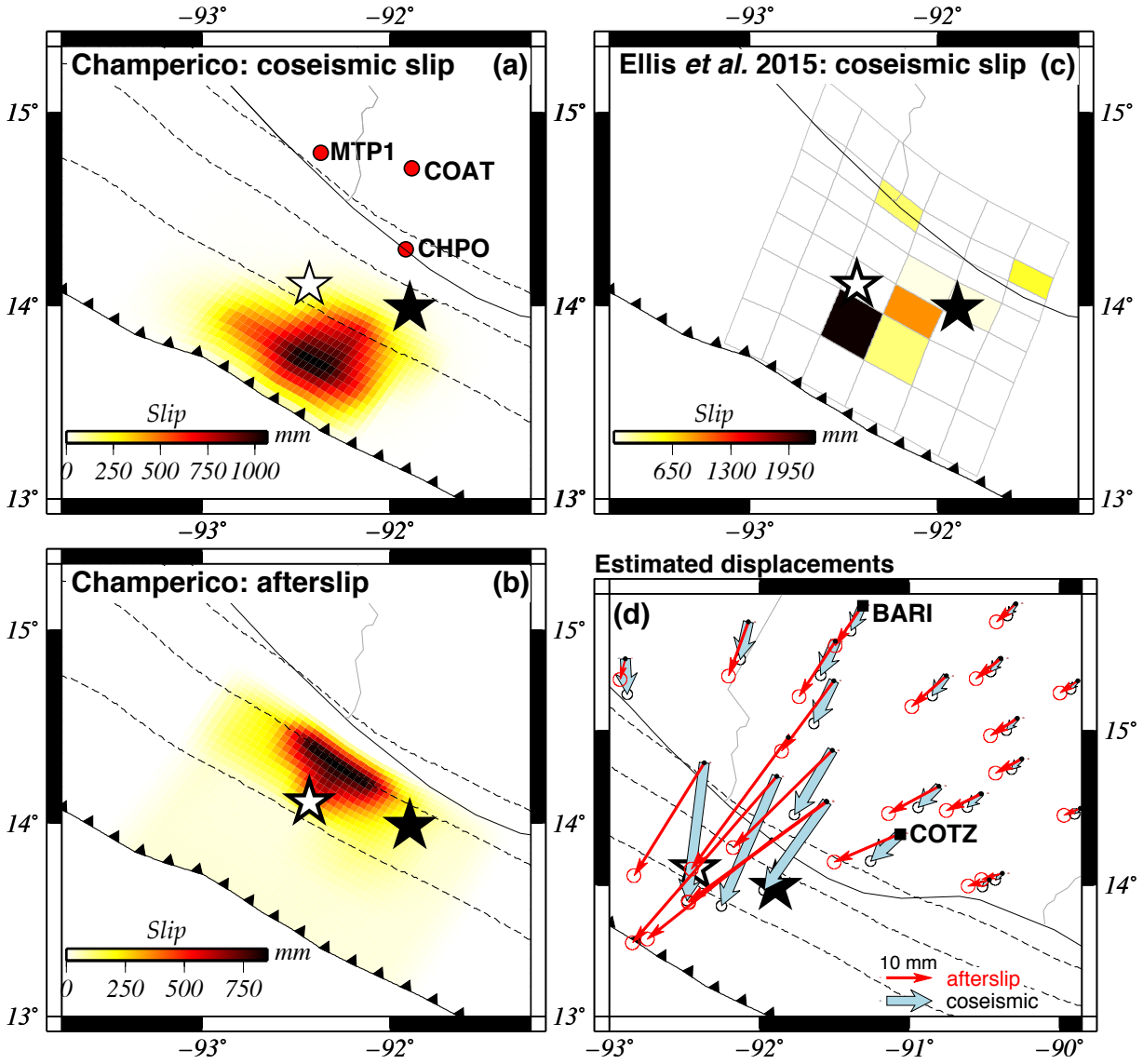

Figure 2.15. (a) TDEFNODE coseismic slip estimate for the 2012 Champerico earthquake. (b) Coseismic slip solution from Ellis *et al.* (2015). (c) TDEFNODE postseismic afterslip estimate for years 2012.852 to 2017.0. (d) Site motions predicted by the coseismic and afterslip solutions in (a) and (c). White and black stars show the earthquake centroid from the Global CMT catalogue (Dziewonski *et al.* 1981; Ekström *et al.* 2012) and the United States Geological Survey, respectively. Named GPS sites are continuous stations. Dashed lines denote subduction slab contours spaced every 20-km in depth.

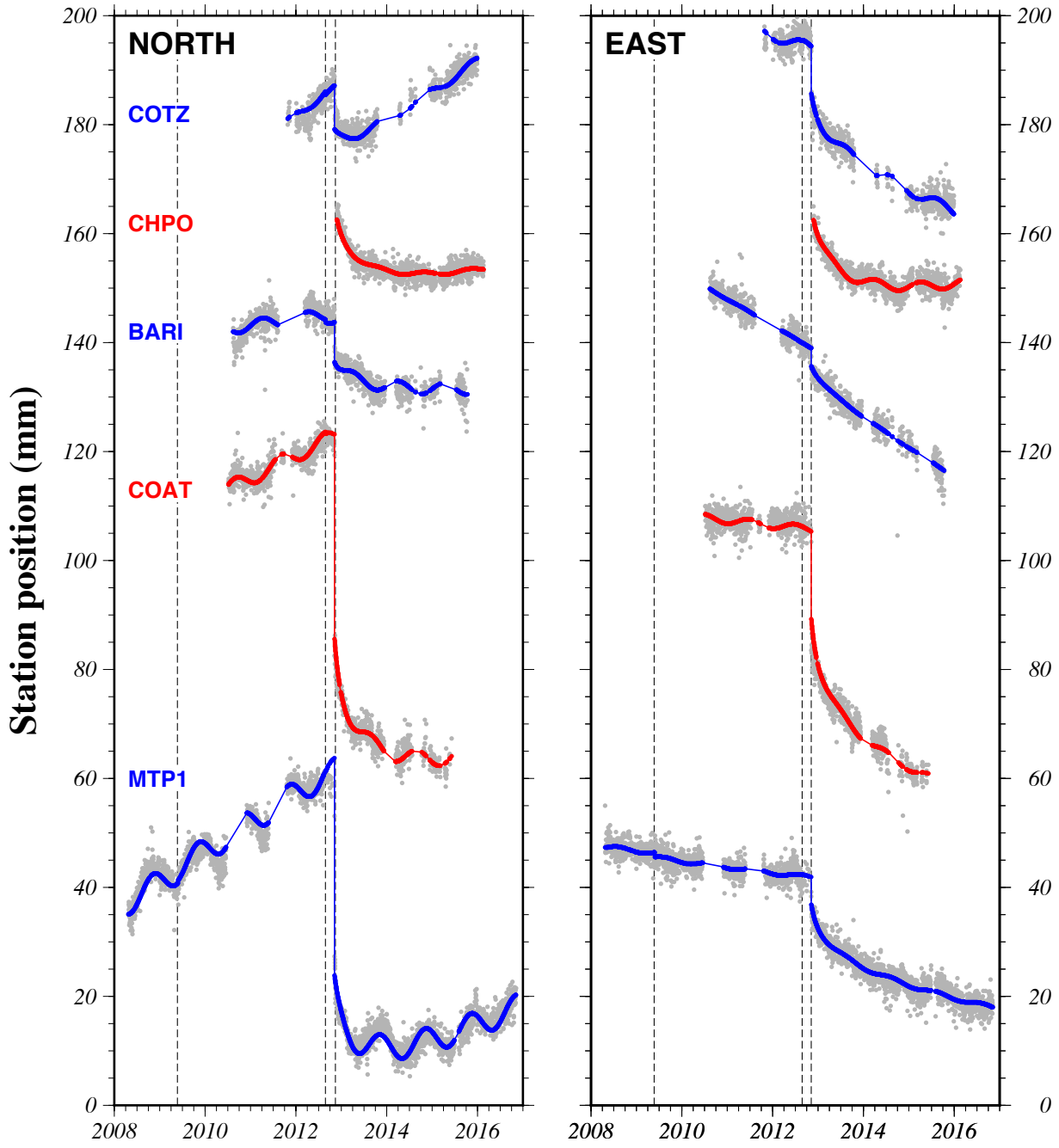

Figure 2.16. TDEFNODE fits (red and blue lines) for continuous sites near the 2012 Champerico earthquake. Gray circles show daily station positions with respect to ITRF08. Dashed lines denote times of the 2009 Swan Islands and 2012 El Salvador and Champerico earthquakes.

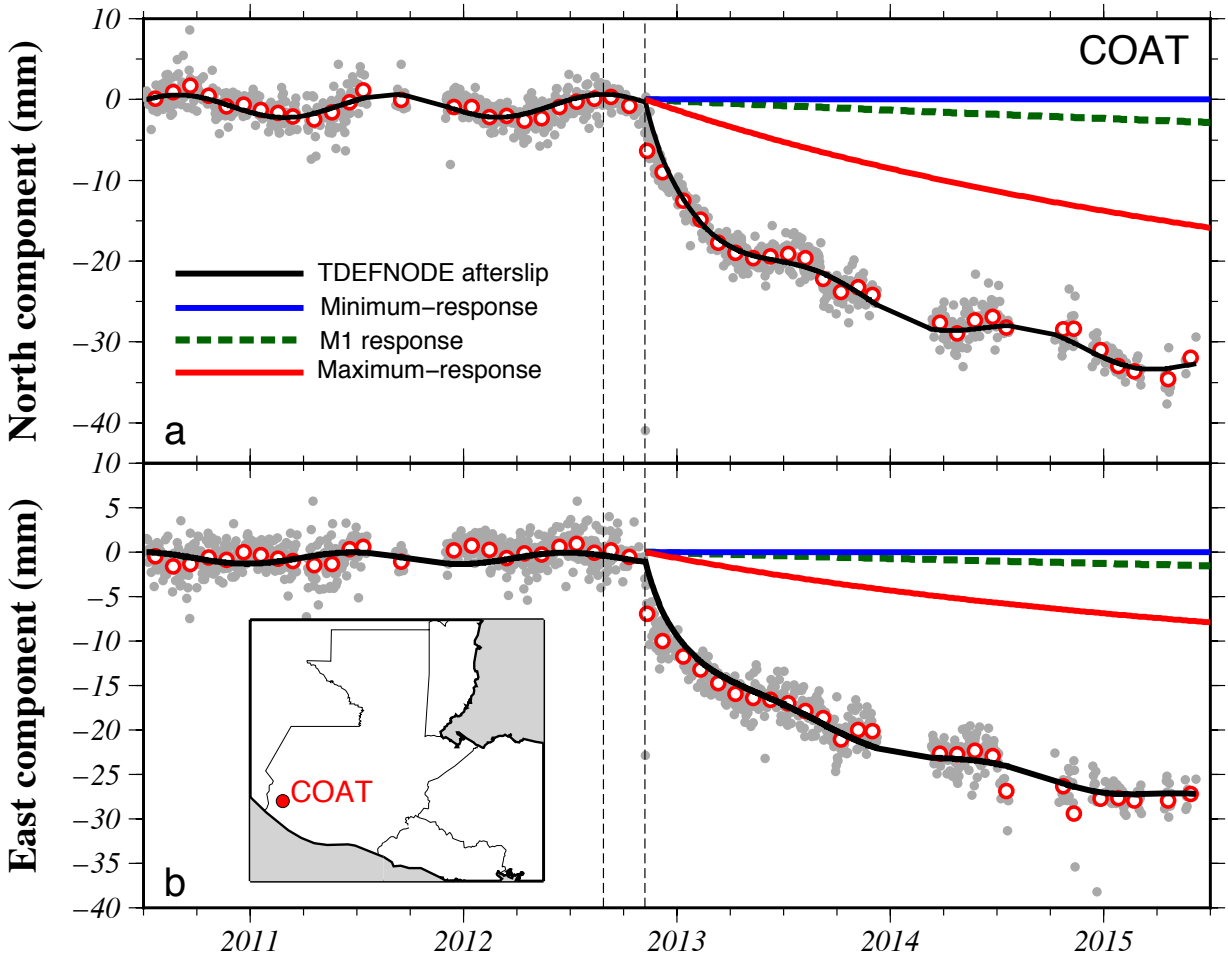

Figure 2.17. North (a) and east (b) daily positions (gray circles) for GPS site COAT reduced by the site's long-term velocity and corrected for any coseismic offsets. See caption to Fig. 2.13 for further information.

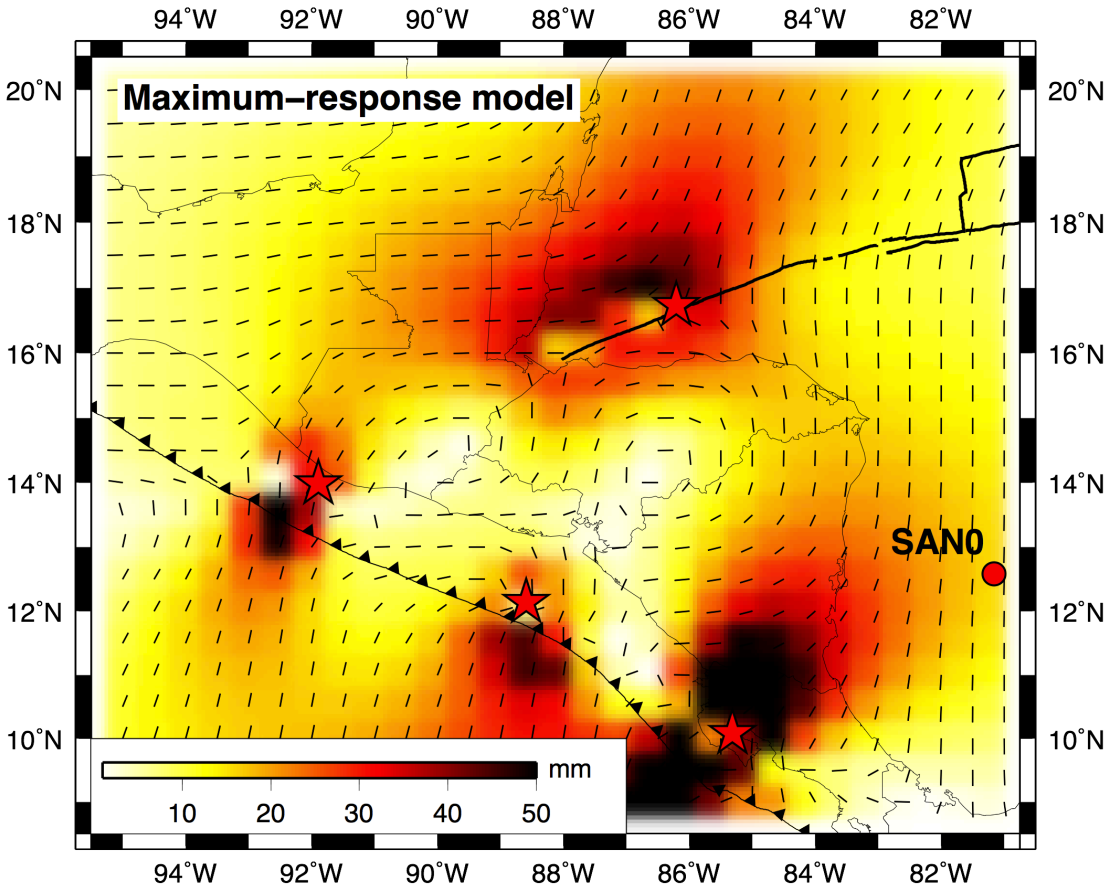

Figure 2.18. Summed viscoelastic deformation for 28 May 2009 to 2017.0 for the 28 May 2009 M_w=7.3 Swan Islands strike-slip earthquake (Fig. 2.5a), the 27 August 2012 M_w=7.3 El Salvador (Fig. 2.10a), the 05 September 2012 M_w=7.6 Nicoya (Costa Rica) (Supplementary Fig. S2.2), and 11 November 2012 M_w=7.4 Champerico (Guatemala) subduction-thrust earthquakes (Fig. 2.15a). Viscoelastic calculations were done with VISCO-1D and for the maximum-response rheological model shown in Fig. 2.4. The coseismic slip solutions used to drive the viscoelastic model are from Figs. 2.5a, 2.10a, and 2.15a, and Protti *et al.* (2013). The tick marks and colors show direction and magnitude of viscoelastic displacements.

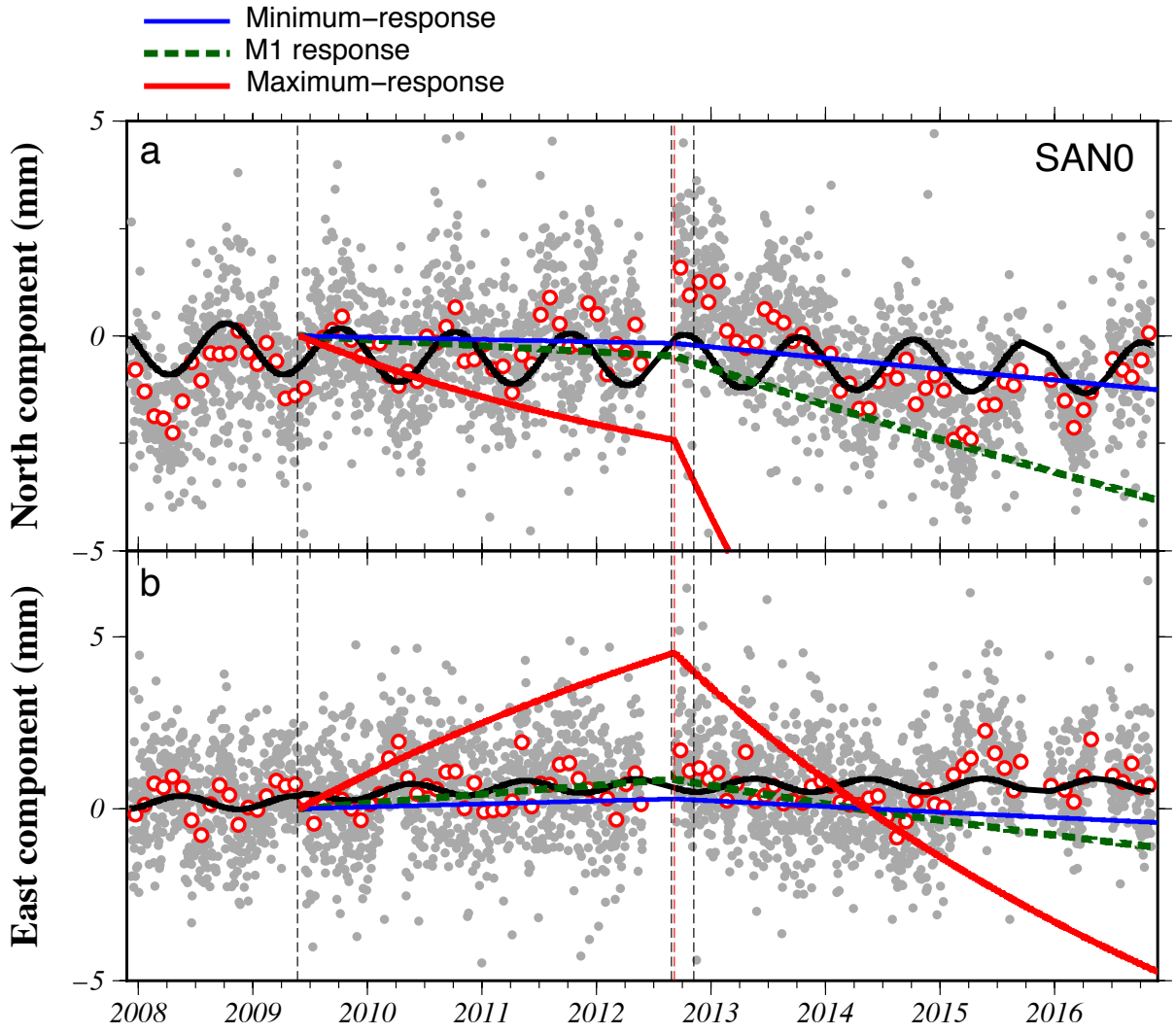

Figure 2.19. Time-dependent viscoelastic deformation at GPS site SAN0 (located in the previous figure) for the four earthquakes listed in the previous figure and all three rheological models shown in Fig. 2.4. The daily north (a) and east (b) station positions, shown by the gray circles, are reduced by the site's long−term velocity and corrected for coseismic offsets (see text). See Fig. 2.13 caption for further description. Black line shows the fit of our best TDEFNODE model, which attributes all postseismic deformation to afterslip.

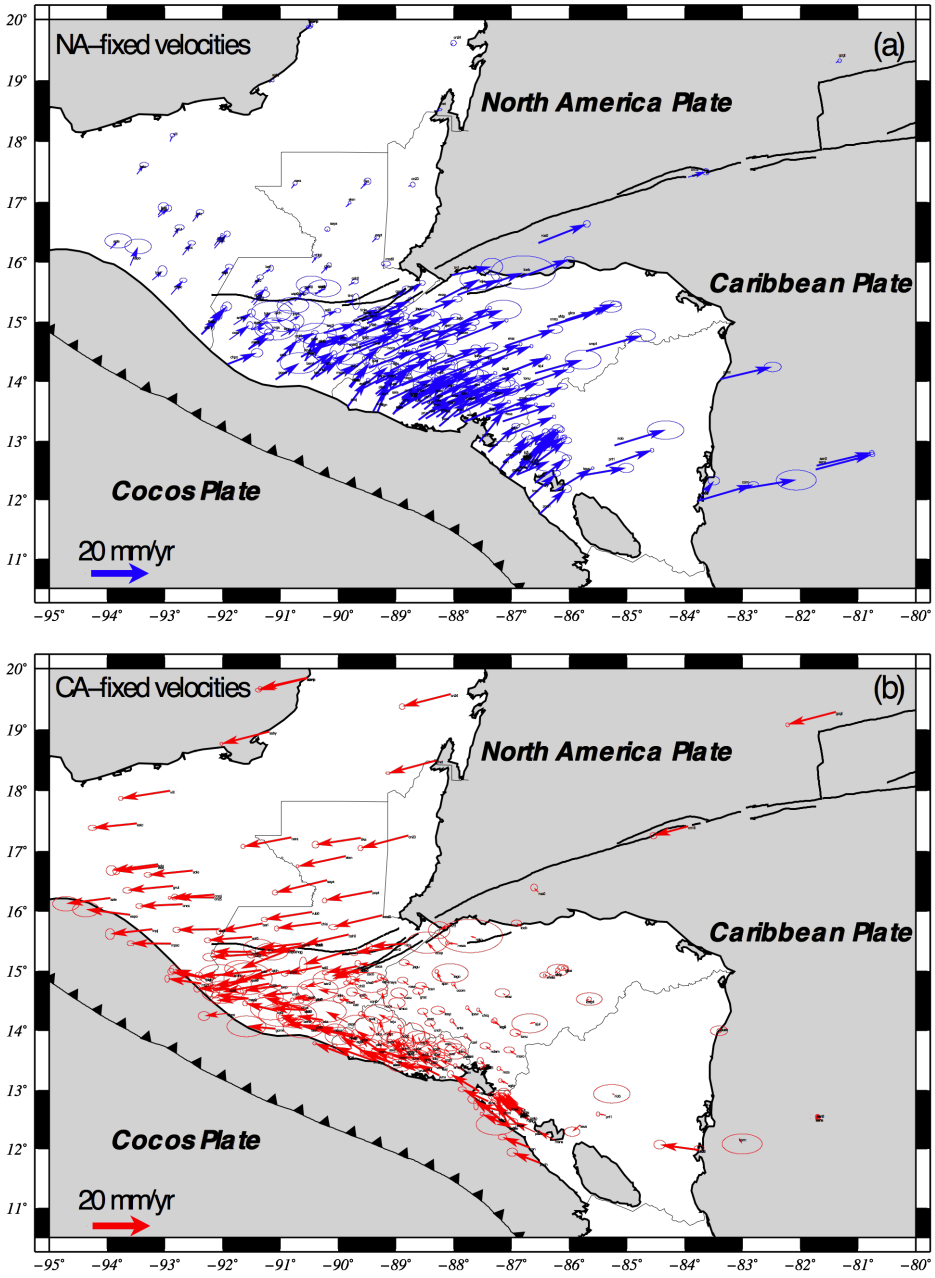

Figure 2.20. New GPS station velocities relative to the North America plate (a) and Caribbean plate (b). All velocities are corrected for estimated coseismic offsets and afterslip transients from the Swan Islands, El Salvador, and Champerico earthquakes.

S2.7 Supplementary information

This supplementary document contains a table showing episodic GPS site information, a figure showing the full time-series for site VMIG prior to filtering, and our TDEFNODE control file for our time-dependent modeling.

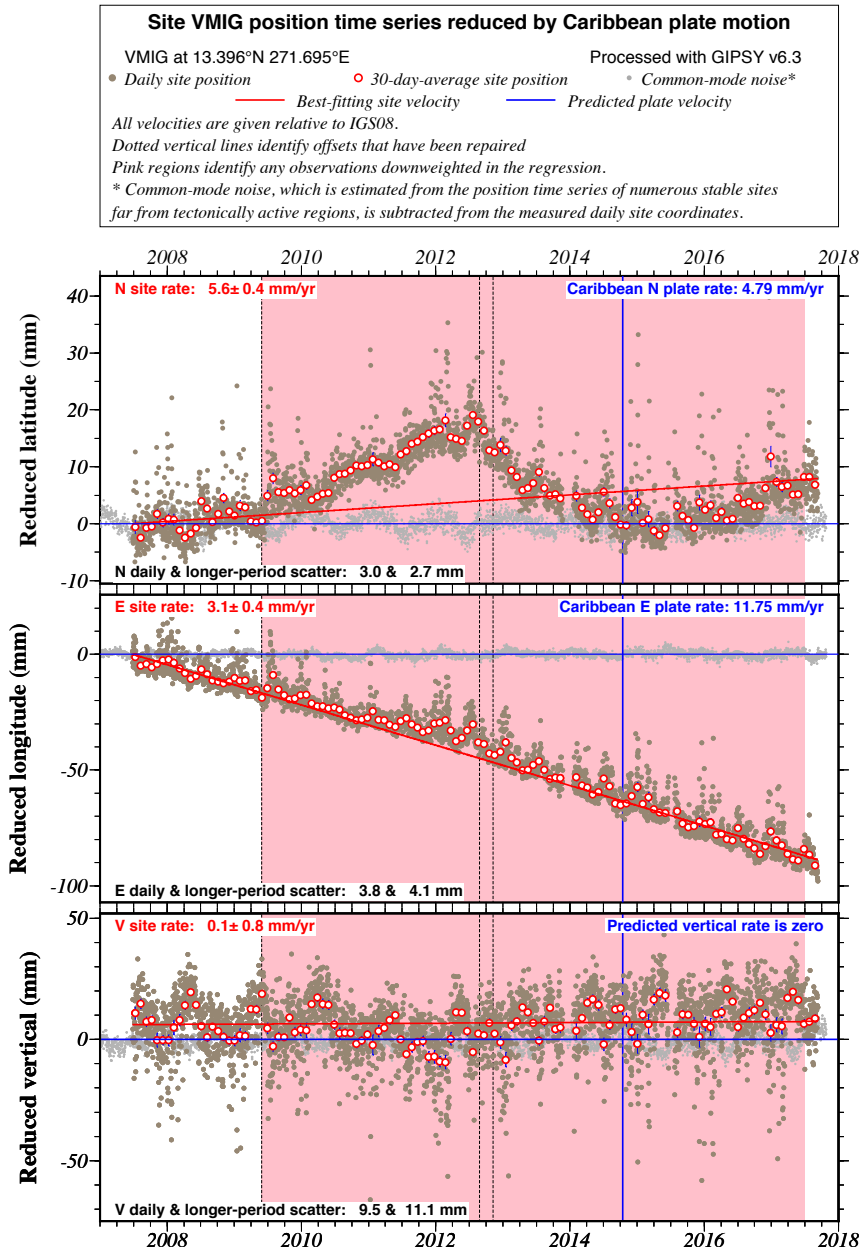

Figure S2.1: Original position time-series for site VMIG, which includes unusually high multipath noise. Site motion is relative to the Caribbean plate. Gray dots are daily positions, and red circles with white fill are 30-day averages. Red line denotes best-fitting interseismic slope. Coseismic offsets from the 2009 Swan Islands, 2012 Gulf of Fonseca, and 2012 Champerico earthquakes have been removed for clarity.

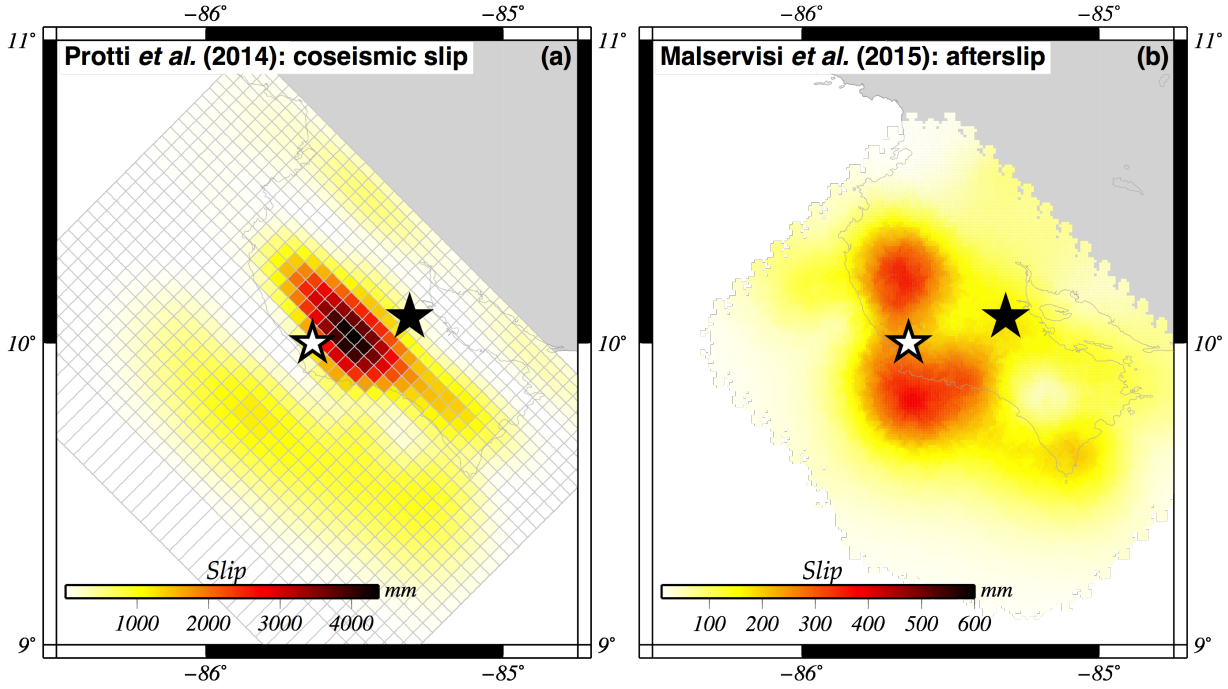

Figure S2.2. (a) Protti *et al.*'s (2013) coseismic slip solution. (b) Malservisi *et al.*'s (2015) afterslip solution for 2012.68 to 2012.87 (70 days relaxation).

```
#TDEFNODE control file for modeling the 2009 Swan Islands and 2012 El Salvador and
#Champerico earthquakes. Includes time-dependent GPS time-series modeling of coseismic and
#postseismic transient event for these three earthquakes.

fl: +pos +pio -pen -cov +vrb +atr
fl: robm +all


ts: ALLc "All_continuous_sites.gts" 2 1.0 0.1 1.0 50.0 1990 2017.25 3 3 3 2 2 2 0 0 15
ts: CAYS "CAYS_timeseries_perm.gts" 2 1.0 0.1 1.0 50.0 1990 2017.25 3 3 3 2 2 2 0 0 15
ts: ALLe "All_campaign_sites.gts" 2 1.0 0.1 1.0 50.0 1990 2017.25 2 2 2 2 2 2 0 0 15

rm: ALLe esti

# SETTINGS FOR INVERSION

sa: 0 3 800
gs: 40 1.0 4 2 5
in: 5 5

# Model space settings:
# do not adjust poles, strains or reference frame
pi: 0
si: 0
gi: 0

--- 2009 EQ ------

### MODEL FOR EQ

mo: al76
pf: "al76/pio" 3

ei: 1 2 3 4 5 6 7 8 9 10 11 12 13 14 15 16

## SWAN ISLAND EQ ##
# cosesimic

es: 1 sp 9 ts 0 ln 271.5995 lt 15.6174 zh 7.5 xw 45.59 ww 15 to 2009.405479 st 238.1 dp 89.9 rk 0
ef: 1 am
ex: 1 am 231.21 282.59
#ex: 1 am 1 5000

es: 2 sp 9 ts 0 ln 271.9338 lt 15.8358 zh 7.5 xw 40.98 ww 15 to 2009.40547 st 233.4 dp 89.9 rk 0
ef: 2 am
ex: 2 824.67 1007.93
```

#ex: 2 am 1 5000

es: 3 sp 9 ts 0 ln 272.379 lt 16.077 zh 7.5 xw 68.91 ww 15 to 2009.40547 st 248.0 dp 89.9 rk 0
ef: 3 am
ex: 3 am 385.92 471.68
#ex: 3 am 1 5000

es: 4 sp 9 ts 0 ln 272.9979 lt 16.3379 zh 7.5 xw 75.65 ww 15 to 2009.40547 st 247.6 dp 89.9 rk 0
ef: 4 am
ex: 4 am 631.53 771.87
#ex: 4 am 1 5000

es: 5 sp 9 ts 0 ln 273.6393 lt 16.5744 zh 7.5 xw 71.09 ww 15 to 2009.405479 st 250.6 dp 89.9 rk 0
ef: 5 am
ex: 5 am 622.53 760.87
#ex: 5 am 1 5000

es: 6 sp 9 ts 0 ln 274.2219 lt 16.7719 zh 7.5 xw 60.67 ww 15 to 2009.405479 st 250.6 dp 89.9 rk 0
ef: 6 am
ex: 6 am 381.06 465.74
#ex: 6 am 1 5000

postseismic
es: 7 sp 9 ts 7 sa 1 to 2009.4 am 1000 tc 32 ln 271.5995 lt 15.6174 zh 7.5 xw 45.59 ww 15 st 238.1 dp 89.9 rk 0
ef: 7 am
ex: 7 am 10 5000

es: 8 sp 9 ts 7 sa 1 to 2009.4 am 1000 tc 32 ln 271.9338 lt 15.8358 zh 7.5 xw 40.98 ww 15 st 233.4 dp 89.9 rk 0
ef: 8 am
ex: 8 am 10 5000

es: 9 sp 9 ts 7 sa 1 to 2009.4 am 1000 tc 32 ln 272.379 lt 16.077 zh 7.5 xw 68.91 ww 15 st 248.0 dp 89.9 rk 0
ef: 9 am
ex: 9 am 10 5000

es: 10 sp 9 ts 7 sa 1 to 2009.4 am 1000 tc 32 ln 272.9979 lt 16.3379 zh 7.5 xw 75.65 ww 15 st 247.6 dp 89.9 rk 0
ef: 10 am
ex: 10 am 10 5000

es: 11 sp 9 ts 7 sa 1 to 2009.4 am 1000 tc 32 ln 273.6393 lt 16.5744 zh 7.5 xw 71.09 ww 15 st 250.6 dp 89.9 rk 0
ef: 11 am

ex: 11 am 10 5000

es: 12 sp 9 ts 7 sa 1 to 2009.4 am 1000 tc 32 ln 274.2219 lt 16.7719 zh 7.5 xw 60.67 ww 15 st 250.6 dp 89.9 rk 0
ef: 12 am
ex: 12 am 10 5000

Gulf of Fonseca (Salvador) 2012 COSEISMIC
es: 13 fa 13 sp 1 am 1800 ts 0 sa 1 to 2012.6530 ln 271.41 lt 12.139 rk 30 mo 1.3e20
ef: 13 am rk
ex: 13 am 1200 10000
exd: 13 az 10 rk 20
nnt: 13 54 6 5 12 1 1 2 1 1.0
smt: 13 2 0.5 0.5 0.5 1.26e20 1.28e20

Salvador Afterslip
es: 14 fa 13 sp 1 ts 7 sa 1 am 3000.0 to 2012.6558 rk 30
ef: 14 am rk tc
ex: 14 am 10 3000 tc 300 1000
exd: 14 rk 20
nnt: 14 54 6 1 20 1 1 3 1 1.0
smt: 14 2 0.005 0.005 0.005 1e1 1e21

Champerico (Guatemala) 2012 COSEISMIC
Gaussian slip
es: 15 fa 13 sp 1 ts 0 sa 1 to 2012.8511 ln 267.532 lt 13.8948 d2 20 rk 30
ef: 15 am rk az
ex: 15 am 1000 2200
exd: 15 d1 10 d2 20 rk 20 az 20
nnt: 15 54 6 28 36 1 2 4 1 1.0
smt: 15 2 0.01 0.01 0.01 1.44e20 1.46e20

####### Guatemala POSTSEISMIC #####
log
es: 16 fa 13 sp 1 tc 20 ts 7 sa 1 am 1000.0 to 2012.852 rk 30
ef: 16 am rk tc
ex: 16 am 10 3000 tc 1 30
exd: 16 rk 20
nnt: 16 54 6 28 36 1 1 5 1 1.0
smt: 16 2 0.005 0.005 0.005 1e1 1e28

ic: 2 1 2 1 2 1 1 1 1 1 1 1 1 1

end model section
em:

```
#############################################################
# FLAG: mkb = make blocks from fault segments (NO)
fl: +mkb

## SETTINGS FOR GREENS FUNCTIONS
gd: A01 40.0 15.0 0 1.0 0.5 1000.0

bc: NOAM 271.147 20.986 1 0
bc: CARI 286.012 13.661 3 0
bc: FONE 271.087 13.311 4 0
bc: FOSW 270.125 12.460 4 0
bc: COCO 265.0 10.0 6 0

bp: NOAM 1 0
bp: ITRF 2 0
bp: CARI 3 0
bp: FONE 4 0
bp: FOSW 4 0
bp: COCO 6 0

# pseudo faults (blocks)
FAult: NOAM 1 NOAM.fault
FAult: CARI 3 CARI.fault
FAult: FONE 4 FORENE.fault
FAult: FODW 5 FORESW.fault
FAult: COCO 6 COCO.fault

# Locked faults
FAult: MOPO 11 MOPO.fault
FAult: VOLC 12 VOLC.fault
FAult: MAT0 13 MAT.fault

end:
```

CHAPTER 3

Deformation in northern Central America from 1999 to 2017 using GPS observations, Part 2: Block rotations, fault slip rates, fault locking, and distributed deformation

SUMMARY

We use an eight-block elastic model and new 209-station GPS velocity field at the deforming western end of the Caribbean plate to derive plate/block rotations, slip rates, and locking estimates for northern Central America, where the Motagua-Polochic fault zone, Middle America trench, and Central America volcanic arc faults pose significant seismic hazard. An inversion of the GPS site velocities, which are corrected for the transient effects of large regional earthquakes, gives a number of important results, including the following: 1) First evidence for a nearly rigid Chortis block that rotates slowly anti-clockwise from the Caribbean plate south of the Motagua fault; 2) Evidence for a southward transfer of 8-9 mm yr^{-1} of slip on the westernmost Motagua fault into the Guatemala City graben and nearby normal faults, thereby terminating the Motagua fault; 3) A well-constrained estimate of partitioning of plate boundary slip by the Motagua and Polochic faults, whereby roughly two-thirds of the ~18 mm yr^{-1} of slip across the two faults occurs on the Motagua fault; 4) New information about slip rate variations along the Central America volcanic arc, including the first slip rate estimate for the poorly-understood Jalpatagua fault in southern Guatemala; 5) Geodetic evidence for significant distributed deformation in the Chiapas Tectonic Province; 6) Evidence for stronger locking offshore southern Mexico and even weaker shallow locking offshore Guatemala and El Salvador than previously estimated; 7) A refined estimate of the rates and distribution of extension across the grabens of western Honduras and southern Guatemala; 8) A first estimate of the angular velocity for Cocos plate subduction below the Central America sliver and evidence that subduction is ~10° clockwise from previous kinematic estimates

for this trench segment; and 9) Evidence for no significant along-strike deformation of the ~700-km-long Central America forearc sliver, but ~10 mm yr^{-1} of E-W extension across the Gulf of Fonseca step-over in the Central America volcanic arc. Our results suggest that assumptions made by previous authors about the factors controlling the regional deformation are correct to first-order, including the importance of the curvature of the Motagua fault, low locking across the Middle America subduction zone, and the obliquity of North America-Caribbean plate motion with respect to the Motagua-Polochic fault zone.

3.1 INTRODUCTION

Geodetic studies of the tectonics of northern Central America began in the late 1990s, with broad goals of better understanding the earthquake cycles of the Middle America subduction zone. Here the Cocos plate subducts northeastward below the continent, and the Motagua and Polochic faults (Fig. 3.1), which pose major seismic hazards to Guatemala as they carry Caribbean-North America plate motion westward toward the Middle America trench (Fig. 3.1). Plafker (1976) first described the principal elements of a tectonic framework for northern Central America (Fig. 3.2), consisting of sinistral slip along the Motagua-Polochic fault zone, east-west extension in areas of Guatemala and Honduras south of the Motagua Fault, and and a rheologically weak Central America volcanic arc. Later modifications of Plafker's tectonic framework include trench-parallel, northwest translation of a Central America forearc sliver along faults in the Central America volcanic arc (Fig. 3.2) (Harlow & White 1985; White & Harlow 1993; White *et al.* 2004), and distributed deformation on folds, thrust faults, and strike-slip faults north of the Polochic Fault (Guzman-Speziale *et al*. 1989; Guzman-Speziale 2010). Numerous seismic, structural, and geomorphologic studies in the region (e.g. Guzman-Speziale & Menese-Rocha 2000; Caceres *et al*. 2005; Corti *et*

al. 2005; Rogers & Mann 2007; Guzman-Speziale 2010; Authemayou *et al*. 2012; Canora *et al.* 2014; Garibaldi *et al*. 2016; Guzman-Speziale & Zuniga 2016) support the tectonic framework shown in Fig. 3.2 and reveal the characteristics of its major faults (Martinez-Diaz *et al.* 2004; Authemayou *et al*. 2011; Ye *et al*. 2013; Brocard *et al*. 2016).

During the past 15 years, efforts to test this tectonic framework and better quantify the regional plate/block kinematics and deformation have proceeded on two related fronts. Alvarez-Gomez *et al.* (2008), LaFemina *et al*. (2009), and Rodriguez *et al*. (2009) each explore the effects of different assumptions about the regional deformation via a series of forward calculations with thin-shell, finite-element meshes driven by Cocos, Caribbean, and North America plate angular velocities. Alvarez-Gomez *et al.* (2008) find that models with low assumed locking across the Middle America subduction interface, a weak volcanic arc, and an accurate Caribbean-North America plate boundary predict strain-rate tensors that agree well with earthquake focal mechanisms in the region (Fig. 3.2). Rodriguez *et al.* (2009) additionally show that thin-shell finite-element models with the characteristics outlined above correctly predict observed GPS velocities throughout Honduras. Farther south in Central America, LaFemina *et al.* (2009) find that the velocities of GPS sites in Costa Rica and Nicaragua are well matched by a finite element model in which the collision of the Cocos Ridge with the Middle America Trench offshore Costa Rica drives lateral, trench-parallel tectonic escape of a Central America forearc sliver, including areas of El Salvador and Guatemala pertinent to this analysis.

In parallel with the above forward modeling studies, campaign and continuous GPS measurements in El Salvador, Guatemala, Honduras, and southern Mexico that began in 1999 and 2000 have corroborated major elements of the tectonic framework illustrated in Fig. 3.2. From measurements at 16 campaign GPS sites in Guatemala, Lyon-Caen *et al.* (2006) quantify

Caribbean-North America plate motion across the Motagua and Polochic Faults, confirm that the two faults accommodate nearly all of the plate motion, and describe unexpected evidence for a westward decrease in the slip rate along the Motagua Fault. Rodriguez *et al.* (2009) describe a progressive east-to-west increase in extension rates measured at 37 GPS sites that span the 400-km-wide extending zone in western Honduras, confirming previously reported evidence for extension based on data from a sparser, 11-station network (DeMets *et al*. 2007). From thin-shell elastic modeling of the velocities of 32 GPS sites on and near the borders of the Central America forearc sliver, Correa-Mora *et al*. (2009) find that locking across the Middle America subduction interface offshore El Salvador is weak, but that the seismically active strike-slip faults in the Salvadoran volcanic arc are strongly locked. Finally, elastic half-space modeling by Franco *et al*. (2012) of the velocities of 40 GPS sites in northern Central America and southern Mexico confirms the east-to-west decrease in slip rates across the Motagua-Polochic Fault Zone first reported by Lyon-Caen *et al.* (2006), predicts up to 15 mm yr^{-1} of dextral slip across the Guatemalan volcanic arc, and shows that locking on the Middle America subduction interface changes from moderate-to-strong locking offshore southern Mexico to weak locking off the coast of southern Guatemala.

Herein, we describe and model newly determined interseismic velocities for 209 GPS sites in northern Central America and southern Mexico to quantify the regional deformation with more precision and in more detail than was previously possible. Via elastic half-space modeling of the velocity field, we estimate angular velocities to describe the rotations of 8 plates or blocks located in our study area, interseismic locking along the faults that separate these blocks/plates, and strain-rate tensors in areas of distributed deformation. Specific topics treated herein include the following: (1) Tests for whether areas south of the Motagua Fault rotate as rigid or nearly-rigid

blocks relative to the Caribbean plate; (2) Improved estimates of the motion of the Central America forearc sliver relative to areas inland and relative to the Cocos plate; (3) An evaluation of whether slip rates along faults in the Central America volcanic arc decrease northwest along the arc, as expected if some slip along volcanic arc faults is transferred gradually northward into grabens north of the volcanic arc in western Honduras and southern Guatemala; (4) A first geodetic estimate of the slip rate for the poorly understood Jalpatagua Fault of southern Guatemala; (5) A revised upper limit for internal deformation of the narrow forearc sliver. (6) A more precise determination of how extension across the broad deforming region south of the Motagua fault is partitioned across normal faults in western Honduras, across the Ipala and Guatemala City grabens of southern Guatemala, and across normal faults west of the Guatemala City graben; and (7) Refined estimates of interseismic locking across the Middle America subduction interface and where the locking transitions from moderate/strong offshore Chiapas (Franco *et al*. 2012) to zero/weak offshore El Salvador (Correa-Mora *et al*. 2009).

Critically, our new velocity field has been corrected for the coseismic and transient postseismic effects of three large regional earthquakes in 2009 and 2012 (described in Section 3.3.1), which affected the motions of most GPS stations in northern Central America. We use identical processing methods for all of the raw GPS data in our analysis and the same geodetic and plate-centric frames of reference to estimate all the station positions and velocities. All of the above help minimize systematic errors that might otherwise affect our GPS site velocities. Further details are given in Section 3.3.

3.2 TECTONIC SETTING OF NORTHERN CENTRAL AMERICA

The tectonics of our study area are dominated by the Cocos, Caribbean, and North America plates, and Central America forearc sliver, which meet in a broad, complexly deforming region in southern Guatemala and southern Mexico (Fig. 3.1). Northeast-directed, nearly trench-normal Cocos plate subduction along the Middle America trench occurs at rates that vary from 70-80 mm yr^{-1} (DeMets *et al.* 2010). Motions between the Caribbean, North America, and Central America forearc sliver plates are accommodated by the Motagua-Polochic fault zone and numerous strike-slip and normal faults concentrated along the Central American volcanic arc (Fig. 3.1), but also include diffusely deforming regions north of the Polochic fault (e.g. Guzman-Speziale *et al.* 1989) and in southern Guatemala and western Honduras south of the Motagua Fault (e.g. Rogers and Mann 2007; Rodriguez *et al.* 2009).

Multiple faults in our study area have long histories of destructive earthquakes. The 22 July 1816 M_w~7.5 earthquake on the Polochic fault (White 1985) and 04 February 1976 M_w=7.5 Motagua fault earthquake (Plafker 1976) clearly established both faults as active parts of the North America-Caribbean plate boundary. The 1976 Motagua fault earthquake triggered numerous smaller earthquakes along normal faults in southern Guatemala (Matumoto & Latham 1976; Langer & Bollinger 1979; Manton 1987), highlighting for the first time the tectonic relationship between major strike-slip faults in Guatemala and the grabens of Honduras and southern Guatemala (Plafker 1976; Manton 1987; Rogers & Mann 2007). Manny small (M~6-6.5) but destructive earthquakes also ruptured strike-slip faults in the Nicaraguan and Salvadoran volcanic arcs during the past century (White 1991). North of the Polochic fault, in the Chiapas and southern Guatemala Strike-slip Fault

Province (Guzman-Speziale & Meneses-Rocha 2000) several shallow thrust-faulting and strike-slip earthquakes, including a M7.2-7.6 earthquake in 1591 and estimated M 7.6-7.8 earthquake in 1902 (Guzman-Speziale 2010), define a poorly-understood diffusely deforming zone.

3.3 Data

3.3.1 GPS interseismic velocities corrected for earthquake transients

In Part 1 (Chapter 2) of our analysis (Ellis *et al., in preparation*), we inverted the daily position time-series data for 219 GPS sites from the western Caribbean region to estimate coseismic and postseismic afterslip deformation caused by the M_w=7.3 Swan Islands (2009), M_w=7.3 Gulf of Fonseca (2012), and M_w=7.4 Champerico (2012) earthquakes. Linear regressions of all 219 GPS position time-series corrected for the coseismic and transient postseismic effects of these earthquakes gives the first interseismic velocity field for northern Central America for which the effects of large regional earthquakes are minimized. Details of the methods used to process the raw GPS data for the time-dependent modeling are given in Part 1 (Chapter 2).

Previously published interseismic velocity fields for northern Central America used only pre-2012 data for their analysis (Correa-Mora *et al.* 2009; Rodriguez *et al.* 2009; Alvarado *et al.* 2009; Franco *et al.* 2012; Staller *et al.* 2016). Our new GPS velocity field (Fig. 3.3; Table 3.1) is derived using data from 1999 to 2017 and includes five times more GPS sites than any previous study of this region. We compiled raw GPS data from all available sources, including Guatemala's Instituto Geografico Nacional, which operates a 12-station national network whose data have not been used to derive any previous velocity field, UNAVCO (unavco.org), and this paper's numerous co-authors. Subsets of the data used herein are described by Lyon-Caen *et al.* (2006), Turner *et al.*

(2007), Correa-Mora *et al.* (2009), LaFemina *et al.* (2009), Rodriguez *et al.* (2009), Alvarado *et al.* (2011), Franco *et al.* (2012), and Staller *et al.* (2016). Overall, we estimated and use velocities for 71 continuous and 138 campaign sites from northern Central America and the Caribbean plate. We also processed daily data from 989 continuous GPS sites in undeforming areas of the North America plate and use their velocities for our analysis (details given below).

3.3.2 Caribbean and North America plate angular velocities

The natural geological frames of reference for studies in the western Caribbean region are the Caribbean and North America plates. To create the basis for transforming our 209 site velocities, which are given relative to ITRF08 in our Part 1 analysis, we estimated Caribbean-ITRF08 and North America-ITRF08 angular velocities.

We estimated a Caribbean-ITRF08 angular velocity (Table 3.2) from the following 11 GPS site velocities: AVES, CAYS, CMP1, CR01, GLCO, MNTO, PUEC, SAN0, SANA, SFDP, VIKH, all on nominally undeforming areas of the Caribbean plate (Supplementary Fig. S3.1). The WRMS misfits to the north and east velocity components for these 11 sites are 0.66 and 0.78 mm yr^{-1}, respectively. The new angular velocity and its covariances are given in Table 3.2.

We estimated a North America-ITRF08 angular velocity (Table 3.2) from the linear velocities of 989 sites nominally located on stable areas of the North America plate interior (Supplementary Fig. S3.2). The best-fitting angular velocity gives WRMS misfits of 0.44 and 0.40 mm yr^{-1} in the north and east velocity components, respectively.

A Caribbean-North America angular velocity derived from the two newly-estimated angular velocities (Table 3.2) predicts 19.0 ± 0.2 mm yr^{-1}, N74.9°E ± 1° (95 per cent limits) motion for the Caribbean plate relative to North America at 14.5°N, 89°W, near the center of our study area. At

the same location, Caribbean-North America angular velocities from DeMets *et al.* (2007), Benford *et al.* (2012), and Symithe *et al.* (2015) predict respective velocities of 19.4 mm yr^{-1} (N75.5°E), 20.1 mm yr^{-1} (N73.9°E), and 17.7 mm yr^{-1} (N76.0°E). Our newly estimated angular velocity thus predicts a velocity that is near the midpoint of previous estimates. The TDEFNODE modeling described in Section 3.5 is constrained by our newly estimated North America-Caribbean plate angular velocity.

3.4 DESCRIPTION OF THE NEW GPS VELOCITY FIELD

Figure 3.3 shows our new regional GPS velocity field relative to the Caribbean and North America plates, where the station velocities used to determine the Caribbean and North America plates angular velocities are shown in Supplementary Figs. S3.1 and S3.2. The characteristics of the velocity field vary significantly across our study area due to the complexity of the regional tectonics. For convenience in describing the new velocity field, we subdivided our study area into three focus regions, one in southern Mexico where the natural frame of reference is the North America plate, a second centered on the Central America forearc sliver and the broad extending region north of the volcanic arc, and a third featuring the Motagua-Polochic fault zone. Our description of the new velocities includes forward calculations for several 1-D elastic models, which are useful guides for interpreting the new velocities. Results from the 2-D inversion that simultaneously estimates the elastic effects of all the faults in our study area are described in Section 3.5.

3.4.1 Elastic shortening and distributed deformation in southern Mexico

Previous geologic studies of deformation in southern Mexico describe evidence for trench-normal shortening and strike-slip faulting in the Chiapas Reverse Faults and Strike-Slip Faults Tectonic Province (Guzman-Speziale *et al.* 1989; Guzman-Speziale & Meneses-Rocha 2000; Guzman-Speziale 2010; Authemayou *et al.* 2011; Franco *et al.* 2012). The deformation is accommodated by faults, reverse faults, and 18 major strike-slip faults in the region (Guzman-Speziale & Meneses-Rocha, *in press*). Annual GPS observations from 2002 to 2005 at eight campaign sites and one continuous site in Chiapas show that all 9 stations moved toward the plate interior. Franco *et al.* (2012) show that the observed site motions are well fit by an elastic model with moderate-to-strong locking on the Middle America subduction interface. Their observations did not address distributed deformation within the Chiapas Tectonic Province.

Figure 3.4 shows our new interseismic velocity field for southern Mexico, consisting of velocities for 8 continuous stations and 9 campaign sites. We reoccupied 7 of the 9 campaign sites in this region in 2015 to extend their time-series by an additional 10 years relative to those used by Franco *et al.* (2012). All 17 stations in this region move toward the plate interior in a direction normal to the trench, as expected for areas inland from a strongly locked subduction zone.

To guide our interpretation of locking along the Middle America trench offshore southern Mexico, we predicted elastic deformation along a 1-D trench-normal profile for an elastic half-space model in which we variously applied 25 per cent, 50 per cent, and 100 per cent uniform locking of the subduction interface, a ~78 mm yr^{-1} Coco-North America plate convergence rate (DeMets *et al.* 2010), and a 0 to 40-km-deep seismogenic zone consistent with seismic and geodetic observations (White *et al.* 2004; Ye *et al.* 2013; Ellis *et al.* 2015). A comparison of the 1-D elastic model predictions to the trench-normal velocity component of sites in southern Mexico

(Fig. 3.5b) suggests that locking is between 50 and 100 per cent, consistent with that estimated by Franco *et al.* (2012).

3.4.2 Central America forearc sliver: subduction and trench-parallel translation

In contrast to the inland-directed station motions in southern Mexico, where the subduction interface is strongly to moderately locked (Franco *et al.* 2012; Fig. 3.5b), stations along the El Salvador forearc sliver move nearly parallel to the trench (blue arrows in Fig. 3.5a; Fig. 3.6). Figure 3.5c compares the trench-normal component of the velocities for GPS sites along the El Salvador segment to deformation predicted by a simple 1-D elastic model for a range of assumed locking values, a Cocos-Caribbean plate convergence velocity of 71 mm yr^{-1} (DeMets *et al.* 2010), and locking restricted to areas of the subduction interface above 20 km. This simple comparison suggests that any shallow locking is less than 25 per cent, in accord with modeling of previous GPS velocity fields for El Salvador (Correa-Mora *et al.* 2009). In our ensuing analysis, we evaluate where the transition between weak locking off the coast of El Salvador and strong locking farther northwest is located.

Destructive strike-slip earthquakes on faults within or near the Central America volcanic arc have occurred every several years over the past century (White 1991; White & Harlow 1993), causing nearly 20,000 fatalities since 1900 (White & Harlow 1993). The earthquakes accommodate trench-parallel, northwestward motion of a forearc sliver (Harlow & White 1985) at an approximate slip rate of 14 mm yr^{-1} relative to areas inland from the arc (DeMets 2001). In Nicaragua, movement of the forearc sliver does not appear to occur along a simple strike-slip fault strand, but is instead accommodated across a right-lateral shear zone several tens of kilometers wide (LaFemina *et al.* 2002; Funk *et al.* 2009). In El Salvador, the forearc sliver motion is

accommodated by well-defined strike-slip strands and pull-apart basins characterized by normal and bookshelf faulting (Corti *et al.* 2005; Agostini *et al.* 2006; Funk *et al.* 2009; Alvarado *et al.* 2011; Canora *et al.* 2012; Garibaldi *et al.* 2016). The poorly understood Jalpatagua fault (location shown in Fig. 3.6) of southern Guatemala is the western-most mapped strike-slip fault in the Central America volcanic arc (Carr 1976; Wunderman & Rose 1984; Authemayou *et al.* 2011).

Fig. 3.6 shows the velocities of GPS sites on and near the Central America volcanic arc. Previous authors have interpreted the trench-parallel motions of sites on the forearc as evidence for 12-15 mm yr^{-1} of northwest translation of a forearc sliver, driven by either oblique convergence (DeMets 2001) or by lateral escape of the sliver from the collision of the Cocos ridge with the trench offshore from Costa Rica (LaFemina *et al.* 2009). Figures 3.7 and 3.8 show a series of arc-normal velocity field transects in which the GPS site velocities have been rotated onto the direction defined by the volcanic arc faults within each transect. The transects centered in Nicaragua (Fig. 3.7a), the Gulf of Fonseca (Fig. 3.7b), and central and western El Salvador (Fig. 3.7c and 3.8a) suggest slip rates of ~10-12 mm yr^{-1} across the volcanic arc faults based on the difference between the velocities of the sites at the far ends of these transects. The velocity gradient for the central El Salvador segment, which crosses the well-mapped San Vicente strike-slip fault in El Salvador (Corti *et al.* 2005), is consistent with significant locking of this fault, in accord with conclusions reached by Correa-Mora *et al.* (2009) and Staller *et al.* (2016). The velocity gradients for the Nicaragua (Fig. 3.7a) and Gulf of Fonseca (Fig. 3.7b) transects are harder to interpret in the context of a single locked fault strand because both transects cross multiple active structures (LaFemina *et al.* 2002; Funk *et al.* 2009; Alvarado *et al.* 2011).

The two transects farthest northwest along the arc (Fig. 3.8b & c) suggest significantly slower shear across the volcanic arc than for the El Salvador and Nicaragua transects. A transect of

the Jalpatagua fault in southern Guatemala (Fig. 3.8b; location shown in Fig. 3.6) suggests an upper slip rate limit of ~8 mm yr^{-1}, although the mostly campaign-based site velocities in this transect still have high uncertainties. A transect of the volcanic arc farther west (Fig. 3.8c), where no arc-parallel faults have been identified, shows a 5 mm yr^{-1} or less difference in the velocities for sites flanking the volcanic arc.

3.4.3 Motagua-Polochic fault zone velocity field and transects

The velocity field spanning the Motagua-Polochic fault zone (Fig. 3.9), which is the principal physiographic and tectonic feature in our study area, clearly shows a sharp velocity gradient centered on the two faults, as first described by Lyon-Caen *et al.* (2006). Based on evidence reported by Lyon-Caen *et al.* (2006) for a westward decrease in slip rates along the Motagua-Polochic fault zone, we display GPS site velocities within four transects that cross the curving fault system (Figs. 3.10 & 3.11). The velocities of sites within the central and eastern transects (Figs. 3.10a and 3.10b) exhibit strong gradients and describe S-shaped patterns, typical of locked strike-slip faults (Savage and Burford 1973). Simple forward elastic half-space modeling with DISL (Larson 1992), assuming the Motagua fault is locked to a depth of 15 km, gives approximate slip rates of 17-19 mm yr^{-1} for both transects (Fig. 3.10). The gradient defined by the velocities closest to the Motagua fault is even steeper than predicted by our simple forward model, possibly indicating that aseismic creep accommodates some of the fault slip. Left-lateral strike-slip motion on these faults has juxtaposed serpentine rocks on both sides of the Motagua fault (Harlow *et al.* 2004; Brocard *et al.* 2016), which may be a prerequisite for aseismic creep (Reinen *et al.* 1991).

Transects that cross the plate boundary at the longitude of Guatemala City (Fig. 3.11b) and the western ~100 km of the Polochic fault (Fig. 3.11a) have more complex velocity gradients that

are influenced by the overlapping elastic effects of the Middle America trench, volcanic arc faults, and the Motagua-Polochic fault system. We interpret and discuss these data in Section 3.6.

3.4.4 Extension in southern Guatemala and western Honduras

The curved Motagua-Polochic fault zone and northwest trending Central America volcanic arc border a wedge-shaped region in southern Guatemala and western Honduras, where structural studies have long defined a series of ~N-S trending grabens (Weyl 1980; Rogers & Mann 2007). Prominent among these are the Guatemala City and Ipala grabens of southern Guatemala (Fig. 3.13) for which we estimate rates of extension as part of this analysis. From the velocities of 37 campaign and continuous GPS sites in central and western Honduras, Rodriguez *et al.* (2009) estimate that extension integrated across the grabens east of the Ipala graben is ~4 mm yr^{-1}. In contrast, the sparser GPS velocity field from Franco *et al.* (2012) suggests that little or no extension occurs east of the Guatemala City graben (see Fig. 3.5 in Franco *et al.* 2012). The only two previous geodetic studies of extension south of the Motagua fault thus disagree on where the extension occurs.

Figure 3.12 shows the GPS velocity field for the extending region in central and western Honduras, including four GPS sites in central Honduras on the stable area of the Caribbean plate. Our velocity field has less scatter than that of Rodriguez *et al.* (2009), an outcome of the improved methods we used to process the raw GPS data and the longer period spanned by our data. Our velocities are also rotated ~10-30° systematically clockwise from earlier estimates. In Section 3.5, we show that our new velocities define a slowly moving Chortis block.

Figure 3.13 shows E-W velocity components for 40 GPS sites spanning the ~600-km-wide zone of extension within the wedge defined above, excluding stations close to the Motagua fault

and Central America volcanic arc where the site velocities are strongly affected by fault-related elastic effects. From east to west, the first significant velocity gradient associated with extension occurs near 86.5°W (Fig. 3.13b), the same as reported by Rodriguez *et al.* (2009). The east velocity components, which are a proxy for stretching across the north-south-trending grabens, change relatively little from 86.5°W to 89°W. Near 89°W, the station directions change from ~NNW to nearly due west (Fig. 3.13a) and the sites begin moving 1-2 mm yr^{-1} more rapidly to the west (Fig. 3.13b). Our observations suggest that ~2 mm yr^{-1} of extension occurs between the Ipala and Guatemala City grabens, such that the extension integrated across all areas east of the Guatemala City graben is 5 ± 1 mm yr^{-1}, in accord with a ~4 mm yr^{-1} estimate from Rodriguez *et al.* (2009).

In detail, our new GPS station velocities in southern Guatemala define a sharp east-west extensional gradient across and west of the Guatemala City graben (Fig. 3.13b & c). Relative to sites PIN0 and GUAT on the eastern edge of the Guatemala City graben, sites CML0, TECP, UVGS, and QUE0 move westward at respective rates of ~5, 8, 11, and 8 mm yr^{-1} (Fig. 3.13b and c). Rapid extension thus occurs across the Guatemala City graben and other normal faults west of the graben (Langer & Bollinger 1979).

3.5 METHOD AND MODELING APPROACH: TDEFNODE

3.5.1 TDEFNODE

We use TDEFNODE (McCaffrey 2009) to invert our 209 GPS site velocities to simultaneously estimate angular velocities for up to 10 elastic blocks, locking for some of the faults bounding the blocks, and one strain-rate tensor for a deforming region in southern Mexico. We adopt the standard definition of interseismic fault locking as the fractional part of the relative plate or block motion that is not accommodated by steady aseismic slip (McCaffrey 2002). The best-fitting

solution minimizes the reduced chi-square statistic subject to the smoothing and *a priori* constraints that we impose on the inversion. Unlike our analysis in Part 1, in which we use TDEFNODE for time-dependent modeling of GPS position time-series, here we use TDEFNODE for modeling of static GPS velocities. Readers are referred to McCaffrey (2002) and McCaffrey (2009) for further information.

The TDEFNODE outputs used and displayed below include GPS site velocities estimated by our best-fitting model, residual site velocities, the elastic-only component of each modeled GPS site velocity, the rotational-only component of each modeled site velocity, WRMS values per block for the GPS site velocity residuals, and strain-rate tensors determined from the residual site velocities for each block. The strain-rate tensors are useful for identifying and quantifying distributed deformation in regions where it is not captured by the model.

3.5.2 Plate/Block configuration and boundaries

Based on geological, geodetic, and seismological evidence, we subdivided northern Central America into as many as 10 tectonic blocks or plates (Fig. 3.14). These include the Cocos, North America, and Caribbean plates, whose motions have been studied and quantified by numerous previous authors. They also include the Central America forearc sliver (Fig. 3.14, light blue region), which is bounded by the Middle America trench and Central America volcanic arc faults, and the Motagua-Polochic block, which is an elongate region bounded by the Motagua and Polochic faults (Fig. 3.14, orange region). We subdivided the deforming, wedge-shaped region between the Motagua fault and volcanic arc into four distinct blocks, named from west to east: the Atitlan, Ipala, western Chortis, and eastern Chortis blocks (Fig. 3.14). The Atitlan block consists of the area west of the Guatemala City graben and north of the volcanic arc. The Ipala block extends

east from the Guatemala City graben to the western edge of the Ipala graben, which serves as the western boundary of the Chortis block.

Based on geologic mapping, Gordon and Muehlberger (1994) define the strike-slip Guayape fault of central Honduras as the Chortis block's eastern boundary (Fig. 2) and suggest that its present slip sense is dextral. GPS measurements at sites spanning the Guayape fault however suggest that any present-day slip is no faster than 2 mm yr^{-1} (DeMets *et al.* 2007). GPS measurements at three stations ~50 km west of the Guayape fault instead suggest that they move with the stable Caribbean plate (Rodriguez *et al.* 2009). We therefore approximate the eastern edge of our geodetically-defined Chortis block with a N-S striking boundary (Fig. 3.14). Our geodetically-defined eastern Chortis block boundary is a free-slip feature in our best-fit model. Its precise location and geometry thus do not affect the model, provided that the Chortis block contains the same subset of GPS sites as our best-fitting model.

In the ensuing analysis, we test a variety of alternative, simpler models in which two or more of these four blocks are combined into larger, composite blocks. Finally, we also define a small Gulf of Fonseca block (Fig. 3.14, magenta region) based on paleomagnetic, structural, and geodetic observations from this ~120-km-wide step-over in the volcanic arc (Alvarado *et al.* 2011).

We digitized the block boundaries from a variety of sources. The Middle America trench contours are adopted from Hayes *et al.* (2012) and approximate the along-strike and downdip geometry of the subducting plate. The traces of the Motagua, Polochic, and Swan Islands faults were digitized from Rosencrantz & Mann (1991) and Authemayou *et al.* (2011). Faults in the volcanic arc were digitized from Funk *et al.* (2009), Alvarado *et al.* (2011), Canora *et al.* (2012), and high-resolution topography maps. All strike-slip faults are assumed to be vertical. The

Motagua, Polochic, and Swan Islands faults extend to 15 km depths, whereas the volcanic arc faults extend to 10 km due to a presumably higher geothermal gradient along the volcanic arc.

The faults above are represented by a series of nodes in TDEFNODE. Along the Middle America subduction interface, we used along-strike and down-dip Laplacian smoothing of the independent node locking estimates to avoid short wavelength artifacts in our fault locking estimates. For the strike-slip faults, we instead linked together nodes every ~30-50 km along faults, occasionally adjusting for the segmentation of the faults based on the locations of step-overs and restraining bends.

3.5.3 Modeling approach

We explored two strategies for our TDEFNODE inversions. We first describe the outcome of an inversion in which only two *a priori* constraints, both described below, were imposed during the inversion (Section 3.5.3.1). The motion of the Cocos plate, which has too few GPS sites to constrain its angular velocity, is constrained by the MORVEL Cocos-Caribbean plate angular velocity (DeMets *et al.* 2010). Movement between the North America and Caribbean plates is prescribed by the angular velocity we determined from 11 Caribbean plate GPS site velocities and 989 North America plate site velocities (Table 3.2). In Section 3.5.3.2, we describe a modified inversion strategy designed to minimize an undesirable tradeoff in the model parameters.

3.5.3.1 Least constrained approach

Inverting our kinematic data with only the two angular velocity constraints described above gives implausible estimates for the forearc sliver angular velocity and locking across the Middle America subduction interface offshore Guatemala, El Salvador, and Nicaragua. In particular, the

angular velocity predicts that the forearc sliver has a ~10 mm yr^{-1} component of motion directly toward the trench. Since the GPS sites on the forearc instead move parallel to the trench (Figs. 3.6, 3.7, and 3.8), TDEFNODE compensates for the misfit by locking the Middle America subduction interface strongly enough to predict ~10 mm yr^{-1} of inland-directed, elastic shortening in the forearc. This tradeoff between the estimates of the forearc sliver angular velocity and the subduction locking gives rise to a tectonically implausible, overly complicated solution with respect to a simpler model where the forearc GPS site motions are well fit by an angular velocity that predicts trench-parallel motion. A variety of alternative approaches to inverting the data failed to eliminate this undesirable tradeoff. We thus elected to invert our observations while constraining the forearc sliver to move parallel to the trench, as described in the next section.

3.5.3.2 Additional model constraints

We enforced trench-parallel motion of the forearc sliver by externally inverting the directions of 41 GPS sites on the Central America forearc (indicated by red arrows in Fig. 3.6) to find their best-fitting pole in a Caribbean plate reference frame. The best-fitting pole, given in Table 3.2, fits the 41 GPS site directions with an WRMS misfit of ~8 degrees (equivalent to ~1.4 mm yr^{-1} WRMS misfit).

We also determined a best-fitting pole for the Fonseca block (Table 3.2) from the directions of 7 GPS sites on the block (Fig. 3.6, magenta region). The Fonseca-Caribbean best-fitting pole fits these 7 directions with WRMS misfit of ~3 degrees.

In all ensuing TDEFNODE inversions, the poles for the forearc sliver and Fonseca block are fixed to the values given in Table 3.2. The forearc and Fonseca blocks thus move parallel to the trench in all of our models. The best angular rates for the forearc sliver and Fonseca block given in

Table 3.2 were determined by inverting all 209 GPS site velocities with TDEFNODE for a range of assumed forearc sliver and Fonseca block angular rates to find the angular rates that minimize the misfit (Fig. 3.15a and b).

All the results and inversions described below use the forearc sliver-Caribbean and Fonseca block-Caribbean angular velocities from Table 3.2 as *a priori* constraints. With these constraints, GPS velocities throughout the study area are well fit and the tradeoff between angular velocity of the forearc sliver and offshore subduction zone locking is avoided.

3.6 RESULTS

3.6.1 Optimizing the block geometry

To find the simplest block geometry that is consistent with our observed GPS velocity field, we tested several alternative block configurations. We first tested whether the site velocities from an assumed Chortis block are significantly better fit if we instead subdivide the block into distinct western and eastern Chortis blocks. The least squares misfit for a TDEFNODE inversion for the latter, more complex model failed to improve the fit relative to that for the simpler, one-block model at the 95 per cent confidence level, as determined with the Stein & Gordon (1984) F-ratio test for an additional plate. We thus use a single Chortis block as depicted in Fig. 3.16 for our ensuing inversions. A similar statistical comparison of the least-squares fits for models with and without an independently moving Ipala block justifies the addition of this small block at high confidence level. We thus include the Ipala block in all subsequent models.

West of the Guatemala City graben between the volcanic arc and the Polochic fault, there are no obvious faults to define the appropriate block geometry (Authemayou *et al.* 2011). We therefore tested four alternative block geometries. The simplest geometry, in which the Motagua-

Polochic fault, an Atitlán block, and the forearc sliver are joined in a single composite block, is rejected at high confidence level. We also tested geometries that assumed that shear occurs across a hypothetical western extension of the Motagua fault and/or along the volcanic arc northwest of Guatemala City (Fig. 3.14). The geometry that yields the best overall fit allows for motion between the forearc sliver and areas inland from the Guatemalan volcanic arc (Fig. 3.16). If we also allow for slip along an assumed western extension of the Motagua fault, thereby creating a narrow Atitlán block shown in Fig. 3.14, the angular velocity that gives the motion between the Atitlán block and Motagua-Polochic block predicts less than 0.5 mm yr^{-1} motion along the western extension of the Motagua fault. On the basis of these tests, we opt to use the block geometry shown in Fig. 3.16, consisting of three major tectonic plates and five smaller continental blocks.

3.6.2 Best-fitting model results

We inverted 418 north and east GPS site velocity components to estimate the 193 parameters that constitute our best-fitting TDEFNODE model, subject to the *a priori* constraints described above. The model parameters consist of plate/block angular velocities, locking estimates on numerous fault nodes, and one uniform, horizontal strain-rate tensor to describe the principal directions and rates of distributed strain in areas of Guatemala and southern Mexico north of the Polochic fault. The only smoothing applied in our model was locking along the Middle America subduction interface, which is represented by numerous fault nodes. Repeated inversions of our data were used to identify the smoothing factor that optimized the tradeoff between the data fit and model complexity. Although this smoothing significantly reduced the number of parameters that describe the subduction zone locking, TDEFNODE does not downward-adjust its estimate of the number of adjusted parameters for any smoothing applied in the model.

The weighted root mean square (WRMS) misfit for our best-fit model to the 418 GPS site velocity components is 1.1 mm yr^{-1}, close to the approximate uncertainties in our campaign site velocities, but approximately twice the uncertainties in our continuous station velocities. The WRMS values vary from only 0.6 mm yr^{-1} for sites on the Caribbean plate to 2.5 mm yr^{-1} for 9 sites on the deforming Fonseca block. These misfits are attributable to imperfect corrections to the GPS site-position time-series for earthquake offsets and transient post-seismic deformation, oversimplifications or possible errors inherent in the block configurations and geometries that we use, distributed deformation within one or more of the assumed-rigid blocks in our model, and random errors in the estimated GPS site velocities.

3.6.3 Middle America subduction zone: locking

Figure 3.17 shows our best locking estimates for the Middle America subduction interface. Our new estimates confirm the transition from strong locking off the coast of Chiapas to weak locking off the coast of southern Guatemala and El Salvador, as previously described by Franco *et al.* (2012). The weak locking along the Nicaragua, El Salvador, and Guatemala segments is consistent with the absence of any inland-directed shortening in these areas.

The elastic deformation predicted by our best TDEFNODE model changes dramatically along the trench (Fig. 3.18). In Chiapas, inland-directed shortening as fast as ~7 mm yr^{-1} is predicted for coastal sites (Fig. 3.18). The elastic shortening declines rapidly southeastward in Guatemala to zero in El Salvador and Nicaragua (Fig. 3.18). Elastic deformation in El Salvador, Nicaragua, and much of coastal Guatemala is dominated by locking of the volcanic arc faults, which gives rise to trench-parallel elastic deformation.

Correa-Mora *et al.* (2009) and Franco *et al.* (2012) estimate that locking across the upper 20 km of the subduction interface off the coasts of Guatemala and El Salvador ranges from 0 to 25 per cent. We estimated a new upper bound for locking of the shallowest part of the subduction interface by setting locking to zero at depths below 20 km for the Guatemala-El Salvador segment, as indicated by our best-fitting model, and incrementally increasing the subduction locking factor from 0 to 100 per cent for the upper 20 km of the subduction interface (Fig. 3.15d). Our data are fit best for assumed, uniform shallow locking value of 0 per cent, which causes almost no degradation of the WRMS fit relative to our best-fitting locking model (Fig. 3.17). Systematically increasing the shallow locking values (Fig. 3.15d) shows that locking values larger than 10 per cent degrade the fit at more than the 99 per cent confidence level as determined via an F-ratio test (Stein & Gordon 1984). Our results thus indicate that no locking occurs at normal seismogenic depths (~20-50 km) and that any locking above 20 km is under 10 per cent. Further discussion of the implications of our modeling for the subduction thrust earthquake cycle in this region is found in Section 3.7.3.

3.6.4 Evidence for distributed deformation north of the Polochic fault

Given the compelling geologic and seismic evidence for distributed shortening and strike-slip faulting in southern Mexico (Guzman-Speziale *et al.* 1989; Guzman-Speziale 2010; Authemayou *et al.* 2011), we evaluated two possible approaches for fitting our GPS velocities with TDEFNODE. We first inverted all 209 GPS site velocities assuming that no long-term deformation occurs north of the Polochic fault. The residual velocities associated with that model, shown by red arrows in Fig. 3.19, point systematically inland in most areas north of the Polochic fault. Numerical experiments in which we allowed locking to extend farther downdip along the

subduction interface offshore southern Mexico and/or varied the slab dip failed to significantly reduce these misfits. The misfit thus appears to originate in the upper plate.

We next inverted the 209 GPS site velocities while estimating a horizontal strain-rate tensor for the deforming area north of the Polochic fault (blue cross in Fig. 3.19). Fig. 3.19 shows the residual velocities for both models. The principal difference in the fits occurs in areas immediately north of the Polochic fault (Fig. 3.19) in a region referred to as the Cuchumatanes Highs (Guzman-Speziale 2010; Authemayou *et al.* 2011). The model misfits in this topographically high, seismically active region are 0-1 mm yr^{-1} for the model that allows for distributed strain via an estimated strain-rate tensor. In contrast, the model misfits are 1-3 mm yr^{-1} for an inversion in which distributed deformation is not permitted north of the Polochic fault. An F-ratio test for the improvement in fit associated with the three additional horizontal strain-rate tensor components shows that they improve the fit at the 95.5 per cent confidence level relative to the simpler model. We thus elected to estimate a strain-rate tensor as part of the best-fitting model described in this study.

The principal contractional strain-rate axis in our best-fitting model (Fig. 3.19) is oriented N-S, ~45 degrees from the principal shortening direction defined by the regional folds and thrust faults, and has magnitude -18 ± 5 nanostrains yr^{-1} (95 per cent). Between the Polochic fault and the northern limit of the Chiapas deforming region ~200 km farther north, the contractional component of the strain-rate tensor predicts 3.6 ± 1 mm yr^{-1} of ~N-S shortening. It seems unlikely that the shortening is distributed evenly within the deforming region. Guzman-Speziale (2010) instead document regions of distinct strike-slip and reverse faulting in southern Mexico. Our modeling in this area is thus only a first step toward describing its deformation. A logical next step

is to estimate strain-rate tensors for sub-regions in southern Mexico. In the long-term, denser GPS coverage of this region is required.

3.6.5 Motagua and Polochic faults: slip rates and locking

Figure 3.9 shows fits to the GPS site velocities along the Motagua-Polochic fault zone. The observed and estimated site directions and rates agree well everywhere along the fault. We next discuss the fits, fault slip rates, and locking estimates for each of the four fault transects that are shown in Figs. 3.10 and 3.11.

3.6.5.1 Eastern and central transects

Along the eastern and central transects, the Motagua-Polochic fault zone is bordered by the North America plate and Chortis block. Our model fits the fault-parallel velocity components for sites within the eastern transect within their 1-sigma uncertainties at most sites (Fig. 3.10b). Our approximation of the plate boundary as two simple strike-slip fault strands thus appears to be adequate. In contrast, the velocities of sites south of the Motagua fault within the central transect are fit more poorly (Fig. 3.10a). We tested whether allowing locking of the Motagua and Polochic faults to extend to a depth of 20 km instead of 15 km significantly reduced the misfit, but it did not. We attribute the misfits to likely over-simplifications in our block model. These include our approximations of the Chortis and Motagua-Polochic blocks (Fig. 3.16) as rigid blocks and our assumption that slip along the volcanic arc is accommodated along a narrow fault zone.

Our best estimates of the Polochic and Motagua fault slip rates for the eastern and central transects are 5.5 and 11.8 mm yr^{-1}, respectively (Fig. 3.20). The Motagua fault thus carries approximately two-thirds of the motion between the Chortis block and North America plate. The

locking indicated by our models ranges from 60 to 100 per cent for the two faults (Fig. 3.17). In Section 3.6.5.4, we evaluate the robustness of these estimates.

3.6.5.2 Transect near Guatemala City

Along the fault-normal transect that includes Guatemala City, the Motagua-Polochic fault zone is bordered to the north and south by the North America plate and Ipala block (Figs. 3.14 and 3.16). Our best-fit model fits the fault parallel velocity components for 13 of the 15 sites in this transect within most of their estimated uncertainties (Fig. 3.11b). Our best locking estimates for the transect near Guatemala City are 0.7 and 1.0 for the two faults (Fig. 3.17). The estimated slip rates are 5 and 8.5 mm yr^{-1} for the Polochic and Motagua faults, respectively (Fig. 3.20). The rate for the Polochic fault is thus the same as for the transects farther east, suggesting that relatively little slip is transferred to structures in the deforming zone north of the Polochic fault. In contrast, the 8.5 mm yr^{-1} slip rate for the Motagua fault is 3.5 mm yr^{-1} slower than locations farther east. In our simplistic model, all 3.5 mm yr^{-1} of slip is transferred off the Motagua fault southward into the Ipala graben, the boundary between the Ipala and Chortis blocks.

3.6.5.3 Western transect

The Motagua fault has no surface or other expression within the western transect shown in Fig. 3.11a. Instead the transect crosses the Central America volcanic arc and Polochic fault. Our model predicts fault-parallel velocity components that are consistent with the observations south of the fault, but systematically misfits the site velocities north of and within ~100 km of the fault by ~1 mm yr^{-1} (Fig. 3.11a). We attribute this small misfit to distributed deformation north of the Polochic fault, previously discussed in Section 3.6.4.

The 5 mm yr^{-1} slip rate that we estimate for the western segment of the Polochic fault (Fig. 3.20) is the same as for the transect near Guatemala City. Locking along this section of the Polochic fault is 100 per cent (Fig. 3.17).

3.6.5.4 Slip rates, partitioning, and locking estimates for the Motagua and Polochic faults

Given that the Motagua and Polochic faults are separated by only ~50 km and thus have overlapping elastic effects, we next discuss the robustness of our estimates of their combined and individual slip rates and locking. The angular velocity that describes the motion between the Chortis block and the North America plate is well determined due to the numerous GPS site observations that constrain both of their motions (989 on North America, 69 on the Chortis block). In eastern Guatemala, the Chortis-North America angular velocity and its covariances predict a net slip rate and direction across the central and eastern segments of the Motagua and Polochic faults of 17.9 ± 0.6 mm yr^{-1} toward N68°E ± 7.5° (95 per cent confidence limits).

Second, our estimate of the partitioning of the plate boundary slip, with two-thirds on the Motagua fault and one-third on the Polochic fault, is robust. To determine this, we ran a series of TDEFNODE inversions in which we systematically increased the assumed Polochic fault slip rate between zero and 17 mm yr^{-1} (Fig. 3.15f). Comparisons of the least-squares fits for these assumed slip rates to that for our best-fitting model indicate that a slip rate slower than 3.6 mm yr^{-1} or faster than 7.2 mm yr^{-1} along the Polochic fault is excluded at the 99 per cent confidence level. Consequently, the best Polochic slip rate and its 99 per cent bounds are 5.5 ± 1.8 mm yr^{-1}. The corresponding 99 per cent bounds on the Motagua fault slip rate are 10.9 to 13.8 mm yr^{-1} with a best estimate of 12.0 mm yr^{-1}.

Third, because extension south of the Motagua fault (Fig. 3.12, Fig. 3.16) transfers progressively more slip from the Motagua fault southward into the grabens that accommodate the extension, the Motagua fault slip rate must decrease westward. One discrete drop in the fault slip rate occurs at the Ipala graben, which is a block boundary in our model. There, the Motagua fault slip rate decreases by 3.5 mm yr^{-1}, equal to the Ipala-Chortis motion across this block boundary. A second, terminal 8.5 mm yr^{-1} drop in the Motagua fault slip rate occurs at the Guatemala City graben, which approximates the western edge of the Ipala block. There, all remaining 8.5 mm yr^{-1} of slip on the Motagua fault appears to transfer southward into the Guatemala City graben and a sequence of normal faults that extend ~70 km west of the graben and terminate at the Motagua fault at their northern ends.

Finally, Fig. 3.15e shows the dependence of our model fits on the assumed degree of locking on the Motagua and Polochic faults. For a simple model in which we enforce uniform locking everywhere along the two faults, we find a best locking value of 90 per cent and a 99 per cent lower bound of 50 per cent. For comparison, locking values for our best-fitting model range from 60 to 100 per cent on the two faults (Fig. 3.17).

3.6.6 Central America forearc sliver motion and slip on the volcanic arc faults

3.6.6.1 Forearc sliver motion and internal deformation

As described in Section 3.5.2, we determined the rotation pole for the Central America forearc sliver from an inversion of the directions of 41 of the 46 stations on the forearc and further determined a best forearc angular rate through a series of TDEFNODE inversions (Fig. 3.15a). The approximate 95 per cent uncertainty in the rate of trench-parallel motion is ± 0.5 mm yr^{-1} based on an F-ratio test to determine upper and lower limits on the forearc angular rate (Fig. 3.15a).

The WRMS misfit for our best TDEFNODE model is 1.5 mm yr^{-1} for the 46 residual GPS site velocities for sites on the forearc (Fig. 3.21). A strain-rate tensor derived from the 46 residual site velocities has a maximum shortening axis parallel to the sliver (Fig. 3.20) with a magnitude of only 0.2 nanostrains per year. For the ~700- km-long sliver, this implies only 0.1 mm yr^{-1} of internal forearc sliver deformation parallel to the sliver's long axis. The forearc sliver thus does not deform measurably. The elongation component of the strain-rate tensor (Fig. 3.20) implies no more than ~1 mm yr^{-1} of internal (arc-normal) deformation.

Our model predicts significant elastic effects at all the GPS sites on the forearc (Fig. 3.18). The elastic effects in Nicaragua, El Salvador and part of southern Guatemala are dominantly parallel to the volcanic arc strike-slip faults. Estimating and accounting for these elastic effects in our best-fitting model is required to accurately estimate the forearc angular rate relative to areas inland of the volcanic arc. The elastic effects in areas of southern Guatemala inboard from locked segments of the Middle America trench point inland (Fig. 3.18), thereby rotating the directions of GPS stations in this region clockwise from the direction of the sliver motion. Since 8 of the 41 GPS site directions we used to determine the forearc angular velocity are for sites onshore from the 2012 Champerico earthquake, we evaluated the sensitivity of our estimate of the forearc sliver pole by excluding these 8 site directions and inverting the remaining 33 site directions. This alternative forearc sliver pole, which lies only 0.8 angular degrees from the estimate in Table 3.2, predicts directions of motion that differ by a maximum of 1.5 degrees from our best-fitting estimate. We conclude that our estimate of forearc sliver motion is robust with respect to the elastic effects in our model.

3.6.6.2 Cocos plate motion relative to the forearc sliver

Our estimate of the angular velocity for the Cocos plate relative to the forearc sliver (Table 3.2) is the first estimate for this plate pair. The new angular velocity predicts Cocos plate subduction rates that range from 71 ± 2.8 mm yr^{-1} to 72 ± 2.7 mm yr^{-1} toward N29-30°E ± 1° offshore our study area. For comparison, the MORVEL Cocos-Caribbean angular velocity that is typically used to estimate convergence along the segment of the Middle America trench predicts 67 ± 2.5 mm yr^{-1} and 73 ± 2.6 mm yr^{-1} toward N20-22° E ± 1° at the same locations. Our new angular velocity thus predicts convergence rates similar to but directions ~10° anti-clockwise from the Cocos-Caribbean MORVEL estimate (DeMets *et al.* 2010). Guzman-Speziale & Zuniga (2016) report a N32°E average direction from the slip directions of 326 subduction thrust earthquakes offshore Guatemala, El Salvador, and Nicaragua. Our newly estimated angular velocity, which was determined without any seismologically-derived slip vectors, thus predicts a N29-30°E convergence direction along the Middle America trench that differs by only 2-3° from the N32°E seismologically derived direction. We conclude that our new angular velocity describes convergence along this section of the trench more accurately than any previous estimate.

3.6.6.3 Nicaragua volcanic arc

Dextral movement of the forearc sliver across the Nicaragua volcanic arc is accommodated in most areas by bookshelf faulting (LaFemina *et al.* 2002), whereas we simplistically represent this block boundary with a single, arc-parallel strike-slip fault in Nicaragua (Fig. 3.14). The fits to the arc-parallel components of the GPS site velocities from Nicaragua (Fig. 3.7a) are generally good despite our oversimplification of the forearc sliver boundary. An analysis of bookshelf faulting in the context of GPS measurements in Nicaragua remains to be done.

The fastest slip rate across the Central America volcanic arc occurs where the Caribbean plate lies directly inland from the volcanic arc (Fig. 3.14). Along this part of the arc, our forearc-Caribbean angular velocity predicts 12.5 ± 0.5 mm yr^{-1} of arc-parallel slip (Fig. 3.20). Our model predicts slower motion at the northwest end of the Nicaraguan volcanic arc (Fig. 3.20), where our block configuration places the Chortis block directly inland from the arc. The apparently slower motion is an artifact of the location we assign to the eastern boundary of the Chortis block where it intersects the volcanic arc (Fig. 3.14). The boundary location is unknown due to the absence of any GPS stations or geologic structures in western Nicaragua that define the approximate eastern boundary of the Chortis block (e.g. Fig. 3.12).

3.6.6.4 Gulf of Fonseca extensional step-over

Dextral movement between the forearc and Chortis block across the Gulf of Fonseca extensional step-over is partitioned between the assumed inland and offshore boundaries of the block (Fig. 3.20). Our model predicts 6.0 mm yr^{-1} of arc-parallel slip across the northern boundary and 4.6 mm yr^{-1} across its southern boundary. Some of the largest misfits in our study area occur for the GPS sites on the Fonseca block (Fig. 3.7b; Fig. 3.12), as might be expected given convincing geologic and seismic evidence for distributed deformation across this wide extending zone (Funk *et al.* 2009; Alvarado *et al.* 2011). The WRMS misfit for the nine Fonseca block GPS site velocities, 2.5 mm yr^{-1}, exceeds by a factor of two the misfit for any of the other blocks in our model. A strain-rate tensor estimated from the nine residual site velocities is accordingly larger than for any other block in our model (Fig. 3.20). Its principal elongation-rate axis is oriented N80°E ± 6°, nearly orthogonal to the numerous normal faults in eastern El Salvador within the deforming block

(Alvarado *et al.* 2011). Its associated strain-rate, 104 ± 10 nanostrains yr^{-1} implies ~10 ± 1 mm yr^{-1} of net ~E-W extension across this ~100-km-wide deforming region.

As a test, we also inverted our velocity field while estimating a horizontal strain-rate tensor for the Gulf of Fonseca block as part of the model inversion. The resulting principal elongation-rate axis is oriented N96°E and has a strain-rate of 93 ± 17 nanostrains yr^{-1}, minimally different from our best-fitting model. Both models exhibit <20 per cent locking offshore El Salvador and Nicaragua.

3.6.6.5 El Salvador volcanic arc faults

In El Salvador, where the forearc sliver motion is accommodated by a series of strike-slip faults and intervening pull-apart basins (Section 3.4.2), the forearc sliver-Chortis block angular velocity (Table 3.2) predicts arc-parallel motion of 10.6 ± 1 mm yr^{-1} (1-σ) at the volcanic arc (Fig. 3.20 and 3.21), ~2 mm yr^{-1} slower than the Nicaraguan volcanic arc slip rate (12.5 ± 0.5 mm yr^{-1}).

Our model fits the GPS site velocities inland of the volcanic arc well, but misfits the velocity gradient defined by stations southwest of the volcanic arc (Fig. 3.7c). Our best model suggests that locking above 5 km depths for the volcanic arc faults is weak or zero (Fig. 3.17), contrary to a previous estimate of strong, shallow locking by Correa-Mora *et al.* (2009). As a test, we evaluated whether stronger assumed locking on the upper 5 km of the volcanic arc faults significantly reduces the misfit to the velocity gradient without degrading the overall model fit (Fig. 3.15c). Locking as high as 90 per cent everywhere along the volcanic arc faults is permitted without degrading the fit to all the data at the 99 per cent confidence level (Fig. 3.7; Fig. 3.8; Fig. 3.15c). Although a high locking value improves the fit to the velocities of sites southwest of the volcanic arc, it degrades the fit to velocities for sites northeast of the volcanic arc (see small gray

triangles in Figs. 3.7 and 3.8). We attribute the difficulty in fitting all of the data to our approximation of the volcanic arc fault zone as a relatively narrow zone of faulting (Garibaldi *et al.* 2016).

3.6.6.6 Jalpatagua Fault: southern Guatemala

Fewer observations constrain the slip rate across the poorly understood Jalpatagua strike-slip fault at the southern edge of the Ipala block (Fig. 3.8b; location shown in Fig. 3.6). Our model predicts a fault-parallel slip rate of 9.3 mm yr^{-1}, approximately 1 mm yr^{-1} slower than in El Salvador and ~3 mm yr^{-1} slower than in Nicaragua (Figs. 3.20 and 3.21). More geodetic data are needed to refine this estimate and geologic observations are needed to test its accuracy.

3.6.6.7 Volcanic arc west of Guatemala City

Due to the absence of well-defined, through-going faults in the volcanic arc northwest of Guatemala City (Authemayou *et al.* 2011) and corresponding uncertainties about the appropriate block geometry in this region (Section 3.6.1), our results for this region are less reliable than elsewhere in our study area.

Figure 3.8c, which shows observations and model fits to GPS sites within a transect of the volcanic arc northwest of Guatemala City, indicates that no more than 3 mm yr^{-1} of dextral shear occurs across the volcanic arc. Movement of the forearc sliver relative to areas inland from the volcanic arc thus diminishes from 9.3 mm yr^{-1} on the Jalpatagua fault to ~3 mm yr^{-1} west of the Guatemala City graben (Fig. 3.20; location shown in Fig. 3.6), reflecting the large amount of slip that is transferred northward off faults in the volcanic arc to the Guatemala City graben and other normal faults north of the arc (Fig. 3.13).

3.6.7 Motion and extension of the Chortis and Ipala blocks: southern Guatemala and western Honduras

Some of our most reliable results are related to the movement of the Chortis and Ipala blocks, the former of which is densely sampled by GPS sites (Fig. 3.16). Elastic deformation in most parts of the Chortis block is only a few tenths of a millimeter per year (Fig. 3.18) and thus not a significant limiting factor in estimating the block angular velocity or its degree of internal deformation. Our best-fitting TDEFNODE model fits the 24 GPS site velocities from the eastern half of the Chortis block with WRMS of only 0.8 mm yr^{-1}. A strain-rate tensor determined from the 24 residual velocities (Fig. 3.20) has a maximum shortening strain-rate of 5 ± 6.6 nanostrains yr^{-1} (95 per cent confidence level). For the ~150-km-wide eastern Chortis block, this deformation implies less than 1 mm yr^{-1} of internal block deformation. By implication, the motions of sites in the eastern half of the block are well described by a rigid block rotation (Fig. 3.16).

In the Chortis block's western half (Fig. 3.14), our best-fitting TDEFNODE model fits the 45 GPS site velocities with WRMS of 1.2 mm yr^{-1}. The larger misfit is consistent with an apparent anti-clockwise rotation and modest increase of the velocities for sites on the westernmost part of the block (Fig. 3.12; Fig. 3.16). A strain-rate tensor determined from the 45 residual velocities has a maximum extensional principal axis that is oriented nearly east-west (Fig. 3.20), roughly orthogonal to the north-south-trending regional grabens. Its associated strain-rate, 12 ± 4 nanostrains yr^{-1} (95 per cent confidence level), gives a 2.5 ± 0.8 mm yr^{-1} east-west stretching rate across the ~220-km-wide western portion of the Chortis block (Fig. 3.20).

In central Honduras, our newly estimated Chortis-Caribbean angular velocity predicts that the Chortis block moves 2.5 ± 0.4 mm yr^{-1} (1-σ) toward N45°W ± 8° (Fig. 3.16) relative to the Caribbean plate interior. Better GPS station coverage in central Honduras (Fig. 3.13) is needed to

determine whether the movement between the Chortis block and Caribbean plate is accommodated across a wide or narrow deforming zone in central Honduras.

The Ipala block has only 5 GPS sites, whose velocities must constrain the block angular velocity and contribute to estimates of fault locking along the block's northern and southern edges. Consequently, our estimates of the Ipala block angular velocity and internal deformation are more uncertain. The principal extensional strain-rate axis, derived from the 5 residual site velocities, is oriented WSW-ENE (Fig. 3.20) and predicts ~2 mm yr^{-1} of east-west extension within this small block.

Relative to the Chortis block, the angular velocity for the Ipala block predicts motion of 3.7 mm yr^{-1} toward S45°W at a point in the Ipala Graben. This agrees well with the ~3 mm yr^{-1} difference in the observed GPS site velocities east and west of the Ipala graben (Fig. 3.13). At the west end of the Ipala block, the angular velocity that describes the motion of the Motagua-Polochic block across the Guatemala City graben (and other nearby normal faults) predicts net westward extension of 8.5 mm yr^{-1}. This prediction agrees well with the extension rates indicated by GPS site velocities from this region (Fig. 3.13b).

3.7 DISCUSSION AND CONCLUSIONS

3.7.1 Deformation south of the Motagua fault: rigid blocks in a deforming continuum

A key question treated herein is whether areas south of the Motagua fault are rotating as rigid or nearly-rigid blocks independent of the Caribbean plate. Our analysis unequivocally indicates that a large region south of the Motagua fault, approximately coinciding with the limits of the geologically defined Chortis block (e.g. Gordon & Muehlberger 1994), rotates slowly anti-clockwise as a nearly rigid block at the western end of the Caribbean plate (Fig. 3.16). The anti-

clockwise block rotation gives rise to slow ~E-W extension along the block's trailing, eastern boundary. Our data argue against an earlier interpretation of dominantly north-directed Chortis block motion based on geologic mapping, remote imagery, and seismic data (Gordon & Muehlberger 1994).

East-west strain rates determined from residual velocities are extensional and statistically significant (12 ± 4 nanostrains yr^{-1}, 95 per cent confidence level) in the west part of the Chortis block (Fig 3.20) and contractional and statistically insignificant (4.7 ± 6.6 nanostrains yr^{-1}, 95 per cent confidence level) in the eastern portion of the block. Integrating the 12 nanostrain yr^{-1} strain rate over the ~220-km-wide western portion of the Chortis block gives a 2.5 ± 0.8 mm yr^{-1} westward motion across the western portion of the Chortis block relative to its eastern boundary. The east to west increase in stretching rates is consistent with a geomorphologic interpretation of more active rifting in the western than the eastern part of the Chortis block (Rogers and Mann 2007).

Based on seismic moment tensors determined from historical and modern earthquakes, Guzman-Speziale (2001) and Caceres *et al.* (2005) estimate ~E-W extension rates of 3-8 mm yr^{-1} across the grabens in northern Central America, including the Ipala graben but not the Guatemala City graben. For comparison, we estimate a 2.5 mm yr^{-1} E-W stretching rate for the western portion of the Chortis block and an additional 2.6 mm yr^{-1} E-W component of opening across the Ipala graben predicted by the Ipala-Chortis block angular velocity. Our best-fit model thus gives a ~5 mm yr^{-1} E-W stretching rate across the grabens of Honduras and the Ipala graben in southern Guatemala, consistent with the seismic estimates.

Alvarez-Gomez *et al.* (2008) and Rodriguez *et al.* (2009) adopt a significantly different approach for modeling deformation south of the Motagua fault, namely using thin shell finite

element modeling and allowing the wedge-shaped region to deform as a continuum. Fig. 3.22 compares long-term velocities predicted by model 103P of Rodriguez *et al.* (2009), one of their preferred models, to the velocities predicted by our block model. The Rodriguez *et al.* (2009) continuum model is remarkably successful at capturing the deformation pattern revealed by GPS. By inference, their assumptions about the primary factors that control the regional deformation are likely to be correct to first-order, as are the similar assumptions applied by Alvarez-Gomez *et al.* (2008). These include the importance of the curvature of the Motagua fault, low locking across the Middle America subduction zone, the obliquity of North America-Caribbean plate motion with respect to the Motagua-Polochic fault zone, and little or no motion between the North America plate and Central America forearc sliver.

3.7.2 Volcanic arc slip rates and relation to extension northeast of the volcanic arc

Previous studies of the seismic and geodetic observations that constrain movement of the Central America forearc sliver variously predict 13.5-15 mm yr^{-1} rates for the sliver relative to areas inland from the volcanic arc (DeMets 2001; Correa-Mora *et al.* 2009; Kobayashi *et al.* 2014). All previous authors assumed that areas inland from the volcanic arc were part of an undeforming Caribbean plate. We instead subdivided areas inland of the volcanic arc into distinct Caribbean, Chortis, and Ipala blocks, thereby allowing slip rates along the volcanic arc faults to change along strike.

As shown in Figs. 3.20 and 3.21, the volcanic arc slip rates estimated with our model decrease systematically from 12.5 mm yr^{-1} in Nicaragua to 10.6 mm yr^{-1} in El Salvador, 9.3 mm yr^{-1} along the Jalpatagua fault (location shown in Fig. 3.6), and 2-3 mm yr^{-1} west of Guatemala City. The changes in slip rate represent transfers of slip from the volcanic arc faults to grabens north of

the volcanic arc. Nearly all (~75-90 per cent) of the slip on the volcanic arc faults is transferred to structures within the extending wedge north of the volcanic arc by a location near the Guatemala City graben. Although our block modeling approach forces the slip to transfer northward at the assumed block boundaries, the east-west oriented, elongation strain-rate tensors in the western Chortis and Ipala blocks (Fig. 3.20) indicate that some slip may be transferred northward in a more distributed manner.

3.7.3 Reconciling weak subduction locking with the 2012 El Salvador megathrust earthquake

The occurrence of the 2012 El Salvador thrust earthquake on the Middle America trench appears to conflict with our own and previous estimates of weak to zero subduction locking at all depths offshore El Salvador. We note however that coseismic slip during the 2012 El Salvador earthquake averaged only 500-800 mm on the earthquake rupture zone (Geirsson *et al.* 2015; Ellis *et al., in preparation*) and that the last earthquake to rupture much of this trench segment was in 1915 (White 2004). If the 1915 earthquake was a thrust event, then our newly estimated angular velocity predicts a net slip deficit between 1915 and 2012 of ~6.9 m (72 mm yr^{-1} x 97 years). Given that only 500-800 mm of slip occurred during the 2012 earthquake, the implied seismic locking ratio is only 7 to 12 per cent. For comparison, we estimate an upper 99 per cent confidence limit for shallow interseismic locking of 5 to 10 per cent based our sensitivity analysis (Fig. 3.15d). The geodetic observations are thus consistent with the seismic rupture history for this trench segment.

One end member interpretation of the apparently low seismic and interseismic locking estimates is that large-magnitude thrust earthquakes occur infrequently and are low-slip events along this part of the trench. If true, subduction thrust earthquakes pose relatively low risk along the El Salvador segment of the Middle America trench. Large-magnitude intraslab faulting events

such as the M_w=7.3 1982 and M_w=7.8 2001 earthquakes may instead pose the primary subduction-related risk along this trench segment (Martinez-Diaz *et al.* 2004; Guzman-Speziale *et al.* 2005; Correa-Mora *et al*. 2009).

An alternative interpretation is that the El Salvador segment is strongly locked but that the strong locking is masked by movement of the forearc sliver that includes a ~10 mm yr^{-1} component towards the trench (Section 3.5.3.1). We cannot categorically exclude this possibility, although it seems less likely given its additional complexity. If the locking is strong, the implied seismic slip deficit along much of the El Salvador segment is a minimum of 7 meters, sufficient for producing M>8 subduction thrust earthquakes.

3.7.4 Comparison to Franco *et al.* 2012 block model results

The only previous elastic block model for this study region is that of Franco *et al.* (2012), who subdivided northern Central America into a North America, Cocos, and Caribbean plates, and a Central America forearc sliver. In their model, all of the lithosphere between the Motagua fault and volcanic arc is treated as an undeforming Caribbean plate and the Motagua-Polochic fault zone is represented by a single fault. Comparisons to a subset of their results follow.

3.7.4.1 Middle America subduction zone

From their inversion of 40 GPS stations velocities from northern Central America, Franco *et al.* (2012) estimate that locking on the Middle America subduction interface changes from 60-80 per cent offshore southern Mexico to 0.25-0.34 offshore southern Guatemala near the Mexico-Guatemala border. Our best-fit model supports their result but has more extreme locking values for

both trench segments. We estimate interseismic locking of 90-100 per cent offshore southern Mexico and 0-10 per cent offshore Guatemala and El Salvador (Fig. 3.17).

3.7.4.2 Motagua-Polochic fault zone

Franco *et al.* (2012) estimate that the slip rate across the Motagua-Polochic fault zone decreases westward from 20 mm yr^{-1} in eastern Guatemala to 16 and 4 mm yr^{-1} in central and western Guatemala. Our data and modeling confirm the east-to-west slip-rate decrease but differ in several respects. First our model predicts 17.5 ± 0.6 mm yr^{-1} between the Chortis block and North America plate (Fig. 3.10 & 3.20) across the Motagua-Polochic fault zone in eastern and central Guatemala, ~10 per cent slower than estimated by Franco *et al.* (2012). The difference between the two is attributable to movement in our model between the Chortis block and Caribbean plate. Second, whereas Franco *et al.* (2012) did not estimate how the fault slip was partitioned between the Motagua and Polochic faults, our best-fitting model indicates that the Polochic fault carries approximately one-third of the plate motion (5.5-6 ± 1.8 mm yr^{-1}; 99 per cent limits) and the Motagua fault the remaining two-thirds (12 ± 1.5 mm yr^{-1}; 99 per cent limits) in eastern and central Guatemala, with tight limits on their estimated slip rates and partitioning (Section 3.6.5.4). Improved estimates of the partitioning will require closer GPS station spacing between the two faults (Fig. 3.10).

Our modeling indicates that the Polochic fault slip rate varies by less than 1 mm yr^{-1} along its length, although we suspect that the actual slip rate diminishes westward as some slip is transferred off the fault onto structures in the Chiapas Tectonic Province north of the fault. Better GPS station coverage in western Guatemala and southern Chiapas is needed to better understand how the leading edge of the Central America forearc sliver interacts with the North America plate

and the Chiapas Tectonic Province and discriminate between alternative models for the tectonic evolution of this region (e.g. Authemayou *et al*. 2011).

3.7.5 Comparison to geological observations and implications

We conclude our analysis by comparing our best-fitting model slip rates for the Motagua and Polochic faults and volcanic arc faults to geological estimates of slip rates using geomorphological, paleoseismicity, and cosmogenic dating methods.

Along the Polochic fault, Authemayou *et al.* (2012) use cosmogenic ^{36}Cl surface exposure dating to estimate fault slip rates from offsets of Quaternary volcanic markers and alluvial fans. For the central portion of the Polochic fault, they estimate a Holocene sinistral slip rate of 4.8 ± 2.3 mm yr^{-1}, consistent with a 2.5-3.3 mm yr^{-1} estimate based on the 25-km tectonic deflection of the Chixoy River over the past 7.5-10 Myr (Brocard *et al.* 2011). Both are consistent with our best-fitting model estimate of 5.5 ± 1.5 mm yr^{-1} (Figs. 3.15 and 3.20) within their combined uncertainties. Burkart (1978, 1983) and Burkart *et. al.* (1987) estimate 123-132 km of total left offset for the Polochic fault most likely since the late Miocene (11.6-5.3 Ma). Assuming this offset occurred since 11.6 Ma, the implied average slip-rate is ~11 mm yr^{-1}. This is twice our best Polochic fault slip-rate estimate and far outside its 99 per cent upper bound (Fig. 3.15).

For the Motagua fault, Quaternary measurements at offset stream terraces give a maximum slip rate of ~6 mm yr^{-1} (Schwartz *et al.* 1979), only half of our 11.8 ± 1.5 mm yr^{-1} best-fitting estimate (Fig. 3.20). Further geological studies of Motagua fault offsets are needed to better understand this discrepancy.

Along the main volcanic arc fault segments in El Salvador, our best-fitting model estimates a 10.6 mm yr^{-1} slip rate between the forearc and Chortis block and 6.0 mm yr^{-1} along the northern

boundary of the Fonseca block (Fig. 3.20). With only one exception (Corti *et al.* 2005), field geological and geomorphological data in El Salvador suggest late Pleistocene-Holocene slip rates that are significantly slower. Canora *et al.* (2012) estimate a 4.1± 0.7 mm yr^{-1} from fault trenching. Canora *et al.* (2014) estimate a slip rate of 4.5 ± 0.6 mm yr^{-1} from geological offsets, paleoseismic analysis, and a river offset. Both interpret the ~5 mm yr^{-1} slip rate difference relative to the faster geodetic estimates (Correa-Mora *et al.* 2009; Alvarado *et al.* 2011) as evidence that deformation may be distributed across multiple faults in the volcanic arc or could be incomplete due to volcanic activity and/or high erosion rates.

ACKNOWLEDGEMENTS

The first author was supported by a UNAVCO Graduate COCONet Fellowship. This work was funded by NSF grant EAR-1144418 (DeMets) and also benefited from National Science Foundation support for UNAVCO under grant EAR-1042906. We thank Central American institutions that provided technical, data, and logistical support, including Universidad Nacional Autonoma de Honduras, Universidad Nacional Autonoma de Mexico, Universidad Mariano Galvez (Guatemala City), Universidad San Carlos (Guatemala City), Ministerios de Medio Ambiente y Recursos Naturales El Salvador, Instituto Geografico Nacional of El Salvador and Guatemala, INSIVUMEH of Guatemala, and CONRED of Guatemala. We also thank Dave Mencin of UNAVCO and Hector Mora Paez of Servicio Geologico Colombiano for providing daily positions from the continuous Colombian GPS site CAYS in the western Caribbean Sea. Figures were prepared using Generic Mapping Tools software (Wessel & Smith 1991).

REFERENCES

Agostini, S., Corti, G., Doglioni, C., Carminati, E., Innocenti, F., Tonarini, S., Manetti, P., Di Vincenzo, G. and Montanari, D., 2006. Tectonic and magmatic evolution of the active volcanic front in El Salvador: insight into the Berlín and Ahuachapán geothermal areas, *Geothermics*, **35**(4), pp.368-408.

Altamimi, Z., Collilieux, X., and Metivier, L., 2011. ITRF2008: an improved solution of the international terrestrial reference frame, *J. Geodyn*., **85**, 457-473.

Alvarado, D., DeMets, C., Tikoff, B., Hernández, D., Wawrzyniec, T.F., Pullinger, C., Mattioli, G., Turner, H.L., Rodriguez, M. and Correa-Mora, F., 2011. Forearc motion and deformation between El Salvador and Nicaragua: GPS, seismic, structural, and paleomagnetic observations, *Lithosphere*, **3**(1), pp.3-21.

Álvarez-Gómez, J.A., Meijer, P.T., Martínez-Díaz, J.J. and Capote, R., 2008. Constraints from finite element modeling on the active tectonics of northern Central America and the Middle America Trench, *Tectonics*, **27**(1).

Authemayou, C., Brocard, G., Teyssier, C., Simon-Labric, T., Guttiérrez, A., Chiquín, E.N. and Morán, S., 2011. The Caribbean–North America–Cocos Triple Junction and the dynamics of the Polochic–Motagua fault systems: Pull-up and zipper models, *Tectonics*, **30**(3).

Authemayou, C., Brocard, G., Teyssier, C., Suski, B., Cosenza, B., Morán-Ical, S., González-Véliz, C.W., Aguilar-Hengstenberg, M.A. and Holliger, K., 2012. Quaternary seismo-tectonic activity of the Polochic Fault, Guatemala, *Journal of Geophysical Research: Solid Earth*, **117**(B7).

Benford, B., DeMets, C., and Calais, E., 2012. GPS estimates of microplate motions, northern Caribbean: Evidence for a Hispaniola microplate and implications for earthquake hazard, *Geophysical Journal International*, **191**(2), 481-490.

Brocard, G., Teyssier, C., Dunlap, W.J., Authemayou, C., Simon-Labric, T., Cacao-Chiquín, E.N., Gutiérrez-Orrego, A. and Morán-Ical, S., 2011. Reorganization of a deeply incised drainage: role of deformation, sedimentation and groundwater flow, *Basin Research*, *23*(6), pp.631-651.

Brocard, G., Anselmetti, F.S. and Teyssier, C., 2016. Guatemala paleoseismicity: from Late Classic Maya collapse to recent fault creep, *Scientific reports*, **6**, p.36976.

Burkart, B., 1978. Offset across the Polochic fault of Guatemala and Chiapas, Mexico. *Geology*, *6*(6), pp.328-332.

Burkart, B., 1983. Neogene North American-Caribbean plate boundary across northern Central America: offset along the Polochic fault. *Tectonophysics*, *99*(2-4), pp.251-270.

Burkart, B., Deaton, B.C., Dengo, C. and Moreno, G., 1987. Tectonic wedges and offset Laramide structures along the Polochic fault of Guatemala and Chiapas, Mexico: reaffirmation of large Neogene displacement. *Tectonics*, *6*(4), pp.411-422.

Cáceres, D., Monterroso, D. and Tavakoli, B., 2005. Crustal deformation in northern Central America, *Tectonophysics*, **404**(1), pp.119-131.

Canora, C., Villamor, P., Martínez-Díaz, J.J., Berryman, K.R., Álvarez-Gómez, J.A., Capote, R. and Hernández, W., 2012. Paleoseismic analysis of the San Vicente segment of the El Salvador Fault Zone, El Salvador, Central America, *Geologica Acta: an international earth science journal*, *10*(2).

Canora, C., Martínez-Díaz, J.J., Villamor, P., Staller, A., Berryman, K., Álvarez-Gómez, J.A., Capote, R. and Díaz, M., 2014. Structural evolution of the El Salvador Fault Zone: an evolving fault system within a volcanic arc, *Journal of Iberian Geology*, **40**(3), p.471.

Carr, M.J., 1976. Underthrusting and Quaternary faulting in northern Central America, *Geological Society of America Bulletin*, **87**(5), pp.825-829.

Correa-Mora, F., DeMets, C., Alvarado, D., Turner, H. L., Mattioli, G., Hernandez, D., and Tenorio, C., 2009. GPS-derived coupling estimates for the Central America subduction zone and volcanic arc faults: El Salvador, Honduras and Nicaragua, *Geophysical Journal International*, **179**(3), 1279-1291.

Corti, G., Carminati, E., Mazzarini, F. and Garcia, M.O., 2005. Active strike-slip faulting in El Salvador, central America. *Geology*, *33*(12), pp.989-992.

DeMets, C., 2001. A new estimate for present-day Cocos-Caribbean plate motion: Implications for slip along the Central American volcanic arc, *Geophysical Research Letters,* **28**(21), 4043-4046.

DeMets, C., Mattioli, G., Jansma, P., Rogers, R.D., Tenorio, C. and Turner, H.L., 2007. Present motion and deformation of the Caribbean plate: Constraints from new GPS geodetic measurements from Honduras and Nicaragua, *Geological Society of America Special Papers*, *428*, pp.21-36.

DeMets, C., Mattioli, G., Jansma, P., Rogers, R. D., Tenorio, C., and Turner, H. L., 2007. Present motion and deformation of the Caribbean plate: Constraints from new GPS geodetic measurements from Honduras and Nicaragua, *Geological Society of America Special Papers*, **428**, 21-36.

DeMets, C., Gordon, R. G., and Argus, D. F., 2010. Geologically current plate motions. *Geophysical Journal International*, **181**(1), 1-80.

Ellis, A. P., DeMets, C., Briole, P., Molina, E., Flores, O., Rivera, J., Lasserre, C., Lyon-Caen, H., and Lord, N., 2015. Geodetic slip solutions for the M_w = 7.4 Champerico (Guatemala) earthquake of 2012 November 7 and its postseismic deformation, *Geophys. J. Int*., **201**(2), 856-868.

Ellis, A.P., DeMets, C., Briole, P., Cosenza, B., Flores, O., Graham, S. E., Guzman-Speziale, G., Hernandez, D., Kostoglodov, V., LaFemina, P., Lord, N., Lasserre, C., Lyon-Caen, H., Maradiaga, M. R., McCaffrey, R., Molina, E., Rivera, J., Rogers, R., and Staller, A, (2018). *Deformation in northern Central America from 1999 to 2016 using GPS observations, Part I: Time-dependent modeling of large regional earthquakes and their postseismic effects,* Manuscript in preparation.

Franco, A., Lasserre, C., Lyon-Caen, H., Kostoglodov, V., Molina, E., Guzmán-Speziale, M., Monterosso, D., Robles, V., Figueroa, C., and Amaya, W., 2012. Fault kinematics in northern Central America and coupling along the subduction interface of the Cocos plate, from GPS data in Chiapas (Mexico), Guatemala and El Salvador, *Geophysical Journal International,* **189**(3): 1223-1236.

Funk, J., Mann, P., McIntosh, K. and Stephens, J., 2009. Cenozoic tectonics of the Nicaraguan depression, Nicaragua, and Median Trough, El Salvador, based on seismic-reflection profiling and remote-sensing data. *Geological Society of America Bulletin*, *121*(11-12), pp.1491-1521.

Garibaldi, N., Tikoff, B. and Hernández, W., 2016. Neotectonic deformation within an extensional stepover in El Salvador magmatic arc, Central America: Implication for the interaction of arc magmatism and deformation, *Tectonophysics*, **693**, pp.327-339.

Geirsson, H., LaFemina, P. C., DeMets, C., Hernandez, D. A., Mattioli, G. S., Rogers, R., Rodriguez, M., Marroquin, G., and Tenorio, V., 2015. The 2012 August 27 M_w 7.3 El Salvador earthquake: expression of weak coupling on the Middle America subduction zone, *Geophys. J. Int.,* **202***,* 1677-1689.

Gordon, M.B. & Muehlberger, W.R., 1994. Rotation of the Chortis block causes dextral slip on the Guayape fault, *Tectonics*, **13**(4), pp.858-872.

Graham, S. E., DeMets, C., DeShon, H. R., Rogers, R., Maradiaga, M. R., Strauch, W., and Wiese, K., 2012. GPS and seismic constraints on the M=7.3 2009 Swan Islands earthquake: implications for stress changes along the Motagua fault and other nearby faults, *Geophys. J. Int.*, **190,** 1625-1639.

Guzmán-Speziale, M., 2001. Active seismic deformation in the grabens of northern Central America and its relationship to the relative motion of the North America–Caribbean plate boundary, *Tectonophysics*, *337*(1), pp.39-51.

Guzmán-Speziale, M., 2010. Beyond the Motagua and Polochic faults: Active strike-slip faulting along the western North America–Caribbean plate boundary zone, *Tectonophysics*, **496**(1), 17-27.

Guzmán-Speziale, M. and Meneses-Rocha, J.J., 2000. The North America–Caribbean plate boundary west of the Motagua–Polochic fault system: a fault jog in Southeastern Mexico, *Journal of South American Earth Sciences*, **13**(4), pp.459-468.

Guzmán-Speziale, M. and Zúñiga, F.R., 2016. Differences and similarities in the Cocos–North America and Cocos–Caribbean convergence, as revealed by seismic moment tensors, *Journal of South American Earth Sciences*, **71**, pp.296-308.

Guzmán-Speziale, M., Pennington, W.D. and Matumoto, T., 1989. The triple junction of the North America, Cocos, and Caribbean plates: Seismicity and tectonics, *Tectonics*, **8**(5), pp.981-997.

Guzmán-Speziale, M., Valdés-González, C., Gómez, J. M., and Molina, E., 2005. Seismic activity along the Central America Volcanic arc: is it related to subduction of the Cocos plate?, *Tectonophysics*, **400**, 241-254.

Harlow, D.H. and White, R.A., 1985. Shallow earthquakes along the volcanic chain in Central America: evidence for oblique subduction, *Earthquake Notes*, **55**(1), p.28.

Harlow, G.E., Hemming, S.R., Lallemant, H.G.A., Sisson, V.B. and Sorensen, S.S., 2004. Two high-pressure–low-temperature serpentinite-matrix mélange belts, Motagua fault zone, Guatemala: a record of Aptian and Maastrichtian collisions, *Geology*, **32**(1), pp.17-20.

Hayes, G. P., Wald, D. J., and Johnson, R. L., 2012. Slab1.0: a three-dimensional model of global subduction zone geometries, *J. geophys. Res*., **117**, B01302, doi:10.1029/2011JB008524.

Kobayashi, D., LaFemina, P., Geirsson, H., Chichaco, E., Abrego, A.A., Mora, H. and Camacho, E., 2014. Kinematics of the western Caribbean: Collision of the Cocos Ridge and upper plate deformation. *Geochemistry, Geophysics, Geosystems*, *15*(5), pp.1671-1683.

LaFemina, P.C., Dixon, T.H. and Strauch, W., 2002. Bookshelf faulting in Nicaragua, *Geology*, **30**(8), pp.751-754.

LaFemina, P., Dixon, T. H., Govers, R., Norabuena, E., Turner, H., Saballos, A., Mattioli, G., and Strauch, W., 2009. Fore-arc motion and Cocos Ridge collision in Central America, *Geochem. Geophys. Geosyst*., **10**(5), Q05S14, doi:10.1029/2008GC002181.

Larsen, S.C., 1992. Displacement modeling of dislocations, PhD thesis, California Institute of Technology, Pasadena, CA.

Lyon-Caen, H., Barrier, E., Lasserre, C., Franco, A., Arzu, I., Chiquin, L., Chiquin, M., Duquesnoy, T., Flores, O., and Galicia, O., 2006. Kinematics of the North American-Caribbean-Cocos plates in Central America from new GPS measurements across the Polochic-Motagua fault system, *Geophysical Research Letters,* **33** (19).

Langer, C.J. & Bollinger, G.A., 1979. Secondary faulting near the terminus of a seismogenic strike-slip fault: Aftershocks of the 1976 Guatemala earthquake, *Bulletin of the Seismological Society of America*, **69**(2), pp.427-444.

Molnar, P. and Sykes, L.R., 1969. Tectonics of the Caribbean and Middle America regions from focal mechanisms and seismicity, *Geological Society of America Bulletin*, **80**(9), pp.1639-1684.

Manton, W.I., 1987. Tectonic interpretation of the morphology of Honduras, *Tectonics*, **6**(5), pp.633-651.

Martínez-Díaz, J.J., Alvarez-Gómez, J.A., Benito, B. and Hernández, D., 2004. Triggering of destructive earthquakes in El Salvador, *Geology*, **32**(1), pp.65-68.

Matumoto, T. and Latham, G.V., 1976. Aftershocks of the Guatemalan earthquake of February 4, 1976, *Geophysical Research Letters*, **3**(10), pp.599-602.

McCaffrey, R., 2002. Crustal block rotations and plate coupling, *Plate boundary zones*, pp.101-122.

McCaffrey, R., 2009. Time-dependent inversion of three-component continuous GPS for steady and transient sources in northern Cascadia, *Geophys. Res. Lett.*, **36**, L07304, doi:10.1029/2008GL036784.

Plafker, G., 1976. Tectonic Aspects of the Guatemala Earthquake of 4 February 1976, *Science*, **103,** 4259.

Reinen, L.A., Weeks, J.D. and Tullis, T.E., 1991. The frictional behavior of serpentinite: Implications for aseismic creep on shallow crustal faults, *Geophysical Research Letters*, **18**(10), pp.1921-1924.

Rodriguez, M., DeMets, C., Rogers, R., Tenorio, C., and Hernandez, D., 2009. A GPS and modelling study of deformation in northern Central America, *Geophys.l J. Int*., **178**, 1733-1754.

Rogers, R. D. and Mann, P., 2007. Transtensional deformation of the western Caribbean-North America plate boundary zone, *Geol. Soc. Am. Spec. Pap.*, **428**, 37-64.

Rosencrantz, E. and Mann, P., 1991. SeaMARC II mapping of transform faults in the Cayman Trough, Caribbean Sea, *Geology*, **19**, 690-693.

Savage, J.C. and Burford, R.O., 1973. Geodetic determination of relative plate motion in central California, *Journal of Geophysical Research*, **78**(5), pp.832-845.

Schwartz, D.P., Cluff, L.S. and Donnelly, T.W., 1979. Quaternary faulting along the Caribbean-North American plate boundary in Central America, *Tectonophysics*, *52*(1-4), pp.431-445.

Staller, A., Martínez-Díaz, J.J., Benito, B., Alonso-Henar, J., Hernández, D., Hernandez-Rey, R. and Diaz, M., 2016. Present-day crustal deformation along the El Salvador Fault Zone from ZFESNet GPS network, *Tectonophysics*, **670**, pp.66-81.

Stein, S. and Gordon, R.G., 1984. Statistical tests of additional plate boundaries from plate motion inversions, *Earth and Planetary Science Letters*, **69**(2), pp.401-412.

Symithe, S., Calais, E., Chabalier, J.B., Robertson, R. and Higgins, M., 2015. Current block motions and strain accumulation on active faults in the Caribbean, *Journal of Geophysical Research: Solid Earth*, **120**(5), pp.3748-3774.

Turner, H.L., LaFemina, P., Saballos, A., Mattioli, G.S., Jansma, P.E. and Dixon, T., 2007. Kinematics of the Nicaraguan forearc from GPS geodesy. *Geophysical Research Letters*, *34*(2).

Wessel, P. and Smith, W.H., 1991. Free software helps map and display data, *Eos, Transactions American Geophysical Union*, **72**(41), pp.441-446.

Weyl, R., 1980. Geology of Central America.

White, R. A. and Harlow, D. H., 1993. Destructive upper-crustal earthquakes of Central America since 1900, *Bulletin of the Seismological Society of America*, **83**(4), 1115-1142.

White, R. A., Ligorría, J. P., and Cifuentes, I. L., 2004. Seismic history of the Middle America subduction zone along El Salvador, Guatemala, and Chiapas, Mexico: 1526-2000, *Special Papers-Geological Society of America,* 379-396.

Wunderman, R.L. and Rose, W.I., 1984. Amatitlan, an actively resurging cauldron 10 km south of Guatemala City, *Journal of Geophysical Research: Solid Earth*, **89**(B10), pp.8525-8539.

Ye, L., Lay, T., and Kanamori, H., 2013. Large earthquake rupture process variations on the Middle America megathrust, *Earth planet, Sci. Lett*., **381**, 147-155.

TABLES

Table 3.1: GPS station velocity information relative to the North America plate

Site name	Longitude (°E)	Latitude (°N)	V_e	V_n	σ_e	σ_n	Correlation coeffiicient
ACAJ	270.17	13.58	6.9	9.3	0.4	0.4	-0.0004
AGLA	270.32	13.84	11.0	8.5	2.4	1.4	0.0000
AHUA	270.19	13.91	6.4	7.7	0.6	0.6	-0.0002
AIES	270.95	13.45	8.0	8.6	0.5	0.6	-0.0001
AMAT	272.00	13.41	13.9	7.0	2.5	1.8	0.0000
AVES	296.38	15.67	18.2	5.4	2.4	1.4	0.0003
AZTE	266.06	16.22	2.7	2.8	3.1	1.6	0.0000
BARB*	300.39	13.09	19.2	5.6	1.5	1.0	0.0008
BARI	268.69	15.80	3.0	2.1	0.5	0.7	-0.0003
BDOS*	300.39	13.09	19.0	4.9	0.5	0.4	0.0060
BEND	269.40	14.18	10.2	6.6	4.9	2.6	0.0000
BLUX$^{\phi}$	276.23	11.99	19.2	5.6	1.1	0.7	0.0003
BT10	271.49	13.53	7.0	5.9	0.5	0.5	0.0000
CABA	271.32	13.73	17.9	9.6	2.7	2.4	0.0000
CAH0	270.18	15.61	2.3	1.4	0.8	0.5	-0.0001
CAM0*	270.94	15.39	5.0	3.4	1.1	0.7	0.0000
CAMP	269.46	19.84	0.8	0.8	0.7	0.4	-0.0002
CARI	272.31	13.83	16.5	6.7	0.4	0.5	0.0002
CATR	270.26	14.46	14.7	6.7	0.6	0.6	-0.0001
CAYS	280.15	15.80	17.6	3.3	1.3	1.0	0.0003
CBSB	280.17	19.71	2.2	0.1	0.4	0.4	0.0019
CEGD	271.10	13.94	17.7	7.5	0.4	0.4	-0.0001
CGUI	272.44	12.98	8.7	11.0	0.7	0.8	0.0001
CH15	271.44	13.62	15.0	6.7	0.4	0.7	0.0000
CHA0	270.48	14.83	13.3	5.5	1.1	0.7	0.0000
CHET	271.70	18.50	1.2	0.5	0.5	0.3	0.0001
CHI0	270.35	14.78	14.5	5.4	0.8	0.5	-0.0001
CHIQ	272.49	14.28	17.1	6.5	0.4	0.4	0.0003
CHIS	269.71	15.81	2.7	2.9	0.5	0.6	-0.0002
CHL0	269.62	14.08	7.9	5.4	0.7	0.5	-0.0002
CHNN	272.86	12.64	9.2	7.4	0.5	1.3	0.0001
CHPO	268.08	14.29	10.3	4.0	1.3	1.0	-0.0001
CHQG	269.25	15.35	3.3	3.6	1.1	0.9	-0.0001
CLV2	273.15	12.57	13.0	13.1	1.3	0.9	0.0001
CML0	269.20	14.64	8.0	3.8	0.8	0.4	-0.0003
CMP1	274.29	14.51	19.6	5.5	3.0	1.4	0.0000
CN18	276.06	17.41	6.2	1.9	0.8	0.7	0.0003
CN21	272.57	13.40	16.4	7.0	0.7	0.7	0.0001
CN22	272.96	12.38	14.2	14.6	1.1	1.1	0.0001

CN23	271.22	17.26	1.4	0.6	0.6	0.6	0.0000
CN24	271.95	19.58	1.0	0.7	0.6	0.6	0.0000
CN25	267.86	16.23	4.4	5.0	0.7	0.7	-0.0003
CN30[♯]	276.23	11.99	5.5	6.9	1.3	1.0	0.0002
CNCC	267.31	16.12	3.1	4.2	0.9	0.5	-0.0003
CNCH	271.66	14.03	17.1	7.0	1.2	0.7	0.0000
CNG2[♯]	273.30	12.50	9.3	13.3	0.6	0.6	0.0002
CNR1*	270.71	13.67	10.1	10.6	0.7	1.0	0.0000
COA0	269.60	15.47	3.2	2.0	3.8	2.0	0.0000
COAT*	268.12	14.70	7.1	5.1	0.7	0.8	-0.0002
COB0	269.61	15.46	2.7	2.1	0.4	0.3	-0.0006
COMI	267.86	16.28	2.6	3.7	0.3	0.3	-0.0016
CON0	270.55	14.52	16.2	6.1	0.8	0.5	-0.0001
CORI[♯]	272.80	12.52	9.6	11.7	1.3	1.0	0.0000
CORN[♯]	276.94	12.18	19.8	3.3	4.6	2.3	0.0000
COTZ*	268.94	14.33	7.4	7.6	0.5	0.6	-0.0003
CPJ0	270.76	14.85	14.7	4.1	3.8	2.3	0.0000
CRM1	271.10	13.73	17.1	7.8	2.5	1.3	0.0000
CRO1	295.42	17.76	18.8	5.5	0.3	0.4	0.0069
CRR1	271.27	13.67	16.2	7.6	2.4	1.3	0.0000
CSJO	271.61	13.49	13.7	6.8	2.5	1.3	0.0000
CUCU	271.14	14.58	16.7	6.1	1.9	1.1	0.0000
DERA	271.18	13.67	17.1	7.8	0.7	0.6	0.0000
DOL2	269.43	14.35	4.0	9.3	4.5	2.5	0.0000
DOLO	269.42	14.35	6.7	5.5	4.7	2.7	0.0000
ECOP	271.68	15.33	15.5	8.0	4.6	2.4	0.0000
ELCO	272.60	12.81	9.6	9.2	0.9	0.5	0.0001
ELEN	270.13	16.92	1.4	1.4	0.3	0.3	-0.0004
ERAN	271.54	14.23	16.9	7.0	1.2	0.7	0.0000
ERAZ	272.89	14.60	17.5	5.8	1.7	0.9	0.0000
ESPI	267.93	15.70	3.7	4.6	0.9	0.6	-0.0003
ESPO	266.40	15.94	2.8	6.7	3.0	1.7	0.0000
ESTC	266.52	17.46	2.5	3.2	1.0	0.6	-0.0003
FMIN	270.33	15.08	7.3	2.7	0.7	0.4	-0.0001
FRT1	271.96	15.78	14.0	3.0	2.5	1.9	0.0000
FSD0[ϕ]	298.85	14.73	17.9	5.0	2.4	1.4	0.0003
GCGT	278.62	19.29	1.2	0.8	0.4	0.4	0.0013
GLCO	273.93	15.03	17.6	5.6	1.2	0.6	0.0001
GOME	268.92	14.03	8.3	5.8	4.4	2.4	0.0000
GRAC	271.42	14.59	17.7	6.5	1.2	0.7	0.0000
GRUT	267.14	16.42	2.3	3.3	1.1	0.6	-0.0002
GUAJ	270.53	14.23	15.6	6.0	0.5	0.5	-0.0001

GUAT	269.48	14.59	12.9	3.5	0.4	0.3	-0.0006
GUAY	270.84	13.84	20.0	8.8	3.0	2.8	0.0000
HERH	273.17	12.61	11.8	10.1	0.6	0.8	0.0002
HON0	270.39	15.03	8.1	2.5	1.6	0.9	0.0000
HON1	270.38	15.03	8.6	1.5	4.4	2.3	0.0000
HOYN	273.17	12.60	11.7	9.0	0.6	0.7	0.0002
HUE0	268.53	15.28	3.3	3.9	1.6	0.9	-0.0001
HUEH	268.50	15.32	5.0	4.9	0.3	0.4	-0.0009
ICAM	269.47	19.85	1.3	1.2	0.4	0.4	-0.0003
ICHA	271.28	13.56	11.6	8.5	2.6	1.3	0.0000
IPA0	270.37	14.62	15.8	5.6	1.2	1.0	0.0000
ISCO	272.94	5.54	54.7	73.2	0.5	0.6	0.0003
ITUX	266.88	16.75	3.6	3.0	0.8	0.7	-0.0003
IXTA	269.73	14.18	9.4	6.4	4.6	2.8	0.0000
JAGU	271.29	15.10	15.4	5.9	1.1	0.7	0.0000
JALA	269.99	14.62	11.5	6.4	4.7	2.5	0.0000
JCFI	273.17	12.68	15.0	7.9	0.5	0.5	0.0003
JOY0	269.17	15.01	3.7	2.1	5.5	3.6	0.0000
JUCU	271.75	13.25	10.5	9.1	0.4	0.4	0.0001
LAGO	272.00	14.94	17.2	5.5	4.1	2.2	0.0000
LCAN	271.56	14.73	15.8	5.6	1.2	0.7	0.0000
LCEB	273.16	15.75	16.8	6.2	1.1	0.6	0.0001
LEME	273.09	12.43	10.4	12.3	0.8	0.5	0.0002
LEON	273.09	12.43	11.5	4.8	4.6	2.4	0.0000
LESP	271.84	14.31	16.2	5.7	1.6	0.9	0.0000
LJAS	272.25	13.60	16.8	6.2	0.5	0.4	0.0002
LNUB	270.22	13.90	6.6	8.8	0.9	1.0	-0.0001
LOLO	271.63	13.56	17.7	6.7	2.5	1.5	0.0000
LPIN	272.08	13.68	15.5	6.7	2.7	1.3	0.0000
LPZW	272.31	14.31	17.0	6.6	0.4	0.4	0.0003
LSSJ	271.80	13.38	9.3	10.8	4.2	2.0	0.0000
MALP	273.32	12.55	12.7	9.4	1.2	0.7	0.0001
MANA$^{\phi}$	273.75	12.15	13.1	8.0	0.3	0.3	0.0011
MAYA	270.87	14.84	15.2	6.2	0.5	0.6	-0.0001
MAZ0	268.45	14.54	6.9	6.1	0.9	0.7	-0.0002
MAZ2$^{\phi}$	268.45	14.54	7.1	4.2	1.0	0.8	-0.0001
MEZA	272.07	15.45	14.7	5.4	0.4	0.5	0.0001
MGL1	271.85	13.53	15.0	6.0	2.3	1.2	0.0000
MNGO	270.80	13.97	16.6	8.8	0.4	0.4	-0.0002
MNTO	273.62	14.92	17.6	5.3	1.2	0.7	0.0001
MOD0	270.77	15.93	1.2	0.9	1.1	0.6	0.0000
MON0	270.14	14.50	15.8	5.6	1.3	0.8	0.0000

MORO	273.08	13.60	16.1	6.6	1.2	0.7	0.0001
MOYU	269.92	14.03	8.1	5.4	4.6	2.4	0.0000
MPSC	267.11	15.46	4.2	4.9	0.8	0.5	-0.0004
MRLS	271.15	15.46	6.1	4.0	0.7	0.6	0.0000
MTP1	267.63	14.79	6.5	6.6	0.5	0.8	-0.0004
NAJO	272.38	15.56	16.5	5.6	7.4	3.8	0.0000
NARA	269.19	17.23	1.3	1.7	0.5	0.5	-0.0003
NDAM	272.64	13.68	16.6	6.4	1.2	0.7	0.0001
NOCO	270.80	14.44	17.6	9.3	1.1	0.7	0.0000
NONU	271.05	13.57	8.7	7.8	2.4	2.1	0.0000
OCOM	272.05	14.70	17.3	6.8	0.4	0.4	0.0002
OPAC	271.63	13.72	15.8	7.8	2.6	1.4	0.0000
OSIC	271.85	13.81	17.4	6.9	0.4	0.4	0.0001
PAM0	269.37	15.46	3.3	3.4	3.5	2.0	0.0000
PASA	272.17	13.59	15.7	6.2	2.5	1.8	0.0000
PAZC	273.41	12.29	11.0	8.7	1.1	0.7	0.0001
PCYA	269.36	14.41	10.0	5.9	0.9	0.7	-0.0001
PIN0	269.62	14.55	13.2	4.1	0.6	0.5	-0.0002
PIN2	269.61	14.55	10.8	5.3	4.5	2.5	0.0000
PLAY	270.65	13.79	11.7	9.4	4.2	3.5	0.0000
POCH	273.49	11.77	9.2	8.7	1.2	0.9	0.0001
POLS	273.19	12.65	14.1	8.3	0.6	0.6	0.0002
PONE	272.98	12.38	8.8	9.5	0.4	0.3	0.0005
POPT	270.59	16.33	1.7	1.8	0.5	0.5	-0.0001
PRT1$^{\phi}$	274.63	12.57	16.1	5.6	0.4	0.5	0.0008
PRUS	271.39	13.35	10.4	7.6	2.4	1.5	0.0000
PUEC	276.62	14.04	18.0	4.3	2.0	1.1	0.0001
QICH	268.85	15.03	4.3	-0.3	4.6	2.4	0.0000
QUE0	268.49	14.87	5.0	0.6	1.6	1.3	-0.0001
QUE1	268.49	14.87	5.5	2.6	0.3	0.3	-0.0013
QUEN	273.15	12.59	12.1	11.4	0.8	0.7	0.0002
RECA	272.85	13.33	17.2	5.7	0.4	0.4	0.0003
RIOB$^{\#}$	274.78	12.92	17.8	5.4	4.2	2.1	0.0000
ROA0$^{\phi}$	273.47	16.32	16.7	6.6	0.8	0.8	0.0001
ROG1	271.42	13.82	17.9	6.6	2.7	1.3	0.0000
ROSA	271.22	14.77	16.3	6.6	1.2	0.7	0.0000
ROTB	273.26	12.52	8.5	12.8	0.7	0.7	0.0002
RUB0	269.55	15.99	1.7	2.3	0.7	0.5	-0.0002
SABY	268.81	18.97	1.2	0.6	0.3	0.3	-0.0009
SAIN	272.18	13.32	15.5	6.9	0.4	0.4	0.0002
SAL0	269.72	15.08	5.4	2.3	0.8	0.5	-0.0002
SALN	273.14	12.62	14.4	11.7	0.8	0.7	0.0001

SAN0	278.28	12.58	19.2	4.6	0.5	0.5	0.0012
SAN2	269.75	14.82	11.5	3.2	0.8	0.5	-0.0002
SANA	278.27	12.52	19.5	5.2	0.6	0.5	0.0010
SAYA*	269.81	16.52	0.1	0.6	0.6	0.6	-0.0002
SBAR	271.65	13.63	16.3	6.9	2.5	1.4	0.0000
SCAR	271.92	13.64	17.1	6.2	2.8	1.6	0.0000
SCW2	272.98	12.70	12.2	9.2	0.8	0.8	0.0001
SELC	267.61	15.28	4.9	5.0	0.9	0.5	-0.0003
SFDP	273.76	14.97	19.3	6.0	2.5	1.3	0.0000
SGTO	272.94	13.10	16.0	6.3	0.4	0.4	0.0004
SIGN	270.68	13.49	5.5	13.7	3.4	2.0	0.0000
SJAN	271.79	14.82	16.7	8.6	0.4	0.4	0.0001
SJUL	273.41	14.14	16.6	4.7	4.1	2.2	0.0000
SLOR	272.56	13.42	17.3	4.0	0.4	0.3	0.0004
SMCO	271.05	14.40	17.8	6.3	1.9	1.2	0.0000
SMHO	268.19	14.95	6.3	4.2	0.9	0.9	-0.0002
SNJE	270.40	13.87	12.9	6.9	0.5	0.5	-0.0002
SNTA	272.05	14.07	16.9	7.0	0.4	0.4	0.0001
SOL0	268.51	15.57	2.9	3.7	0.8	0.5	-0.0003
SOLE	267.48	16.68	2.6	3.3	0.9	0.5	-0.0003
SSAS	270.95	13.45	7.9	9.7	0.5	0.5	-0.0001
SSIA	270.88	13.70	15.4	7.1	0.4	0.4	-0.0001
SUNZ	270.61	13.50	5.2	9.7	0.5	0.6	-0.0001
SVCI	271.21	13.64	12.2	8.1	0.8	0.9	0.0000
SVIC	271.21	13.63	13.2	9.8	2.6	1.7	0.0000
TACA	270.65	13.97	16.0	7.2	3.1	2.2	0.0000
TAXI	269.53	14.03	8.1	8.9	0.6	0.8	-0.0001
TECF	273.16	12.60	10.9	11.7	0.6	0.6	0.0002
TECP	269.01	14.76	5.4	3.1	0.8	0.7	-0.0002
TEG2	272.79	14.09	16.9	6.6	0.6	0.6	0.0002
TEGU	272.79	14.09	16.2	6.5	0.4	0.3	0.0005
TEJU	270.90	14.18	14.4	7.0	3.3	2.1	0.0000
TELN	273.17	12.61	12.0	9.7	0.6	0.5	0.0002
TEUS$^{\phi}$	274.19	12.41	15.9	2.7	1.8	1.1	0.0001
TGIG	266.88	16.78	2.0	2.7	1.2	1.1	-0.0001
THIG	267.70	14.88	7.5	7.9	1.1	1.0	-0.0001
TIKA	270.39	17.22	2.4	2.6	0.8	0.8	-0.0001
TINT	270.12	15.32	3.8	0.5	0.9	1.8	0.0000
TNPJ	266.78	15.70	3.6	3.2	1.0	1.2	-0.0001
TONU	273.16	13.93	16.6	5.8	1.2	0.8	0.0001
TOTO	268.67	15.02	3.6	3.1	4.6	2.4	0.0000
TPCH	267.70	14.88	6.4	7.1	0.7	0.7	-0.0003

TRAN[ϕ]	273.31	12.03	9.4	8.6	1.0	0.7	0.0001
USP0	269.13	15.35	1.8	-1.5	3.6	1.9	0.0000
USUL	271.52	13.38	9.5	5.7	2.6	1.4	0.0000
UVGS	268.81	14.79	2.1	1.9	4.7	2.5	0.0000
VIEJ[♯]	271.01	13.51	11.5	7.4	1.3	1.0	0.0000
VIKH	295.20	17.72	19.1	5.2	0.3	0.4	0.0071
VILL	267.09	18.00	0.8	2.1	0.5	0.4	-0.0007
VMIG	271.70	13.40	12.0	8.1	0.9	0.7	0.0000
ZAC0	270.50	14.98	12.5	5.0	0.9	0.6	-0.0001
ZACA	270.64	15.11	12.3	5.3	0.7	0.7	-0.0001
ZAPO	270.17	14.14	10.9	8.8	4.6	2.5	0.0000

Notes: East (V_e) and north (V_n) components of site velocities are given relative to the North America plate are in unites of millimeters per year. Uncertainties are standard errors. The correlation coefficient specifies the dependence between the east and north velocity uncertainties.

*identifies sites whose velocities were determined solely with pre-May 2009 data due to unsatisfactory fit of the time-dependent TDEFNODE mode in Part 1 of the study

[♯] identifies sites whose velocities are not used in the block modeling inversion due to too short of time-series

[ϕ] identifies sites whose velocities are not used in the block modeling invesion due to effects on stable Caribbean plate angular velocity or highy ananomous velocity

Table 3.2 Best-fitting angular velocities

Moving	Fixed	Lat.	Long.	ώ	Variances and covariances					
plate	plate	(°N)	(°E)	(° Myr^{-1})	σ_{xx}	σ_{yy}	σ_{zz}	σ_{xy}	σ_{xz}	σ_{yz}
NOAM	ITRF08	-6.9	271.4	0.184	0.00001	0.00042	0.00023	-0.00001	0.00001	-0.00030
CARI	ITRF08	37.0	258.7	0.254	0.00265	0.03498	0.00370	-0.00741	0.00208	-0.00953
CARI	NOAM	74.8	201.0	0.181	0.00266	0.03540	0.00393	-0.00742	0.00209	-0.00982
COCO	NOAM	31.0	226.3	1.073	0.34	0.48	0.39	-0.05	-0.28	-0.08
COCO*	CARI*	23.3	227.6	0.955	0.34	0.44	0.38	-0.04	-0.28	-0.07
COCO	CAFS	31.6	188.9	0.665	0.35	7.60	0.70	-0.03	-0.26	-1.45
CAFS	CARI	2.9	-93.2	0.562	0.01	7.15	0.32	0.01	0.02	-1.37
CAFS	NOAM	19.3	-97.4	0.617	0.02	7.19	0.32	0.00	0.02	-1.38
CHRT	CAFS	3.5	-92.1	0.506	0.03	13.02	0.68	-0.18	0.07	-2.81
CHRT	CARI	-2.1	-102.8	0.057	0.02	5.38	0.34	-0.19	0.05	-1.34
CHRT	NOAM	61.9	-128.0	0.196	0.01	5.24	0.33	-0.16	0.04	-1.31

The Cocos-Caribbean angular velocity is the MORVEL estimate from DeMets *et al*. (2010). Angular rotation rates ώ are positive anti-clockwise. The angular velocity covariances are Cartesian and have units of 10^{-4} $degrees^2$ Myr^{-2}. Abbreviations are as follows: CAFS - Central America forearc sliver; CARI - Caribbean plate; CHRT - Chortis block; COCO - Cocos plate; ITRF08 - International Terrestrial Reference Frame 2008; NOAM - North America plate. Angular velocities for the Ipala, Fonseca, and Motagua-Polochic blocks are omitted due to large uncertainties in two of their three angular velocity components.

FIGURES

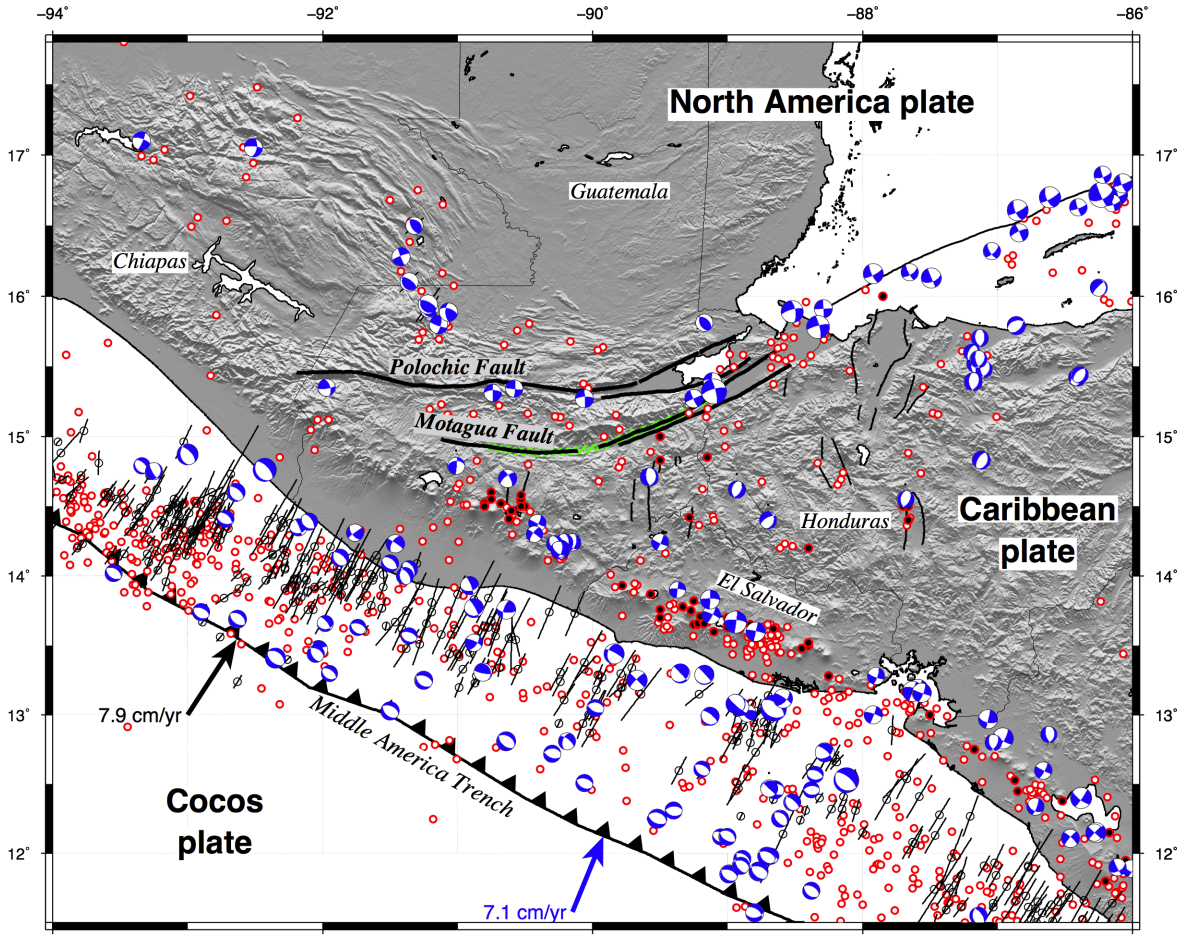

Figure 3.1. Topography, earthquake epicenters, and earthquake focal mechanisms in northern Central America. Focal mechanisms include all global centroid-moment tensor solutions for 1976 to mid-2016, and pre-1976 focal mechanisms from Molnar and Sykes (1969), Guzman-Speziale *et al.* (2010), and White and Harlow (1993). Red/white and red/black circles show earthquake epicenters respectively from the 1964-2008 International Seismological Centre catalog for 1964 to 2008 and the Guzman-Speziale *et al.* (2005) compilation for historic earthquakes since 1586. The green-patterned region shows the rupture limits of the 1976 M_w=7.5 Motagua Fault earthquake. For clarity, focal mechanisms for offshore earthquakes are shown only for normal-faulting and strike-slip earthquakes. Information about the offshore subduction-thrust earthquakes is limited to P-axis orientations (black lines) that we determined from their focal mechanisms. Black and blue vectors show Cocos Plate velocities relative to the North America and Caribbean plates, respectively (DeMets *et al.* 2010).

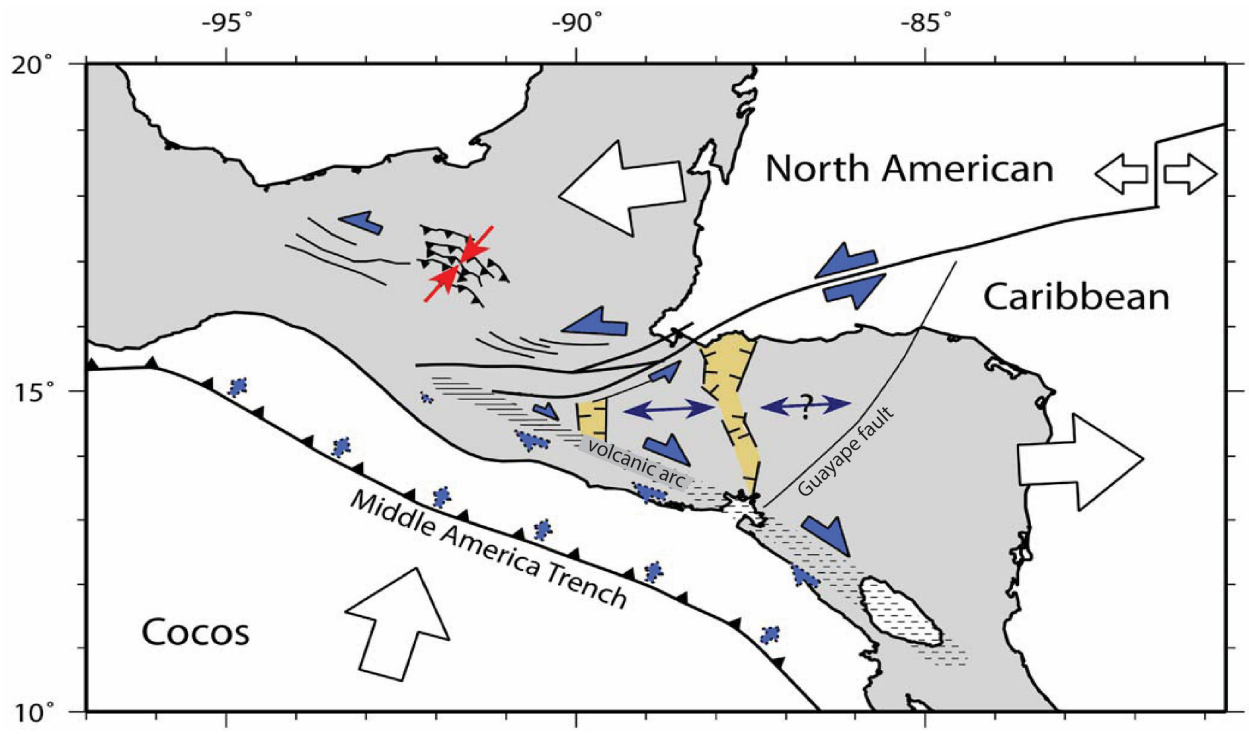

Figure 3.2. Conceptual model for forces that may determine the present deformation in northern Central America. Figure is from Rodriguez *et al.* (2009). Colored arrows approximate relative motions across the major faults in the study area and open arrows approximate the directions of motion of the major plates relative to a fixed mantle reference frame. Arrows are not drawn to scale. Hatched region denotes Central America volcanic arc region. Yellow shading represents areas within north-south trending grabens in southern Guatemala and Honduras.

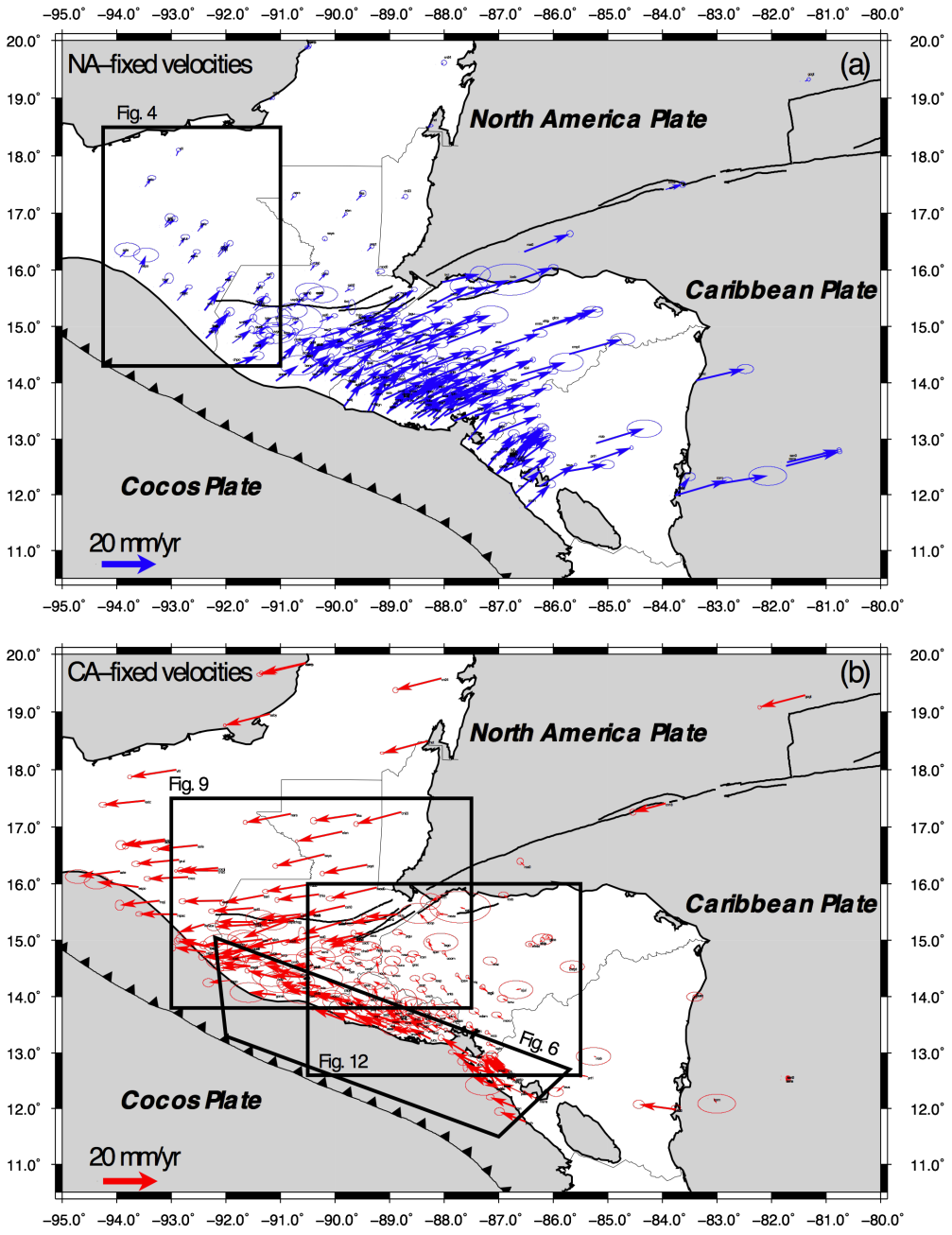

Figure 3.3. New GPS station velocities relative to the North America plate (a) and Caribbean plate (b). All velocities are corrected for estimated coseismic offsets and afterslip transients from the Swan Islands, El Salvador, and Champerico earthquakes. Boxes identify regions shown in other figures in this study.

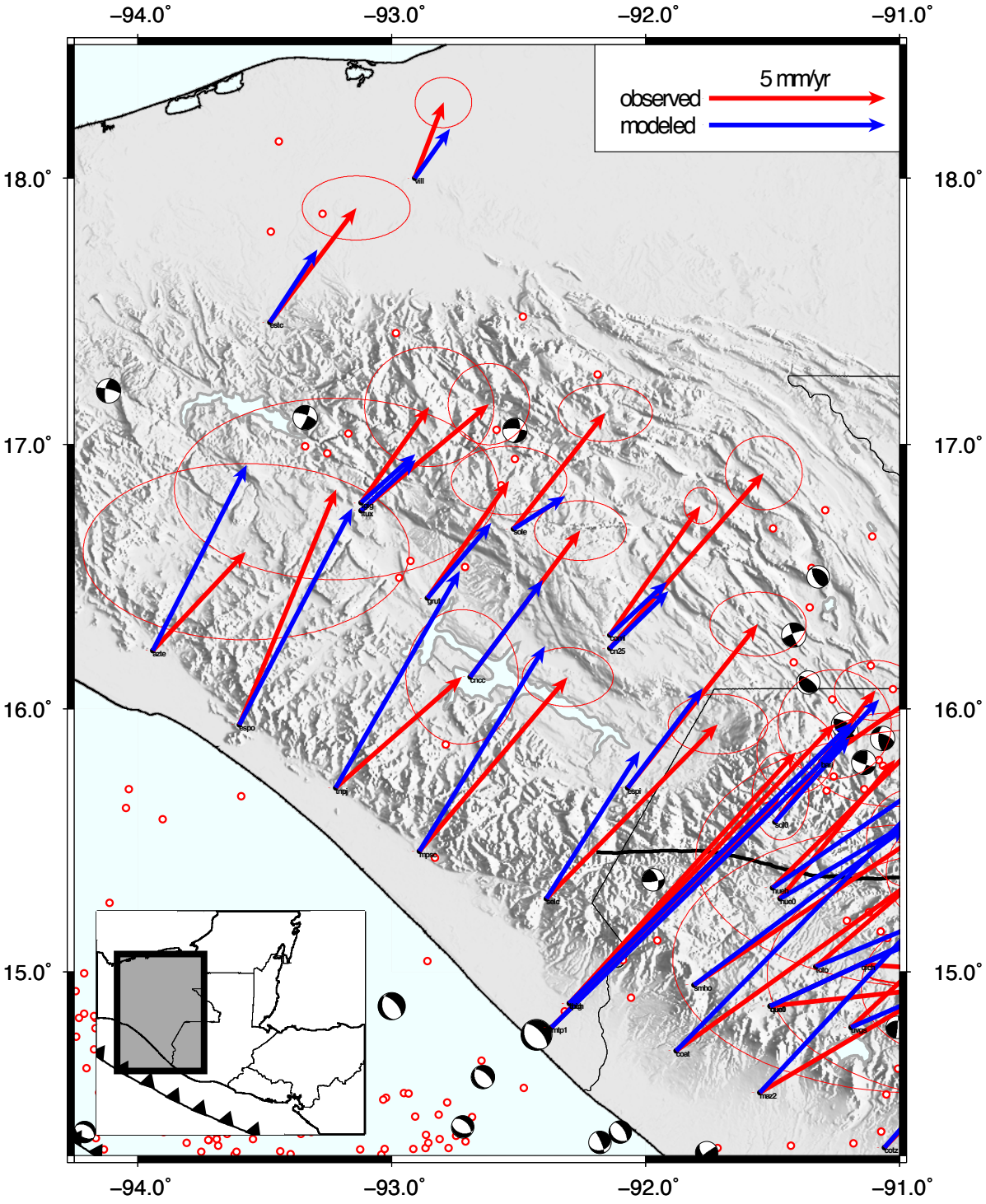

Figure 3.4. Observed (red arrows) and model estimated (blue arrows) GPS station velocities in Chiapas (southern Mexico) relative to the North America plate with 1-σ velocity uncertainty ellipses. Red and white circles show earthquake epicenter from the 1964-2008 International Seismological Centre catalog for 1964 to 2008 and the Guzman-Speziale *et al*. (2005) compilation for historic earthquakes since 1586. See Fig. 3.1 for focal mechanism details. The name for each site is visible upon magnification of the figure.

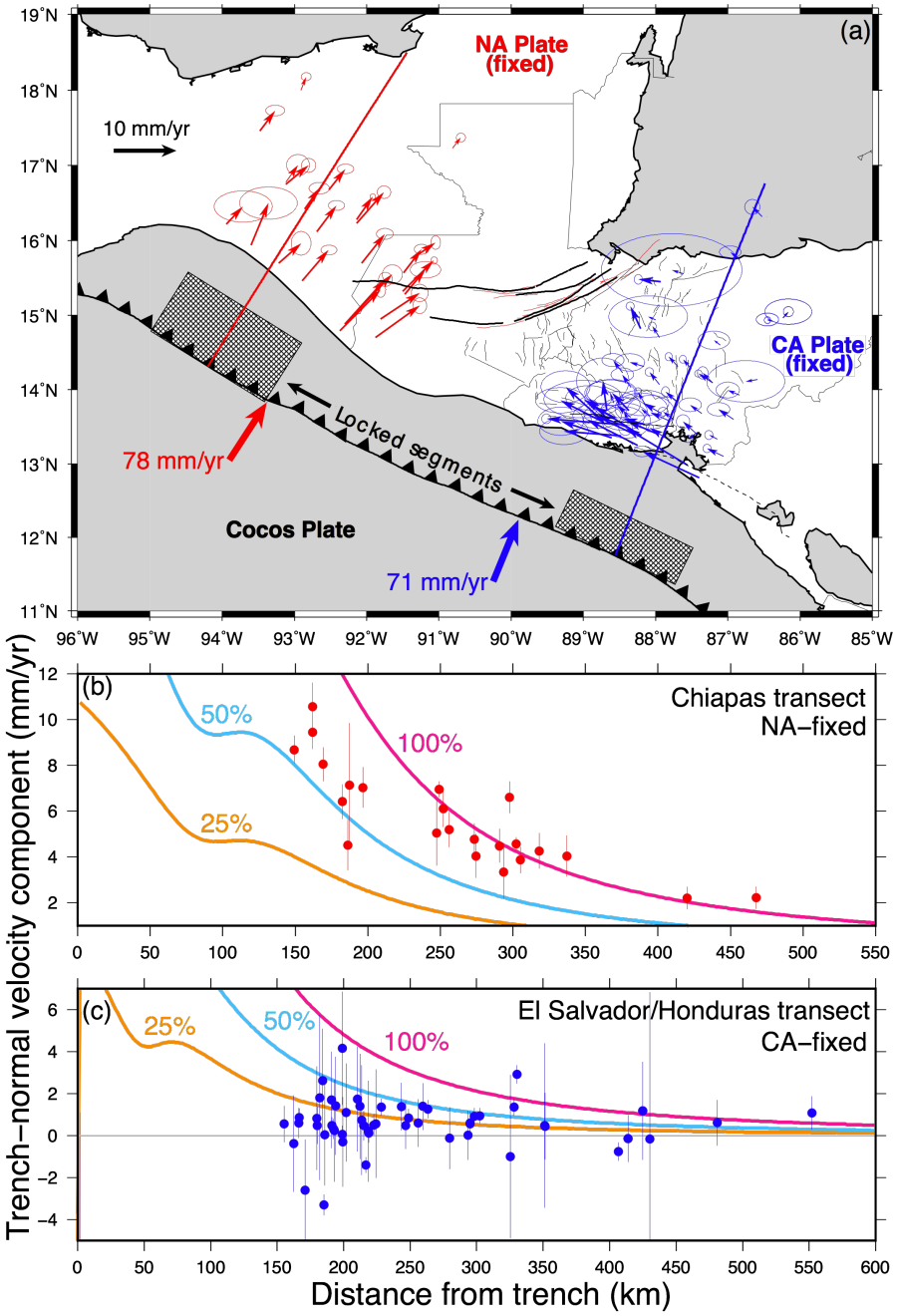

Figure 3.5. GPS velocity transects with velocities rotated onto N31.9°E (b) and N21.6°E (c), approximately perpendicular to the Middle America trench off the western coast of northern Central America. GPS velocities relative to North America (red) and Caribbean (blue) are subdivided into transects of Chiapas (southern Mexico) and El Salvador/Honduras, respectively. The colored curves show velocities predicted from forward elastic half-space models that assume 25%, 50%, and 100% locking of the subduction interface to depths of 40 km offshore from Chiapas and 20 km offshore from El Salvador (locked areas are indicated by the shaded region in panel (a)).

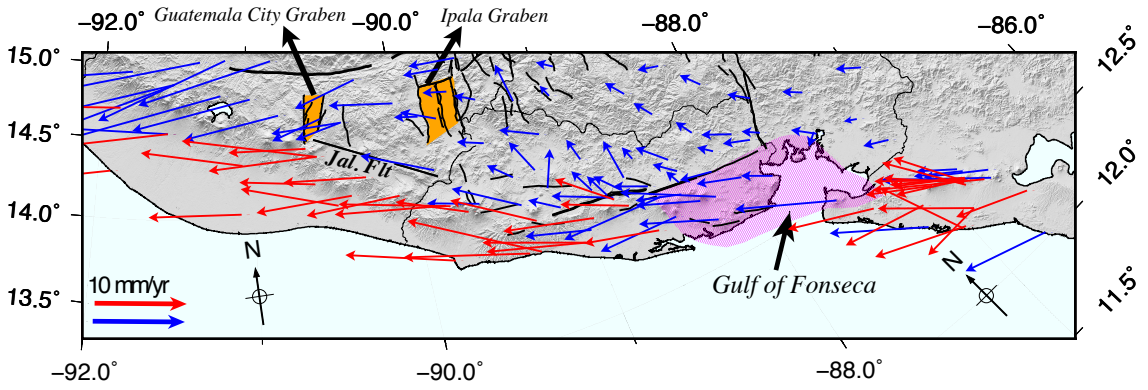

Figure 3.6. Oblique Mercator projection of El Salvador and southwest Guatemala centered on the pole (89.3°W, 13.7°N) that best fits the directions of the 41 forearc sites (red arrows) relative to the Caribbean plate. Orange shaded regions show the locations of the Guatemala City and Ipala grabens, and the magenta shaded region identifies the Gulf of Fonseca block. Fault name abbreviation: Jal. Flt, Jalpatagua Fault.

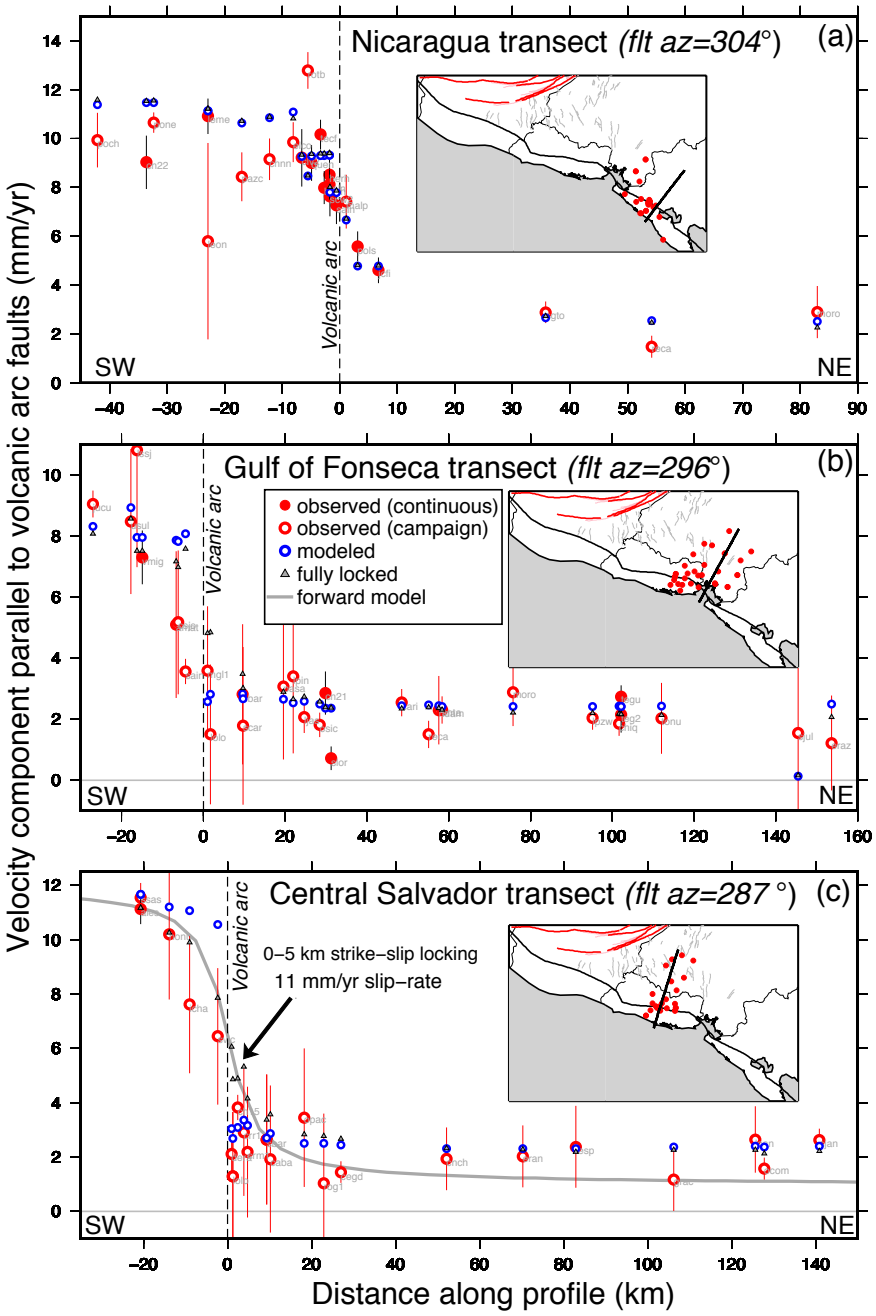

Figure 3.7. GPS velocity transects of Nicaragua (a), Gulf of Fonseca (b), and central El Salvador (c) rotated onto N56°W, N64°W, and N73°W, respectively, locally parallel to fault in the Central America volcanic arc. Transect locations are shown in inset maps. Filled and open red circles denote observed velocities from continuous and campaign GPS sites, respectively, with 1-sigma uncertainties. Blue open circles denote our best-fitting model velocity estimates. Small gray triangles are model velocity estimates for a fully locked volcanic arc. GPS velocities are relative to the Caribbean plate. Solid gray curve shows velocities predicted from elastic forward model that assumes 100% locking of the fault interface to a depth of 5 km. Vertical dashed lines show volcanic arc fault locations along the transects. The name for each site is visible upon magnification of the figure.

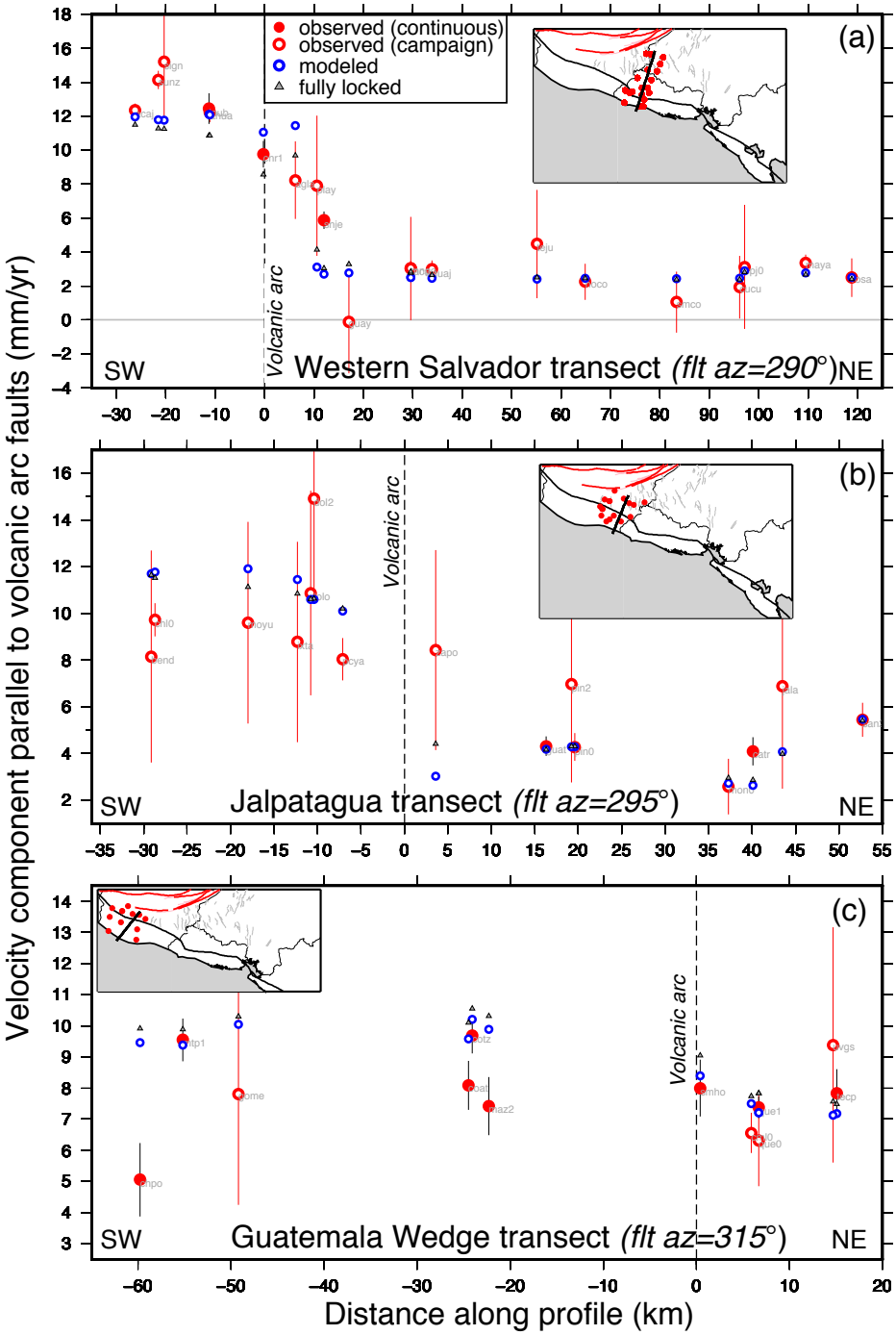

Figure 3.8. GPS velocity transects of Western Salvador (a), Jalpatagua (b), and Guatemala Wedge (c) rotated onto N70°W, N65°W, and N45°W (respectively), locally parallel to faults in the Central America volcanic arc. Transect locations are shown in inset maps. Filled and open red circles denote observed velocities from continuous and campaign GPS sites, respectively, with 1-sigma uncertainties. Blue open circles denote our best-fitting model velocity estimates. Small gray triangles are model velocity estimates for a fully locked volcanic arc. GPS velocities are relative to the Caribbean plate. Vertical dashed lines volcanic arc location along the transects.

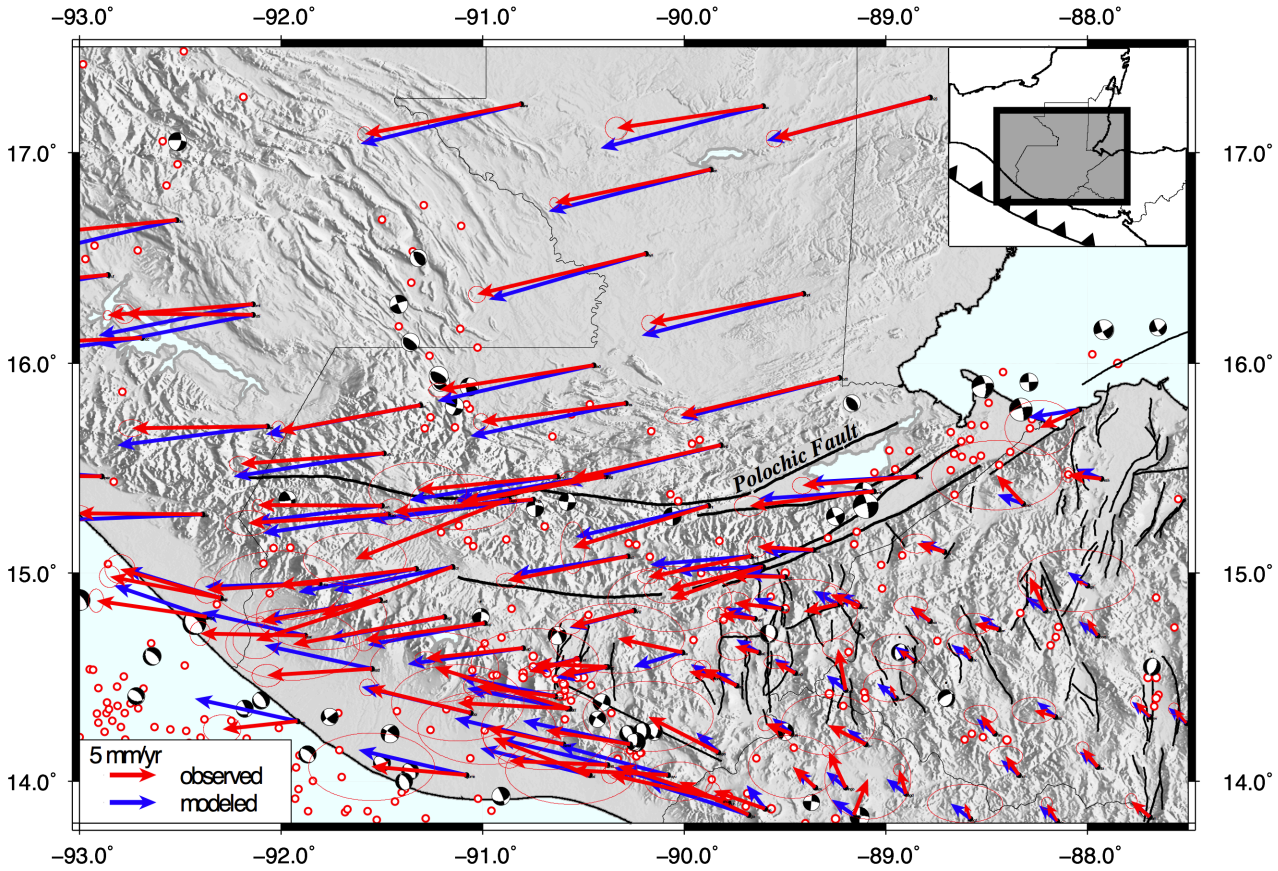

Figure 3.9. Observed (red arrows) and model estimated (blue arrows) GPS station velocities in Guatemala relative to the Caribbean plate with 1-σ velocity uncertainty ellipses. Red and white circles show earthquake epicenter from the 1964-2008 International Seismological Centre catalog for 1964 to 2008 and the Guzman-Speziale *et al*. (2005) compilation for historic earthquakes since 1586. See Fig. 3.1 for focal mechanism details. The name for each site is visible upon magnification of the figure.

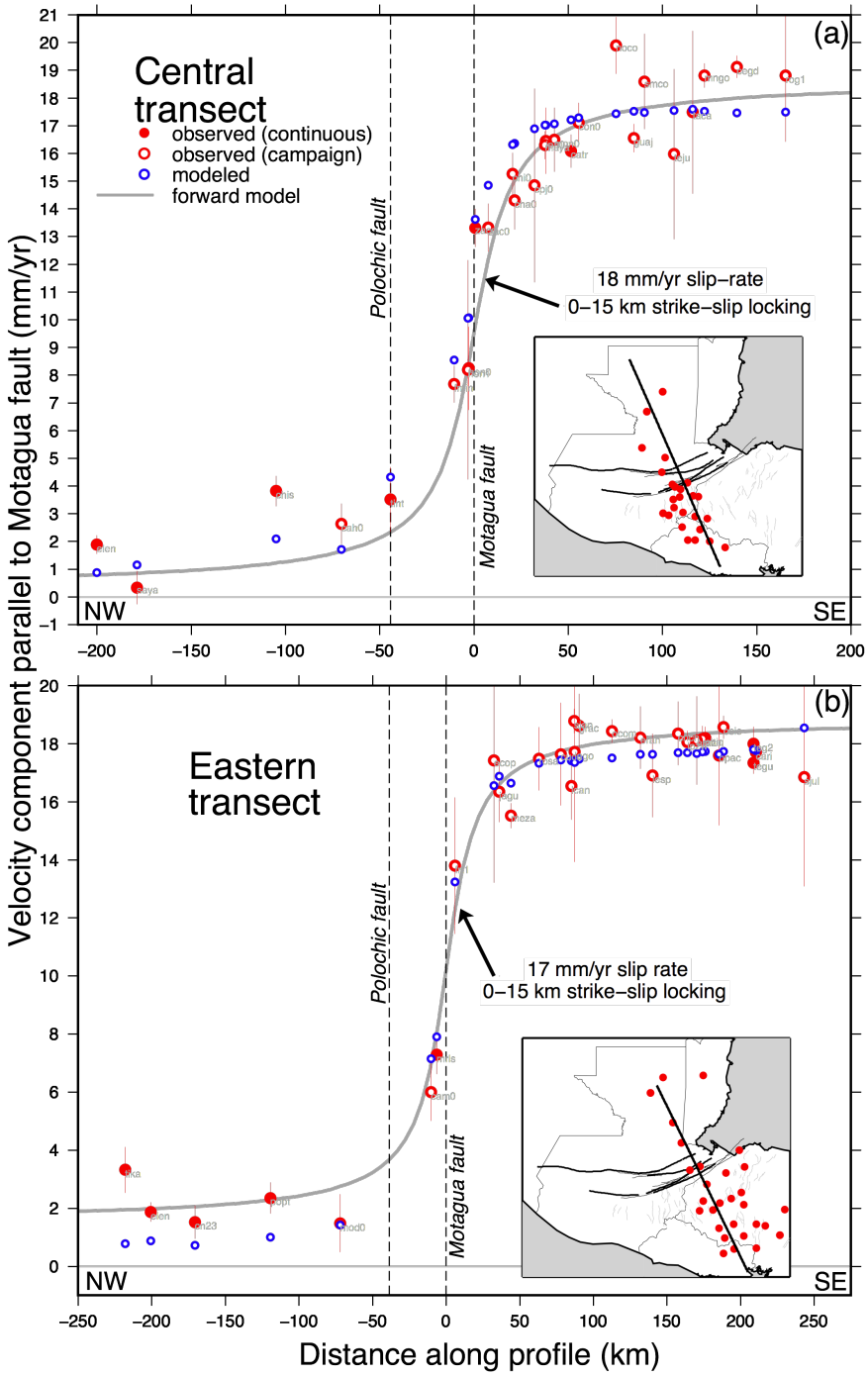

Figure 3.10. GPS velocity transects of the central (a) and eastern (b) segments of the Motagua-Polochic fault system. Velocities are rotated onto N60.5°E (a) and N62°E (b), locally parallel to the faults. Filled and open red circles denote observed velocities from continuous and campaign GPS sites, respectively. Blue open circles denote our best-fitting model velocity estimates. GPS velocities are relative to the North America plate. Solid gray curve shows velocities predicted from forward model that assumes 100% locking of the Motagua fault interface to depth of 15 km. Vertical dashed lines show Polochic and Motagua fault locations along the transects. The name for each site is visible upon magnification of the figure.

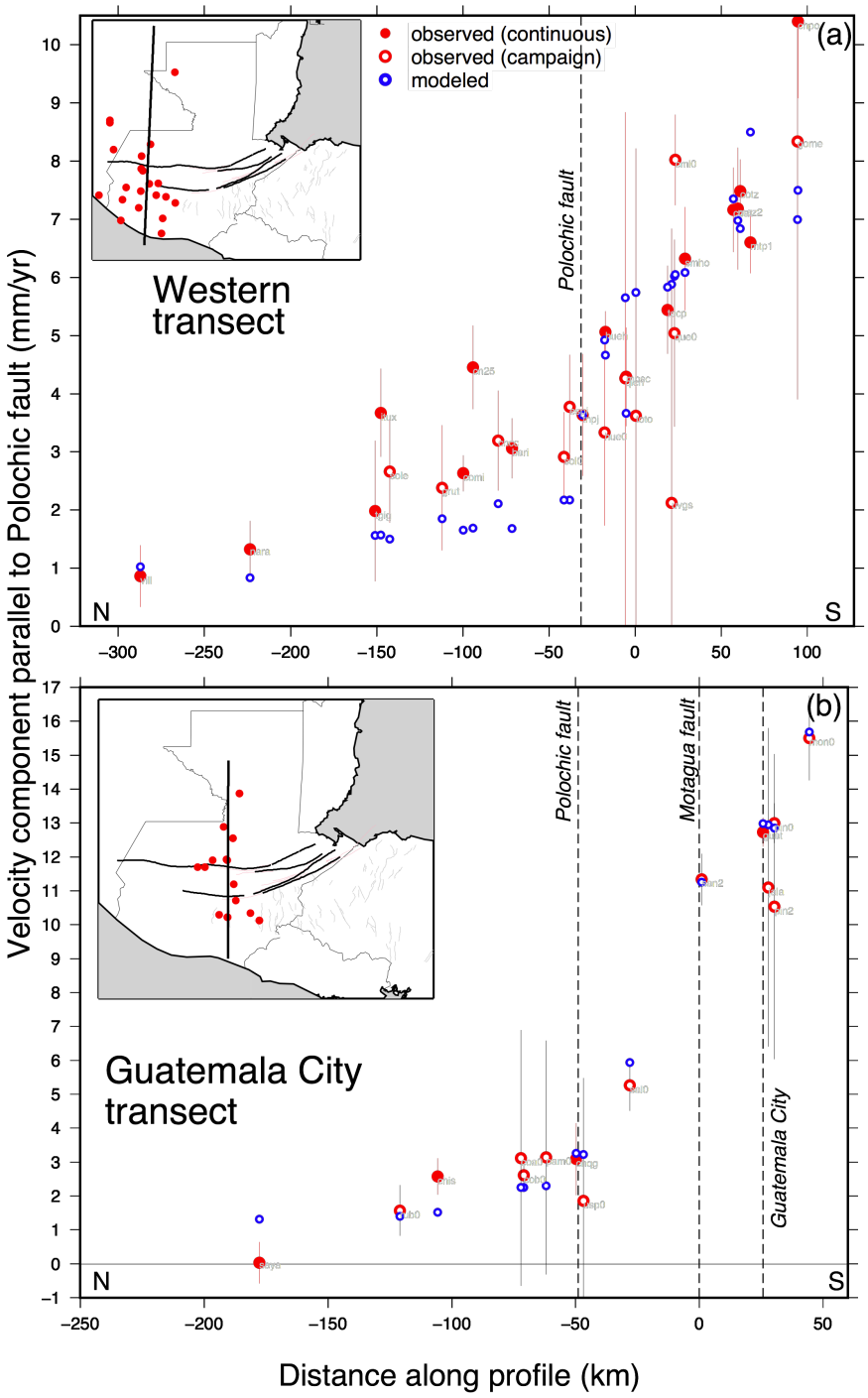

Figure 3.11. GPS velocity transects of the western (a) and Guatemala City (b) segments of the Motagua-Polochic fault system. Velocities are rotated onto N89°E (a) and S93°E (b), locally parallel to the faults. Filled and open red circles denote observed velocities from continuous and campaign GPS sites, respectively. Blue open circles denote our best-fitting model velocity estimates. GPS velocities are relative to the North America plate. Vertical dashed lines show Polochic and Motagua fault locations along the transects. The name for each site is visible upon magnification of the figure.

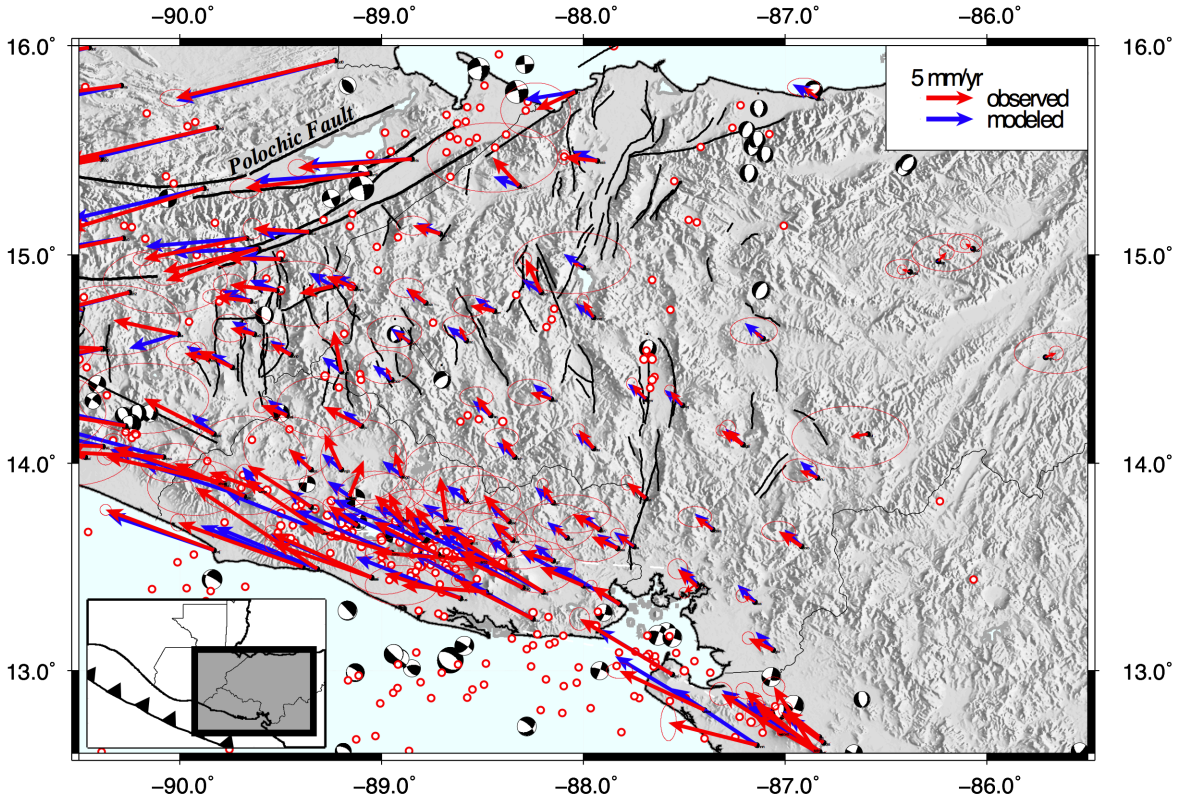

Figure 3.12. Observed (red arrows) and modeled (blue arrows) GPS station velocities in Honduras and El Salvador relative to the Caribbean plate with 1-σ velocity uncertainty ellipses. Red and white circles show earthquake epicenters from the 1964-2008 International Seismological Centre catalog for 1964 to 2008 and the Guzman-Speziale *et al*. (2005) compilation for historic earthquakes since 1586. The name for each site is visible upon magnification of the figure.

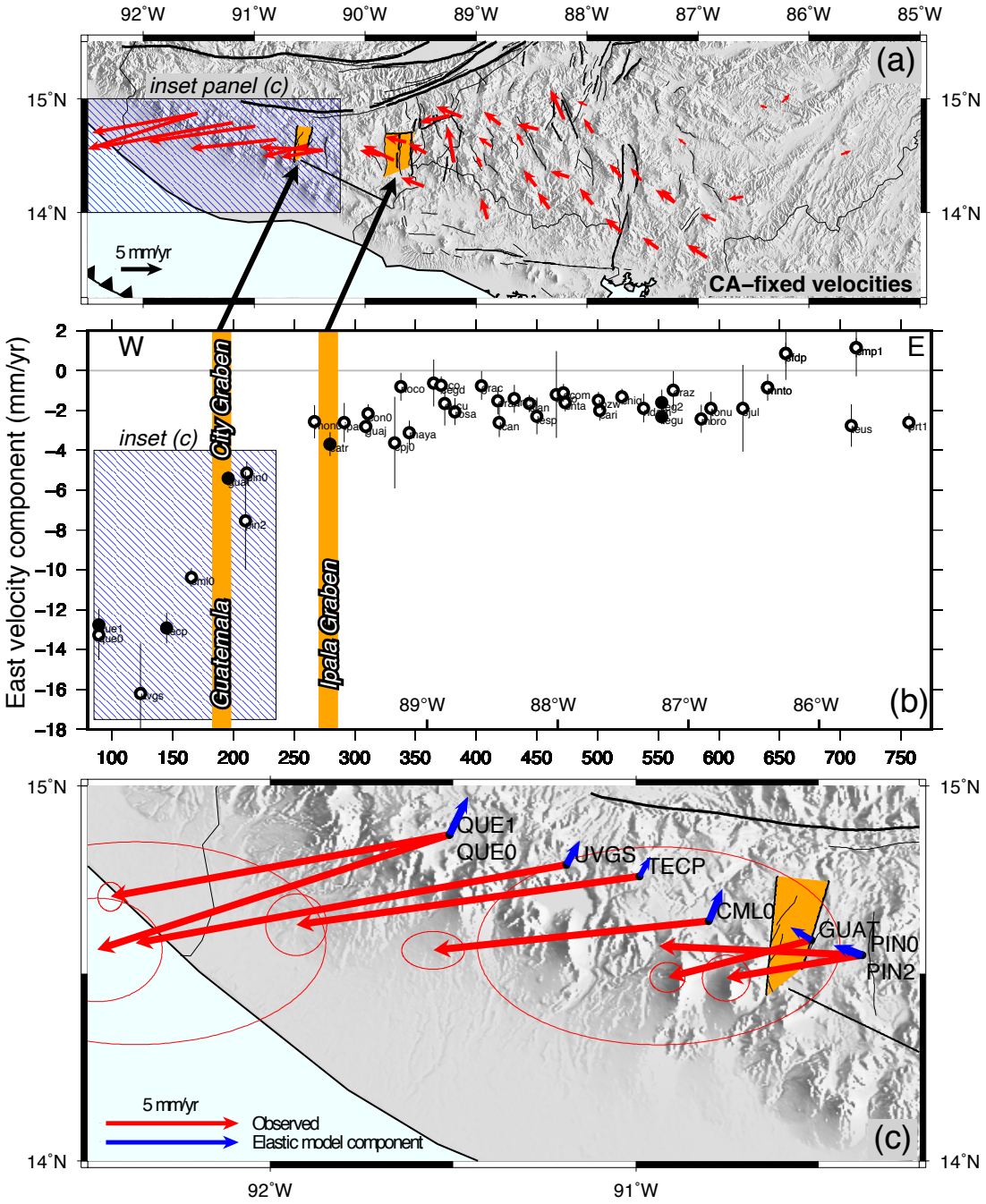

Figure 3.13. Velocities of GPS sites in an east-to-west transect of the Honduras and southern Guatemala extensional zones between the Motagua fault and volcanic arc. (a) Map showing topography, GPS horizontal velocities, and Guatemala City and Ipala, north-south trending grabens (orange). East (b) component of the GPS site velocities to the Central America grabens are shown along a west to east profile. Filled and open circles denote velocities from continuous and campaign GPS sites, respectively. Vertical shaded regions show where the Guatemala City graben (orange) and the Ipala graben (orange) intersect the profiles. Panel (c) shows detail of GPS site velocities, both observed and elastic model component vectors, west of the Guatemala City graben. GPS velocities are relative to the Caribbean plate. Uncertainties are 1-σ.

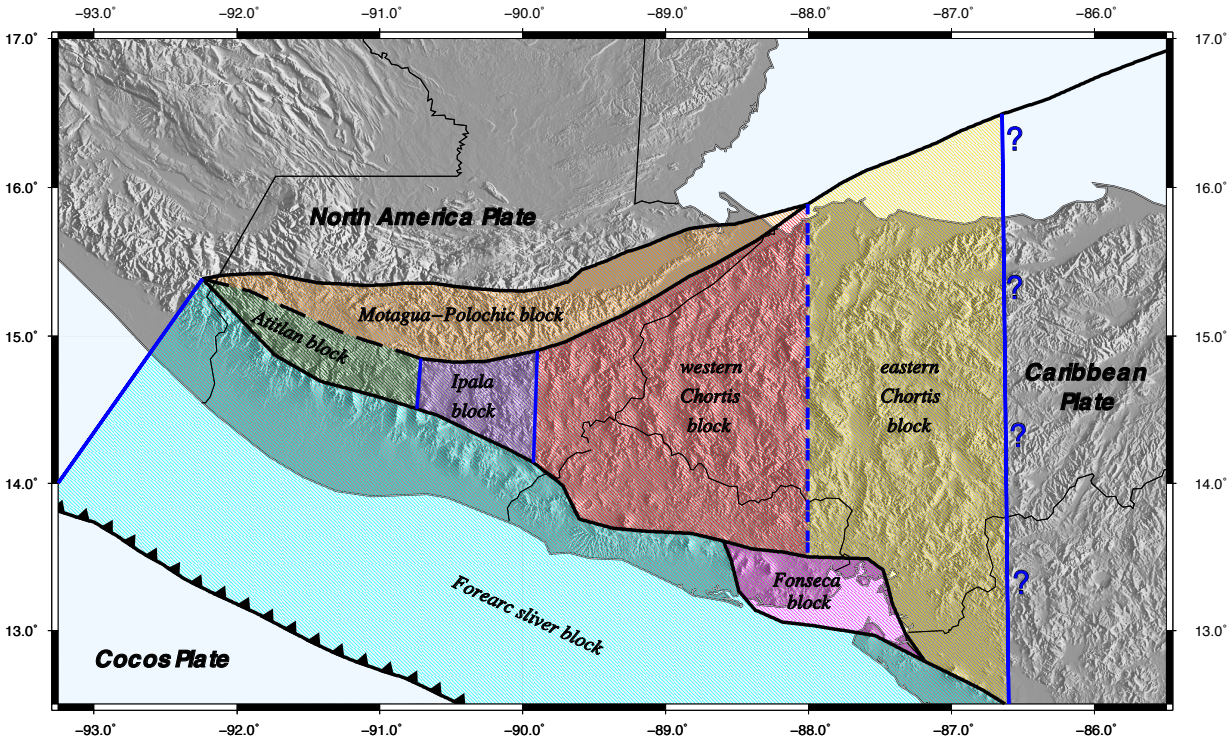

Figure 3.14. The most complex tectonic block configuration considered in this study. Color shaded interiors show block boundaries. Tectonics plates are also considered block boundaries, and their areas extend beyond the map's extent. Heavy black lines are block boundaries where locking is applied. Blue lines are free-slip block boundaries. Dashed lines indicate block boundaries that are not used in best-fitting model. Block names are shown in bold italics. Blue line with question marks denotes a free-slip boundary that approximates the eastern edge of the geodetically-defined Chortis block.

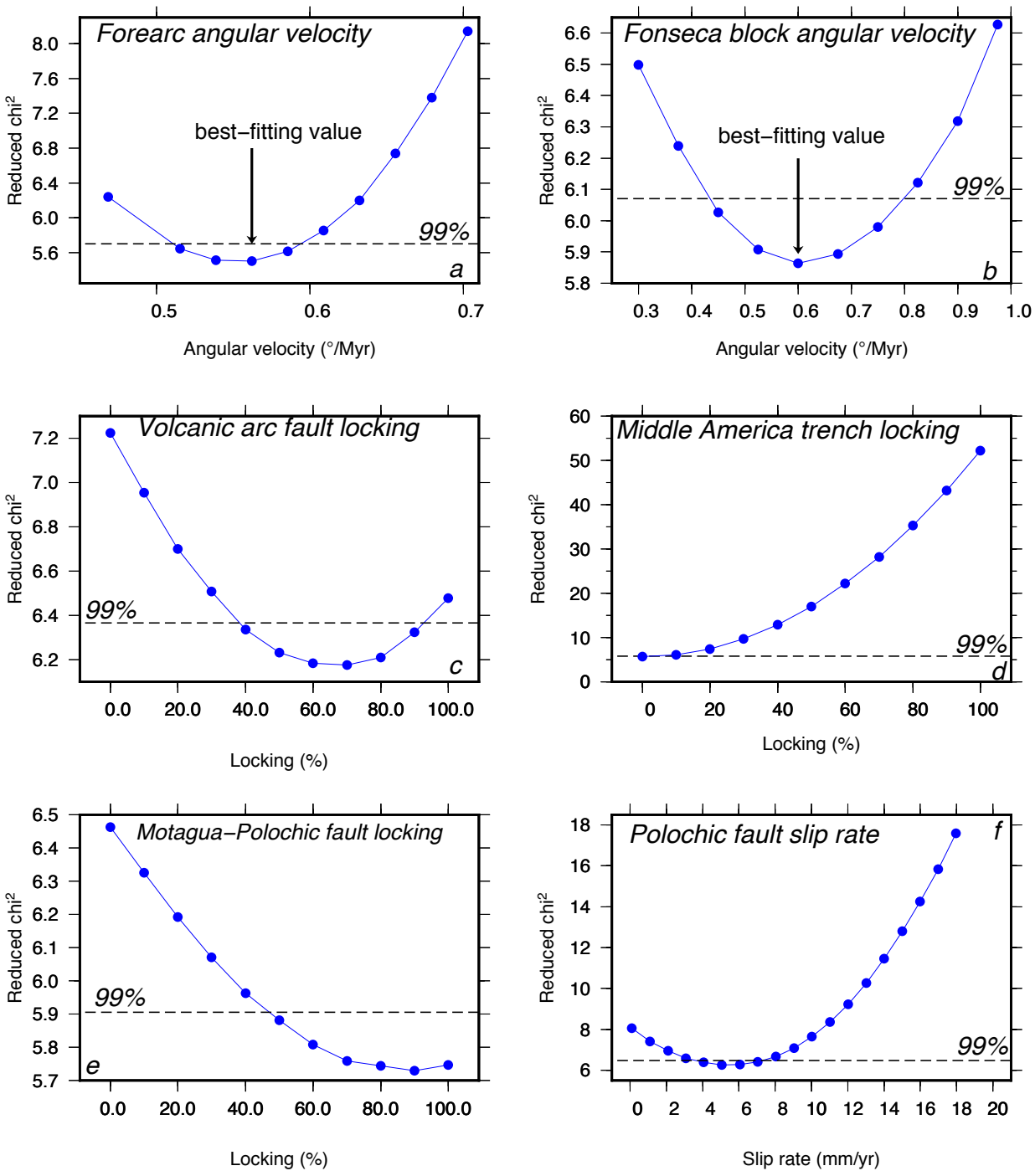

Figure 3.15. Variations in our reduced chi-square fits of TDEFNODE models to the 209 GPS site velocities as a function of different assumed values for a) the angular rate for the forearc relative to the Caribbean plate, b) the angular rate for the Fonseca block relative to the Caribbean plate, c) uniform locking of faults in the Central America volcanic arc, d) uniform locking of the upper 20 km of the Middle America subduction interface, e) uniform locking along the Motagua and Polochic faults, and f) the slip rate across the Polochic fault. Dashed horizontal lines show the 99 per cent confidence limit for each parameter based on an F-ratio test.

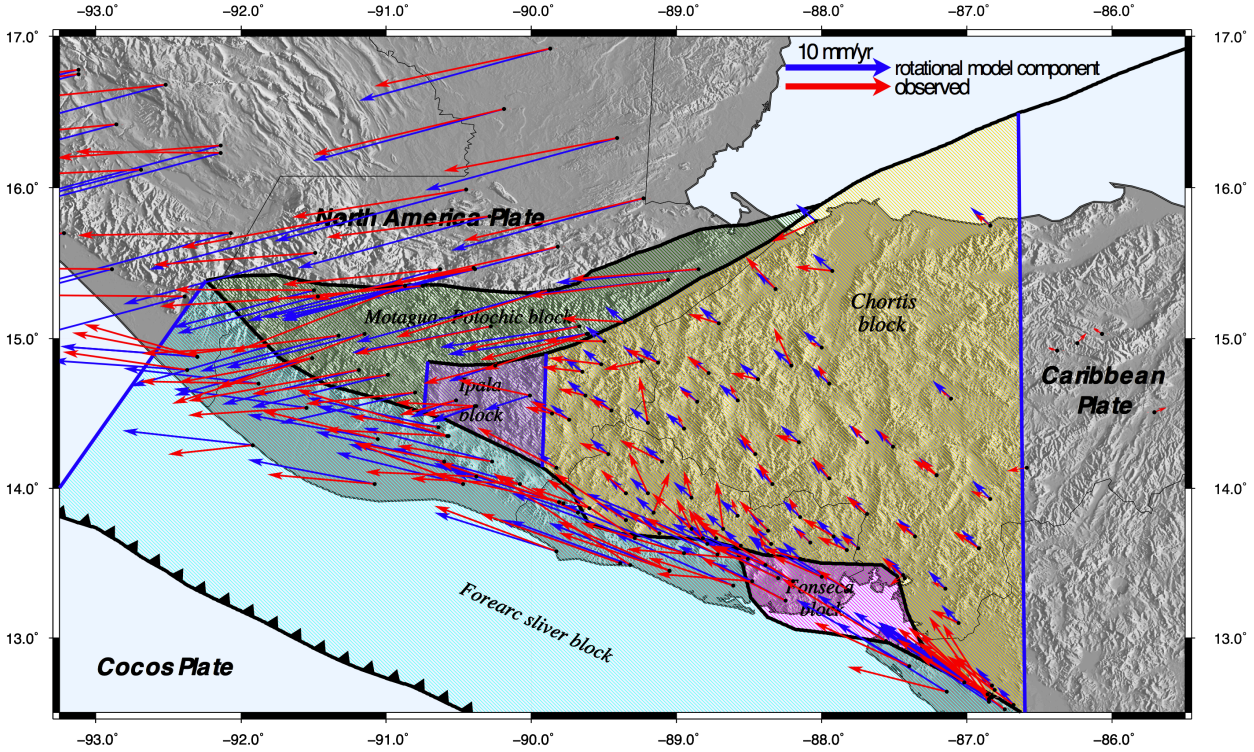

Figure 3.16. Observed GPS station velocities (red arrows) and rotational velocity component for best-fitting model (blue arrows) relative to the Caribbean plate. Color shaded interiors show block boundaries for the best-fitting model. Tectonics plates are also considered block boundaries, and their areas extend beyond the map's extent. All elastic effects have been estimated and removed from the modeled site motions, thereby isolating the long-term plate or block rotations for this figure. Dashed blue line with question marks denotes a free boundary that approximates the eastern edge of the geodetically-defined Chortis block

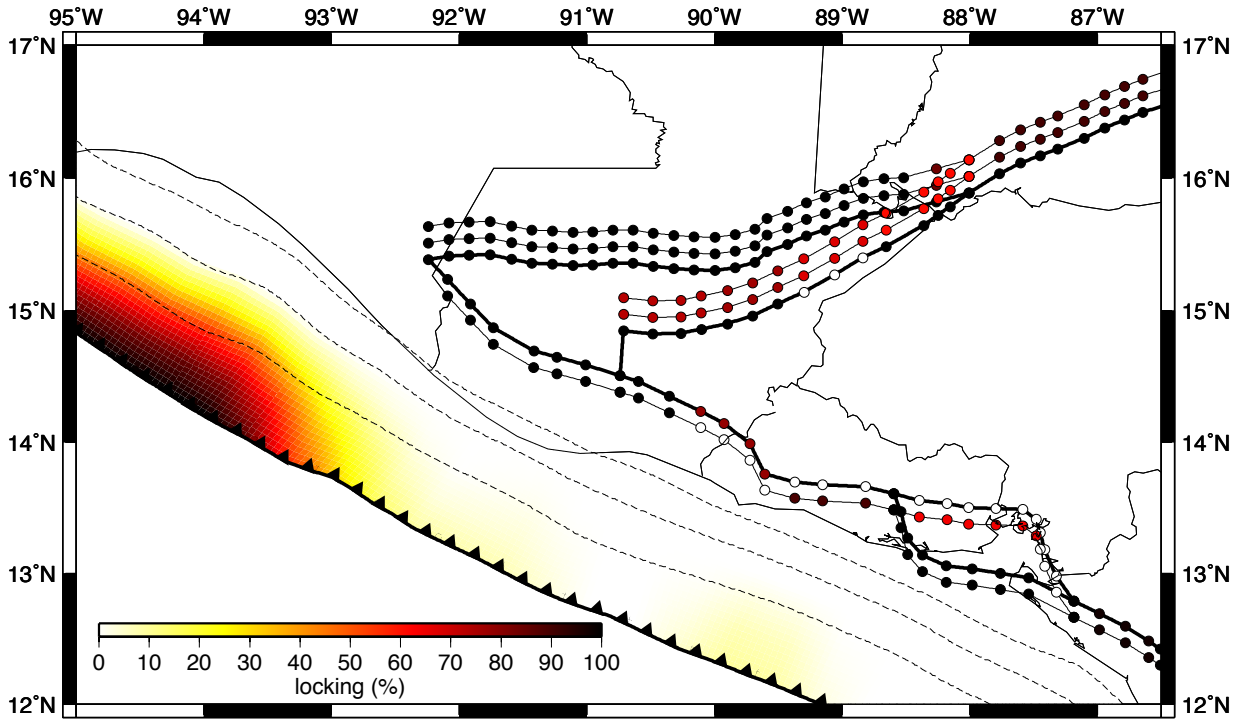

Figure 3.17. Best-fitting estimates of interseismic locking for faults along the Central America volcanic arc, the Motagua and Polochic faults, and the Middle America trench. Bold lines mark the model block boundaries. Thin lines connect fault nodes along strike and/or downdip. Along the Motagua and Polochic faults, the uppermost, intermediate, and bottom lines of connected fault nodes represent locking at respective depths of 0-5 km, 5-10 km, and 10-15 km. Along the volcanic arc, the top and bottom nodes show locking for 0-5 km and 5-10 km, respectively. Dashed lines denote subduction slab contours spaced every 20-km in depth.

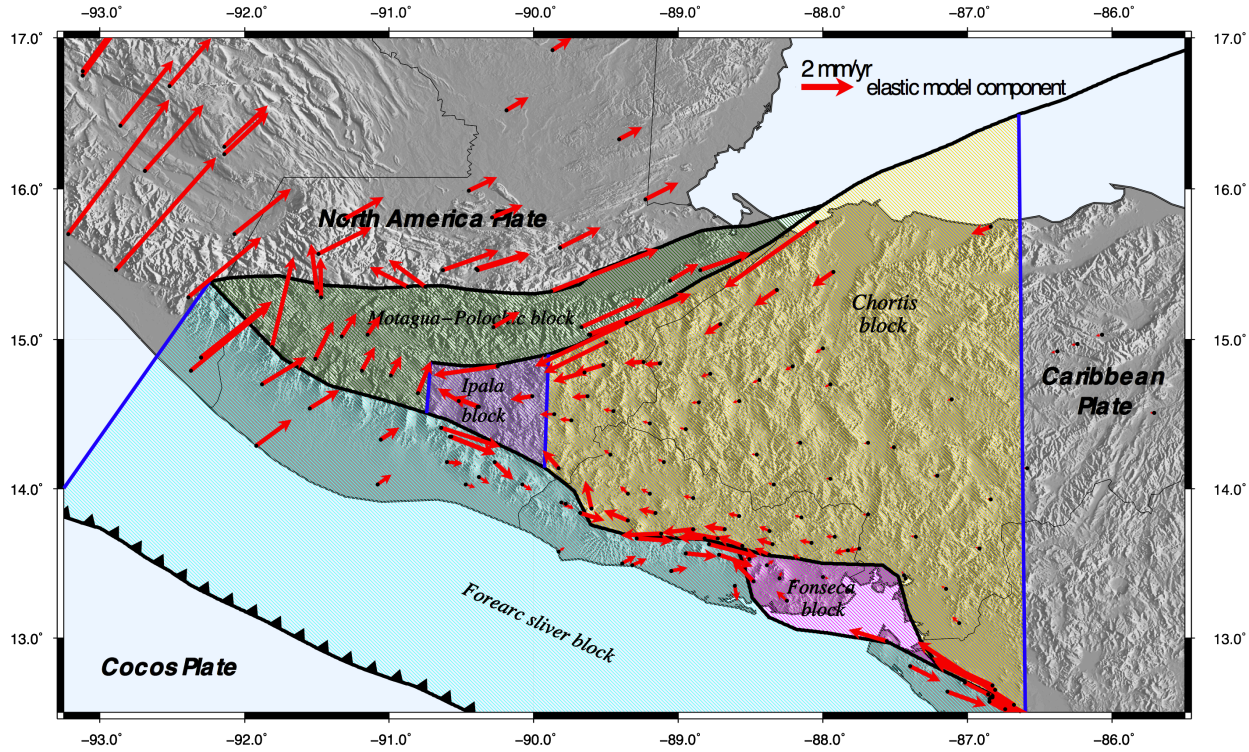

Figure 3.18. Elastic velocity component for best-fitting model (red arrows; frame independent). Dashed blue line with question marks denotes a free boundary that approximates the eastern edge of the geodetically-defined Chortis block.

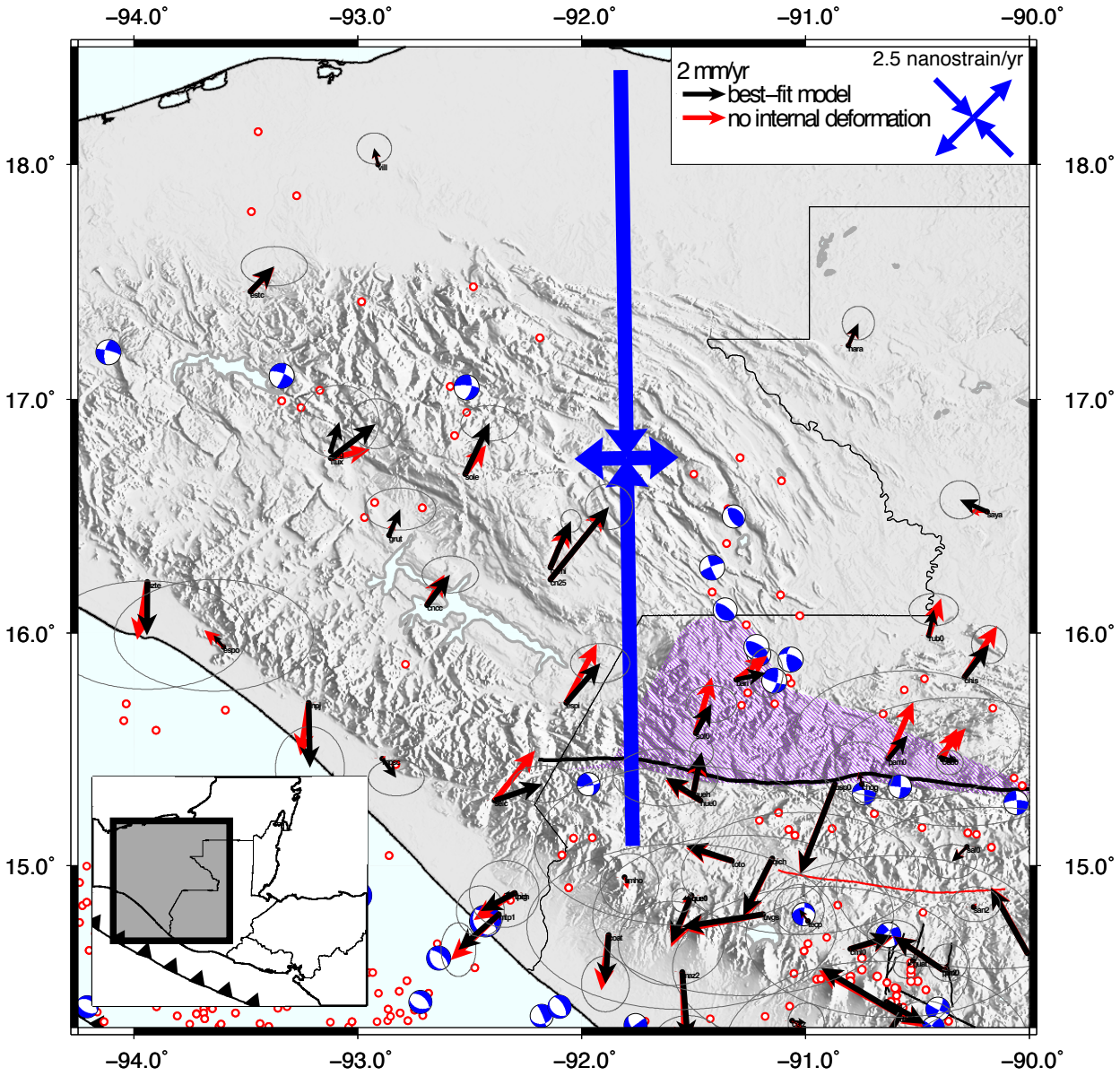

Figure 3.19. Residual velocities for best-fitting model (black arrows) with 1-σ velocity uncertainty ellipses and for alternative model where no strain-rate tensor is estimated for the deforming region north of the Polochic fault (red arrows). Bold blue arrows represent principal strain-rate axes and magnitudes predicted by the best-fitting inversion model for the deforming area north of the Polochic fault. Red and white circles show earthquake epicenters from the 1964-2008 International Seismological Centre catalog for 1964 to 2008 and the Guzman-Speziale *et al*. (2005) compilation for historic earthquakes since 1586. Purple shaded area denotes Cuchumatanes Highs region.

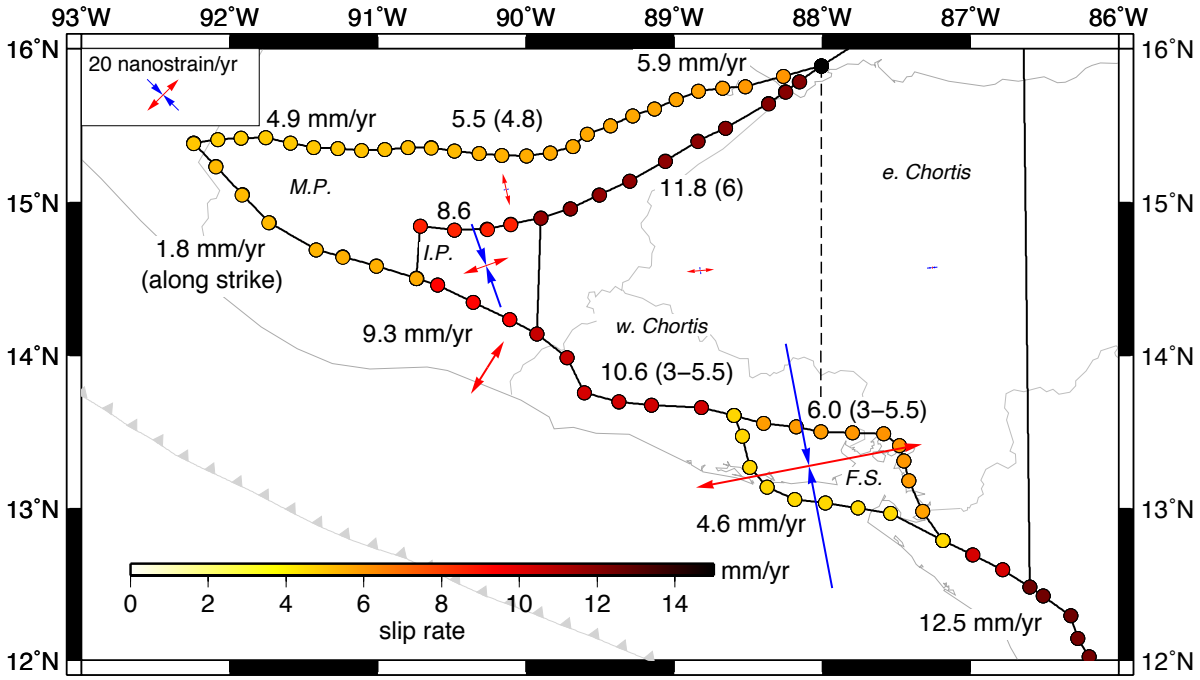

Figure 3.20. Map showing GPS and some geologic fault slip rates (mm yr^{-1}) along block boundaries and residual strain-rates determined from our best-fitting model. Dashed line marks the boundary used to define residual strain-rate tensors for the eastern and western portions of the Chortis block. Numbers listed first are fault-parallel strike-slip rates from our best-fitting model. Any parenthetical values are observed geological slip rates (mm yr^{-1}) from studies referenced in Section 3.7.5. Abbreviations: M.P.; Motagua-Polochic block, I.P.; Ipala block, F.S.; Gulf of Fonseca block, w. Chortis; western Chortis block, and e. Chortis; eastern Chortis block.

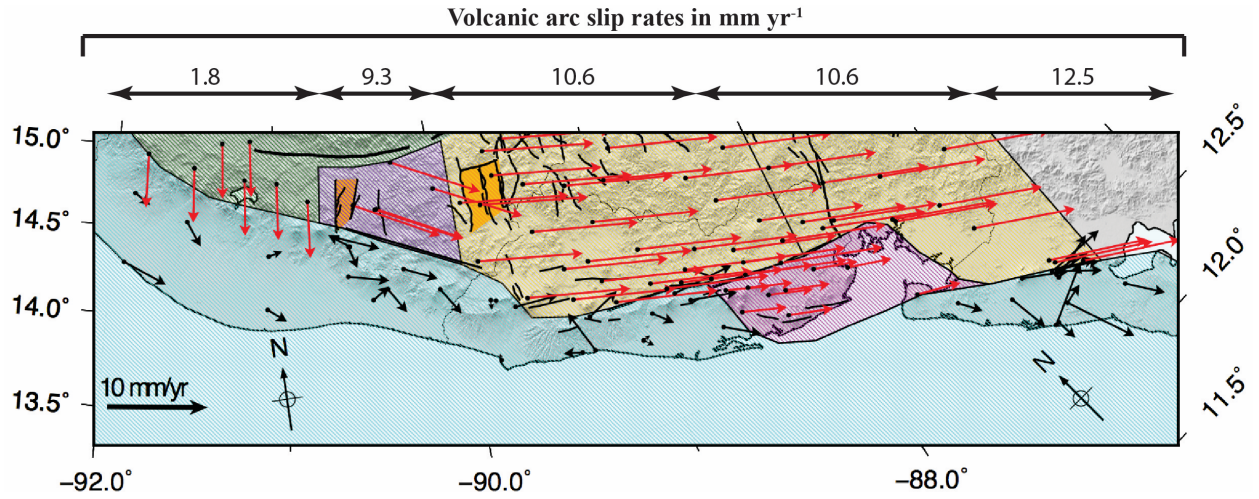

Figure 3.21. Oblique Mercator projection of El Salvador and southwest Guatemala centered on the pole (89.3°W, 13.7°N) showing residual forearc velocities (black arrows on cyan shading) and estimated rotational model component relative to the forearc sliver (red arrows). Preferred block configuration shown with shaded regions. Best-fit slip rates (mm yr^{-1}) along the volcanic arc are shown above the map.

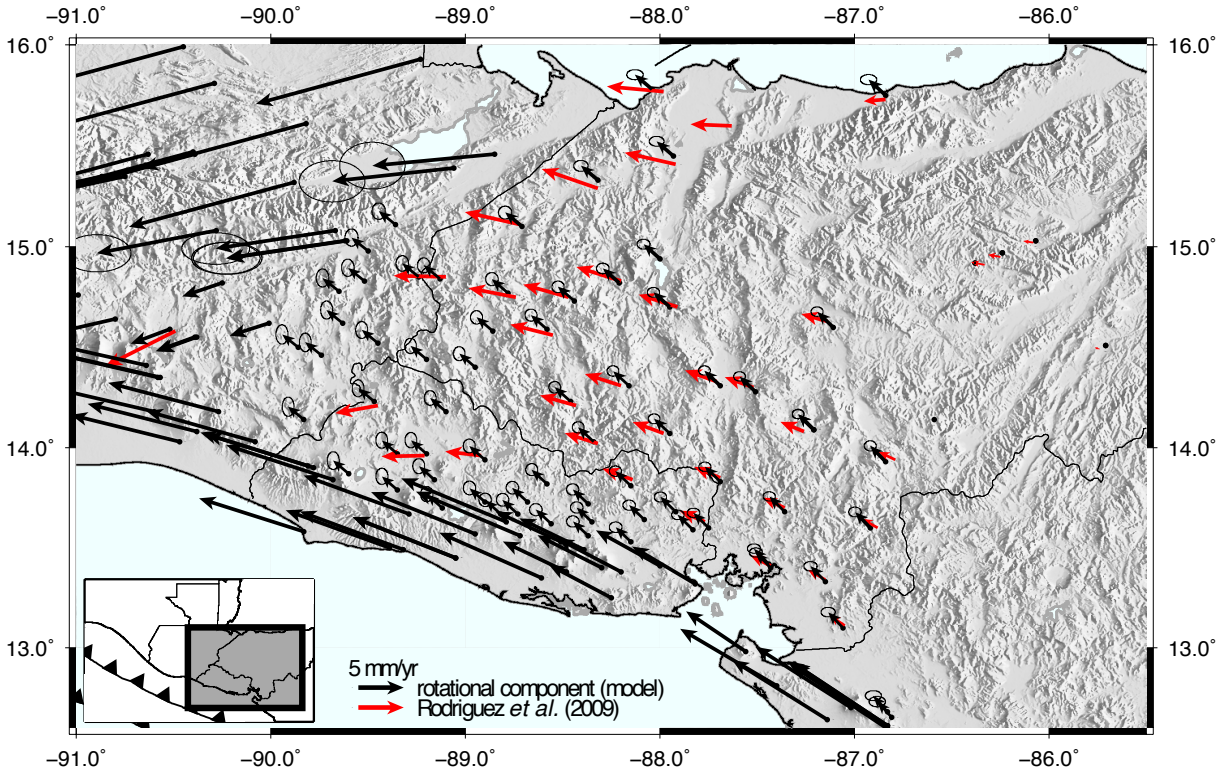

Figure 3.22. Comparison of site velocities relative to the Caribbean plate predicted by angular velocities from Table 3.2 (black arrows) and GPS velocities predicted from the Rodriguez *et al.* (2009) forward 103P model (red arrows).

S3.8 Supplementary information

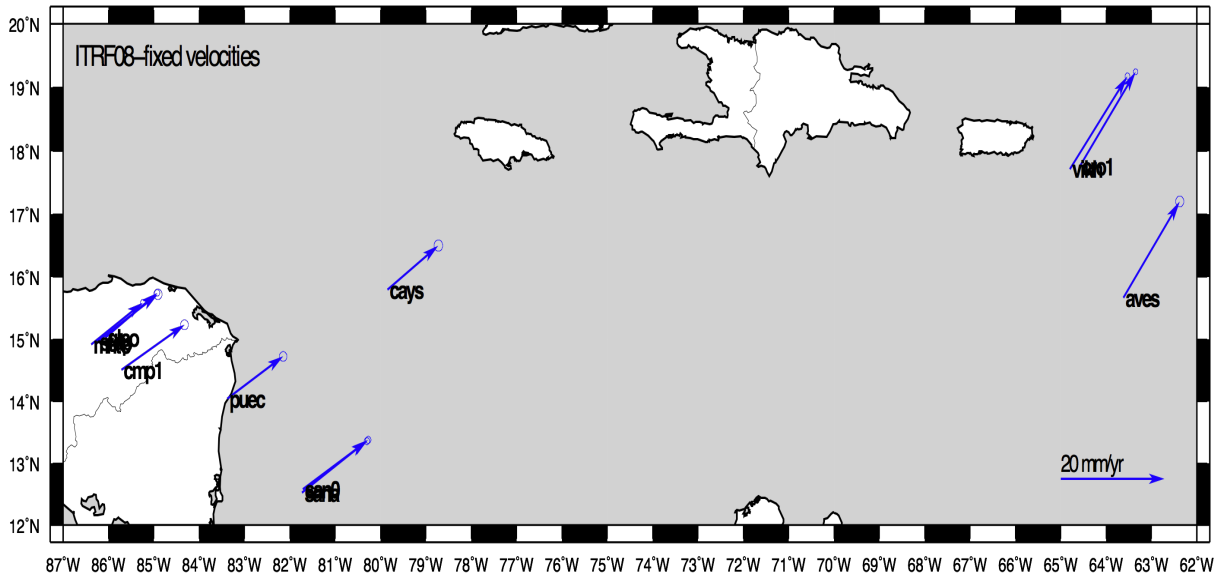

Figure S3.1. GPS site velocities relative to ITRF08 used to constrain Caribbean plate motion in our study (see Table 3.2).

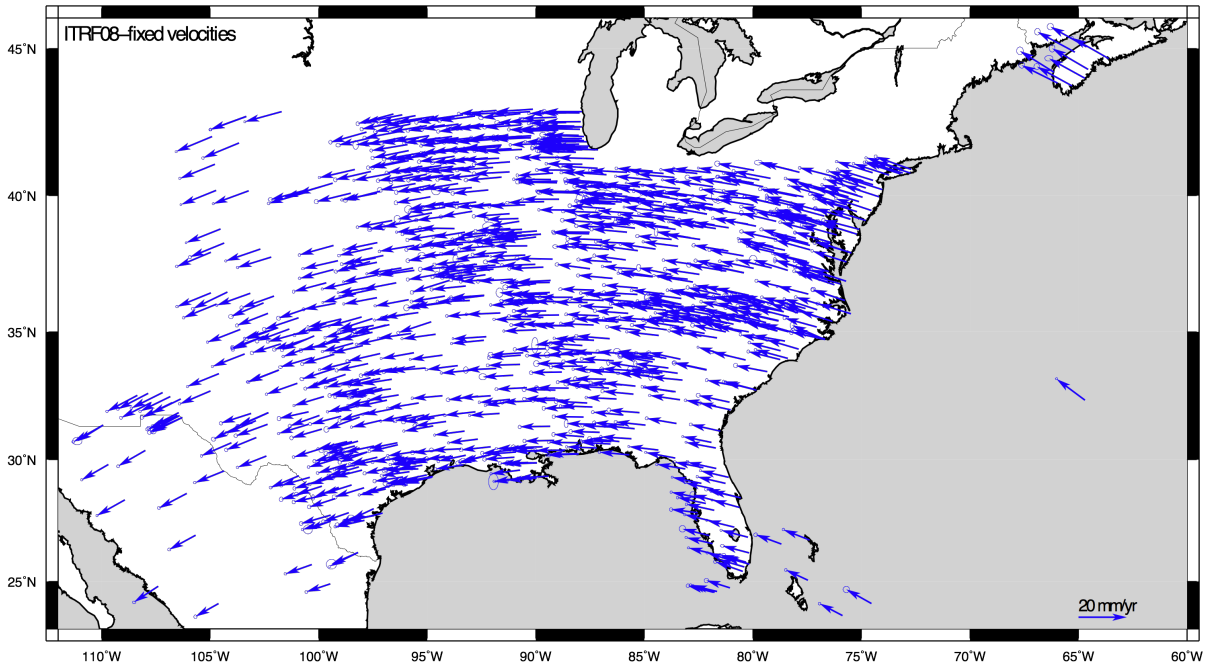

Figure S3.2. GPS site velocities relative to ITRF08 used to constrain North America plate motion in our study (see Table 3.2).

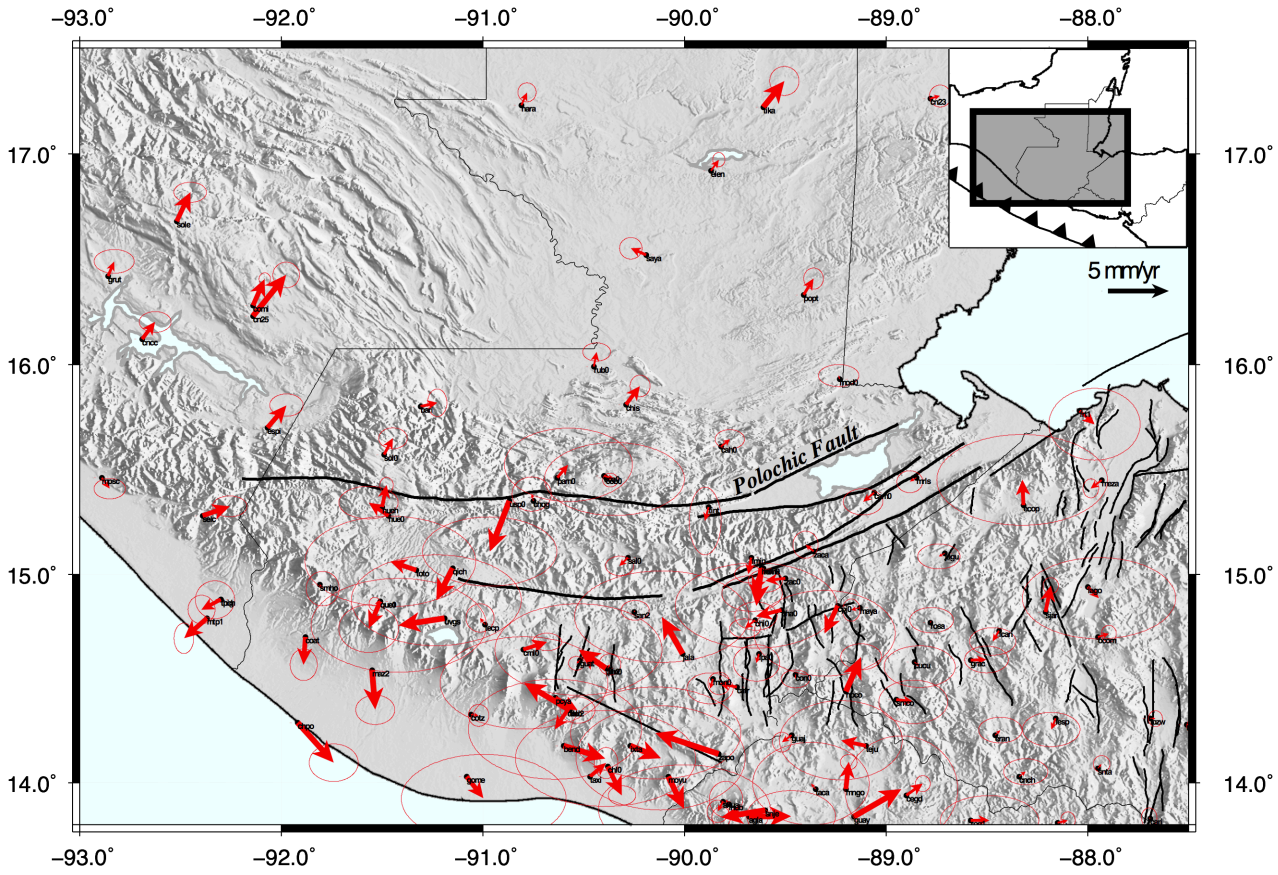

Figure S3.3. Residual velocities for best-fitting model with 1-σ velocity uncertainty ellipses.

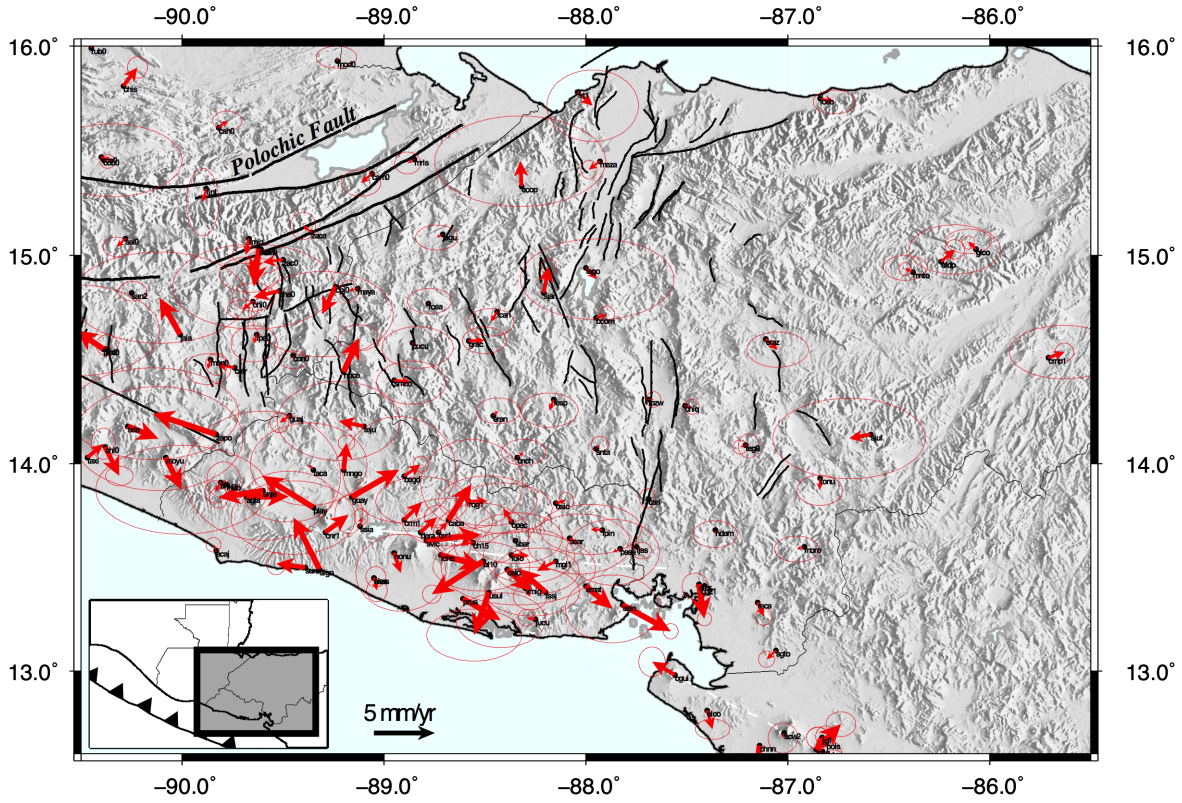

Figure S3.4. Residual velocities for best-fitting model with 1-σ velocity uncertainty ellipses.

```
#TDEFNODE model for best-fitting block model
# control file code, Ellis 2017

## Flags
fl: +pos +pio -pen +cov +vrb +atr +wcv +dgt
fl:robm +all

# GPS site velocities
gp: ALLL "vels_for_psvel_al176_CA" 3 1.0 0.0 0.0 0.0 1900.0 2017 0 5.0 0 1 1 0


# Basic model space
sa: 0 5 1500

rm: ALLL cori viej mana cn30 esti teus prt1 cng2 blu2 corn riob maz0 tran roa0 blux fsd0

#grid search
gs:  90  0.5  8  2  5

# IC = iteration control
#  Controls iteration order; 1= simulated annealing, 2= grid search
ic: 2 1 1 1 1 1 1 1 1 1 1 1 1 1 2 1 1 1 1 1 1 1 1 1 2

# IN = fault interpolation step sizes
in: 5 5

--- 2012 EQ ------
## MODEL FOR EQ

mo: c117
pf: "c117/pio" 3

em:

*****************************
## SET UP FOR MODEL SPACE

# PO = angular velocities (poles) for blocks
# po: N Lat Lon Omega; N = pole number
# NOAM pole
pole :  3 0.0 0.0 0.0

# Cocos-Caribbean pole from MORVEL
pole: 6  23.28 -132.36 0.955

# fix forearc pole from GCCM
```

```
pole: 4 2.9 -93.2 0.5621

#CA-fixed- NA moving pole
pole: 1 -74.82 20.999 0.1813

#CAfixed - Fonseca moving pole (iterating to find best solution)
pole: 13 7.3 -91.4 0.6

# Calculate strain tensor for Chiapas/southern Mexico block in inversion
si: 14

# block poles to estimate
pi: 8 10 11

###### FAULT LOCKING
ff: +20 +21 +22 +23 +24 +25 +26 +27 +28

# set fault 11 (MOPO) to type 0 (free nodes)
ft: 20 0
ft: 21 0
ft: 22 0
ft: 23 0
ft: 24 0
ft: 25 0
ft: 26 0
ft: 27 0
ft: 28 0

# Polochic
nng: 20 27 3
1 2 2 2 3 3 3 4 4 4 5 5 5 6 6 6 6 6 6 8 8 8 9 9 9 10 10
1 2 2 2 3 3 3 4 4 4 5 5 5 6 6 6 6 6 6 8 8 8 9 9 9 10 10
20 11 11 11 12 12 12 13 13 13 14 14 14 15 15 15 15 15 15 17 17 17 18 18 18 19 19

# Motagua
nng: 21 16 3
0 4 4 4 4 5 5 5 6 6 6 7 7 7 7 7
0 4 4 4 4 5 5 5 6 6 6 7 7 7 7 7
0 13 13 13 13 14 14 14 15 15 15 16 16 16 16 16

#Swan Islands
nng: 22 18 3
1 1 1 1 1 1 1 1 1 1 1 1 1 1 1 1 1 1
1 1 1 1 1 1 1 1 1 1 1 1 1 1 1 1 1 1
2 2 2 2 2 2 2 2 2 2 2 2 2 2 2 2 2 2
```

```
#Vol0
nng: 27 8 2
2 2 2 2 3 3 3 3
11 11 11 11 12 12 12 12

# Vol1
nng: 23 11 2
1 1 1 1 2 2 2 2 3 3 3
6 6 6 6 7 7 7 7 8 8 8


# Vol2
nng: 24 11 2
1 1 1 1 2 2 2 2 2 2 2 2
3 3 3 3 4 4 4 4 4 4 4 4

# Vol3
nng: 25 21 2
1 1 1 1 1 2 2 2 3 3 3 4 4 4 5 5 5 6 6 6 6
10 10 10 10 10 11 11 11 12 12 12 13 13 13 14 14 14 15 15 15 15

# MAT 0
nng: 26 45 4
1 1 1 1 1 1 1 1 1 2 3 4 5 6 7 8 9 10 11 12 13 14 15 16 17 18 19 20 21 22 23 24 25 26 27 28 29 30
31 32 32 32 32 32
33 33 33 33 33 33 33 33 33 33 34 35 36 37 38 39 40 41 42 43 44 45 46 47 48 49 50 51 52 53 54 55
56 57 58 59 60 61 62 63 64 64 64 64 64
65 65 65 65 65 65 65 65 65 65 66 67 68 69 70 71 72 73 74 75 76 77 78 79 80 81 82 83 84 85 86 87
88 89 90 91 92 93 94 95 96 96 96 96 96
97 97 97 97 97 97 97 97 97 97 97 97 97 97 97 97 98 99 100 101 102 103 104 105 106 107 108 109
110 111 112 113 114 115 116 117 118 119 120 121 122 123 123 123 123 123

# optimized LaPlacian smoothing
sm: 26 3 5e7 5e7 0.0


# Fonseca block
nng: 28 9 2
1 1 1 1 2 2 2 2 2
4 4 4 4 5 5 5 5 5


############################################################
fl: +mkb

## SETTINGS FOR GREENS FUNCTIONS
```

```
gd: a01 5.0 3.0 0 1.0 5.0 5000.0

# BLOCK/FAULT GEOMETRIES
bc: NOAM 271.147 20.986 1 1
bc: CARI 286.012 13.661 3 3
bc: FONE 269.740 13.923 4 4
bc: FOSW 270.125 12.460 4 4
bc: COCO 265.0 10.0 6 6
bc: WED2 269.731 14.588 8 8
bc: WED3 271.177 14.556 10 9
bc: WED4 272.743 14.576 10 10
bc: SLIV 269.866 15.085 11 11
bc: FONS 271.910 13.279 13 13
bc: CHIA 268.000 16.250  1 14

bp: NOAM 1 1
bp: ITRF 2 2
bp: CARI 3 3
bp: FONE 4 4
bp: FOSW 4 4
bp: COCO 6 6
bp: WED2 8 8
bp: WED3 10 9
bp: WED4 10 10
bp: SLIV 11 11
bp: FONS 13 13
bp: CHIA 1 14

## pseudo faults (blocks)
FAult: NOAM 1 NOAM.fault
FAult: CARI 3 CARI.fault
FAult: FONE 4 FORENE.fault
FAult: FOSW 5 FORESW.fault
FAult: COCO 6 COCO.fault
#FAult: WED1 7 WEDGE1.fault
FAult: WED2 8 WEDGE2.fault
FAult: WED3 9 WEDGE3.fault
FAult: WED4 10 WEDGE4.fault
FAult: CHIA 14 CHIAPAS.fault

# Locking fauts
FAult: POLO 20 POLO.fault
FAult: MOTA 21 MOTAGUA.fault
FAult: SWAN 22 SWANISLANDS.fault
FAult: VOL1 23 VOLC1.fault
FAult: VOL2 24 VOLC2.fault
```

FAult: VOL3 25 VOLC3.fault
FAult: MAT0 26 MAT_long.fault
Fault: VOL0 27 VOLC0.fault
FAult: GFON 28 FONSECA.fault

end: